REPORT DOCUMENTATION PAGE

Form Approved
OMB No. 0704-0188

Public reporting burden for this collection of information is estimated to average 1 hour per response, including the time for reviewing instructions, searching existing data sources, gathering and maintaining the data needed, and completing and reviewing the collection of information. Send comments regarding this burden estimate or any other aspect of this collection of information, including suggestions for reducing this burden, to Washington Headquarters Services, Directorate for information Operations and Reports, 1215 Jefferson Davis Highway, Suite 1204, Arlington, VA 22202-4302, and to the Office of management and Budget, Paperwork Reduction Project (0704-0188) Washington, DC 20503.

1. AGENCY USE ONLY (Leave Blank)	2. REPORT DATE June 1995	3. REPORT TYPE AND DATES COVERED Final

4. TITLE AND SUBTITLE
Finite Difference-Time Domain Analysis of Electromagnetic Interference and Radiation Problems

5. FUNDING NUMBERS

6. AUTHORS
Kevin Li

7. PERFORMING ORGANIZATION NAME(S) AND ADDRESS(ES)
Massachusetts Institute of Technology

AFRL-SR-BL-TR-98-
0037

9. SPONSORING/MONITORING AGENCY NAME(S) AND ADDRESS(ES)
AFOSR/NI
110 Duncan Avenue, Room B-115
Bolling Air Force Base, DC 20332-8080

11. SUPPLEMENTARY NOTES

12a. DISTRIBUTION AVAILABILITY STATEMENT
Approved for Public Release

12b. DISTRIBUTION CODE

13. ABSTRACT *(Maximum 200 words)*
See attached.

14. SUBJECT TERMS

19980115 227

15. NUMBER OF PAGES

16. PRICE CODE

17. SECURITY CLASSIFICATION OF REPORT	18. SECURITY CLASSIFICATION OF THIS PAGE	19. SECURITY CLASSIFICATION OF ABSTRACT	20. LIMITATION OF ABSTRACT
Unclassified	Unclassified	Unclassified	UL

FINITE DIFFERENCE-TIME DOMAIN ANALYSIS
OF ELECTROMAGNETIC INTERFERENCE
AND RADIATION PROBLEMS

by

KEVIN LI

S.B. Electrical Engineering and Computer Science,
Massachusetts Institute of Technology, Cambridge
June 1990

S.M. Electrical Engineering and Computer Science,
Massachusetts Institute of Technology, Cambridge
June 1990

E.E. Electrical Engineering and Computer Science,
Massachusetts Institute of Technology, Cambridge
June 1991

Submitted to the Department of Electrical
Engineering and Computer Science in Partial
Fulfillment of the Requirements for the Degree of

DOCTOR OF PHILOSOPHY

at the

MASSACHUSETTS INSTITUTE OF TECHNOLOGY

June 1995

Signature of Author _____

Department of Electrical Engineering and Computer Science
June 1995

Certified by _____

Professor Jin Au Kong
Thesis Supervisor

Certified by _____

Dr. Robert T. Shin
Thesis Supervisor

Accepted by _____

Professor F. R. Morgenthaler
Chairman, Departmental Committee on Graduate Students

1

MAY 1 8 1995

2

FINITE DIFFERENCE-TIME DOMAIN ANALYSIS OF ELECTROMAGNETIC INTERFERENCE AND RADIATION PROBLEMS

by

KEVIN LI

Submitted to the Department of Electrical Engineering and Computer Science
May 1995 in partial fulfillment of the requirements for the Degree of
Doctor of Philosophy

ABSTRACT

The application of the finite difference-time domain (FD-TD) technique to problems in electromagnetic interference and radiation is examined, and enhancements to the method in order to increase its accuracy and efficiency are considered. The primary motivation for studying electromagnetic radiation from various structures which compose a computer is that computers are now operating at faster speeds (i.e. 100's of MHz) and consuming more power resulting in significantly increased levels of power at higher frequencies. Three electromagnetic interference problems associated with computers are analyzed. First, electromagnetic radiation from VLSI heatsink configurations is examined. Next, electromagnetic emissions from modules-on-backplane configurations are analyzed. The third problem involves the analysis of coupling of electromagnetic energy by wires exiting from metallic enclosures. In addition to these interference problems, the effects of non-uniform substrates on radiation by microstrip patch antennas are studied. In particular the use of non-uniform substrates to reduce loss due to surface waves is examined.

The electromagnetic radiation from a VLSI chip package and heatsink structure is analyzed using the finite difference-time domain technique. The dimensions of a typical configuration calls for a multi-zone gridding scheme in the FD-TD algorithm to accommodate fine grid cells in the vicinity of the heatsink and package cavity and sparse gridding in the remainder of the computational domain. The issues pertaining to the effects of the heatsink in influencing the overall radiating capacity of the configuration are addressed. Analyses are facilitated by using simplified heatsink models and by using dipole elements as sources of electromagnetic energy to model the VLSI chip. The potential for enhancement of spurious emissions by the heatsink structure is illustrated. For heatsinks of typical dimensions, resonance is possible within the low gigahertz frequency range. The exploitation of the heatsink as an emissions shield by appropriate implementation schemes is discussed and evaluated.

The electromagnetic radiation from a modules-on-backplane configuration found

in computers is analyzed by means of the finite-difference time-domain technique. The issues pertaining to the effects of the modules in influencing the overall radiating capacity of the configuration are addressed. Analyses are facilitated by using simplified modules-on-backplane models and by using a voltage source as the source of electromagnetic energy at a connector between a module and the backplane. The potential for enhancement of spurious emissions by the module-on-backplane configuration is demonstrated. For modules of typical dimensions, resonance is observed at the hundreds of megahertz frequency range. Comparisons between numerical predictions and measurements are conducted to validate the numerical method.

The finite difference-time domain technique is used to analyze coupling of electromagnetic energy through metallic enclosures by wires and cables which exit them. Simplified configurations are considered in order to focus on the coupling of electromagnetic energy by a wire which penetrates the metallic enclosure. A lumped element model is introduced to reduce the computational domain size by replacing the external wire with a lumped element at the aperture in the metallic enclosure. The lumped element consists of a parallel set of series RLC circuits, and is designed to match the radiation admittance of the external wire as closely as possible. The potential for significant coupling of electromagnetic energy is demonstrated in the hundreds of megahertz frequency range. Comparisons between FD-TD simulations using the lumped element model and FD-TD simulations modeling the the entire external wire region are conducted to validate the numerical method and evaluate the lumped element model.

The analysis of microstrip patches on non-uniform substrates with special emphasis on the reduction of surface wave losses is conducted using the finite difference-time domain technique. The alteration to the uniform substrate involves removing a rectangular ring of the dielectric substrate which surrounds the radiating element. A perfectly matched layer absorbing boundary condition is used for enhanced performance especially where the dielectric substrate intersects the outer boundary. Simple dipole antennas and a microstrip patch antenna on non-uniform substrates are examined. It is demonstrated that the guided powers for these configurations are significantly less than those for the equivalent uniform substrate configurations.

Thesis Supervisors: Professor J. A. Kong
                   Dr. Robert T. Shin

Reader: Professor F. Morgenthaler

ACKNOWLEDGMENTS

running smoothly.

I would also like to thank Professor Morgenthaler for his time and effort in participating in my Area exam and as a reader for this thesis.

In addition to all the people who aided me in my academic studies, there are the numerous individuals who helped make my stay here at MIT enjoyable. My four years living at Next House were perhaps some of the most enjoyable ones in my life, and I thank all the residents there for contributing to making it a great place to live. In particular, I'd like to thank my two closest friends from my undergraduate years, Eric Tang and Victor Liau, for their friendship and support over the years. During my time at Edgerton House, I've met people who have helped me maintain my equilibrium by providing me with the occasional diversion from the daily grind of graduate studies. To these people, thanks for everything. I wish to thank Bob Atkins for all the help he's given me in my studies, and for his friendship. To Matt Kamon, thanks for all the sports that we played together.

To my brother and sister, Patrick and Ruby, thanks for always being there, and helping out with so many different things. I'll always appreciate having an older brother and sister who put up with and looked out for their little brother.

I wish to thank my darling, Frances Lam, for her encouragement at the end of my studies. I'll always appreciate our insightful conversations and I'll always be grateful to her for helping me grow in areas beyond electromagnetics.

Finally, I wish to thank my parents for without their support, understanding and encouragement, I would never have achieved all that I have. Mom, Dad, I hope I've made you proud of me.

To My Family

8

Contents

List of Figures

12

13

14

15

16

17

List of Tables

Chapter 1

Introduction

This thesis examines the application of the finite difference-time domain (FD-TD) technique to problems in electromagnetic interference and radiation, and the enhancement of the method in order to increase its accuracy and/or efficiency. In particular, three electromagnetic interference problems associated with computers are analyzed. First, electromagnetic radiation from VLSI heatsink configurations is examined. Next, electromagnetic emissions from modules-on-backplane configurations is analyzed. The third problem involves the analysis of coupling of electromagnetic energy by wires exiting from metallic enclosures. In addition to these interference problems, the effects of non-uniform substrates on microstrip patch antennas is studied with an emphasis on the reduction of surface wave generation.

1.1 Introduction to Finite Difference-Time Domain Technique

The finite difference-time domain (FD-TD) technique was introduced by K. S. Yee in 1966 [1], and has since been applied to many problems in electromagnetics [2]-[83].

This method directly solves Maxwell's time-dependent curl equations by discretizing them in space and time. The discretization in space is such that the shortest wavelengths of interest are resolved by 10 or more cells, and the time step is determined by stability criteria. Electric and magnetic fields are interlaced on a spatial grid, and calculated in a leap-frog manner which allows time marching.

The FD-TD method has grown in popularity and usefulness as computers have grown in size and speed. The FD-TD method has filled a niche in the electromagnetics community by offering an alternative to other numerical methods, such as method of moments [84]-[91], various high frequency techniques [92]-[97], and finite elements [11], for analyzing electromagnetic phenomena. The FD-TD technique has notable advantages over each of these other methods. The FD-TD method, finite element method and method of moments are all essentially exact methods, in that Maxwell's equations are solved numerically and one of the most significant sources of error introduced is due to the finite discretization of the problem. The FD-TD method is most similar to the finite element method and is in fact a subset of the finite element method. The basic condition imposed on finite elements to convert to finite difference methods, is the assumption that the fields are assumed constant over a single cell, instead of having some pre-defined spatial dependence over a single cell, such as linear or piece-wise sinusoidal dependencies. With finite element methods the computational domain is broken into a grid which typically conforms to the object under study, and the fields are approximated by basis functions associated with each cell. With FD-TD, the computational domain is also broken into a grid, which more often than not, does not conform to the object under study, and the fields are assumed

to be constant within single cells. Since the grid frequently does not conform to the object under study, the discretization of the object is only approximate, unlike typical finite element implementations. In particular, with the most popular rectangular grid in FD-TD, curved surfaces are approximated by staircase approximations. Both of the methods are based on the differential form of Maxwell's equations and inherently have unbounded computational domains. Hence, it is necessary to limit the size of the computational domain by applying an artificial absorbing boundary condition which simulates unbounded space at the outer boundary of the computational domain [67]-[83].

The FD-TD method differs from the method of moments, in that the former is based on the differential form of Maxwell's equations in the time domain and the latter is based on the integral form of Maxwell's equations in the frequency domain. One particular advantage of the method of moments is that since an integral equation is used, the problem is bounded, and hence the only errors introduced are due to the discretization of the currents, as no artificial truncation of the computational domain is required. Another advantage of the method of moments is that once the impedance matrix has been calculated from the integral equation and then inverted, the scattered fields for different excitation configurations can be calculated relatively quickly.

Certain advantages of the FD-TD method are that since it is a time domain method, it can be used to solve multiple frequencies simultaneously, and it is more flexible in implementing modifications to models. However, one drawback of exciting multiple frequencies is that if the structure is highly resonant and the resonant frequency is excited then achieving steady state will require significantly more time

steps. The number of time steps required to obtain steady state will be proportional to the Q of the resonant structure. However, extrapolation schemes based on Prony's method [114] and other methods [115] have been developed to obtain the late time response of highly resonant structures, thus reducing the computational burden associated with analyzing resonant structures with the FD-TD technique. For comparison, the method of moments is more efficient at obtaining monostatic radar cross sections for multiple observation angles at a single frequency, while FD-TD is more efficient at obtaining monostatic radar cross sections for multiple frequencies at a single observation angle.

The high-frequency techniques, which include physical optics, and physical, geometrical, and uniform theories of diffraction, are popular for studying electrically large objects. They are usually the only feasible method for studying objects which are over 20 wavelengths in size, because the previous numerical exact methods are all memory and computationally intensive, and current computers, in general, cannot handle problems of this size. However, they are inapplicable to low frequency or electrically small problems and are approximate methods, in that they do not include various higher order effects, such as multiple interactions. So, in contrast with the previous methods, including the FD-TD method, these high-frequency techniques are approximate instead of exact solutions.

One class of problems which have been investigated using the FD-TD technique is prediction of electromagnetic scattering and radar cross section [2]-[18],[98]-[101]. This class of problems included scattering from canonical shapes, surface features, and actual aircraft. In addition, calculation of radiation characteristics of wire, mi-

crostrip patch, and other antennas has been performed [19],[20]. Various microwave components, such as vias, striplines, microwave filters, and microstrip lines have been studied [21]-[25]. The characteristic impedance and effective wavenumber of guiding structures have been calculated using the FD-TD technique [26]-[29]. The FD-TD method has been used in the analysis of electromagnetic interference problems associated with aircraft and computers [30]-[39],[102]-[105]. The technique has also been used to study scattering from periodic media [40]-[45]. Since the conception of FD-TD method for electromagnetics in 1966, it has been extensively modified to increase its range of applicability, its accuracy, and its efficiency. The first implementation of the FD-TD technique, which is still perhaps the most popular, utilized a regular rectangular lattice [2],[6]. One difficulty with rectangular grids is that curved or slanted surfaces are approximated by staircases. In certain problems the staircase approximation can cause significant errors due to unwanted scattering from the staircases. In an effort to address this shortcoming of rectangular grids, other grids have been investigated, such as triangular grids [46],[47], a grid in spherical coordinates [48], and a generalized non-orthogonal grid [49]-[51]. However, each of these alternative grids have not been used as extensively, primarily because the grid generation is a difficult task and typically requires extensive user input and requires significantly more memory storage since a description of each non-uniform node in the grid must be kept. An additional problem which arises with non-uniform grid dimensions is that the stability criteria for the time step size is determined by the smallest cell in the grid. If there are small cells anywhere within the grid, the time step must be reduced to accommodate those small cells; this will in turn require more time steps to be executed to achieve steady state.

In addition, modifications have been made to the rectangular grid to allow subgridding for increased resolution [52]-[55], and local deformations to the grid to better model curved surfaces [8],[51]. Subgridding is particularly useful in cases where there are smaller but important features in the object under study which must be carefully modeled. In these cases a smaller grid is used only in the region required. Hence, subgridding potentially allows higher resolution where needed without excessively increasing the memory required or the number of computations per time step. One drawback with subgridding is that the time step must be chosen to accommodate the smallest cell, which imposes additional computational costs similar to those incurred with non-uniform grids. The subgridding scheme incurs some additional complexity to the FD-TD algorithm. Local deformations to the rectangular grid reduces or eliminates the problem of staircase approximations to curved surfaces. The generation of the deformed grid typically requires some user input, however it is far easier to generate than a triangular grid. While those cells which include deformed edges require additional information, the majority of the cells in the computational domain will remain standard rectangular cells which are very efficient in memory and computational usage.

Regardless of which grid is used, an absorbing boundary condition (ABC) is needed at the outer boundary of the computational domain, in order to truncate the computational domain and to simulate unbounded space [67]-[83]. One of the earlier forms of ABC was to actually model a layer of lossy material at the outer boundary which hopefully absorbed most of the outgoing waves and incurred minimal reflections. This solution was somewhat undesirable because the outer layer

tended to be fairly large, and sometimes imposed a severe computational penalty. So ABCs, which are approximations to the one-way wave equation, were developed and displayed fairly good characteristics and were efficient [67]-[77]. Essentially, these one-way wave equations factor the wave equation into inward and outward traveling waves, and the square root associated with these one-way wave equations is approximated using various polynomial expansions. These ABCs typically perform better at angles near normal incidence, although certain implementations can be tailored to have minimized reflections at user specified angles. However, significant reflections occur at angles near grazing to the outer boundary. These ABCs have been applied to the various types of grids. Recently, a perfectly matched layer (PML) ABC has been developed which inserts a reflectionless lossy layer of finite thickness at the outer boundary of the computational domain [78]-[83]. This reflectionless layer is achieved by modifying Maxwell's equations (non-physical) in the perfectly matched layer. The performance of this PML ABC has been exceptionally good with reasonable computational and memory costs. In particular, the angular performance of the PML ABC appears to be better than most of the one-way wave equation ABCs.

The earliest implementations of the FD-TD technique dealt primarily with perfectly conducting bodies, but has since been extended to dielectric, conductive and magnetic media [2], and more recently to dispersive [9],[10],[56],[57], gyrotropic [58], and anisotropic media [21]. Modifications to the FD-TD method for thin dielectric and conducting layers have been performed in order to avoid decreasing the cell size to the thickness of the dielectric layer [59]-[65]. In addition, modeling of small apertures (sub-cell dimensions) in perfectly conducting screens has been recently im-

plemented in the FD-TD method through the use of modified or "smart" FD-TD cells [15]. In each of these prior cases, reducing the cell size locally would not in itself be prohibitively difficult, however the associated reduction in the time step size to accommodate the small cells would be computationally cumbersome.

1.2 Technical Discussion

The finite difference-time domain technique is highly accurate, and can generate virtually exact solutions for scattering and radiation problems [1]-[12]. The approximations associated with the finite difference-time domain technique include the use of difference equations in place of differential equations and the use of an absorbing boundary condition which simulates unbounded space. Theoretically, the computational domain is unbounded, consisting of the infinite region surrounding the scatterer. However, an absorbing boundary condition can be utilized at an artificial outer boundary to make the computational domain finite and to simulate the unbounded space beyond. Within the finite computational domain, Maxwell's equations are discretized on a grid. In order to obtain accurate results, the spacing between the nodes in the grid must be on the order of a tenth of a wavelength. Given the excitation sources, the electromagnetic scattering from the object can be found by marching in time.

The most popular formulation of the FD-TD technique is Yee's algorithm [1]. Yee discretizes the electric and magnetic fields on a rectangular grid [See Figure 1.1]. The spatial and temporal partial derivatives in Maxwell's equations are replaced with centered difference approximations. Two major advantages associated with Yee's algorithm are that objects of arbitrary geometry can be easily modeled, and that the algorithm is easily implemented. This algorithm has second-order accuracy in both time and space. The disadvantages of rectangular grids include the use of staircase approximations for curved or slanted surfaces and the use of a rectangular outer boundary. Generally, the staircase approximation can model curved surfaces reasonably well. However, for some cases such as when strong surface waves are
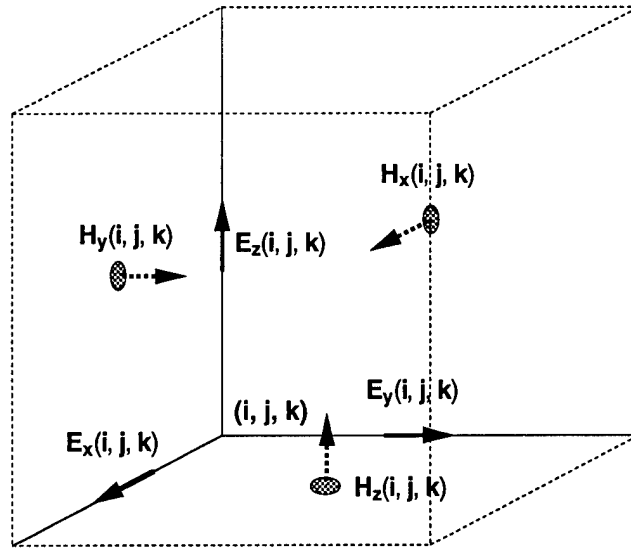
Figure 1.1: Field components in Yee's rectangular grid.

present, a very fine resolution rectangular grid must be employed to obtain accurate results.

On the outer boundary of this grid, an absorbing boundary condition (ABC) must be used to simulate unbounded space [67]-[83]. Ideally, the absorbing boundary will absorb all outgoing waves, thus producing no reflections. Realistically, the absorbing boundary condition is chosen to minimize the reflections over all possible angles. The absorbing boundary condition must be well posed in order to construct stable difference approximations. Also the absorbing boundary condition should be local in time and space, so that only a limited number of time steps of information near the outer boundary need be stored. A commonly employed local absorbing boundary condition for rectangular grids is the second-order approximation derived by Engquist and Majda [68]. In treating the edges of the outer boundary, a first-order absorbing boundary condition is utilized since tangential differences are unavailable.

This combination of absorbing boundary conditions has been shown to be effective [2],[67],[77].

In addition to the boundary conditions at the outer boundary, boundary conditions at material interfaces are enforced. In particular, at perfectly conducting surfaces the tangential electric fields are set to zero. For interfaces between different dielectric and magnetic materials, the tangential electric and magnetic fields are kept continuous.

In using the finite difference-time domain technique, the fields propagate through the computational domain in discrete time steps. The time marching is executed such that the electric and magnetic fields are calculated in an alternating manner. In order to insure the stability of the time stepping algorithm, the size of the time step must satisfy Equation 1.1 for three-dimensional rectangular grids [6].

$$\Delta t \leq \frac{1}{c}\left(\frac{1}{\Delta x^2} + \frac{1}{\Delta y^2} + \frac{1}{\Delta z^2}\right)^{-1/2} \tag{1.1}$$

where Δx, Δy, and Δz are the dimensions of the cell, Δt is the time step, and c is the speed of light.

Various excitation sources such as plane waves, dipoles, or voltage or current sources can be used. The time dependence of these sources can be sinusoidal or a Gaussian pulse. The Gaussian pulse can be used for analyzing multiple frequencies by Fourier transforming the time response of the system. Frequently, the computational domain will be separated into two regions when a plane wave excitation is used. In the inner region near the object, the total fields are calculated, whereas in the

outer region, the scattered fields are calculated. At the boundary between the two
regions, the incident field is added/subtracted from the scattered/total fields needed
to calculate the total/scattered fields on the opposite side of the boundary.

The FD-TD simulation is normally begun with zero fields everywhere within the
computational domain. At each following time step, the magnetic fields are calculated
in terms of the electric and magnetic fields of the previous half and full time steps using
the difference equations obtained from Maxwell's equations. Next the electric fields
are calculated in a similar manner. The absorbing boundary conditions are applied
to the electric fields tangential to the outer boundary. The electric fields tangential
to any perfectly conducting surfaces are set to zero. The excitation source can be
implemented at cells containing a voltage or current source, or a dipole. Alternatively
with a plane wave source, the implementation occurs at the interface between the total
and scattered field regions. These steps are essentially repeated until steady state is
reached for a sinusoidal excitation, or until all the transient scattered fields have
propagated out of the computational domain for a Gaussian pulse excitation.

During the FD-TD simulation, certain electric and magnetic fields are stored
for post-processing. For Gaussian pulse time-dependent excitations, it is necessary
to store the entire time response so that it can be Fourier transformed and frequency
domain information can be extracted. With sinusoidal time-dependent excitations,
it is only necessary to determine the magnitude and phase. In cases where the near-
field response at a particular location is desired, then only the field values at the cell
containing that location need be stored. Alternatively with voltage or current sources,
it is occasionally desirable to store the voltage and current at the source location, from

which the radiation impedance of an antenna can be determined. Frequently the tangential scattered fields on a surface enclosing the object of interest are calculated. From these scattered fields, the radiated power and the far-field response can be easily obtained [106]-[109].

1.3   Description of Thesis

This thesis deals exclusively with the application of the finite difference-time domain (FD-TD) technique to solve new problems, and the enhancement of the method in order to increase its accuracy and/or efficiency. Following the introduction in Chapter 1, the finite difference-time domain technique is described in detail in Chapter 2. Those aspects of the method which are common to each of the problems examined are addressed, while modifications to the method for specific problems are discussed in the chapters describing the problem. Difference equations for free space and dielectric/magnetic media are derived, as well as difference equations for the treatment of interfaces between dielectric/magnetic media, and perfect electric and magnetic conductors. Stability and accuracy issues are discussed. In addition, the implementation of infinite plane wave sources as well as local voltage or current sources are examined. The treatment of the outer boundary by an absorbing boundary condition is also reviewed. The conversion of near-field data to far-field data is also addressed. Finally some limitations of the method and its overall capabilities are discussed.

The next three chapters concentrate on electromagnetic interference in computer systems. The extension of regulatory electromagnetic emissions limits to the gigahertz range of frequencies for high-performance computing equipment necessitates caution in the design and implementation of components within computing systems [102],[104],[105]. The avoidance of potentially efficient radiators at the design and development phases is of interest. The objective is to minimize the need for cost-prohibitive corrective measures commonly invoked when problems are encountered in tests on assembled systems.

In Chapter 3, the effects of a heatsink placed over a chip package on the electromagnetic emissions characteristics of the configuration are examined [31]-[33]. Such an interest is justified for the following reasons. The heatsink is typically metallic and in close proximity to the chip which utilizes large amounts of power. The heatsink will display radiation characteristics similar to those of a microstrip patch antenna [111]-[112]. The electrical dimensions of the heatsink structure are comparable to the wavelengths of concern. In light of the ever-increasing power levels used in high-performance integrated circuits, the heatsink is and will continue to be an indispensable component of the VLSI chip packaging configuration. The objectives are to identify and quantify the effects of the heatsink on the radiating properties of the package structure; to understand and exploit the radiation mechanisms; and to evaluate viable heatsink implementation schemes for minimizing the overall radiating capacity.

The electromagnetic radiation properties of a heatsink and integrated circuit (IC) package configuration are analyzed by means of suitable models. A typical heatsink/package configuration of interest is shown in Figure 1.2. The heatsink may be modeled as a perfectly conducting rectangular slab positioned over a finite-size dielectric medium representing the chip package. The chip package is supported in turn by a dielectric layer of infinite extent over an infinite ground plane which models the substrate or printed wiring board (PWB) with (at least) one reference layer. The electromagnetic sources used to model the active chip include electric and magnetic dipoles of vertical and horizontal orientations positioned on the package/substrate dielectric interface. The choice of such elements circumvents the problem of deriving

                                    ┌─ MOUNTING SCREW
                                        ┌─ HEATSINK

CERAMIC CHIP ─
CARRIER
                                                    ─ SUPPORT FRAME
                                                    ─ PRINTED WIRING BOARD

                                        ─ SUPPORT ASSEMBLY
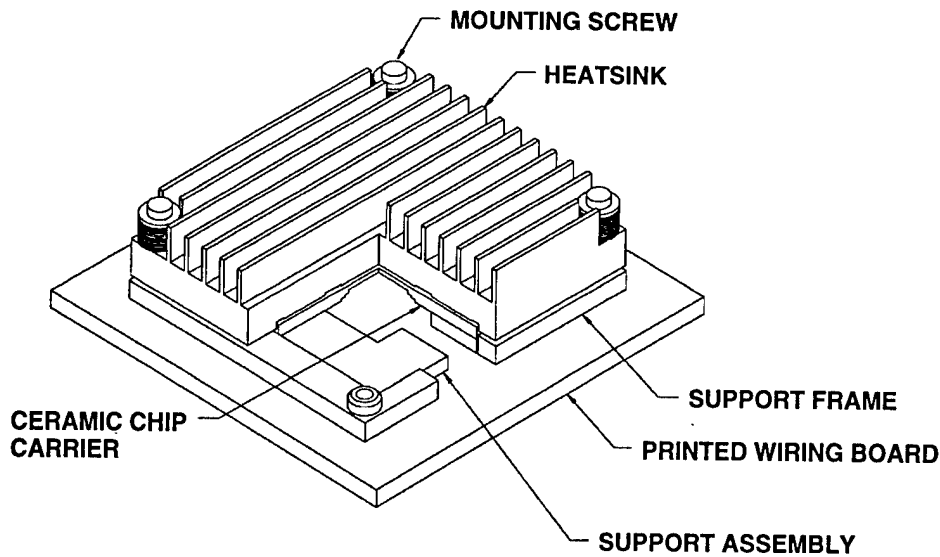
Figure 1.2: Cut away view of a VLSI package/heatsink configuration.

a rigorous model for the VLSI circuitry as an electromagnetic source and eliminates
factors which may otherwise clutter the understanding and interpretation of the phys-
ical processes associated with the spurious radiation study. The resulting model of
an electromagnetically-coupled slab structure is shown in Figure 1.3. The use of a
model with reduced complexity for both source and heatsink is to facilitate the in-
terpretation of results based on underlying physics. The extension to other heatsink
configurations (e.g., circular or finned) and source models may be accomplished with
the numerical solution employed. With sufficiently fine grids, circular heatsinks may
be adequately modeled. The model in Figure 1.3 is readily modified to model vari-
ous heatsink implementation schemes proposed for emissions reduction consideration.
Field strengths, and radiated powers are computed for quantitative analysis and eval-
uation.

    Certain technical issues in the application of the FD-TD technique to this prob-

TOP VIEW

SOURCE

IC PACKAGE

SIDE VIEW

HEATSINK (CONDUCTING SLAB)

REFERENCE PLANE
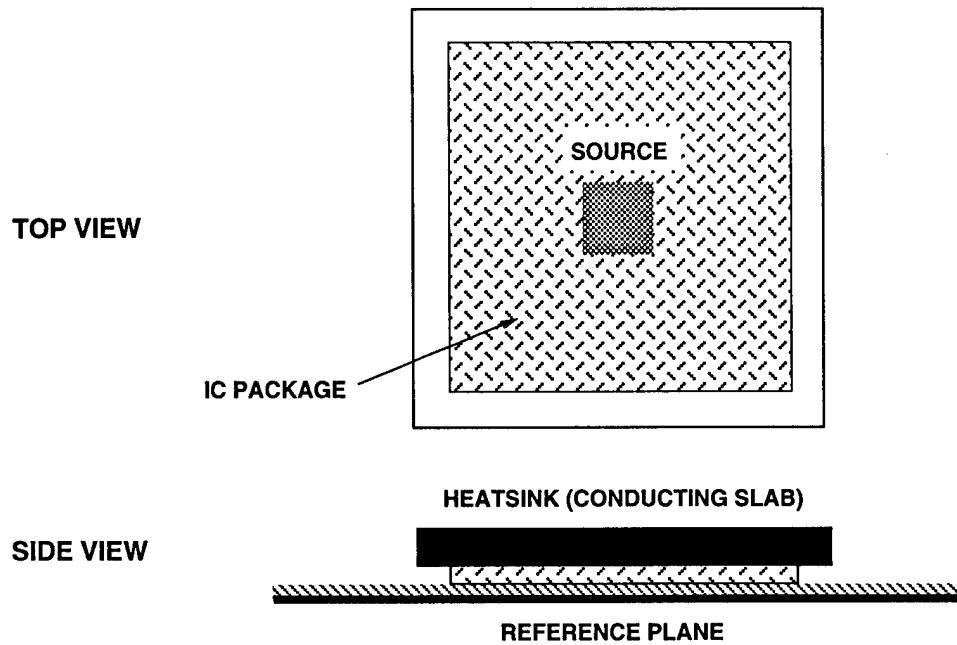
Figure 1.3: Cross-sectional view of simplified package/heatsink model.

lem will be addressed. The use of a multizone gridding scheme to accommodate fine grid cells in the vicinity of the heatsink and package cavity and sparse grids in the remainder of the computational domain [10],[31],[52]-[55]. This modification allows increased resolution and accuracy where needed, while not sacrificing too much computational power in regions where the increased resolution is unnecessary. The implementation of the electric and magnetic dipoles of vertical and horizontal orientations in the FD-TD scheme requires normalization. Since the dipoles are implemented by exciting the fields at a single node in the rectangular grid, the dimensions of the dipole, and hence their dipole moments, are not precisely defined. The error associated with the dipole size ambiguity is small, although it does increase with increasing frequency. So the necessary normalization can be accomplished by performing an ad-

ditional FD-TD simulation of a simplified configuration and relating those results with analytical solutions [10],[31], although the error associated with these small current sources is small [15].

The radiation enhancement for various dipole sources are examined and quantified. The effects of the height of the heatsink cavity and the dielectric loading of the cavity are examined. The changes to the radiation characteristics due to the addition of fins to the heatsink are analyzed. Two modifications for reducing the overall radiation from the heatsink configuration are considered: the use of metallic posts for grounding the heatsink to the ground plane and the application of a conducting gasket around the lip of the heatsink/ground plane cavity. Finally some comments are made regarding the overall radiation characteristics of heatsinks, the effectiveness of the two radiation reduction measures examined, and the application of the FD-TD method to this problem.

In Chapter 4, the electromagnetic emissions characteristics of a modules-on-backplane configuration found in computers are examined [34],[35]. The modules-on-backplane is of interest because it is a common packaging hierarchy. Also a typical modules-on-backplane configuration has reference plane dimensions which are appreciable electrically at frequencies in the hundreds of megahertz, and the structure, as a whole, may function as an antenna. The objective is to identify and quantify the radiation mechanisms in a modules-on-backplane configuration and to validate the numerical model with measurements.

A typical configuration for the modules-on-backplane is shown in Figure 1.4. The elements of the packaging hierarchy of interest in this study are the backplane,
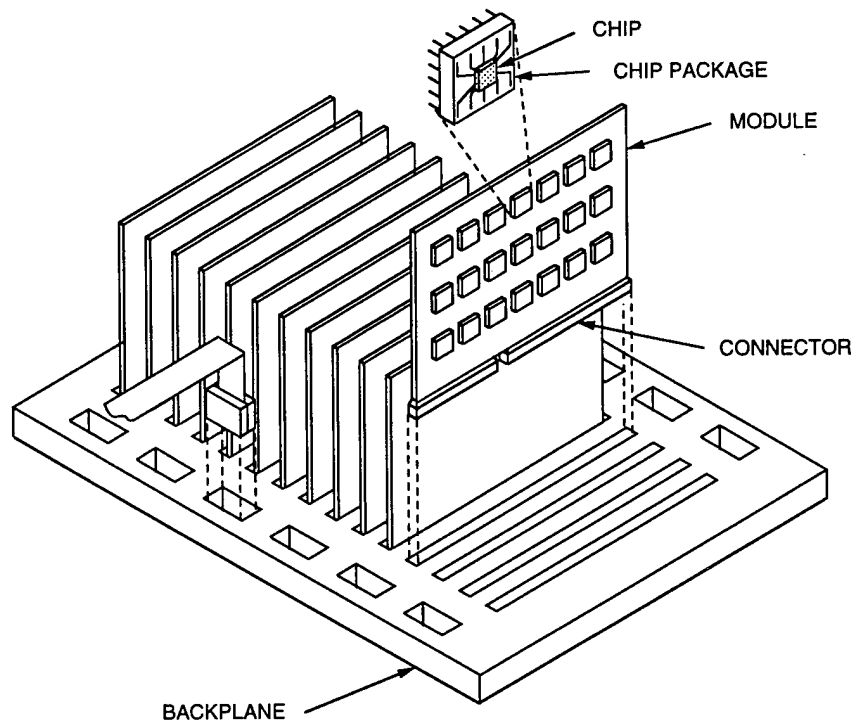
Figure 1.4: A typical modules-on-backplane configuration.

the connector and the module. The modules and backplane are printed wiring boards with at least one reference layer. The connector contains numerous wires for carrying signals and for providing power to the various reference layers. Due to the complexity of the modules-on-backplane configuration, it is necessary to simplify the problem to some reasonable level of detail. The modules and backplanes are populated with numerous chips and contain many signal paths. However, the single largest conductor or signal path in them is typically one of the ground or reference planes. These reference planes, because of their larger dimensions, tend to enhance radiation more at lower frequencies than the other elements associated with the modules/backplane. For this reason, the modules and backplane will be modeled as perfectly conducting plates. The source considered is the transient, inductive voltage developed across the
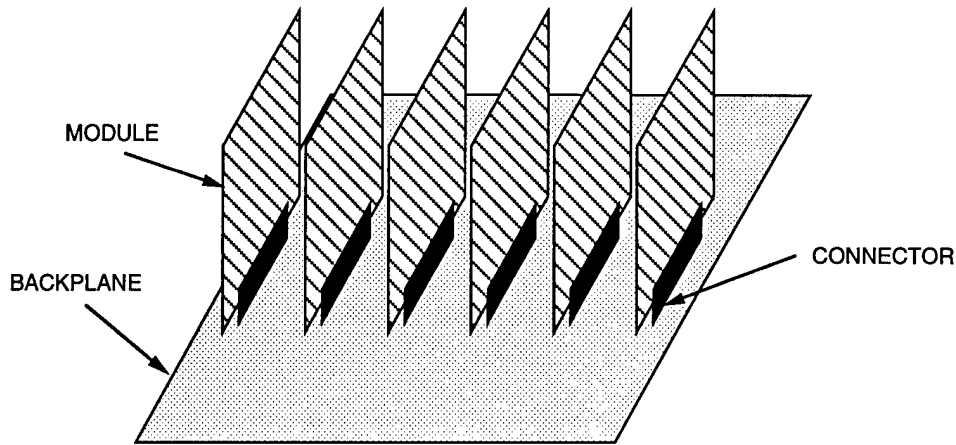
Figure 1.5: Simplified model of the modules-on-backplane configuration.

connector between the module and the backplane [113]. This source is implemented
by applying a voltage source between the module and the backplane. The result-
ing simplified model of the modules-on-backplane configuration is shown in Figure
1.5. The simplified modules-on-backplane and source configuration avoids many of
the complex interactions inherent in a real modules-on-backplane configuration which
would otherwise clutter or mask the fundamental radiation mechanisms. The exten-
sion to other modules-on-backplane configurations (e.g., multiple modules, enclosed)
and source models may be accomplished with the numerical method employed.

In this problem, the source modeling in the FD-TD algorithm for this configura-
tion is of some concern. The transient voltage source is implemented by imposing the
electric field values in the vertical direction at the location of the connector [24],[25].
This implementation models a matched source coaxial cable transmission line excita-
tion.

In applying the FD-TD technique to certain of the more resonant modules-on-

MODULE-ON-BACKPLANE MODEL

HP 8510 NETWORK ANALYZER

PORT 1

SEMI-RIGID COAXIAL CABLE

TEST PORT CABLE
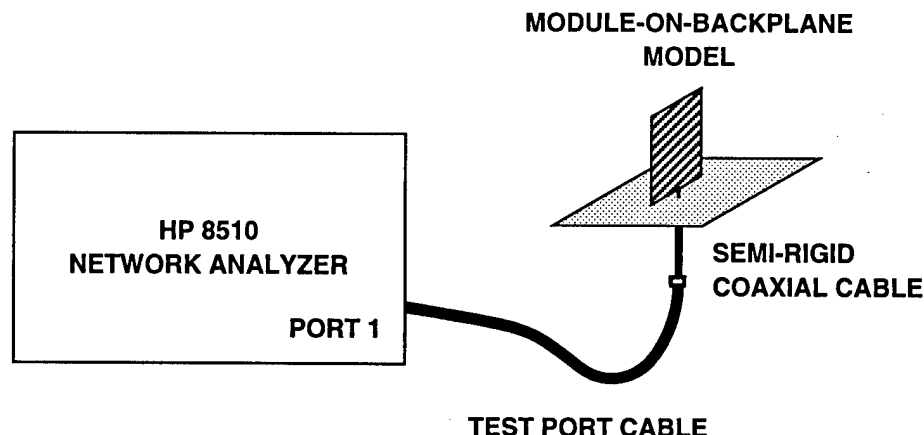
Figure 1.6: Measurement setup for modules-on-backplane configurations.

backplane configurations, a large number of time steps (on the order of thousands) are required in order to achieve steady state. An extrapolation scheme based on Prony's method is used in conjunction with a relatively short FD-TD time response to efficiently obtain the late time response [114]. This extrapolation method was applied to the time response of the current and voltage on the connector. The FD-TD simulation is executed long enough such that the remaining time response approximately contains only a few decaying complex exponentials. Prony's method approximately determines the complex amplitudes and complex frequencies of these exponentials. Once the complex amplitudes and frequencies are determined, then the time response is extrapolated to the desired extent.

Measurements were performed using an HP 8510 Network Analyzer. The network analyzer was connected to the modules-on-backplane configuration to be tested by a test port cable and semi-rigid coaxial cable [see Figure 1.6]. In each of the measurements, the center conductor of the coaxial cable was soldered to the module

under test such that the coaxial cable was in contact with at least one of the reference planes in the module. S-parameter data (S_{11}) was recorded using this set-up and are used to derive the radiation impedances and radiated powers of the various configurations tested.

Calculations for various single module-on-backplane configurations are conducted and compared with measurements in order to determine their correlation. Next multiple module-on-backplane configurations are examined and compared with measurements. A partially enclosed configuration is analyzed, and FD-TD predictions and measurements are compared. Finally observations are made about the overall accuracy of the FD-TD technique and the general radiation characteristics of modules-on-backplane configurations.

In Chapter 5, the coupling of electromagnetic energy by wires exiting from metallic enclosures is examined. Metallic enclosures are commonly used to house computer systems and usually have cables and wires exiting from them. A simplified configuration is shown in Figure 1.7. Since the metallic enclosure functions both as a electromagnetic shield and as a resonator structure, the most important sources of radiation from the box come from any holes in the box used for ventilation and from any cables exiting from the box used for power or data transfer [15],[39]. In particular for cables, the currents on the interior surface of the enclosure can couple to wires exiting the enclosure, and the wire can function as an antenna in the hundreds of MHz frequency range [20],[66]. For these reasons, the coupling of electromagnetic energy out of the metallic enclosure by cables is of great interest. One of the goals of this study is to determine the efficiency of the coupling of electromagnetic energy

MODULES-ON-BACKPLANE AS SOURCE

METAL ENCLOSURE

**SMALL
APERTURE**
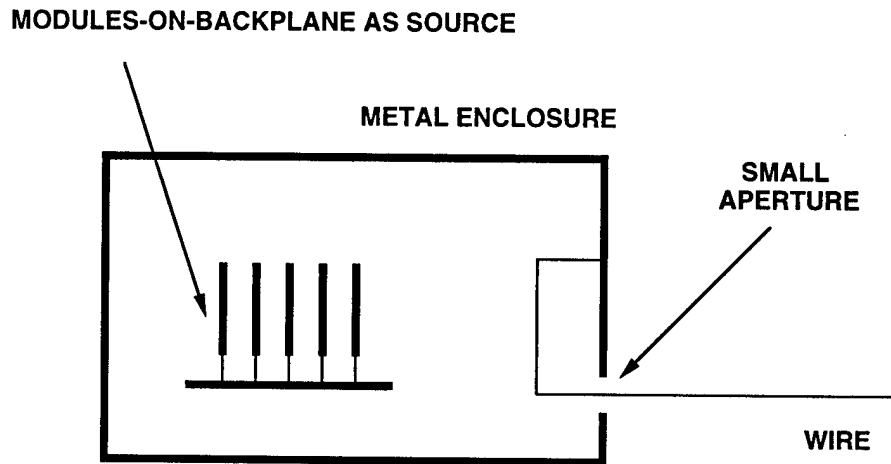
WIRE

Figure 1.7: A simple wire exiting a metallic enclosure configuration.

from sources inside the enclosure to the region outside through a cable exiting the enclosure.

In analyzing the problem, the following assumptions and simplifications are used. The radiation admittance of the outer portion of the wire is assumed to be simple enough such that it can be adequately modeled by a set of of series RLC circuits which are in parallel [116]-[118]. Essentially, one RLC circuit is used to match each resonance present in the wire's radiation admittance. Hence, an important aspect of this research is the development of a model for this circuit within the FD-TD algorithm [22],[23]. An additional assumption is that the radiation mechanism is primarily due to the current on the wire and not the fields traveling through the aperture, since the aperture size is only being modeled in a simple manner and will depend on the FD-TD cell size. The enclosure and wires are all assumed to be perfectly conducting.

The motivation for using the lumped element model within the FD-TD technique instead of a full FD-TD simulation is to obtain significant computational savings. In particular, the lumped element model replaces the model of the region outside the enclosure, thus eliminating the need to include the outer region in the FD-TD simulation. The computational requirements of the lumped element model are a mere fraction of the remaining FD-TD requirements, on the order of tens of storage variables compared to tens of thousands of storage variables, and similar ratios for arithmetic operations. Hence, if the computational domain can be reduced by 50 percent, then the computational savings will be very close to 50 percent.

In addition, if the external region is simple enough, the radiation admittance of the wire can be approximated using analytical solutions for wires over infinite ground planes. Hence, the external problem can be solved first, and then the internal region can be analyzed using the lumped element model with the FD-TD technique. Also by splitting the problem into two regions, the probable problem of a significant difference in scale between features in the two regions is naturally resolved, as each region can be examined separately using whatever scale is most appropriate for each region.

Two simplified configurations are considered in analyzing the real configuration. The simplest model involves a wire over an infinite ground plane being excited by a coaxial line. This first model is used to validate the lumped element model, since analytical solutions exist for a complex load terminating a coaxial transmission line. This model will also provide a measure for how well the lumped element can model the true radiation admittance. The next model involves a wire connected to an infinite metal screen exiting through a small aperture, with a dipole source on the

"inner" side of the metal screen. In each of these two cases, the radiation admittance and total radiated power are examined for FD-TD simulations modeling the entire structure and FD-TD simulations using the lumped element model. Finally, the usefulness of the lumped element model, and the overall radiation characteristics of this configuration are summarized.

In Chapter 6, the effects of a non-uniform substrate on the radiation characteristics of microstrip patch antennas is examined using the finite difference-time domain technique [147]-[152],[111],[119]-[144]. The substrate is altered by the removal of a rectangular ring from the dielectric substrate which surrounds the patch antenna as shown in Figure 1.8. A microstrip patch antenna is examined because it is a popular antenna which is printed on a substrate. In designing microstrip antennas, some features, which are commonly optimized, include minimizing the overall antenna size, maximizing the antenna's bandwidth in frequency and minimizing the losses due to surface waves. A higher dielectric constant substrate can be used to reduce the antenna size as the wavelength is reduced in the dielectric with increasing dielectric constant [111],[140],[141]. The bandwidth is proportional to the height of the microstrip patch. However, in achieving these two goals, the loss due to surface waves is increased which is undesirable. The introduction of this discontinuity into the substrate allows a significant portion of the power in the surface waves to be reflected at the free space/dielectric interface and be radiated into the free space region.

The generation of surface waves is undesirable for the following reasons. First, power coupled into guided waves is power which is not radiated which lowers the overall radiation efficiency of the antenna [140]. Also, with a finite size substrate, the

TOP VIEW

SIDE VIEW

Figure 1.8: Microstrip patch antenna on a non-uniform dielectric substrate.
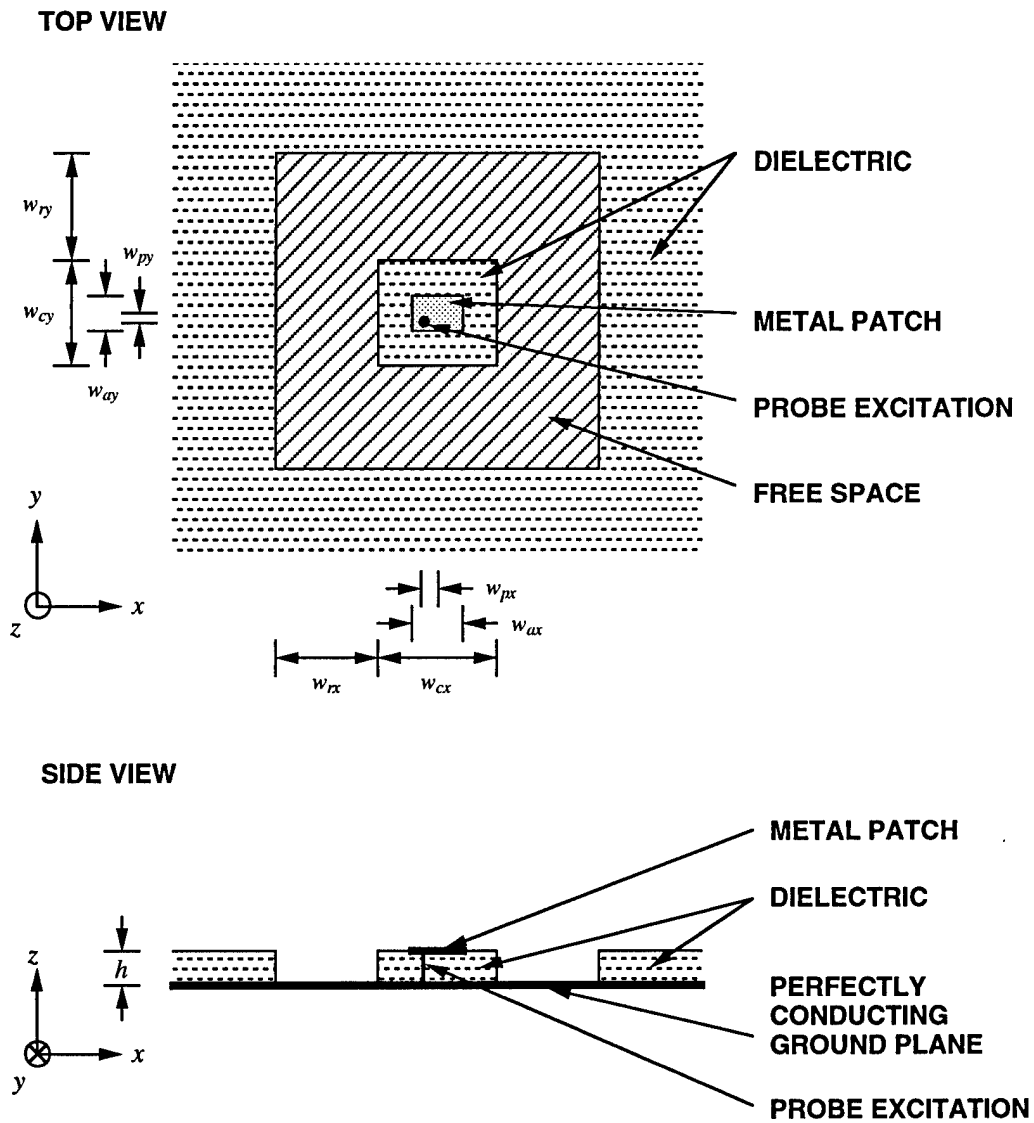
guided waves could cause unwanted high side lobes or back lobes due to interaction with the truncation of the substrate. When phased arrays are mounted on a common substrate, significant coupling between elements can occur which can cause limitations in the scanning range of the array [147],[148].

A perfectly matched layer (PML) absorbing boundary condition (ABC) [78]-[83] is utilized instead of the standard one-way wave equation absorbing boundary condition [67]-[74]. The PML ABC is chosen for its superior performance in general and in particular for its handling of dielectric interfaces at the outer boundary.

In comparing microstrip patch antennas over uniform and non-uniform substrates, the following radiation characteristics were examined. The effects of the addition of the non-uniformity on resonant frequency and bandwidth are observed. The guided power for each configuration is also calculated. The guided power is approximated by integrating the Poynting power passing through the portion of a closed surface enclosing the antenna which also lies within the substrate. The non-uniformity is shown to reduce the amount of power coupled into surface waves. In addition, the gain patterns of the two configurations are examined. Finally, the advantages and disadvantages of using a non-uniform substrate is discussed.

Chapter 7 summarizes the work presented, highlights some of the more significant results, and suggests future directions for research.

Chapter 2

Finite Difference-Time Domain Technique

2.1 Introduction

The first step in applying the FD-TD technique involves approximating Maxwell's equations in differential form by center differences in space and time. The locations at which electric and magnetic fields are calculated are positioned on some sort of grid. For three-dimensional problems, the most popular grid is a rectangular mesh [1]. A significant advantage of using rectangular grids over other grids [48]-[51] is greater simplicity. However, since objects are discretized on a rectangular grid, curves and slanted lines are approximated by staircases.

To begin the FD-TD simulation, all the fields within the computational domain are initially set to zero. At each time step, the electric fields are calculated in terms of the electric and magnetic fields of the previous time step using the difference equations obtained from Maxwell's equations. Next, the magnetic fields are calculated in a similar manner. Boundary conditions are enforced at the outer boundary of

49

the computational domain and at all dielectric and conducting interfaces. At the outer boundary a second-order absorbing boundary condition is utilized in order to simulate unbounded space beyond the computational domain [67]-[74]. The tangential electric fields are set to zero at the conducting surfaces, and the tangential electric and magnetic fields are kept continuous at the dielectric/magnetic boundaries. The implementation of the excitation source typically requires that certain electric and magnetic fields be updated at each time step. These steps are essentially repeated until steady state is reached for a sinusoidal excitation, or until all the transient scattered fields have propagated out of the computational domain for a Gaussian pulse excitation.

2.2   Maxwell's Equations in Rectangular Coordinates

In implementing the finite difference-time domain technique, Maxwell's equations must be discretized in space and time. In this case, Yee's lattice, which is a rectangular grid, is utilized because of its simplicity [1]. Maxwell's equations in vector differential form in an isotropic and homogeneous dielectric and magnetic material are

$$\nabla \times \overline{E} = -\frac{\partial \overline{B}}{\partial t} - \sigma_m \overline{H} \qquad (2.1)$$

$$\nabla \times \overline{H} = \frac{\partial \overline{D}}{\partial t} + \sigma \overline{E} \qquad (2.2)$$

$$\nabla \cdot \overline{D} = \rho \qquad (2.3)$$

$$\nabla \cdot \overline{B} = \rho_m \qquad (2.4)$$

and the constitutive relations are

$$\overline{B} = \mu\overline{H} = \mu_r\mu_0\overline{H} \tag{2.5}$$

$$\overline{D} = \epsilon\overline{E} = \epsilon_r\epsilon_0\overline{E} \tag{2.6}$$

where ϵ_0 is the free-space permittivity, 8.854×10^{-12} F/m and μ_0 is the free-space permeability, $4\pi \times 10^{-7}$ H/m. In addition, ϵ_r and μ_r are respectively the relative permittivity and permeability, ρ and ρ_m are electric and magnetic charge, and σ and σ_m are electric and magnetic conductivities, respectively. The magnetic charge and conductivity are simply mathematical constructs in order to facilitate the analysis of lossy magnetic materials. Maxwell's divergence equations, (2.3) and (2.4), are satisfied in the finite difference scheme by applying appropriate initial and boundary conditions. The actual difference equations used in the FD-TD technique are based upon Maxwell's curl equations, (2.1) and (2.2), and the constitutive relations, (2.5) and (2.6).

In a rectangular coordinate system, Equations (2.1), (2.2), (2.5) and (2.6), can be written as the following set of scalar equations,

$$\mu_r\mu_0\frac{\partial H_x}{\partial t} = \frac{\partial E_y}{\partial z} - \frac{\partial E_z}{\partial y} - \sigma_m H_x \tag{2.7}$$

$$\mu_r\mu_0\frac{\partial H_y}{\partial t} = \frac{\partial E_z}{\partial x} - \frac{\partial E_x}{\partial z} - \sigma_m H_y \tag{2.8}$$

$$\mu_r\mu_0\frac{\partial H_z}{\partial t} = \frac{\partial E_x}{\partial y} - \frac{\partial E_y}{\partial x} - \sigma_m H_z \tag{2.9}$$

$$\epsilon_r\epsilon_0\frac{\partial E_x}{\partial t} = \frac{\partial H_z}{\partial y} - \frac{\partial H_y}{\partial z} - \sigma E_x \tag{2.10}$$

$$\epsilon_r \epsilon_0 \frac{\partial E_y}{\partial t} = \frac{\partial H_x}{\partial z} - \frac{\partial H_z}{\partial x} - \sigma E_y \qquad (2.11)$$

$$\epsilon_r \epsilon_0 \frac{\partial E_z}{\partial t} = \frac{\partial H_y}{\partial x} - \frac{\partial H_x}{\partial y} - \sigma E_z \qquad (2.12)$$

In free space, where $\epsilon_r = \mu_r = 1$ and $\sigma = \sigma_m = 0$, Equations (2.7) to (2.12) simplify to

$$\mu_0 \frac{\partial H_x}{\partial t} = \frac{\partial E_y}{\partial z} - \frac{\partial E_z}{\partial y} \qquad (2.13)$$

$$\mu_0 \frac{\partial H_y}{\partial t} = \frac{\partial E_z}{\partial x} - \frac{\partial E_x}{\partial z} \qquad (2.14)$$

$$\mu_0 \frac{\partial H_z}{\partial t} = \frac{\partial E_x}{\partial y} - \frac{\partial E_y}{\partial x} \qquad (2.15)$$

$$\epsilon_0 \frac{\partial E_x}{\partial t} = \frac{\partial H_z}{\partial y} - \frac{\partial H_y}{\partial z} \qquad (2.16)$$

$$\epsilon_0 \frac{\partial E_y}{\partial t} = \frac{\partial H_x}{\partial z} - \frac{\partial H_z}{\partial x} \qquad (2.17)$$

$$\epsilon_0 \frac{\partial E_z}{\partial t} = \frac{\partial H_y}{\partial x} - \frac{\partial H_x}{\partial y} \qquad (2.18)$$

2.3   Center Differences and the Unit Cell

The following notation for any function of time and space will be used in the finite difference equations,

$$f(i\Delta x, j\Delta y, k\Delta z, n\Delta t) = f^n(i, j, k) \qquad (2.19)$$

The partial derivatives in space and time, within Maxwell's equations, are ap-
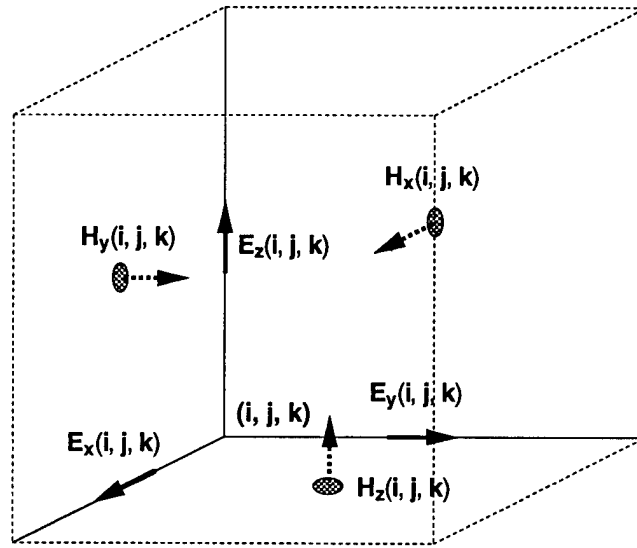
Figure 2.1: Field locations on three-dimensional rectangular grid.

proximated using center differences,

$$\frac{\partial f(\xi)}{\partial \xi} \approx \frac{f(\xi + \Delta\xi/2) - f(\xi - \Delta\xi/2)}{\Delta\xi} \tag{2.20}$$

The electric and magnetic field components are interlaced in time, and are calculated in a leap-frog manner (i.e., first the electric fields are calculated, then the magnetic fields are calculated, and the sequence is repeated). The electric and magnetic field components are interlaced spatially a half grid cell apart. The locations of the field components on a unit cell of the rectangular grid are shown in Figure 2.1.

2.4   Difference Equations in Free Space

The finite difference equations in free space, are obtained by applying center differences to Equations (2.13) to (2.18).

$$
\epsilon_0 \frac{E_x^{n+1}(i+\frac{1}{2},j,k) - E_x^n(i+\frac{1}{2},j,k)}{\Delta t} =
$$

$$
\frac{H_z^{n+\frac{1}{2}}(i+\frac{1}{2},j+\frac{1}{2},k) - H_z^{n+\frac{1}{2}}(i+\frac{1}{2},j-\frac{1}{2},k)}{\Delta y}
$$

$$
- \frac{H_y^{n+\frac{1}{2}}(i+\frac{1}{2},j,k+\frac{1}{2}) - H_y^{n+\frac{1}{2}}(i+\frac{1}{2},j,k-\frac{1}{2})}{\Delta z} \tag{2.21}
$$

$$
\epsilon_0 \frac{E_y^{n+1}(i,j+\frac{1}{2},k) - E_y^n(i,j+\frac{1}{2},k)}{\Delta t} =
$$

$$
\frac{H_x^{n+\frac{1}{2}}(i,j+\frac{1}{2},k+\frac{1}{2}) - H_x^{n+\frac{1}{2}}(i,j+\frac{1}{2},k-\frac{1}{2})}{\Delta z}
$$

$$
- \frac{H_z^{n+\frac{1}{2}}(i+\frac{1}{2},j+\frac{1}{2},k) - H_z^{n+\frac{1}{2}}(i-\frac{1}{2},j+\frac{1}{2},k)}{\Delta x} \tag{2.22}
$$

$$
\epsilon_0 \frac{E_z^{n+1}(i,j,k+\frac{1}{2}) - E_z^n(i,j,k+\frac{1}{2})}{\Delta t} =
$$

$$
\frac{H_y^{n+\frac{1}{2}}(i+\frac{1}{2},j,k+\frac{1}{2}) - H_y^{n+\frac{1}{2}}(i-\frac{1}{2},j,k+\frac{1}{2})}{\Delta x}
$$

$$
- \frac{H_x^{n+\frac{1}{2}}(i,j+\frac{1}{2},k+\frac{1}{2}) - H_x^{n+\frac{1}{2}}(i,j-\frac{1}{2},k+\frac{1}{2})}{\Delta y} \tag{2.23}
$$

$$
\mu_0 \frac{H_x^{n+\frac{1}{2}}(i,j+\frac{1}{2},k+\frac{1}{2}) - H_x^{n-\frac{1}{2}}(i,j+\frac{1}{2},k+\frac{1}{2})}{\Delta t} =
$$

$$\frac{E_y^n(i, j + \frac{1}{2}, k + 1) - E_y^n(i, j + \frac{1}{2}, k)}{\Delta z}$$

$$-\frac{E_z^n(i, j + 1, k + \frac{1}{2}) - E_z^n(i, j, k + \frac{1}{2})}{\Delta y} \tag{2.24}$$

$$\mu_0 \frac{H_y^{n+\frac{1}{2}}(i + \frac{1}{2}, j, k + \frac{1}{2}) - H_y^{n-\frac{1}{2}}(i + \frac{1}{2}, j, k + \frac{1}{2})}{\Delta t} =$$

$$\frac{E_z^n(i + 1, j, k + \frac{1}{2}) - E_z^n(i, j, k + \frac{1}{2})}{\Delta x}$$

$$-\frac{E_x^n(i + \frac{1}{2}, j, k + 1) - E_x^n(i + \frac{1}{2}, j, k)}{\Delta z} \tag{2.25}$$

$$\mu_0 \frac{H_z^{n+\frac{1}{2}}(i + \frac{1}{2}, j + \frac{1}{2}, k) - H_z^{n-\frac{1}{2}}(i + \frac{1}{2}, j + \frac{1}{2}, k)}{\Delta t} =$$

$$\frac{E_x^n(i + \frac{1}{2}, j + 1, k) - E_x^n(i + \frac{1}{2}, j, k)}{\Delta y}$$

$$-\frac{E_y^n(i + 1, j + \frac{1}{2}, k) - E_y^n(i, j + \frac{1}{2}, k)}{\Delta x} \tag{2.26}$$

Rearranging terms,

$$E_x^{n+1}(i + \tfrac{1}{2}, j, k) = E_x^n(i + \tfrac{1}{2}, j, k)$$

$$+\eta_0 \frac{\Delta \tau}{\Delta y} \left[H_z^{n+\frac{1}{2}}(i + \tfrac{1}{2}, j + \tfrac{1}{2}, k) - H_z^{n+\frac{1}{2}}(i + \tfrac{1}{2}, j - \tfrac{1}{2}, k) \right]$$

$$-\eta_0 \frac{\Delta \tau}{\Delta z} \left[H_y^{n+\frac{1}{2}}(i + \tfrac{1}{2}, j, k + \tfrac{1}{2}) - H_y^{n+\frac{1}{2}}(i + \tfrac{1}{2}, j, k - \tfrac{1}{2}) \right] \tag{2.27}$$

$$E_y^{n+1}(i, j + \tfrac{1}{2}, k) = E_y^n(i, j + \tfrac{1}{2}, k)$$

$$+\eta_0 \frac{\Delta \tau}{\Delta z} \left[H_x^{n+\frac{1}{2}}(i, j + \tfrac{1}{2}, k + \tfrac{1}{2}) - H_x^{n+\frac{1}{2}}(i, j + \tfrac{1}{2}, k - \tfrac{1}{2}) \right]$$

$$-\eta_0 \frac{\Delta \tau}{\Delta x} \left[H_z^{n+\frac{1}{2}}(i + \tfrac{1}{2}, j + \tfrac{1}{2}, k) - H_z^{n+\frac{1}{2}}(i - \tfrac{1}{2}, j + \tfrac{1}{2}, k) \right] \tag{2.28}$$

$$E_z^{n+1}(i,j,k+\tfrac{1}{2}) = E_z^n(i,j,k+\tfrac{1}{2})$$

$$+\eta_0 \frac{\Delta\tau}{\Delta x}\left[H_y^{n+\frac{1}{2}}(i+\tfrac{1}{2},j,k+\tfrac{1}{2}) - H_y^{n+\frac{1}{2}}(i-\tfrac{1}{2},j,k+\tfrac{1}{2})\right]$$

$$-\eta_0 \frac{\Delta\tau}{\Delta y}\left[H_x^{n+\frac{1}{2}}(i,j+\tfrac{1}{2},k+\tfrac{1}{2}) - H_x^{n+\frac{1}{2}}(i,j-\tfrac{1}{2},k+\tfrac{1}{2})\right] \qquad (2.29)$$

$$H_x^{n+\frac{1}{2}}(i,j+\tfrac{1}{2},k+\tfrac{1}{2}) = H_x^{n-\frac{1}{2}}(i,j+\tfrac{1}{2},k+\tfrac{1}{2})$$

$$+\frac{1}{\eta_0}\frac{\Delta\tau}{\Delta z}\left[E_y^n(i,j+\tfrac{1}{2},k+1) - E_y^n(i,j+\tfrac{1}{2},k)\right]$$

$$-\frac{1}{\eta_0}\frac{\Delta\tau}{\Delta y}\left[E_z^n(i,j+1,k+\tfrac{1}{2}) - E_y^n(i,j,k+\tfrac{1}{2})\right] \qquad (2.30)$$

$$H_y^{n+\frac{1}{2}}(i+\tfrac{1}{2},j,k+\tfrac{1}{2}) = H_y^{n-\frac{1}{2}}(i+\tfrac{1}{2},j,k+\tfrac{1}{2})$$

$$+\frac{1}{\eta_0}\frac{\Delta\tau}{\Delta x}\left[E_z^n(i+1,j,k+\tfrac{1}{2}) - E_z^n(i,j,k+\tfrac{1}{2})\right]$$

$$-\frac{1}{\eta_0}\frac{\Delta\tau}{\Delta z}\left[E_x^n(i+\tfrac{1}{2},j,k+1) - E_x^n(i+\tfrac{1}{2},j,k)\right] \qquad (2.31)$$

$$H_z^{n+\frac{1}{2}}(i+\tfrac{1}{2},j+\tfrac{1}{2},k) = H_z^{n-\frac{1}{2}}(i+\tfrac{1}{2},j+\tfrac{1}{2},k)$$

$$+\frac{1}{\eta_0}\frac{\Delta\tau}{\Delta y}\left[E_x^n(i+\tfrac{1}{2},j+1,k) - E_x^n(i+\tfrac{1}{2},j,k)\right]$$

$$-\frac{1}{\eta_0}\frac{\Delta\tau}{\Delta x}\left[E_y^n(i+1,j+\tfrac{1}{2},k) - E_y^n(i,j+\tfrac{1}{2},k)\right] \qquad (2.32)$$

where

$$\eta_0 = \sqrt{\frac{\mu_0}{\epsilon_0}} \qquad (2.33)$$

$$\tau = c_0 t = \frac{t}{\sqrt{\mu_0\epsilon_0}} \qquad (2.34)$$

where η_0 is the free space impedance and c_0 is the speed of light in free space.

2.5 Difference Equations for Dielectric and Magnetic Media

The finite difference equations in an isotropic, homogeneous, dielectric and magnetic material are obtained by discretizing Equations (2.7) to (2.12). The derivatives are replaced by center differences and the electric and magnetic field terms involving electric and magnetic conductivities are approximated by using an average of the field values at a half time step before and after the desired time.

The finite difference equations approximations for Maxwell's equations in dielectric and magnetic material are

$$\epsilon_r \epsilon_0 \frac{E_x^{n+1}(i+\frac{1}{2},j,k) - E_x^n(i+\frac{1}{2},j,k)}{\Delta t} =$$

$$\frac{H_z^{n+\frac{1}{2}}(i+\frac{1}{2},j+\frac{1}{2},k) - H_z^{n+\frac{1}{2}}(i+\frac{1}{2},j-\frac{1}{2},k)}{\Delta y}$$

$$-\frac{H_y^{n+\frac{1}{2}}(i+\frac{1}{2},j,k+\frac{1}{2}) - H_y^{n+\frac{1}{2}}(i+\frac{1}{2},j,k-\frac{1}{2})}{\Delta z}$$

$$-\sigma \frac{E_x^{n+1}(i+\frac{1}{2},j,k) + E_x^n(i+\frac{1}{2},j,k)}{2} \tag{2.35}$$

$$\epsilon_r \epsilon_0 \frac{E_y^{n+1}(i,j+\frac{1}{2},k) - E_y^n(i,j+\frac{1}{2},k)}{\Delta t} =$$

$$\frac{H_x^{n+\frac{1}{2}}(i,j+\frac{1}{2},k+\frac{1}{2}) - H_x^{n+\frac{1}{2}}(i,j+\frac{1}{2},k-\frac{1}{2})}{\Delta z}$$

$$-\frac{H_z^{n+\frac{1}{2}}(i+\frac{1}{2},j+\frac{1}{2},k) - H_z^{n+\frac{1}{2}}(i-\frac{1}{2},j+\frac{1}{2},k)}{\Delta x}$$

$$-\sigma \frac{E_y^{n+1}(i, j + \frac{1}{2}, k) + E_y^n(i, j + \frac{1}{2}, k)}{2} \tag{2.36}$$

$$\epsilon_r \epsilon_0 \frac{E_z^{n+1}(i, j, k + \frac{1}{2}) - E_z^n(i, j, k + \frac{1}{2})}{\Delta t} =$$

$$\frac{H_y^{n+\frac{1}{2}}(i + \frac{1}{2}, j, k + \frac{1}{2}) - H_y^{n+\frac{1}{2}}(i - \frac{1}{2}, j, k + \frac{1}{2})}{\Delta x}$$

$$-\frac{H_x^{n+\frac{1}{2}}(i, j + \frac{1}{2}, k + \frac{1}{2}) - H_x^{n+\frac{1}{2}}(i, j - \frac{1}{2}, k + \frac{1}{2})}{\Delta y}$$

$$-\sigma \frac{E_z^{n+1}(i, j, k + \frac{1}{2}) + E_z^n(i, j, k + \frac{1}{2})}{2} = \tag{2.37}$$

$$\mu_r \mu_0 \frac{H_x^{n+\frac{1}{2}}(i, j + \frac{1}{2}, k + \frac{1}{2}) - H_x^{n-\frac{1}{2}}(i, j + \frac{1}{2}, k + \frac{1}{2})}{\Delta t} =$$

$$\frac{E_y^n(i, j + \frac{1}{2}, k + 1) - E_y^n(i, j + \frac{1}{2}, k)}{\Delta z}$$

$$-\frac{E_z^n(i, j + 1, k + \frac{1}{2}) - E_z^n(i, j, k + \frac{1}{2})}{\Delta y}$$

$$-\sigma_m \frac{H_x^{n+\frac{1}{2}}(i, j + \frac{1}{2}, k + \frac{1}{2}) + H_x^{n-\frac{1}{2}}(i, j + \frac{1}{2}, k + \frac{1}{2})}{2} \tag{2.38}$$

$$\mu_r \mu_0 \frac{H_y^{n+\frac{1}{2}}(i + \frac{1}{2}, j, k + \frac{1}{2}) - H_y^{n-\frac{1}{2}}(i + \frac{1}{2}, j, k + \frac{1}{2})}{\Delta t} =$$

$$\frac{E_z^n(i + 1, j, k + \frac{1}{2}) - E_z^n(i, j, k + \frac{1}{2})}{\Delta x}$$

$$-\frac{E_x^n(i + \frac{1}{2}, j, k + 1) - E_x^n(i + \frac{1}{2}, j, k)}{\Delta z}$$

$$-\sigma_m \frac{H_y^{n+\frac{1}{2}}(i + \frac{1}{2}, j, k + \frac{1}{2}) + H_y^{n-\frac{1}{2}}(i + \frac{1}{2}, j, k + \frac{1}{2})}{2} \tag{2.39}$$

$$\mu_r \mu_0 \frac{H_z^{n+\frac{1}{2}}(i + \frac{1}{2}, j + \frac{1}{2}, k) - H_z^{n-\frac{1}{2}}(i + \frac{1}{2}, j + \frac{1}{2}, k)}{\Delta t} =$$

$$\frac{E_x^n(i + \frac{1}{2}, j + 1, k) - E_x^n(i + \frac{1}{2}, j, k)}{\Delta y}$$

$$-\frac{E_y^n(i + 1, j + \frac{1}{2}, k) - E_y^n(i, j + \frac{1}{2}, k)}{\Delta x}$$

$$-\sigma_m \frac{H_z^{n+\frac{1}{2}}(i + \frac{1}{2}, j + \frac{1}{2}, k) + H_z^{n-\frac{1}{2}}(i + \frac{1}{2}, j + \frac{1}{2}, k)}{2} \tag{2.40}$$

Rearranging terms,

$$E_x^{n+1}(i + \tfrac{1}{2}, j, k) = E_x^n(i + \tfrac{1}{2}, j, k) \left(\frac{2\epsilon_r - \sigma\eta_0\Delta\tau}{2\epsilon_r + \sigma\eta_0\Delta\tau} \right)$$

$$+\eta_0 \left[\frac{2\Delta\tau}{2\epsilon_r + \sigma\eta_0\Delta\tau} \right] \left\{ \frac{1}{\Delta y} \left[H_z^{n+\frac{1}{2}}(i + \tfrac{1}{2}, j + \tfrac{1}{2}, k) - H_z^{n+\frac{1}{2}}(i + \tfrac{1}{2}, j - \tfrac{1}{2}, k) \right] \right.$$

$$\left. - \frac{1}{\Delta z} \left[H_y^{n+\frac{1}{2}}(i + \tfrac{1}{2}, j, k + \tfrac{1}{2}) - H_y^{n+\frac{1}{2}}(i + \tfrac{1}{2}, j, k - \tfrac{1}{2}) \right] \right\} \tag{2.41}$$

$$E_y^{n+1}(i, j + \tfrac{1}{2}, k) = E_y^n(i, j + \tfrac{1}{2}, k) \left(\frac{2\epsilon_r - \sigma\eta_0\Delta\tau}{2\epsilon_r + \sigma\eta_0\Delta\tau} \right)$$

$$+\eta_0 \left[\frac{2\Delta\tau}{2\epsilon_r + \sigma\eta_0\Delta\tau} \right] \left\{ \frac{1}{\Delta z} \left[H_x^{n+\frac{1}{2}}(i, j + \tfrac{1}{2}, k + \tfrac{1}{2}) - H_x^{n+\frac{1}{2}}(i, j + \tfrac{1}{2}, k - \tfrac{1}{2}) \right] \right.$$

$$\left. - \frac{1}{\Delta x} \left[H_z^{n+\frac{1}{2}}(i + \tfrac{1}{2}, j + \tfrac{1}{2}, k) - H_z^{n+\frac{1}{2}}(i - \tfrac{1}{2}, j + \tfrac{1}{2}, k) \right] \right\} \tag{2.42}$$

$$E_z^{n+1}(i, j, k + \tfrac{1}{2}) = E_z^n(i, j, k + \tfrac{1}{2}) \left(\frac{2\epsilon_r - \sigma\eta_0\Delta\tau}{2\epsilon_r + \sigma\eta_0\Delta\tau} \right)$$

$$+\eta_0 \left[\frac{2\Delta\tau}{2\epsilon_r + \sigma\eta_0\Delta\tau} \right] \left\{ \frac{1}{\Delta x} \left[H_y^{n+\frac{1}{2}}(i + \tfrac{1}{2}, j, k + \tfrac{1}{2}) - H_y^{n+\frac{1}{2}}(i - \tfrac{1}{2}, j, k + \tfrac{1}{2}) \right] \right.$$

$$\left. - \frac{1}{\Delta y} \left[H_x^{n+\frac{1}{2}}(i, j + \tfrac{1}{2}, k + \tfrac{1}{2}) - H_x^{n+\frac{1}{2}}(i, j - \tfrac{1}{2}, k + \tfrac{1}{2}) \right] \right\} \tag{2.43}$$

$$H_x^{n+\frac{1}{2}}(i, j + \tfrac{1}{2}, k + \tfrac{1}{2}) = H_x^{n-\frac{1}{2}}(i, j + \tfrac{1}{2}, k + \tfrac{1}{2}) \left(\frac{2\mu_r - \sigma_m\Delta\tau/\eta_0}{2\mu_r + \sigma_m\Delta\tau/\eta_0} \right)$$

$$+\frac{1}{\eta_0}\left[\frac{2\Delta\tau}{2\mu_r+\sigma_m\Delta\tau/\eta_0}\right]\left\{\frac{1}{\Delta z}\left[E_y^n(i,j+\tfrac{1}{2},k+1)-E_y^n(i,j+\tfrac{1}{2},k)\right]\right.$$

$$\left.-\frac{1}{\Delta y}\left[E_z^n(i,j+1,k+\tfrac{1}{2})-E_z^n(i,j,k+\tfrac{1}{2})\right]\right\} \tag{2.44}$$

$$H_y^{n+\frac{1}{2}}(i+\tfrac{1}{2},j,k+\tfrac{1}{2})=H_y^{n-\frac{1}{2}}(i+\tfrac{1}{2},j,k+\tfrac{1}{2})\left(\frac{2\mu_r-\sigma_m\Delta\tau/\eta_0}{2\mu_r+\sigma_m\Delta\tau/\eta_0}\right)$$

$$+\frac{1}{\eta_0}\left[\frac{2\Delta\tau}{2\mu_r+\sigma_m\Delta\tau/\eta_0}\right]\left\{\frac{1}{\Delta x}\left[E_z^n(i+1,j,k+\tfrac{1}{2})-E_z^n(i,j,k+\tfrac{1}{2})\right]\right.$$

$$\left.-\frac{1}{\Delta z}\left[E_x^n(i+\tfrac{1}{2},j,k+1)-E_x^n(i+\tfrac{1}{2},j,k)\right]\right\} \tag{2.45}$$

$$H_z^{n+\frac{1}{2}}(i+\tfrac{1}{2},j+\tfrac{1}{2},k)=H_z^{n-\frac{1}{2}}(i+\tfrac{1}{2},j+\tfrac{1}{2},k)\left(\frac{2\mu_r-\sigma_m\Delta\tau/\eta_0}{2\mu_r+\sigma_m\Delta\tau/\eta_0}\right)$$

$$+\frac{1}{\eta_0}\left[\frac{2\Delta\tau}{2\mu_r+\sigma_m\Delta\tau/\eta_0}\right]\left\{\frac{1}{\Delta y}\left[E_x^n(i+\tfrac{1}{2},j+1,k)-E_x^n(i+\tfrac{1}{2},j,k)\right]\right.$$

$$\left.-\frac{1}{\Delta x}\left[E_y^n(i+1,j+\tfrac{1}{2},k)-E_y^n(i,j+\tfrac{1}{2},k)\right]\right\} \tag{2.46}$$

2.6 Treatment of Interfaces Between Two Media

The interface between any two media is chosen to occur at integer nodes (i,j,k), hence the electric fields are tangential and magnetic fields are normal to the surface of the interface. At an interface in the x-y plane between two arbitrary media, the finite difference equations for E_x, E_y and H_z must be treated carefully [See Figures 2.2 and 2.3]. Since the normal component of the magnetic field is not continuous across the interface, H_z must be calculated at points just above and just below the
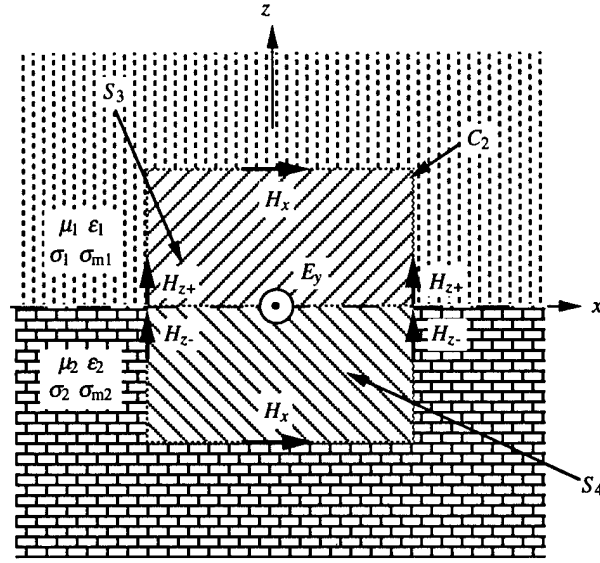
Figure 2.2: Interface on the x-y plane between two arbitrary media viewed in the x-z plane.

interface.

$$H_{z-}^{n+\frac{1}{2}}(i+\tfrac{1}{2},j+\tfrac{1}{2},k) = H_{z-}^{n-\frac{1}{2}}(i+\tfrac{1}{2},j+\tfrac{1}{2},k) \left(\frac{2\mu_{r1} - \sigma_{m1}\Delta\tau/\eta_0}{2\mu_{r1} + \sigma_{m1}\Delta\tau/\eta_0}\right)$$

$$+\frac{1}{\eta_0}\left[\frac{2\Delta\tau}{2\mu_{r1} + \sigma_{m1}\Delta\tau/\eta_0}\right]\left\{\frac{1}{\Delta y}\left[E_x^n(i+\tfrac{1}{2},j+1,k) - E_x^n(i+\tfrac{1}{2},j,k)\right]\right.$$

$$\left. - \frac{1}{\Delta x}\left[E_y^n(i+1,j+\tfrac{1}{2},k) - E_y^n(i,j+\tfrac{1}{2},k)\right]\right\} \qquad (2.47)$$

$$H_{z+}^{n+\frac{1}{2}}(i+\tfrac{1}{2},j+\tfrac{1}{2},k) = H_{z+}^{n-\frac{1}{2}}(i+\tfrac{1}{2},j+\tfrac{1}{2},k) \left(\frac{2\mu_{r2} - \sigma_{m2}\Delta\tau/\eta_0}{2\mu_{r2} + \sigma_{m2}\Delta\tau/\eta_0}\right)$$

$$+\frac{1}{\eta_0}\left[\frac{2\Delta\tau}{2\mu_{r2} + \sigma_{m2}\Delta\tau/\eta_0}\right]\left\{\frac{1}{\Delta y}\left[E_x^n(i+\tfrac{1}{2},j+1,k) - E_x^n(i+\tfrac{1}{2},j,k)\right]\right.$$

$$\left. - \frac{1}{\Delta x}\left[E_y^n(i+1,j+\tfrac{1}{2},k) - E_y^n(i,j+\tfrac{1}{2},k)\right]\right\} \qquad (2.48)$$
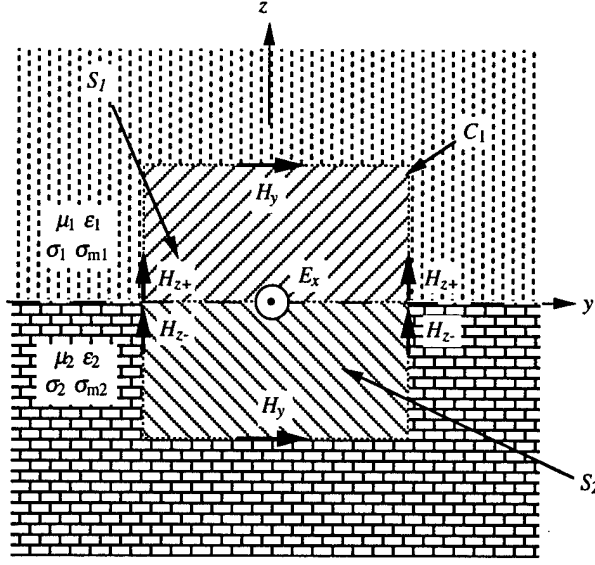
Figure 2.3: Interface on the x-y plane between two arbitrary media viewed in the y-z plane.

Using the integral form of Equation (2.2) to calculate E_y yields [See Figure 2.2]

$$\oint_{C_1} \overline{H} \cdot d\overline{l} = \iint_{S_1+S_2} \left(\frac{\partial \overline{D}}{\partial t} + \sigma \overline{E} \right) \cdot d\overline{S}$$

$$= \iint_{S_1} \left(\epsilon_1 \frac{\partial \overline{E}}{\partial t} + \sigma_1 \overline{E} \right) \cdot d\overline{S} + \iint_{S_2} \left(\epsilon_2 \frac{\partial \overline{E}}{\partial t} + \sigma_2 \overline{E} \right) \cdot d\overline{S} \quad (2.49)$$

Converting Equation (2.49) to a finite difference equation yields

$$E_y^{n+1}(i,j+\tfrac{1}{2},k) = E_y^n(i,j+\tfrac{1}{2},k) \left(\frac{2\epsilon_{r1} - \sigma_1\eta_0\Delta\tau + 2\epsilon_{r2} - \sigma_2\eta_0\Delta\tau}{2\epsilon_{r1} + \sigma_1\eta_0\Delta\tau + 2\epsilon_{r2} + \sigma_2\eta_0\Delta\tau} \right) \quad (2.50)$$

$$+\eta_0 \left[\frac{4\Delta\tau}{2\epsilon_{r1} + \sigma_1\eta_0\Delta\tau + 2\epsilon_{r2} + \sigma_2\eta_0\Delta\tau} \right] \left\{ \frac{1}{\Delta z} \left[H_x^{n+\frac{1}{2}}(i,j+\tfrac{1}{2},k+\tfrac{1}{2}) \right. \right.$$

$$\left. - H_x^{n+\frac{1}{2}}(i,j+\tfrac{1}{2},k-\tfrac{1}{2}) \right] - \frac{1}{2\Delta x} \left[H_{z+}^{n+\frac{1}{2}}(i+\tfrac{1}{2},j+\tfrac{1}{2},k) - H_{z+}^{n+\frac{1}{2}}(i-\tfrac{1}{2},j+\tfrac{1}{2},k) \right.$$

$$\left. \left. + H_{z-}^{n+\frac{1}{2}}(i+\tfrac{1}{2},j+\tfrac{1}{2},k) - H_{z-}^{n+\frac{1}{2}}(i-\tfrac{1}{2},j+\tfrac{1}{2},k) \right] \right\}$$

Applying the integral form of Equation (2.2) to calculate E_x results in [See Figure 2.3]

$$\oint_{C_2} \overline{H} \cdot d\bar{l} = \iint_{S_3+S_4} \left(\frac{\partial \overline{D}}{\partial t} + \sigma \overline{E} \right) \cdot d\overline{S}$$

$$= \iint_{S_3} \left(\epsilon_1 \frac{\partial \overline{E}}{\partial t} + \sigma_1 \overline{E} \right) \cdot d\overline{S} + \iint_{S_4} \left(\epsilon_2 \frac{\partial \overline{E}}{\partial t} + \sigma_2 \overline{E} \right) \cdot d\overline{S} \quad (2.51)$$

Transforming Equation (2.51) to a finite difference equation yields

$$E_x^{n+1}(i + \tfrac{1}{2}, j, k) = E_x^n(i + \tfrac{1}{2}, j, k) \left(\frac{2\epsilon_{r1} - \sigma_1 \eta_0 \Delta \tau + 2\epsilon_{r2} - \sigma_2 \eta_0 \Delta \tau}{2\epsilon_{r1} + \sigma_1 \eta_0 \Delta \tau + 2\epsilon_{r2} + \sigma_2 \eta_0 \Delta \tau} \right)$$

$$+ \eta_0 \left[\frac{4\Delta\tau}{2\epsilon_{r1} + \sigma_1 \eta_0 \Delta \tau + 2\epsilon_{r2} + \sigma_2 \eta_0 \Delta \tau} \right] \left\{ \frac{1}{2\Delta y} \left[H_{z+}^{n+\frac{1}{2}}(i + \tfrac{1}{2}, j + \tfrac{1}{2}, k) \right. \right.$$

$$\left. - H_{z+}^{n+\frac{1}{2}}(i + \tfrac{1}{2}, j - \tfrac{1}{2}, k) + H_{z-}^{n+\frac{1}{2}}(i + \tfrac{1}{2}, j + \tfrac{1}{2}, k) - H_{z-}^{n+\frac{1}{2}}(i + \tfrac{1}{2}, j - \tfrac{1}{2}, k) \right]$$

$$\left. - \frac{1}{\Delta z} \left[H_y^{n+\frac{1}{2}}(i + \tfrac{1}{2}, j, k + \tfrac{1}{2}) - H_y^{n+\frac{1}{2}}(i + \tfrac{1}{2}, j, k - \tfrac{1}{2}) \right] \right\} \quad (2.52)$$

2.7 Treatment of Perfect Electric Conductor

The boundary condition at perfect electric conductors states that the tangential electric field must be zero,

$$\hat{n} \times \overline{E} = 0 \tag{2.53}$$

Since media interfaces are chosen to occur at integer node (i, j, k) locations, it is clear from Figure 2.1 that the electric fields are always tangential to the surface. Thus, in the finite difference-time domain scheme, the boundary condition at the perfect electric conductor can be satisfied by simply setting these electric fields equal to zero at each time step.

2.8 Treatment of Perfect Magnetic Conductor

At a perfect magnetic conductor the tangential magnetic field must be zero,

$$\hat{n} \times \overline{H} = 0 \tag{2.54}$$

This boundary condition is satisfied when the tangential electric field at the surface of the perfect magnetic conductor is calculated. One way of obtaining a difference equation for the tangential electric field (i.e., E_x) is to simplify the original problem [Figure 2.4] by using image theory [Figure 2.5]. The difference equation for E_x at the interface between a perfect magnetic conductor and a dielectric and magnetic
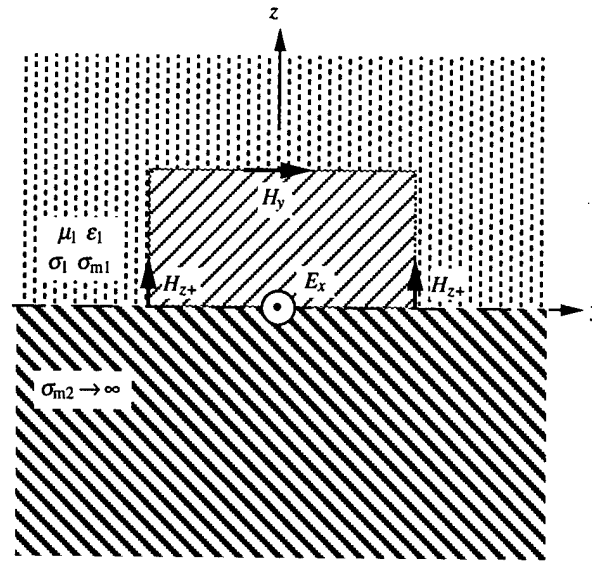
Figure 2.4: Interface on the x-y plane between a media and a perfect magnetic conductor viewed in the y-z plane.

material is given by

$$E_x^{n+1}(i + \tfrac{1}{2}, j, k) = E_x^n(i + \tfrac{1}{2}, j, k) \left(\frac{2\epsilon_r - \sigma\eta_0\Delta\tau}{2\epsilon_r + \sigma\eta_0\Delta\tau} \right) \tag{2.55}$$

$$-\eta_0 \left[\frac{2\Delta\tau}{2\epsilon_r + \sigma\eta_0\Delta\tau} \right] \left\{ \frac{2}{\Delta z} H_y^{n+\frac{1}{2}}(i + \tfrac{1}{2}, j, k + \tfrac{1}{2}) \right.$$

$$\left. - \frac{1}{\Delta y} \left[H_z^{n+\frac{1}{2}}(i + \tfrac{1}{2}, j + \tfrac{1}{2}, k) - H_z^{n+\frac{1}{2}}(i + \tfrac{1}{2}, j - \tfrac{1}{2}, k) \right] \right\}$$
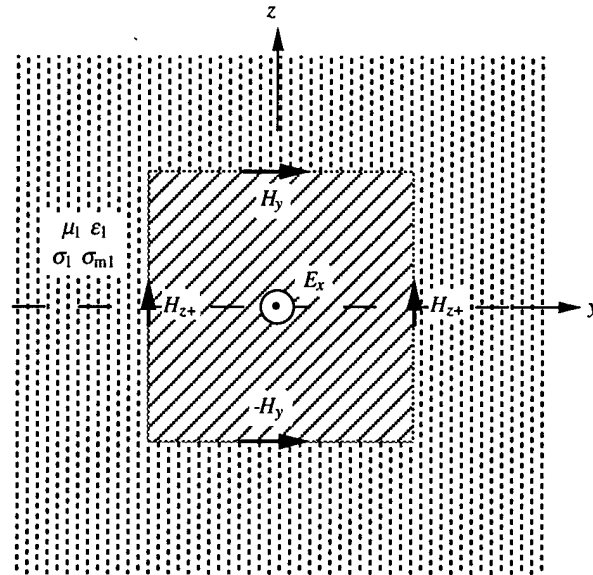
Figure 2.5: Image problem of interface on the x-y plane between a media and a perfect magnetic conductor viewed in the y-z plane.

2.9   Stability and Accuracy

The choices of Δx, Δy, Δz, and $\Delta \tau$, are motivated by reasons of accuracy and stability [6],[69]. In general, to obtain accurate results, Δx, Δy and Δz must be a small fraction ($\sim 1/10$) of the smallest wavelength in any media expected in the model or of the smallest dimension of the scatterer. To ensure the stability of this time stepping algorithm, $\Delta \tau$ must satisfy the following condition [6].

$$\Delta \tau = c_0 \Delta t \leq \left(\frac{1}{\Delta x^2} + \frac{1}{\Delta y^2} + \frac{1}{\Delta z^2} \right)^{-\frac{1}{2}} \tag{2.56}$$

2.10   Implementation of Excitation Source

The two basic types of sources, which are plane waves and current sources, are treated differently. When the excitation source is assumed to be either a sinusoidal or Gaussian pulse plane wave, the computational domain is separated into two regions in order to facilitate the treatment of the excitation source [Figures 2.6-2.7].

For a finite scatterer, within the inner region, total fields are calculated, while in the outer region, only scattered fields are calculated [Figure 2.6]. The scattered fields are defined to be the difference between the total fields and the incident plane wave.

$$\overline{H}_s(x, z, t) = \overline{H}_t(x, z, t) - \overline{H}_i(x, z, t) \tag{2.57}$$

$$\overline{E}_s(x, z, t) = \overline{E}_t(x, z, t) - \overline{E}_i(x, z, t) \tag{2.58}$$
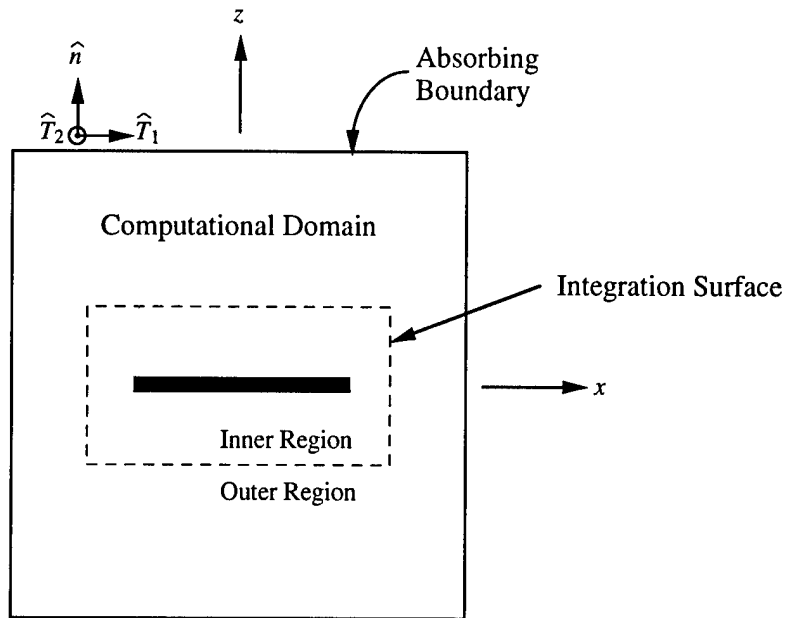
Figure 2.6: Absorbing boundary, computational domain and closed surface on which fields are sampled with a finite scatterer.
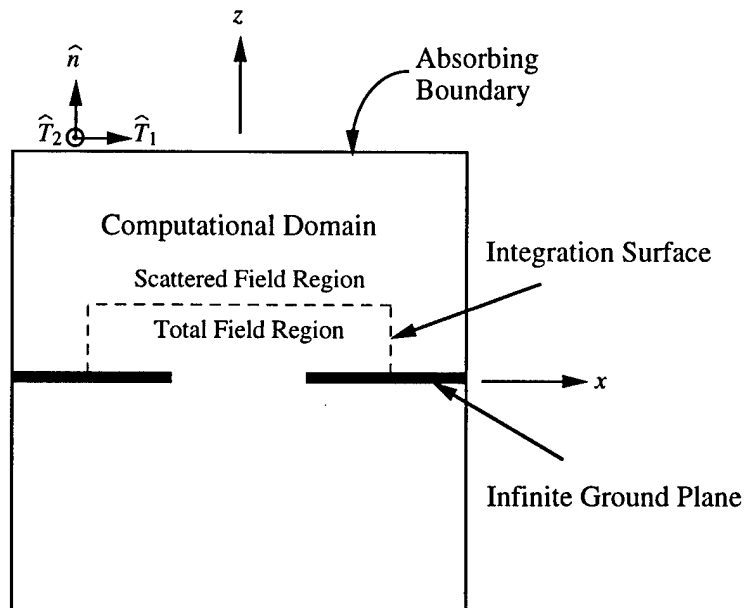
Figure 2.7: Absorbing boundary, computational domain and surface on which fields are sampled with an infinite ground plane geometry.

The incident fields are subtracted from field quantities just within the inner regions, when they are used to calculate field quantities just beyond the inner region. The incident fields are added to field quantities just outside the inner regions, when they are used to calculate field quantities just within the inner region [67].

The finite difference equations for the fields in the vicinity of an x-y plane interface between the total and scattered field regions are

$$E_{tx}^{n+1}(i+\tfrac{1}{2},j,k) = E_{tx}^n(i+\tfrac{1}{2},j,k) + \eta_0\frac{\Delta\tau}{\Delta y}\left[H_{tz}^{n+\frac{1}{2}}(i+\tfrac{1}{2},j+\tfrac{1}{2},k)\right.$$

$$\left. - H_{tz}^{n+\frac{1}{2}}(i+\tfrac{1}{2},j-\tfrac{1}{2},k)\right] - \eta_0\frac{\Delta\tau}{\Delta z}\left\{\left[H_{sy}^{n+\frac{1}{2}}(i+\tfrac{1}{2},j,k+\tfrac{1}{2})\right.\right. \tag{2.59}$$

$$\left.\left. + H_{iy}^{n+\frac{1}{2}}(i+\tfrac{1}{2},j,k+\tfrac{1}{2})\right] - H_{ty}^{n+\frac{1}{2}}(i+\tfrac{1}{2},j,k-\tfrac{1}{2})\right\}$$

$$E_{ty}^{n+1}(i,j+\tfrac{1}{2},k) = E_{ty}^n(i,j+\tfrac{1}{2},k) + \eta_0\frac{\Delta\tau}{\Delta z}\left\{\left[H_{sx}^{n+\frac{1}{2}}(i,j+\tfrac{1}{2},k+\tfrac{1}{2})\right.\right.$$

$$\left.\left. + H_{ix}^{n+\frac{1}{2}}(i,j+\tfrac{1}{2},k+\tfrac{1}{2})\right] - H_{tx}^{n+\frac{1}{2}}(i,j+\tfrac{1}{2},k-\tfrac{1}{2})\right\} \tag{2.60}$$

$$-\eta_0\frac{\Delta\tau}{\Delta x}\left[H_{tz}^{n+\frac{1}{2}}(i+\tfrac{1}{2},j+\tfrac{1}{2},k) - H_{tz}^{n+\frac{1}{2}}(i-\tfrac{1}{2},j+\tfrac{1}{2},k)\right]$$

$$E_{sz}^{n+1}(i,j,k+\tfrac{1}{2}) = E_{sz}^n(i,j,k+\tfrac{1}{2})$$

$$+\eta_0\frac{\Delta\tau}{\Delta x}\left[H_{sy}^{n+\frac{1}{2}}(i+\tfrac{1}{2},j,k+\tfrac{1}{2}) - H_{sy}^{n+\frac{1}{2}}(i-\tfrac{1}{2},j,k+\tfrac{1}{2})\right] \tag{2.61}$$

$$-\eta_0\frac{\Delta\tau}{\Delta y}\left[H_{sx}^{n+\frac{1}{2}}(i,j+\tfrac{1}{2},k+\tfrac{1}{2}) - H_{sx}^{n+\frac{1}{2}}(i,j-\tfrac{1}{2},k+\tfrac{1}{2})\right]$$

$$H_{sx}^{n+\frac{1}{2}}(i,j+\tfrac{1}{2},k+\tfrac{1}{2}) = H_{sx}^{n-\frac{1}{2}}(i,j+\tfrac{1}{2},k+\tfrac{1}{2})$$

$$+\frac{1}{\eta_0}\frac{\Delta\tau}{\Delta z}\left\{E_{sy}^n(i,j+\tfrac{1}{2},k+1) - \left[E_{ty}^n(i,j+\tfrac{1}{2},k)\right.\right. \tag{2.62}$$

$$- E_{iy}^n(i, j + \tfrac{1}{2}, k)] \Big\} - \frac{1}{\eta_0} \frac{\Delta \tau}{\Delta y} \left[E_{sz}^n(i, j + 1, K + \tfrac{1}{2}) - E_{sy}^n(i, j, k + \tfrac{1}{2}) \right]$$

$$H_{sy}^{n+\frac{1}{2}}(i + \tfrac{1}{2}, j, k + \tfrac{1}{2}) = H_{sy}^{n-\frac{1}{2}}(i + \tfrac{1}{2}, j, k + \tfrac{1}{2})$$

$$+ \frac{1}{\eta_0} \frac{\Delta \tau}{\Delta x} \left[E_{sz}^n(i + 1, j, k + \tfrac{1}{2}) - E_{sz}^n(i, j, k + \tfrac{1}{2}) \right] \qquad (2.63)$$

$$- \frac{1}{\eta_0} \frac{\Delta \tau}{\Delta z} \left\{ E_{sx}^n(i + \tfrac{1}{2}, j, k + 1) - \left[E_{tx}^n(i + \tfrac{1}{2}, j, k) - E_{ix}^n(i + \tfrac{1}{2}, j, k) \right] \right\}$$

$$H_{tz}^{n+\frac{1}{2}}(i + \tfrac{1}{2}, j + \tfrac{1}{2}, k) = H_{tz}^{n-\frac{1}{2}}(i + \tfrac{1}{2}, j + \tfrac{1}{2}, k)$$

$$+ \frac{1}{\eta_0} \frac{\Delta \tau}{\Delta y} \left[E_{tx}^n(i + \tfrac{1}{2}, j + 1, k) - E_{tx}^n(i + \tfrac{1}{2}, j, k) \right] \qquad (2.64)$$

$$- \frac{1}{\eta_0} \frac{\Delta \tau}{\Delta x} \left[E_{ty}^n(i + 1, j + \tfrac{1}{2}, k) - E_{ty}^n(i, j + \tfrac{1}{2}, k) \right]$$

For an infinite ground plane configuration, the computational domain is basically divided into the region above the ground plane and the region below the ground plane [Figure 2.7]. For plane wave illumination from the upper half space, total fields are calculated in the lower region, while in the upper region, only scattered fields are calculated. In this case, the scattered fields are defined to be the total fields minus the incident plane wave and the plane wave that would have been reflected from a uniform infinite ground plane,

$$\overline{H}_s(x, z, t) = \overline{H}_t(x, z, t) - \overline{H}_i(x, z, t) - \overline{H}_r(x, z, t) \qquad (2.65)$$

$$\overline{E}_s(x, z, t) = \overline{E}_t(x, z, t) - \overline{E}_i(x, z, t) - \overline{E}_r(x, z, t) \qquad (2.66)$$

The removal of the reflected plane wave from the upper half space is essential because

the reflected plane wave is infinite in size and could not otherwise be adequately modeled within the finite computational domain. For plane wave illumination from the lower half space the total and scattered fields are simply calculated in the opposite regions. The implementation of a plane wave is basically identical to the implementation for a finite scatterer except with the slightly different definition of the scattered field.

The implementation of current sources is straightforward. In this situation, total fields are calculated within the entire computational domain. Both electric and magnetic current sources can be implemented. The current sources are implemented by adding the appropriate current term in Maxwell's curl equations.

$$\mu_r \mu_0 \frac{\partial H_x}{\partial t} = \frac{\partial E_y}{\partial z} - \frac{\partial E_z}{\partial y} - J_{mx} \tag{2.67}$$

$$\mu_r \mu_0 \frac{\partial H_y}{\partial t} = \frac{\partial E_z}{\partial x} - \frac{\partial E_x}{\partial z} - J_{my} \tag{2.68}$$

$$\mu_r \mu_0 \frac{\partial H_z}{\partial t} = \frac{\partial E_x}{\partial y} - \frac{\partial E_y}{\partial x} - J_{mz} \tag{2.69}$$

$$\epsilon_r \epsilon_0 \frac{\partial E_x}{\partial t} = \frac{\partial H_z}{\partial y} - \frac{\partial H_y}{\partial z} - J_x \tag{2.70}$$

$$\epsilon_r \epsilon_0 \frac{\partial E_y}{\partial t} = \frac{\partial H_x}{\partial z} - \frac{\partial H_z}{\partial x} - J_y \tag{2.71}$$

$$\epsilon_r \epsilon_0 \frac{\partial E_z}{\partial t} = \frac{\partial H_y}{\partial x} - \frac{\partial H_x}{\partial y} - J_z \tag{2.72}$$

where J and J_m are the electric and magnetic current densities. Applying center

differences results in

$$E_x^{n+1}(i+\tfrac{1}{2},j,k) = E_x^n(i+\tfrac{1}{2},j,k) - \Delta\tau\eta_0 J_x$$

$$+\eta_0\frac{\Delta\tau}{\Delta y}\left[H_z^{n+\frac{1}{2}}(i+\tfrac{1}{2},j+\tfrac{1}{2},k) - H_z^{n+\frac{1}{2}}(i+\tfrac{1}{2},j-\tfrac{1}{2},k)\right]$$

$$-\eta_0\frac{\Delta\tau}{\Delta z}\left[H_y^{n+\frac{1}{2}}(i+\tfrac{1}{2},j,k+\tfrac{1}{2}) - H_y^{n+\frac{1}{2}}(i+\tfrac{1}{2},j,k-\tfrac{1}{2})\right] \qquad (2.73)$$

$$E_y^{n+1}(i,j+\tfrac{1}{2},k) = E_y^n(i,j+\tfrac{1}{2},k) - \Delta\tau\eta_0 J_y$$

$$+\eta_0\frac{\Delta\tau}{\Delta z}\left[H_x^{n+\frac{1}{2}}(i,j+\tfrac{1}{2},k+\tfrac{1}{2}) - H_x^{n+\frac{1}{2}}(i,j+\tfrac{1}{2},k-\tfrac{1}{2})\right]$$

$$-\eta_0\frac{\Delta\tau}{\Delta x}\left[H_z^{n+\frac{1}{2}}(i+\tfrac{1}{2},j+\tfrac{1}{2},k) - H_z^{n+\frac{1}{2}}(i-\tfrac{1}{2},j+\tfrac{1}{2},k)\right] \qquad (2.74)$$

$$E_z^{n+1}(i,j,k+\tfrac{1}{2}) = E_z^n(i,j,k+\tfrac{1}{2}) - \Delta\tau\eta_0 J_z$$

$$+\eta_0\frac{\Delta\tau}{\Delta x}\left[H_y^{n+\frac{1}{2}}(i+\tfrac{1}{2},j,k+\tfrac{1}{2}) - H_y^{n+\frac{1}{2}}(i-\tfrac{1}{2},j,k+\tfrac{1}{2})\right]$$

$$-\eta_0\frac{\Delta\tau}{\Delta y}\left[H_x^{n+\frac{1}{2}}(i,j+\tfrac{1}{2},k+\tfrac{1}{2}) - H_x^{n+\frac{1}{2}}(i,j-\tfrac{1}{2},k+\tfrac{1}{2})\right] \qquad (2.75)$$

$$H_x^{n+\frac{1}{2}}(i,j+\tfrac{1}{2},k+\tfrac{1}{2}) = H_x^{n-\frac{1}{2}}(i,j+\tfrac{1}{2},k+\tfrac{1}{2}) - \frac{\Delta\tau J_{mx}}{\eta_0}$$

$$+\frac{1}{\eta_0}\frac{\Delta\tau}{\Delta z}\left[E_y^n(i,j+\tfrac{1}{2},k+1) - E_y^n(i,j+\tfrac{1}{2},k)\right]$$

$$-\frac{1}{\eta_0}\frac{\Delta\tau}{\Delta y}\left[E_z^n(i,j+1,k+\tfrac{1}{2}) - E_y^n(i,j,k+\tfrac{1}{2})\right] \qquad (2.76)$$

$$H_y^{n+\frac{1}{2}}(i+\tfrac{1}{2},j,k+\tfrac{1}{2}) = H_y^{n-\frac{1}{2}}(i+\tfrac{1}{2},j,k+\tfrac{1}{2}) - \frac{\Delta\tau J_{my}}{\eta_0}$$

$$+\frac{1}{\eta_0}\frac{\Delta\tau}{\Delta x}\left[E_z^n(i+1,j,k+\tfrac{1}{2}) - E_z^n(i,j,k+\tfrac{1}{2})\right]$$

$$-\frac{1}{\eta_0}\frac{\Delta\tau}{\Delta z}\left[E_x^n(i+\tfrac{1}{2},j,k+1) - E_x^n(i+\tfrac{1}{2},j,k)\right] \qquad (2.77)$$

$$H_z^{n+\frac{1}{2}}(i+\tfrac{1}{2},j+\tfrac{1}{2},k) = H_z^{n-\frac{1}{2}}(i+\tfrac{1}{2},j+\tfrac{1}{2},k) - \frac{\Delta\tau J_{mz}}{\eta_0}$$

$$+\frac{1}{\eta_0}\frac{\Delta\tau}{\Delta y}\left[E_x^n(i+\tfrac{1}{2},j+1,k) - E_x^n(i+\tfrac{1}{2},j,k)\right]$$

$$-\frac{1}{\eta_0}\frac{\Delta\tau}{\Delta x}\left[E_y^n(i+1,j+\tfrac{1}{2},k) - E_y^n(i,j+\tfrac{1}{2},k)\right] \qquad (2.78)$$

For a current source in the z direction, the electric or magnetic current density, J_z or

J_{mz}, is assumed to have length Δz and a cross section of $\Delta x \Delta y$ [15].

2.11   Absorbing Boundary Conditions

An absorbing boundary condition (ABC) at the outer boundary is needed to make the computational domain finite, and to simulate unbounded space beyond the computational domain [Figures 2.6-2.7] [67]-[74]. The absorbing boundary condition used for this problem is the second-order approximation derived by Engquist and Majda [68],

$$\left[\frac{\partial^2}{\partial n \partial \tau} + \frac{\partial^2}{\partial \tau^2} - \frac{1}{2}\left(\frac{\partial^2}{\partial T_1^2} + \frac{\partial^2}{\partial T_2^2}\right)\right] w = 0 \qquad (2.79)$$

where w is a field quantity which is tangential to the absorbing boundary, $\hat{n}$ is the normal direction, $\hat{T}_1$, $\hat{T}_2$ are the tangential directions, and τ is time normalized with respect to the speed of light. This second-order absorbing boundary condition is applied at the faces of the computational domain [Figure 2.8]. The second-order absorbing boundary condition works very well for waves which are at or near normal incidence, and does not work as well for waves which are incident at grazing angles.

In treating points at the edges of the outer boundary, a first-order absorbing boundary condition is used for field components which are tangential to the faces on which the edges reside [Figure 2.8]. The first-order ABC is characterized by the following equation,

$$\left(\frac{\partial}{\partial n} + \frac{\partial}{\partial \tau}\right) w = 0 \qquad (2.80)$$

where $\hat{n}$ is the normal direction.
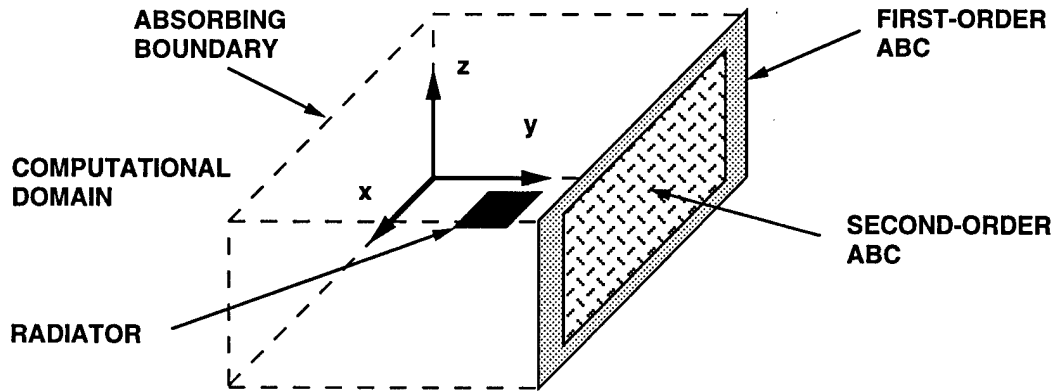
Figure 2.8: First- and second-order absorbing boundary conditions for a three-dimensional computational domain.

The absorbing boundary condition at the edges is not as important as the one at the faces, because there are fewer points on the edges than the faces. Thus, in general, using the first-order boundary at the edges will not cause significant deterioration in the accuracy of the algorithm.

The absorbing boundary conditions are applied to the electric fields which are tangential to the outer boundary. Applying center differences to Equation (2.79) for the $+x$ boundary $(i = I^+)$, and then using temporal and spatial averages to obtain E_y, and E_z at positions and times where they are calculated, yields

$$E_y^{n+1}(I^+, j + \tfrac{1}{2}, k) = -E_y^{n-1}(I^+ - 1, j + \tfrac{1}{2}, k)$$

$$+ \frac{\Delta\tau - \Delta x}{\Delta\tau + \Delta x}\left[E_y^{n+1}(I^+ - 1, j + \tfrac{1}{2}, k) + E_y^{n-1}(I^+, j + \tfrac{1}{2}, k)\right]$$

$$+ \frac{2\Delta x}{\Delta\tau + \Delta x}\left[E_y^n(I^+, j + \tfrac{1}{2}, k) + E_y^n(I^+ - 1, j + \tfrac{1}{2}, k)\right]$$

$$+\frac{\Delta\tau^2\Delta x}{2\Delta y^2(\Delta\tau+\Delta x)}\left\{E_y^n(I^+,j+\tfrac{3}{2},k)+E_y^n(I^+-1,j+\tfrac{3}{2},k)\right.$$

$$-2\left[E_y^n(I^+,j+\tfrac{1}{2},k)+E_y^n(I^+-1,j+\tfrac{1}{2},k)\right]$$

$$\left.+E_y^n(I^+,j-\tfrac{1}{2},k)+E_y^n(I^+-1,j-\tfrac{1}{2},k)\right\}$$

$$+\frac{\Delta\tau^2\Delta x}{2\Delta z^2(\Delta\tau+\Delta x)}\left\{E_y^n(I^+,j+\tfrac{1}{2},k+1)+E_y^n(I^+-1,j+\tfrac{1}{2},k+1)\right.$$

$$-2\left[E_y^n(I^+,j+\tfrac{1}{2},k)+E_y^n(I^+-1,j+\tfrac{1}{2},k)\right]$$

$$\left.+E_y^n(I^+,j+\tfrac{1}{2},k-1)+E_y^n(I^+-1,j+\tfrac{1}{2},k-1)\right\} \tag{2.81}$$

$$E_z^{n+1}(I^+,j,k+\tfrac{1}{2})=-E_z^{n-1}(I^+-1,j,k+\tfrac{1}{2})$$

$$+\frac{\Delta\tau-\Delta x}{\Delta\tau+\Delta x}\left[E_z^{n+1}(I^+-1,j,k+\tfrac{1}{2})+E_z^{n-1}(I^+,j,k+\tfrac{1}{2})\right]$$

$$+\frac{2\Delta x}{\Delta\tau+\Delta x}\left[E_z^n(I^+,j,k+\tfrac{1}{2})+E_z^n(I^+-1,j,k+\tfrac{1}{2})\right]$$

$$+\frac{\Delta\tau^2\Delta x}{2\Delta y^2(\Delta\tau+\Delta x)}\left\{E_z^n(I^+,j+1,k+\tfrac{1}{2})+E_z^n(I^+-1,j+1,k+\tfrac{1}{2})\right.$$

$$-2\left[E_z^n(I^+,j,k+\tfrac{1}{2})+E_z^n(I^+-1,j,k+\tfrac{1}{2})\right]$$

$$\left.+E_z^n(I^+,j-1,k+\tfrac{1}{2})+E_z^n(I^+-1,j-1,k+\tfrac{1}{2})\right\}$$

$$+\frac{\Delta\tau^2\Delta x}{2\Delta z^2(\Delta\tau+\Delta x)}\left\{E_z^n(I^+,j,k+\tfrac{3}{2})+E_z^n(I^+-1,j,k+\tfrac{3}{2})\right.$$

$$-2\left[E_z^n(I^+,j,k+\tfrac{1}{2})+E_z^n(I^+-1,j,k+\tfrac{1}{2})\right]$$

$$\left.+E_z^n(I^+,j,k-\tfrac{1}{2})+E_z^n(I^+-1,j,k-\tfrac{1}{2})\right\} \tag{2.82}$$

When E_y lies on both a perfectly conducting ground plane and the absorbing boundary, it must simply satisfy the boundary condition for the perfect conductor, and is set to zero. However, when E_z lies just above a perfectly conducting ground plane and on the absorbing boundary, image points are used in conjunction with the second-order absorbing boundary condition. The difference equation for E_z at $\frac{1}{2}\Delta z$ above a perfectly conducting ground plane lying in the x-y plane at $z = k\Delta z$, and on the $+x$ face absorbing boundary $(i = I^+)$, is

$$
E_z^{n+1}(I^+, j, k + \tfrac{1}{2}) = -E_z^{n-1}(I^+ - 1, j, k + \tfrac{1}{2})
$$

$$
+ \frac{\Delta\tau - \Delta x}{\Delta\tau + \Delta x}\left[E_z^{n+1}(I^+ - 1, j, k + \tfrac{1}{2}) + E_z^{n-1}(I^+, j, k + \tfrac{1}{2})\right]
$$

$$
+ \frac{2\Delta x}{\Delta\tau + \Delta x}\left[E_z^n(I^+, j, k + \tfrac{1}{2}) + E_z^n(I^+ - 1, j, k + \tfrac{1}{2})\right]
$$

$$
+ \frac{\Delta\tau^2\Delta x}{2\Delta y^2(\Delta\tau + \Delta x)}\left\{E_z^n(I^+, j+1, k + \tfrac{1}{2}) + E_z^n(I^+ - 1, j+1, k + \tfrac{1}{2})\right.
$$

$$
-2\left[E_z^n(I^+, j, k + \tfrac{1}{2}) + E_z^n(I^+ - 1, j, k + \tfrac{1}{2})\right]
$$

$$
+ E_z^n(I^+, j-1, k + \tfrac{1}{2}) + E_z^n(I^+ - 1, j-1, k + \tfrac{1}{2})\Big\}
$$

$$
+ \frac{\Delta\tau^2\Delta x}{2\Delta z^2(\Delta\tau + \Delta x)}\left\{E_z^n(I^+, j, k + \tfrac{3}{2}) + E_z^n(I^+ - 1, j, k + \tfrac{3}{2})\right.
$$

$$
- \left[E_z^n(I^+, j, k + \tfrac{1}{2}) + E_z^n(I^+ - 1, j, k + \tfrac{1}{2})\right]\Big\} \tag{2.83}
$$

$$
\tag{2.84}
$$

Applying center differences to Equation (2.80) at the $+y$ edge of the $+x$ face, for E_y $((i = I^+, j = J^+ - \tfrac{1}{2})$ and E_z $(i = I^+, j = J^+ - 1)$, and then using temporal and

spatial averages to obtain E_y and E_z at positions and times where they are calculated, yields

$$E_y^{n+1}(I^+, J^+ - \tfrac{1}{2}, k) = E_y^n(I^+ - 1, J^+ - \tfrac{1}{2}, k) \tag{2.85}$$

$$+ \frac{\Delta\tau - \Delta x}{\Delta\tau + \Delta x} \left[E_y^{n+1}(I^+ - 1, J^+ - \tfrac{1}{2}, k) + E_y^n(I^+, J^+ - \tfrac{1}{2}, k) \right]$$

$$E_z^{n+1}(I^+, J^+, k + \tfrac{1}{2}) = E_z^n(I^+ - 1, J^+, k + \tfrac{1}{2}) \tag{2.86}$$

$$+ \frac{\Delta\tau - \Delta x}{\Delta\tau + \Delta x} \left[E_z^{n+1}(I^+ - 1, J^+, k + \tfrac{1}{2}) + E_z^n(I^+, J^+, k + \tfrac{1}{2}) \right]$$

The difference equations satisfying the ABC for the tangential electric fields at the other edges and faces of the computational domain have the same form, and hence are not shown here.

The absorbing boundary is not required to absorb the incident plane wave, because the scattered fields, from which the incident plane wave has been analytically removed, are calculated outside the inner region. With infinite ground planes, the reflected plane wave is also analytically removed from the scattered field region and need not be absorbed by the absorbing boundary. Since the scattered field radiates from the scatterer, the outgoing scattered fields will not be incident on the absorbing boundary at grazing angles, which allows the ABC to absorb a large percentage of the outgoing scattered fields.

2.12 Calculation of Radiation or Scattering Patterns

The calculation of the radiation or scattering patterns requires the use of Huygens' principle. Huygens' principle states that the field solution in a region is completely determined by the tangential fields on a surface which completely surrounds the region [106]. The mathematical formulation of Huygens' principle for free space in three-dimensions, assuming an $e^{-i\omega t}$ time dependence, has the following forms:

$$\overline{E}(\overline{r}) = \oiint_{S'} dS' \left\{ i\omega\mu_0 \overline{\overline{G}}(\overline{r},\overline{r}') \cdot \hat{n} \times \overline{H}(\overline{r}') + \nabla \times \overline{\overline{G}}(\overline{r},\overline{r}') \cdot \hat{n} \times \overline{E}(\overline{r}') \right\} \quad (2.87)$$

$$\overline{H}(\overline{r}) = \oiint_{S'} dS' \left\{ -i\omega\epsilon_0 \overline{\overline{G}}(\overline{r},\overline{r}') \cdot \hat{n} \times \overline{E}(\overline{r}') + \nabla \times \overline{\overline{G}}(\overline{r},\overline{r}') \cdot \hat{n} \times \overline{H}(\overline{r}') \right\} \quad (2.88)$$

$$\overline{r} = \hat{x}x + \hat{y}y + \hat{z}z = \hat{r}r \quad (2.89)$$

$$\overline{r}' = \hat{x}x' + \hat{y}y' + \hat{z}z' = \hat{r}r' \quad (2.90)$$

$$r = \sqrt{x^2 + y^2 + z^2} \quad (2.91)$$

$$\theta = \tan^{-1}\frac{z}{\sqrt{x^2 + y^2}} \quad (2.92)$$

$$\phi = \tan^{-1}\frac{x}{y} \quad (2.93)$$

$$\hat{r} = \hat{x}\sin\theta\cos\phi + \hat{y}\sin\theta\sin\phi + \hat{z}\cos\theta \quad (2.94)$$

$$\hat{\theta} = \hat{x}\cos\theta\cos\phi + \hat{y}\cos\theta\sin\phi - \hat{z}\sin\theta \quad (2.95)$$

$$\hat{\phi} = -\hat{x}\sin\phi + \hat{y}\cos\phi \tag{2.96}$$

$$\overline{\overline{G}} = \left[\overline{\overline{I}} + \frac{1}{k_0^2}\nabla\nabla\right]\frac{e^{ik_0|\overline{r}-\overline{r}'|}}{4\pi|\overline{r}-\overline{r}'|} \tag{2.97}$$

In the far-field, ∇ can be approximated as $ik_0\hat{r}$.

$$
\begin{aligned}
\overline{E}(\overline{r}) &= \oiint_{S'} dS' \left\{ i\omega\mu_0 \left[\overline{\overline{I}} - \hat{r}\hat{r}\right]\frac{e^{ik_0|\overline{r}-\overline{r}'|}}{4\pi|\overline{r}-\overline{r}'|}\cdot\hat{n}\times\overline{H}(\overline{r}') \right. \\
&\qquad\qquad \left. + ik_0\hat{r}\times\left[\overline{\overline{I}} - \hat{r}\hat{r}\right]\frac{e^{ik_0|\overline{r}-\overline{r}'|}}{4\pi|\overline{r}-\overline{r}'|}\cdot\hat{n}\times\overline{E}(\overline{r}') \right\} \\[4pt]
&= \oiint_{S'} dS' \left\{ i\omega\mu_0 \left[\hat{\theta}\hat{\theta} + \hat{\phi}\hat{\phi}\right]\cdot\hat{n}\times\overline{H}(\overline{r}') \right. \\
&\qquad\qquad \left. + ik_0\left[\hat{\phi}\hat{\theta} - \hat{\theta}\hat{\phi}\right]\cdot\hat{n}\times\overline{E}(\overline{r}') \right\}\frac{e^{ik_0|\overline{r}-\overline{r}'|}}{4\pi|\overline{r}-\overline{r}'|}
\end{aligned}
\tag{2.98}
$$

$$
\begin{aligned}
\overline{H}(\overline{r}) &= \oiint_{S'} dS' \left\{ -i\omega\epsilon_0 \left[\overline{\overline{I}} - \hat{r}\hat{r}\right]\frac{e^{ik_0|\overline{r}-\overline{r}'|}}{4\pi|\overline{r}-\overline{r}'|}\cdot\hat{n}\times\overline{E}(\overline{r}') \right. \\
&\qquad\qquad \left. + ik_0\hat{r}\times\left[\overline{\overline{I}} - \hat{r}\hat{r}\right]\frac{e^{ik_0|\overline{r}-\overline{r}'|}}{4\pi|\overline{r}-\overline{r}'|}\cdot\hat{n}\times\overline{H}(\overline{r}') \right\} \\[4pt]
&= \oiint_{S'} dS' \left\{ -i\omega\epsilon_0 \left[\hat{\theta}\hat{\theta} + \hat{\phi}\hat{\phi}\right]\cdot\hat{n}\times\overline{E}(\overline{r}') \right. \\
&\qquad\qquad \left. + ik_0\left[\hat{\phi}\hat{\theta} - \hat{\theta}\hat{\phi}\right]\cdot\hat{n}\times\overline{H}(\overline{r}') \right\}\frac{e^{ik_0|\overline{r}-\overline{r}'|}}{4\pi|\overline{r}-\overline{r}'|}
\end{aligned}
\tag{2.99}
$$

In the finite difference-time domain scheme, it is relatively simple to obtain the fields over a closed surface. For a finite geometry, the scattered fields can be sampled on a rectangular box which encloses the entire geometry [Figure 2.6]. For an infinite ground plane geometry, the scattered fields are sampled on the sides of a

box which encloses any discontinuities in or above the infinite ground plane [Figure 2.7]. Image theory allows the replacement of the infinite ground plane with image sources. Using the appropriate image fields for infinite perfect electric and magnetic conducting planes, it is possible to obtain the tangential fields over a closed surface. Note that the field solution obtained using the image sources is not valid in the image half space.

Sinusoidal and Gaussian pulse time dependent excitations are treated differently in order to obtain the necessary time harmonic complex amplitudes of the fields on a closed surface. For sinusoidal time dependent excitations, it is relatively simple to obtain the complex amplitudes of the fields by sampling the fields after steady state has been reached. The amplitudes can be obtained by recording the maximum values of the fields. The relative phases can be obtained by recording and comparing the time of the maximum values of the fields. For Gaussian pulse time dependent excitations, Fourier transformation of the excitation source and the fields is performed. At a particular frequency, by dividing the complex Fourier amplitudes of the fields by the Fourier amplitude of the excitation, the complex amplitudes of the fields can be obtained for an excitation source with unity amplitude. For sinusoidal time dependent excitations, fields and hence radiation patterns can only be obtained for a single frequency. However, for Gaussian pulse time dependent excitations, fields and radiation patterns can be obtained for multiple frequencies. Some limitations to the range of frequencies that can be analyzed, are that the grid must be fine enough to adequately model the frequency of interest and that the Gaussian pulse must contain a significant amount of energy at that frequency.

2.13　Limitations

While the FD-TD technique can provide very accurate predictions and solutions to various electromagnetic phenomena, there are a number of approximations inherent to the technique. The center difference approximations applied to Maxwell's equations are accurate to the second order (i.e., the error term is proportional to the square of the grid size (Δ^2)). This error can be kept to a minimum by choosing the grid size to be less than a tenth of the shortest wavelength of interest. Some dispersion is introduced by the discretization of Maxwell's equations (i.e., different frequency components travel at slightly different velocities). Geometries are discretized on a rectangular grid. Hence, the dimensions of any scatterer are restricted to integer multiples of the grid size, and curved surfaces must be approximated with staircases. In general, as long as the grid size is small compared to the dimensions of the scatterer, the scatterer can be adequately modeled on rectangular grids. At the outer boundary some reflections will occur because the absorbing boundary condition is an approximate condition. These reflections can be kept tolerable by locating the outer boundary at least half a wavelength away from the scatterer [10].

2.14　Summary

The main features of the FD-TD technique are the following. It is essentially an "exact" numerical method, with most of the errors being introduced to the finite discretization of space and time. The method is well suited for complex geometries. Since it is a time domain method, the fields can be viewed as a function of time, and

through the use of Fourier transforms, multiple frequencies can be analyzed with a single FD-TD simulation.

Chapter 3

EM Radiation from a VLSI Chip Package and Heatsink Structure

3.1   Introduction

The extension of regulatory electromagnetic emissions limits to the gigahertz range of frequencies for high performance computing equipment has necessitated caution in the design and implementation of components, down to the VLSI chip package level, for computing systems. The avoidance of potentially efficient radiators at the design and development phases is of interest. The objective is to minimize the need for cost-prohibitive corrective measures commonly invoked in reaction to problems encountered in tests on assembled systems.

In this chapter the effects of a heatsink, placed over a chip package, on the electromagnetic emissions characteristics of the chip and package configuration are addressed [31]-[33]. Such an interest is justified by the following reasons. The heatsink is typically metallic and is in close proximity to a major energy source — the chip. The radiation characteristics of the heatsink will be similar to those of a microstrip

85

patch antenna [116]-[118],[111]. The electrical dimensions of the heatsink structure are comparable to the wavelengths of concern. In light of the ever-increasing power levels of high performance integrated circuitry, the heatsink is an indispensable component of the VLSI chip packaging configuration. The objectives are to identify and quantify the effects of the heatsink on the radiating properties of the package structure; to understand and exploit the radiation mechanisms; and to evaluate viable heatsink implementation schemes for minimizing the overall radiating capacity.

In Section 3.2, the model used to analyze the problem is presented. The method of solution, namely the finite-difference time-domain technique, is discussed in Section 3.3. In Section 3.4, results are shown for two example heatsinks. Observations are made regarding the general radiation characteristics of the VLSI chip package and heatsink structure. Two implementation schemes to reduce the radiation are also explored and evaluated. Overall observations are made in Section 3.5 regarding the effectiveness of the analysis technique and the radiation characteristics of the heatsink and chip package.

3.2 Problem Configuration and Model

The electromagnetic radiation properties of a heatsink and integrated circuit (IC) package configuration are analyzed by means of suitable models. A typical heatsink/ package configuration of interest is shown in Figure 3.1. The heatsink may be modeled as a perfectly conducting rectangular slab positioned over a finite-size dielectric medium representing the chip package. The chip package is supported in turn by a dielectric layer of infinite extent over an infinite ground plane which models the substrate or printed wiring board (PWB) with (at least) one reference layer. The electromagnetic sources used to model the active chip include electric and magnetic dipoles of vertical and horizontal orientations positioned on the package/substrate dielectric interface. The choice of such elements circumvents the problem of deriving a rigorous model for the VLSI circuitry as an electromagnetic source and eliminates factors which may otherwise clutter the understanding and interpretation of the physical processes associated with the spurious radiation study. The resulting model of an electromagnetically-coupled slab structure is shown in Figure 3.2. The use of a model with reduced complexity for both source and heatsink is to facilitate the interpretation of results based on underlying physics. The extension to other heatsink configurations (e.g., circular or finned) and source models may be accomplished with the numerical solution employed. With sufficiently fine grids, circular heatsinks may be adequately modeled. As illustrated in Section 3.4, the model in Figure 3.2 is readily modified to model various heatsink implementation schemes proposed for emissions reduction consideration. Field strengths, and radiated powers are computed for quantitative analysis and evaluation.

MOUNTING SCREW

HEATSINK

CERAMIC CHIP
CARRIER

SUPPORT FRAME

PRINTED WIRING BOARD

SUPPORT ASSEMBLY
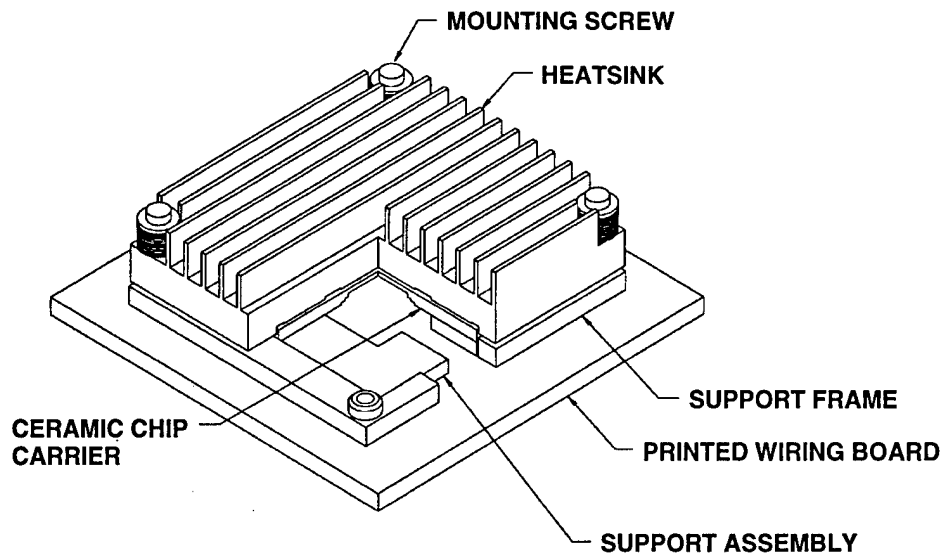
Figure 3.1: Cut away view of a VLSI package/heatsink configuration.

SOURCE

TOP VIEW

IC PACKAGE

HEATSINK (CONDUCTING SLAB)

SIDE VIEW

REFERENCE PLANE
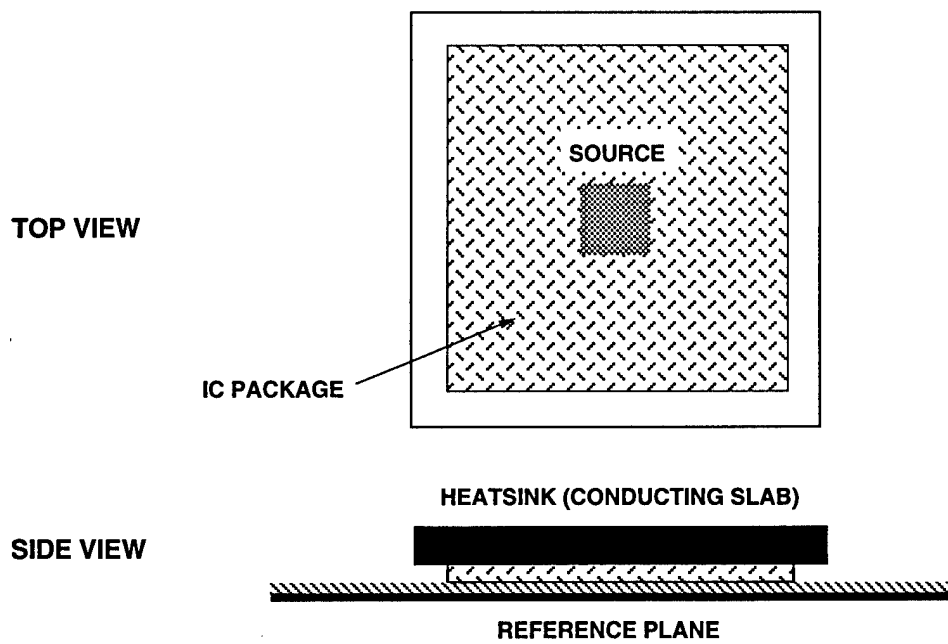
Figure 3.2: Cross sectional view of simplified package/heatsink model.

3.3 Method of Solution

The method employed in the analysis is the finite-difference time-domain (FD-TD) technique [1]-[12]. A more in depth discussion of the FD-TD technique is provided in Chapter 2. It is based on the discretization of the electric and magnetic fields over rectangular grids together with the finite difference approximation of the spatial and temporal derivatives appearing in the differential form of Maxwell's equations. The reasons for which the FD-TD methodology was selected include the relative ease of implementation for complicated geometries with dielectrics, the requirement of only simple arithmetic operations in the solution process, and the flexibility for time- and frequency-domain analyses.

In the FD-TD technique, a computational domain is first defined and divided into rectangular cells. Electric and magnetic fields are spatially discretized in a staggered manner [1]. Electric fields are assigned to half-integer $(n + 1/2)$ time steps and magnetic fields are assigned to integer (n) time steps for the temporal discretization of fields. Next, the spatial and temporal derivatives of the two Maxwell's curl equations are approximated using center differences. Maxwell's divergence equations are ignored since the curl equations with appropriate boundary conditions uniquely determine the solution. In rectilinear coordinates, the curl equations can be rewritten as a set of six scalar equations. Difference equations are derived from these six equations by applying center differencing. The center difference ensures that the spatial and temporal discretizations are of second-order accuracy, where errors are proportional to the square of the cell size and time increment [1]. Finally, with appropriate initial and boundary conditions, the solutions to the difference equations are obtained

through explicit leapfrog time marching. This corresponds to alternating the advance of electric and magnetic fields [6]. To achieve accurate results, the cell sizes are taken to be a fraction ($\sim 1/20$) of the smallest wavelength. The time increment and the cell size are related by the stability criterion [6],

$$\Delta t \leq \frac{1}{c_0\sqrt{(1/\Delta x)^2 + (1/\Delta y)^2 + (1/\Delta z)^2}} \tag{3.1}$$

where c_0 is the speed of light in free space. Fields are set to be zero initially everywhere to satisfy the causality condition consistent with zero excitation for time less than zero. The boundary conditions are continuity of tangential electric and magnetic fields on material interfaces, vanishing tangential electric fields on perfect conductors, and the absorbing boundary conditions (ABC) on the boundary of the computational domain [67]-[75]. First and second-order absorbing boundary conditions [67] are used to limit the computational domain by simulating unbounded space.

The size of the discretization cells should be reasonably small in order to model features of the heatsink and capture correct field variations. On the other hand, the heatsink should not be too close to the computational boundary in order to avoid significant reflections from the ABC. The cell count in the region outside the heatsink will be very large when a small cell size is used with uniform gridding. To avoid the excessive number of cells which would otherwise be generated, a three-zone gridding scheme [10],[31]-[33] is used (Figure 3.3). The first zone contains the heatsink and dipole source; it has the finest grid among the three zones. The second zone has the same height as the first and extends horizontally from the heatsink to the outer boundary of the computational domain. The cells in this zone have the same vertical

dimension as those in the first zone in order to properly resolve the PWB structure. However, these cells have horizontal dimensions which may be a few times larger than those of the cells in the first zone. The remainder of the computational domain belongs to the third zone, where the cells have the same horizontal dimensions as the cells in the second zone, and have a vertical dimension which may be a few times larger than the vertical dimension of the cells in the first or second zones. Field quantities at nodes on an interface between two zones are calculated via a combination of parabolic curve fitting and linear interpolation, which maintains the second-order accuracy of the algorithm [10],[31],[32]. For example, in Figure 3.4, the partial derivative of H_y with respect to the vertical direction z at position of $E_x(i, j, k)$ at the nth time step is given by

$$\frac{\partial H_y}{\partial z}\bigg|_{E_x(i,j,k)}^n \simeq \frac{8}{\Delta(1+a)(3+a)}H_y^n(i, j, k)$$

$$+\frac{a-3}{\Delta(1+a)}H_y^n(i, j, k-1)$$

$$+\frac{1-a}{\Delta(3+a)}H_y^n(i, j, k-2)$$

$$+\frac{4a^3+13a^2-9}{24(a+1)(a+3)}\Delta^2\frac{\partial^3 H_y}{\partial z^3}\bigg|_{E_x(i,j,k)}^n \tag{3.2}$$

where a is the ratio between the cell sizes in the two regions. As seen from the last term in the above equation, second order accuracy is maintained everywhere. Although the discretization scheme is second-order in all three zones, the proportionality constants for the discretization errors are different due to different cell sizes. Reasonable accuracy is maintained due to the fact that the spatial variation of the

ABSORBING BOUNDARY CONDITION
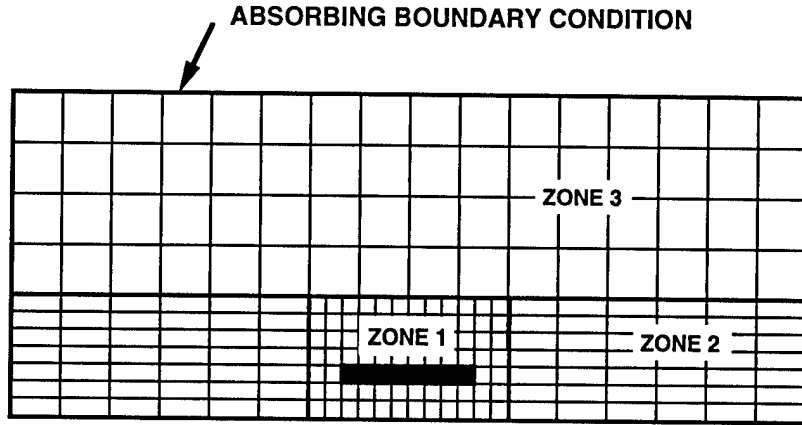
Figure 3.3: A three-zone gridding scheme for multi-zone gridding. The heatsink is in zone 1.

fields outside the first zone is gradual and that all cell sizes remain a fraction of the smallest wavelength. The size of the time step is primarily determined by the smallest grid dimension. For simplicity, the variable time step implementation [51] is not used.

The implementation of the electric and magnetic dipoles of vertical and horizontal orientation in the FD-TD scheme requires normalization. Since the dipoles are implemented by exciting the fields at a single node in the rectangular grid, the dimensions of the dipole, and hence their dipole moments, are not precisely defined. In addition to performing a FD-TD simulation of the heatsink configuration, a simulation is done using the same grid dimensions for the same dipole in an infinite parallel plate structure. The radiated power for a dipole in a parallel plate waveguide can be analytically related to its dipole moment [106]. So, the radiated power from the second FD-TD simulation is used to obtain the dipole moment, which in turn is used

$E_x(i,j,k\text{-}1)$ $E_x(i,j,k)$ $E_x(i,j,k\text{+}1)$

$H_y(i,j,k\text{-}2)$ $H_y(i,j,k\text{-}1)$ $H_y(i,j,k)$

Δ

$a\Delta$
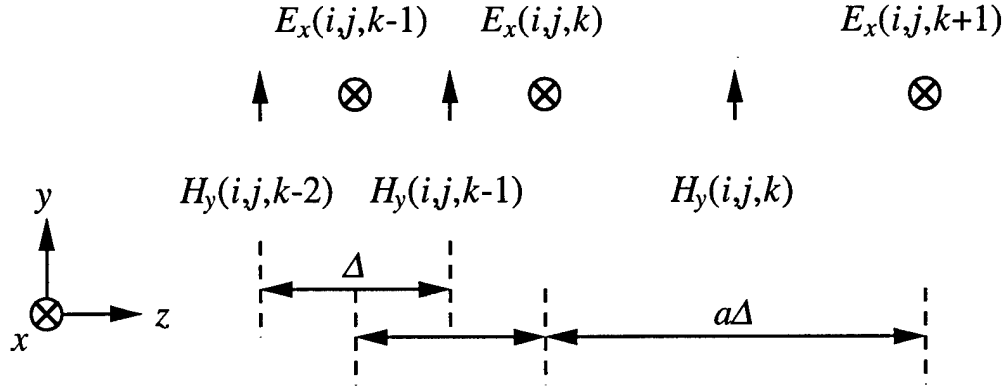
Figure 3.4: Node and field designations for multi-zone gridding in vertical direction.

to normalize the dipole in the first simulation.

In order to obtain certain frequency domain parameters, such as the radiated power or the radiation pattern, the complex field amplitudes on a closed surface must be obtained. The post-processing of full time domain information for the purpose of generating frequency domain data is expensive in storage and is inefficient. The complex field amplitudes are instead calculated at selected multiple frequencies. To obtain multi-frequency data, the time waveforms of the dipole excitations are chosen to be modulated Gaussian pulses, i.e., $\simeq \cos(\omega_0(t - t_0)) \exp[-((t - t_0)/T)^2]$, where ω_0 is the center frequency of the excitation, t_0 is the delay, and T determines the pulse-width. The Gaussian pulse is modulated in order to concentrate the energy in the frequency range of interest. Complex amplitudes at each frequency are calculated simultaneously on a selected surface outside the first zone using the discrete Fourier transform. The total radiated power is found by integrating the Poynting vector over

a closed surface. Once the complex field amplitudes on a closed surface have been stored, the far-field radiation pattern can be calculated using Huygens' principle [106].

3.4   Results and Discussion

The basic model described in Figure 3.2 is analyzed with the use of horizontal electric and magnetic dipoles and vertical electric and magnetic dipoles as sources. Of these sources only the horizontal magnetic dipole (HMD) and vertical electric dipole (VED) show radiation enhancement in the presence of the heatsink. The frequency range considered does not exceed 10 GHz. The dominant horizontal (electric field) polarization generated by the other 2 sources remains below cutoff within this frequency range and for the typical dimensions considered. Both classes of sources are found in VLSI chip package configurations — the VED in the form of current carrying vias and pins and the HMD as vertically configured signal and return paths. Results and discussions will focus on the VED and HMD sources.

As stated previously, the choice of the dipoles for sources facilitates the understanding of the overall problem and the interpretation of the simulation results while deferring the electromagnetic modeling of a VLSI chip. From a practical viewpoint, the drawback of such models lies in the resulting difficulty for designers to determine the radiation levels of the actual heatsink and package configurations. A knowledge of the electromagnetic source characteristics has to be combined with a physical model (e.g., a conducting patch) of the VLSI chip to meet this practical requirement.

3.4.1   Radiation Enhancement by Heatsinks

The configuration of heatsink A is the same as the heatsink illustrated in Figure 3.2, except that no dielectrics are present. The dimensions of the square conducting slab

are $w_{hs} = 4.8$ cm, $t_{hs} = 2.5$ mm, and $h = 7.5$ mm, where w_{hs} is the width, t_{hs} is the thickness, and h is the height of the heatsink above the ground plane. The dipole source is located within the three-dimensional rectangular grid at the node closest to the center of the heatsink/ground plane cavity.

Figure 3.5 compares the normalized radiated power of an HMD over a ground plane in the presence and absence of heatsink A for a frequency range of 1 to 6.5 GHz. Normalization is with respect to the total radiated power of an identical dipole in unbounded space (no heatsink or ground plane). The resonant behavior around 2.3 and 5.5 GHz in the presence of the heatsink is evident, with the first resonance showing significant enhancement of radiation over the case without the heatsink. The 3 dB level plotted corresponds approximately to the normalized dipole radiation with the ground plane but in the absence of the heatsink.

It may be inferred from the heatsink dimensions and the field patterns generated by a centered HMD, that the resonant frequency at approximately 2.3 GHz corresponds to the lowest resonance. The electric fields generated by a HMD are anti-symmetric in directions orthogonal to the dipole axis. Hence, a centered HMD will only excite modes with at least one degree of anti-symmetry in the horizontal direction which is orthogonal to the dipole axis.

Figure 3.6 shows the corresponding results over the frequency range of 1 to 8 GHz with a centered VED as the source. Again, substantial enhancement in radiated power in the presence of a heatsink occurs at the primary resonance of 4.9 GHz, and at the second resonance near 7 GHz. The electric fields generated by the VED are symmetric about the dipole axis, hence only symmetric cavity modes are expected to

NORMALIZED RADIATED POWER WITH/WITHOUT HEATSINK

NORMALIZED TO DIPOLE RADIATION
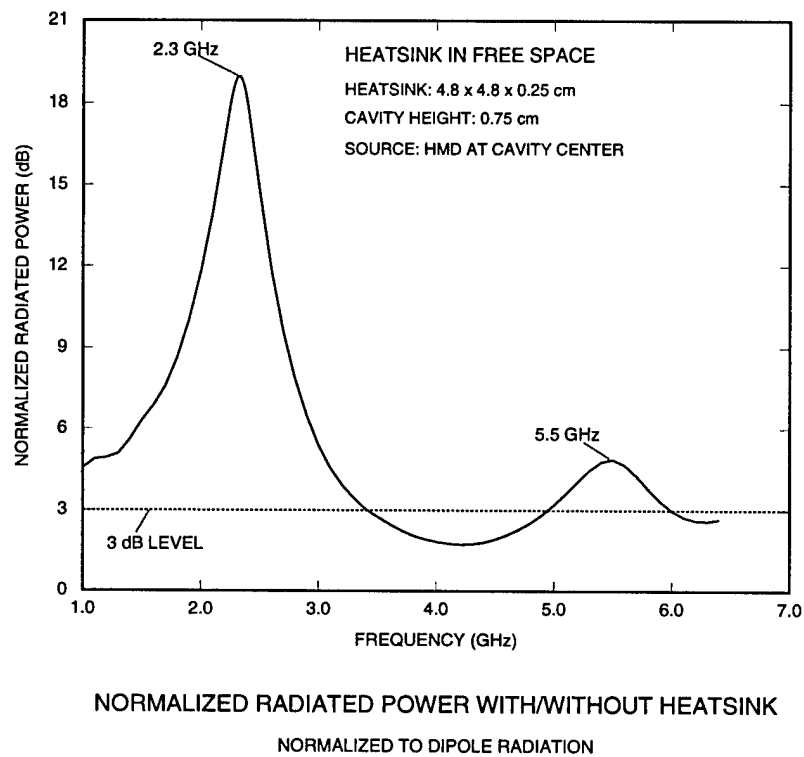
Figure 3.5: Comparison of normalized total radiated power in presence and absence of heatsink *A* with a HMD source.

NORMALIZED RADIATED POWER WITH/WITHOUT HEATSINK

NORMALIZED TO DIPOLE RADIATION
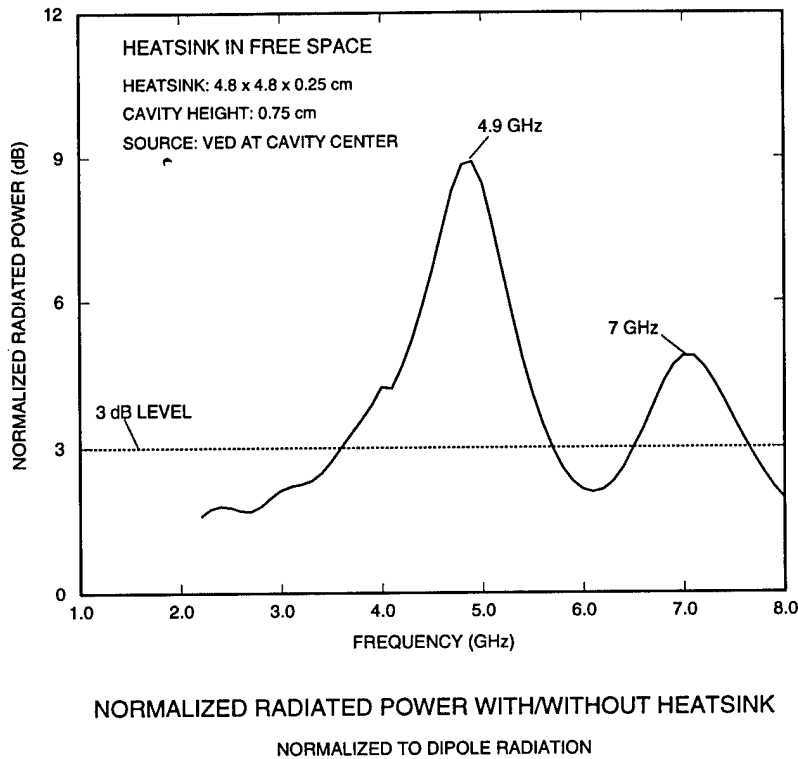
Figure 3.6: Comparison of normalized total radiated power in presence and absence of heatsink A with an VED source.

be excited.

The enhancement of the total radiated power over when the heatsink is absent in the vicinity of the resonance is evident. In particular, for the lowest resonant frequency near 2.3 GHz, 16 dB enhancement is observed with the addition of the heatsink to the ground plane. The actual degree of enhancement will be influenced by the physical chip model, the module and system environment. It is observed, in the cases shown, that the resonances are not sharp, i.e., they are of relatively low quality factor, Q. For instance, in Figure 3.5, the radiation enhancement is higher than 10 dB over a frequency range of 2.05 GHz to 2.55 GHz. The 500 MHz-wide band could fit 4–5 harmonics of a 100 MHz clock signal, thereby enhancing radiation at a

multitude of frequencies in general. An approximate determination of the resonant frequencies is of interest and warrants further discussion.

A simple but less accurate method of determining the resonant frequencies for such a configuration is the magnetic-wall approximation [116],[111]. The associated formula is determined from the assumption of perfect open-circuited boundaries and also assumes very small cavity height. The formula for the frequency associated with the (m, n) mode takes the form

$$f_{m,n} = \frac{c}{2}\sqrt{\left(\frac{m}{W_x}\right)^2 + \left(\frac{n}{W_y}\right)^2} \tag{3.3}$$

where c is the speed of light within the cavity medium. In the above equation, m and n are used to denote the mode index corresponding to the m (n) half-wavelength field variation in the x (y) direction. Because the cavity height is small at all frequencies of interest, the third index for field variation in the vertical direction is not used, and is implicitly zero. W_x and W_y are the effective horizontal dimensions derived from enlarging the width and depth to reflect the effect of fringing fields. Such enlargement formulas abound in microstrip literature [111], and are dependent on conductor thickness, cavity height and the dielectric environment. No simple formulas are available which include the effects of the corners.

Table 3.1 lists the first few resonances for the heatsink configuration examined in Figures 3.5 and 3.6 as predicted by the magnetic-wall formula using effective dimensions. Using the dimensions for heatsink A, the effective width (W_x) and depth (W_y) are approximately 5.0 cm. Also shown are the corresponding resonant frequen-

Mode		Resonant Frequency $f_{m,n}$		FD-TD Source Type
m	n	Magnetic-Wall (GHz)	FD-TD (GHz)	
0	1	3.0	2.3	centered HMD
0	2	6.0	4.9	centered VED
1	1	4.3	3.4	off-center HMD
1	2	6.7	5.5	centered HMD
2	2	8.5	7.0	centered VED

Table 3.1: Magnetic-wall resonances and corresponding FD-TD predicted resonant frequencies for heatsink A.

cies derived from the source-dependent FD-TD simulations. In particular, the first resonant mode corresponds to the longer effective dimension being equal to one-half of the wavelength of the associated resonant frequency with no field variation in the other dimension. This may be excited by a HMD located at the center of the cavity. The lowest resonance excited by a centered VED is the (2,0) mode which corresponds to the longer dimension having 1-wavelength variation and no variation in the other dimension.

Noted are the discrepancies in values attributed to the low height and limited fringing field constraints on the magnetic-wall solution. Also notable is the absence of correspondence in the FD-TD simulations illustrated in Figures 3.5 and 3.6 for the (1,1) magnetic-wall resonance. This resonance is excited by off-center dipoles and will be illustrated in Figure 3.8.

For the heatsink configuration examined in Figure 3.5, Figure 3.7 shows the surface plots of the vertical electric field amplitudes at 4 different time steps over a horizontal plane that traverses the heatsink and ground plane cavity and spans the computational domain. Each plot is normalized to the maximum value for the

respective time step. The absence of any obvious reflected disturbances from the edges of the computational domain illustrates the efficiency of the absorbing boundary conditions implemented. The sustained resonant mode pattern corresponds to the (1,0) mode and is evident after 1000 time steps.

Heatsink B, which is a little larger than heatsink A is also analyzed. Heatsink B has dimensions of $w_{hs} = 5.8$ cm, $t_{hs} = 1.0$ cm, and $h = 1.3$ cm (Figure 3.2) and this model contains no dielectrics. The dipole source is again located at the node closest to the center of the heatsink/ground plane cavity unless stated otherwise.

Figure 3.8 compares the normalized total radiated power of an HMD over a ground plane in the presence and absence of heatsink B for a frequency range of 1 to 3 GHz. The first resonance occurs at 1.75 GHz, and shows radiation enhancement of approximately 13 dB over when the heatsink is absent. In comparison to the normalized radiated power with heatsink A, the normalized radiated power with heatsink B has a lower resonant frequency and has a broader response in frequency. This is consistent with the larger dimensions of heatsink B and its larger displacement from the ground plane compared to heatsink A [116],[111]. Figure 3.8 also shows the corresponding response for an off-center HMD source for the same physical configuration. A weaker excitation of the lowest resonance and the excitation of the next resonance at 2.7 GHz, absent for centered dipole excitation, are manifested.

In considering the radiation enhancement as a function of frequency, the concern begins with the lowest resonance which is excited by a centered HMD source. The remaining illustrations will be based on the centered HMD as the source.
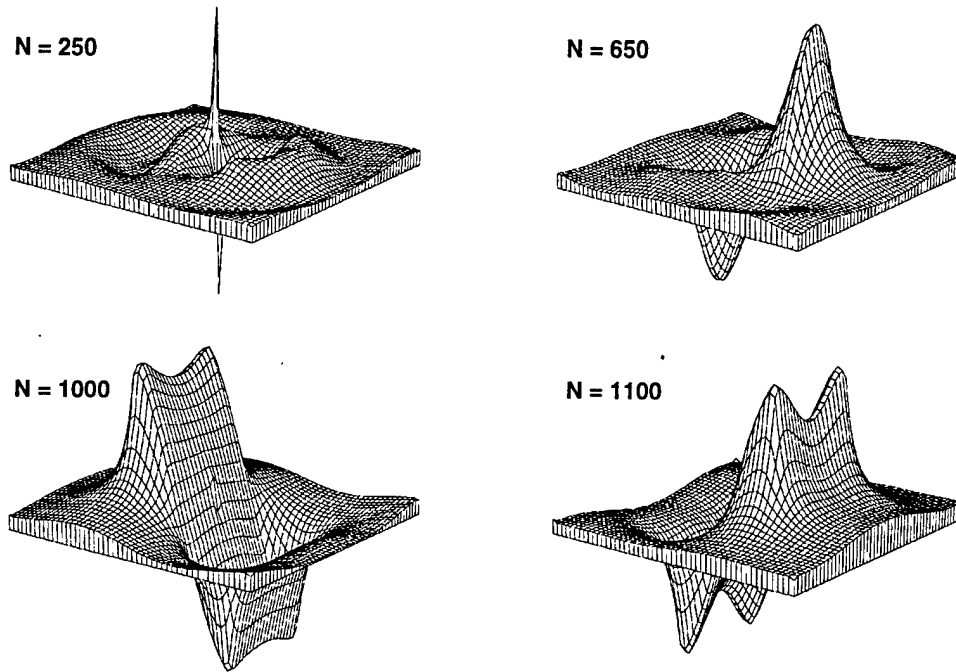
Figure 3.7: Vertical electric field amplitude plots over horizontal plane through heatsink/ ground plane cavity for HMD source. Source function $\sim$ $\cos(\omega_0(t - t_0))\exp[-((t - t_0)/T)^2]$, where $\omega_0 = 5\pi \times 10^9$ rad/s, $t_0 = 4T = 0.8$ ns. N is the number of time steps elapsed, and each time step corresponds approximately to 2.2 picoseconds.

NORMALIZED RADIATED POWER WITH/WITHOUT HEATSINK

CENTERED (0,0,5) AND OFF-CENTER (9,9,5) HMD
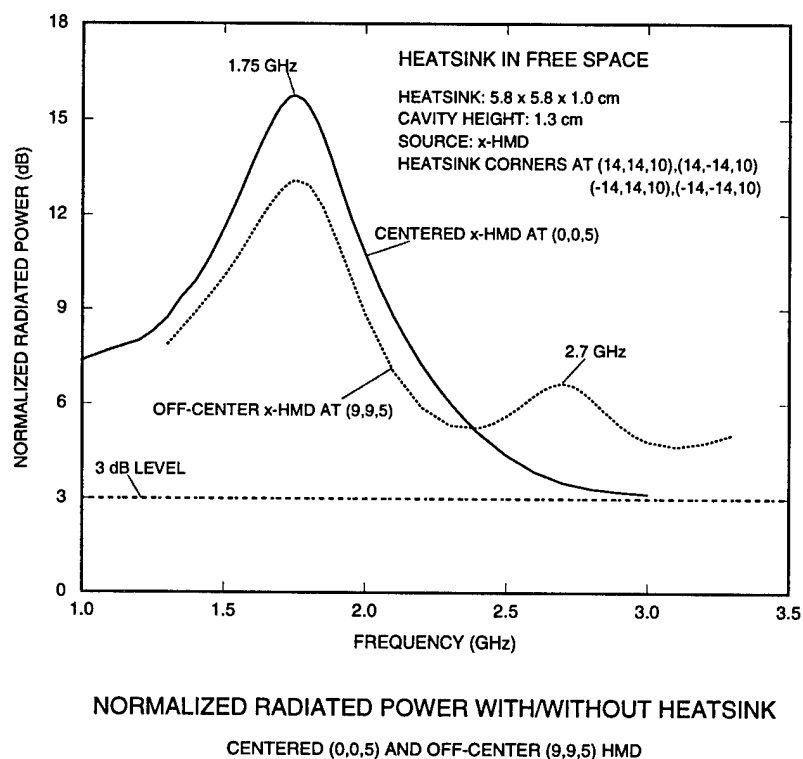
Figure 3.8: Comparison of normalized total radiated power in presence and absence of heatsink B with a centered and an off-center HMD source.

NORMALIZED RADIATED POWER WITH HEATSINK

HMD - HEATSINK (5.8 x 5.8 x 1.0 cm) CAVITY WITH VARIABLE HEIGHT
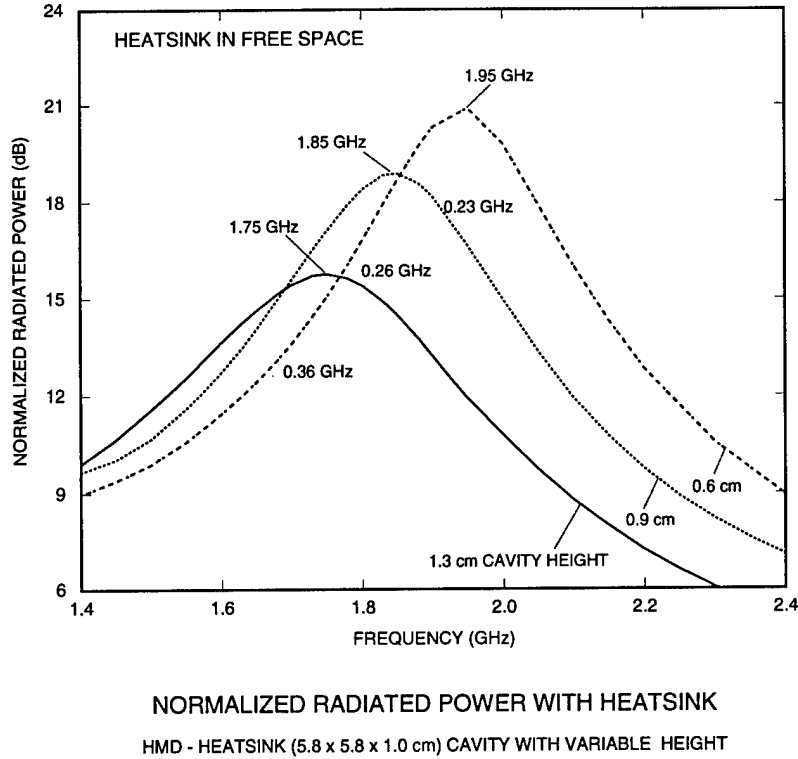
Figure 3.9: Comparison of normalized total radiated power with HMD source for heatsink B as a function of cavity height.

In Figure 3.9, the variation in the normalized total radiated power for heatsink B with changes in the cavity height is shown. The three cavity heights considered are 0.6 cm, 0.9 cm and 1.3 cm. The downward shift in resonant frequency with increasing cavity height is consistent with the increased fringing fields which results in larger effective dimensions. The broadening of the peaks in the curves indicates decreasing Q's which is expected for increasing cavity heights.

The consideration of a heatsink without dielectrics so far has allowed the verification of expected behavior and trends. It is appropriate to verify the performance of the algorithms for the more realistic case where dielectrics such as the PWB and the chip package are included. The dimensions of this model (Figure 3.2) are $w_{hs} = 5.8$

cm, $t_{hs} = 1.0$ cm, $h = 1.3$ cm, $t_{pwb} = 2.5$ mm, and $w_{ic} = 5.1$ cm, $t_{ic} = 6.4$ mm. The PWB is modeled as a lossless dielectric with dielectric constant of 4.0 and the chip package as a dielectric with dielectric constant of 9.0 and a small conductivity of 0.0001 mhos/m. The normalized total radiated power results are shown in Figure 3.10. The expected trend of lower resonant frequencies and higher Q in the presence of dielectric material is manifested. The inclusion of the dielectric material results in an effective dielectric constant larger than 1, leading to a shorter wavelength than in free space. Hence, the heatsink appears larger electrically, and has lower resonant frequencies. It is noted that no alternative methods to the FD-TD method are readily available for the analysis of the 3-dimensional mixed-dielectric problem that results when the PWB and the chip package models are considered together with the heatsink.

A typical heatsink with fins has been modeled in the preceding sections as a perfectly conducting rectangular slab. The validity of such an approximation is examined in the following discussion. The dimensions of the finned heatsink are such that it would fit exactly within heatsink B. The fins are 7.5 mm in height and are evenly distributed across the surface of the heatsink. The fins begin at a distance of 2.5 mm from the lower surface of the heatsink, and are of zero thickness for simplicity in modeling. The horizontal dimensions and the total vertical dimension of the finned heatsink are the same as the corresponding dimensions of heatsink B.

Figure 3.11 compares the normalized total radiated power for a centered x-directed HMD in the presence of plain and finned heatsink models, the latter of which bear fins with either x or y orientations. Emphasis is on the characteristics near their
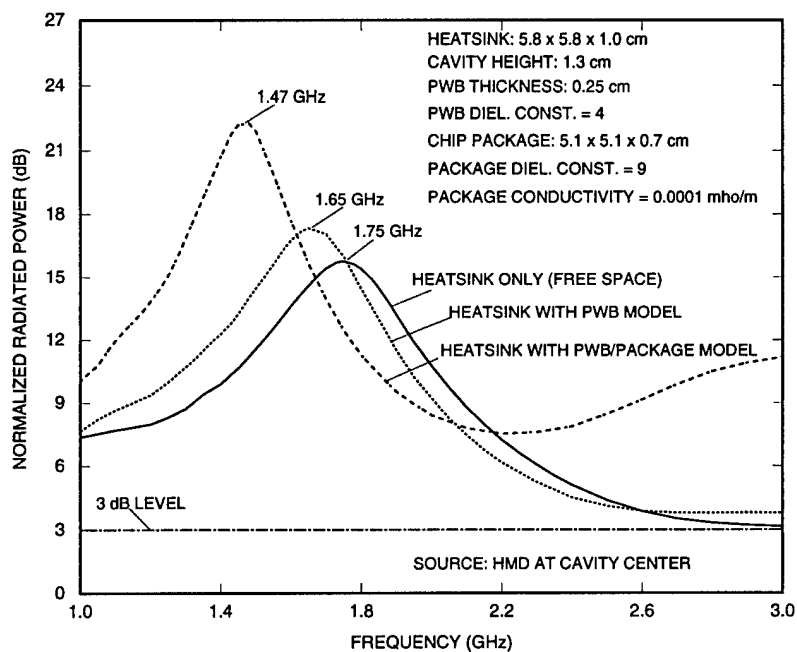
NORMALIZED RADIATED POWER WITH/WITHOUT HEATSINK

VARIATION WITH PACKAGE AND PWB DIELECTRIC MODELS

Figure 3.10: Comparison of normalized total radiated power with HMD source for heatsink B only, with PWB model, and with PWB and IC package models.
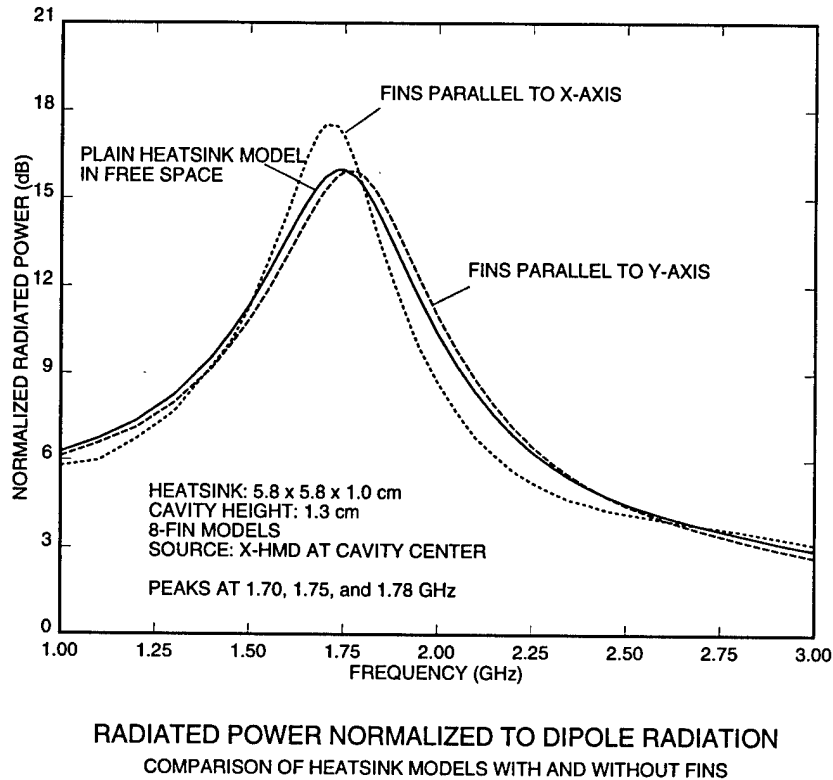
Figure 3.11: Comparison of normalized total radiated power with x-directed HMD source for plain and finned versions of heatsink B.

respective first resonances. The minor differences in the resonance position among the 3 models are attributable to the difference in heatsink features in the vicinity of the dominant fringing fields (at the $\pm y$ faces) corresponding to the lowest resonance. In the case of a plain heatsink model, the fringing fields result from a uniformly thick conductor (lowest resonant frequency of 1.75 GHz). For the model with fins parallel to the y direction, the dominant fringing fields correspond to a thinner heatsink, leading to an effectively smaller cavity with a higher resonant frequency (1.78 GHz). For the model with fins parallel to the x direction, the height of the fins together with the fields existing in the finned environment together results in an effectively larger cavity leading to a reduction in resonance frequency (1.70 GHz).

The differences, nevertheless, appear insignificant and help support the application of the plain model in the analyses. As further demonstration of the validity of the plain model and to demonstrate the capacity of the FD-TD method in facilitating post-processing for radiation characteristics, Figure 3.12 shows the gain patterns at the respective first resonances for the finned and plain heatsink models excited by a centered x-directed HMD. In addition, Figure 3.13 displays the electric field pattern at resonance over a vertical plane for a dipole moment of 10^{-6} A-m, and at a distance of 3 meters. The results for the HMD radiating in the absence of the heatsink are also included in both figures for reference. The Huygens' surface utilized to calculate the gain and field patterns is a box which entirely encloses the heatsink structure.
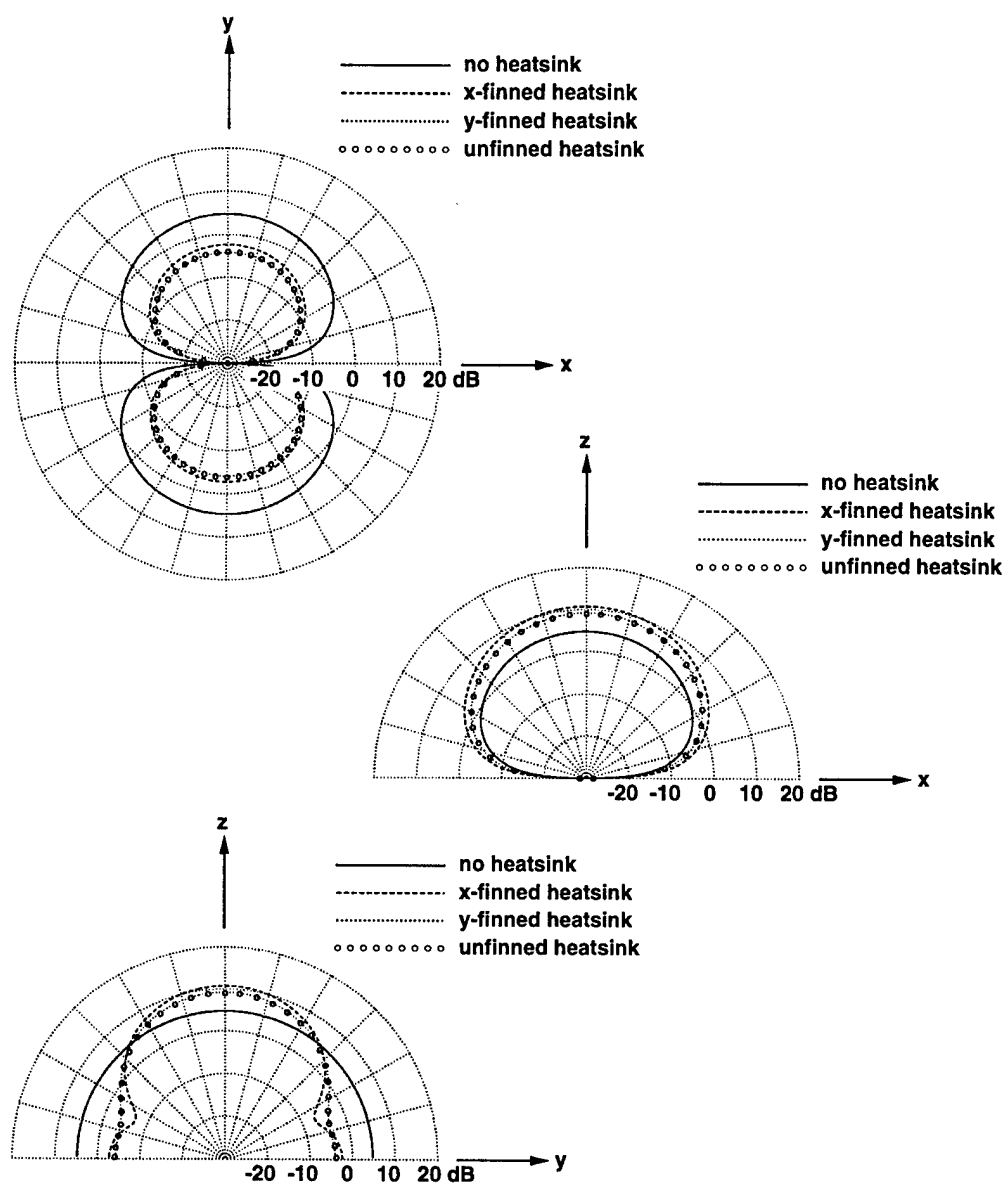
Figure 3.12: Gain patterns at the respective resonances (1.75, 1.70, 1.78 GHz) of unfinned, x- and y-directed finned heatsink models excited by a centered x-directed HMD. The gain pattern for a HMD (1.75 GHz) radiation without a heatsink is also included.
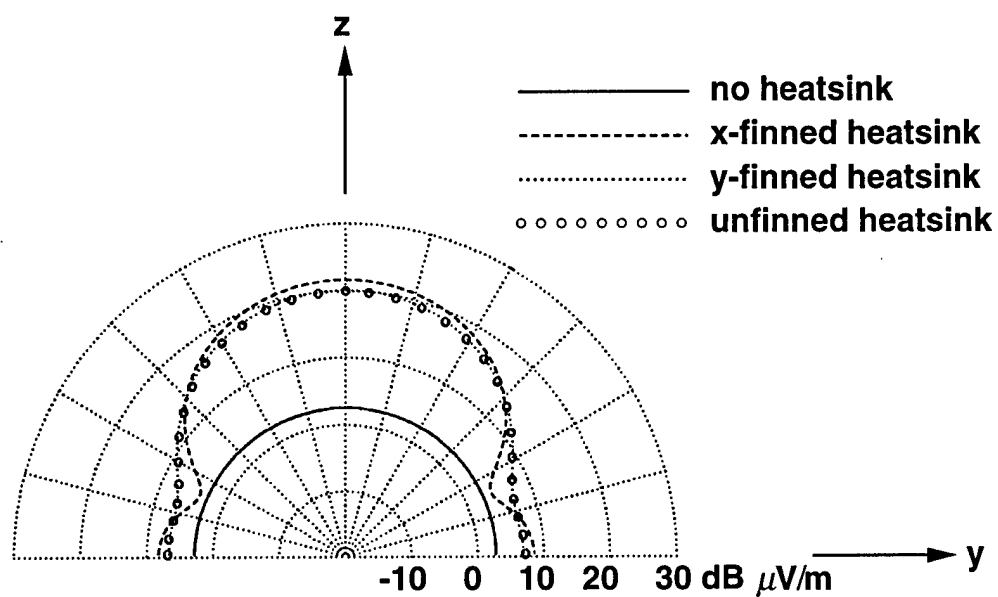
Figure 3.13: Electric field patterns at the respective resonances (1.75, 1.70, 1.78 GHz) of unfinned, x- and y-directed finned heatsink models excited by a centered x-directed HMD. The distance is 3 meters and the dipole moment is 10^{-6} A-m.

3.4.2 Heatsink Implementation Options for Reduction of Radiation

From the simplified model for the heatsink configuration it is evident that cavity resonances exist, which may enhance radiation over when the heatsink is absent. The major assumptions have been the neglect of any adjacent modules, and other components on a module; the neglect of metalization in the heatsink cavity attributed to interconnects, e.g., package references, leads, and pins; and the assumption that basic dipole sources are adequate source models.

Under such circumstances, and given that the heatsink will likely continue as an indispensable component of the VLSI packaging environment, it is of interest to explore the feasibility of some implementation schemes which exploit the heatsink presence to reduce the level of radiation.

To this end, two implementation options are analyzed: the use of metallic posts connecting the edges of the heatsink to the reference plane and the application of a conducting gasket around the lip of the heatsink/reference plane cavity. Both configurations are shown in Figures 3.14 and 3.15.

In the posting option, two cases are considered: the use of a single post at each of the 4 corners (4-post option) or at the corners and centers of the edges (8-post option). Numerical, FD-TD, simulations are performed assuming perfect connections between the posts, heatsink and reference plane. In the gasketing option, the ring of gasket material is excised at the base of each of the 4 faces to model openings which may be required for interconnect passage. The gasket material is modeled as
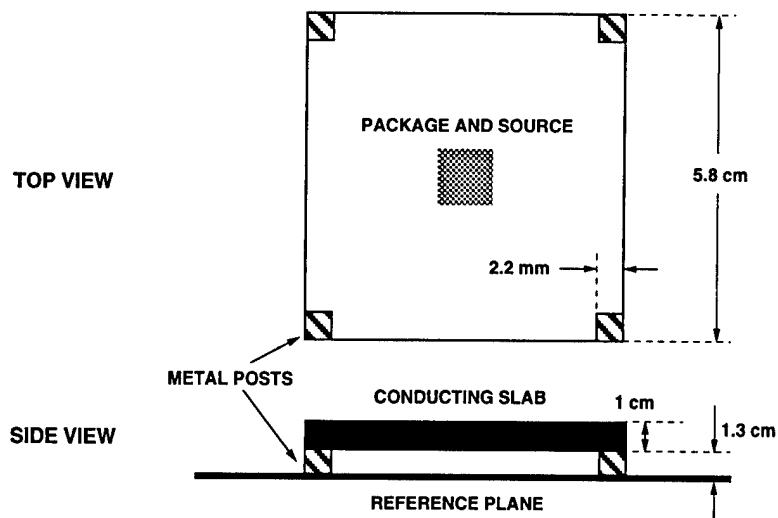
Figure 3.14: Model for heatsink B with 4 support posts connected to reference plane.
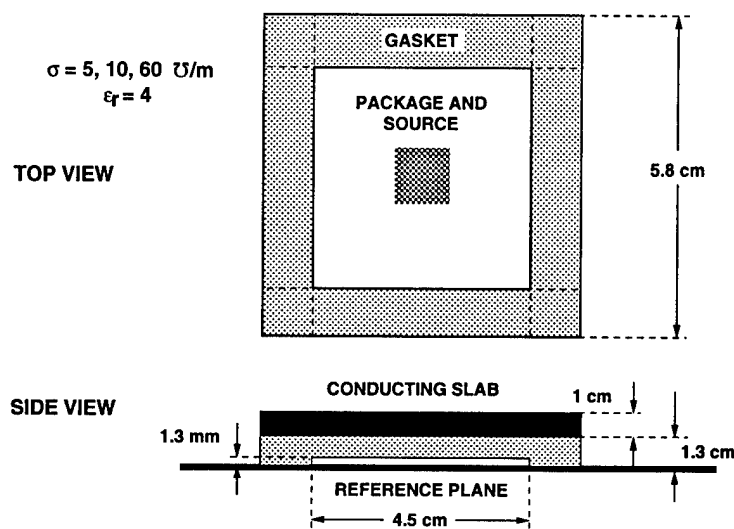
Figure 3.15: Model for heatsink B with a conducting gasket.

RADIATED POWER NORMALIZED TO DIPOLE RADIATION

MULTIPLE POSTS OPTION
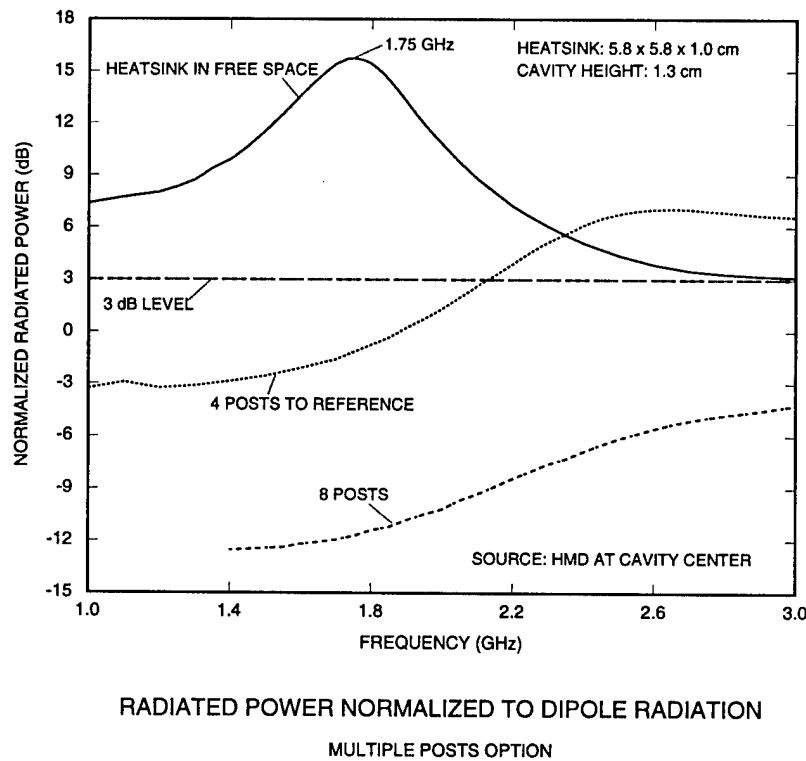
Figure 3.16: Comparison of normalized total radiated power with HMD source for heatsink *B* with 4 and 8 posts and without posts.

a conducting dielectric.

Detailed dimensions of the 4-post model with heatsink *B* are shown in Figure 3.14. Figure 3.16 shows the results from simulations on the 4- and 8-post models. The normalized total radiated power is plotted as a function of frequency over the range of 1 to 3 GHz. The suppression of the original resonance at 1.75 GHz is rather dramatic with 4 posts and even more so with 8 posts. However, the suppression is not uniform with frequency and what is clear from the results is that new resonances have appeared with posting. These occur at higher frequencies — 2.6 GHz and greater than 3 GHz respectively for 4 and 8 posts. This is of significance if the new resonances may be shifted beyond the frequency range where emissions limits apply.

The gasketed heatsink model for heatsink B is shown in Figure 3.15. Figure 3.17 presents the results from simulations on this configuration. The normalized total radiated power is shown over a frequency range from 1 to 3 GHz. The gasketing option appears more effective at higher frequencies and may have a slight adverse effect at the lower frequency end. The improvement at high frequencies is not unexpected since, with the finite material conductivity, the skin depth decreases with frequency and confines as well as dissipates the electromagnetic energy within the heatsink/reference plane cavity more efficiently. A possible explanation for the low frequency behavior is the assumed low conductivity of the gasket material leading to significant current flow on the outer surface of the gasket material. There is then an increased area over which current flows and contributes to the radiation. The effect of varying the conductivity of the gasket is also examined in Figure 3.17. The gradual reduction of the lower frequency peak as gasket conductivity increases is noted. This is consistent with the earlier discussion regarding the behavior of gasketing at low frequencies. The performance at a lower conductivity of 5 mhos/m near 1 GHz worsens, while at a higher conductivity of 60 mhos/m, suppression near 1 GHz is manifested. For reference, the skin depths at 1 GHz for conductivities of 5, 10, and 60 mhos/m are approximately 7, 5 and 2 mm respectively while the gasket thickness for this configuration is approximately 6.5 mm. The skin depth rule may also be misleading since it is derived from plane wave (far-field) arguments and need not apply in this environment where the gasket material is so close to the energy source.

For all three conductivities, the effect of cavity resonance near 1.75 GHz is still evident. The lossy, dielectric, gasket model perturbs the field patterns and affects the

RADIATED POWER NORMALIZED TO DIPOLE RADIATION

VARIATION OF GASKET CONDUCTIVITY
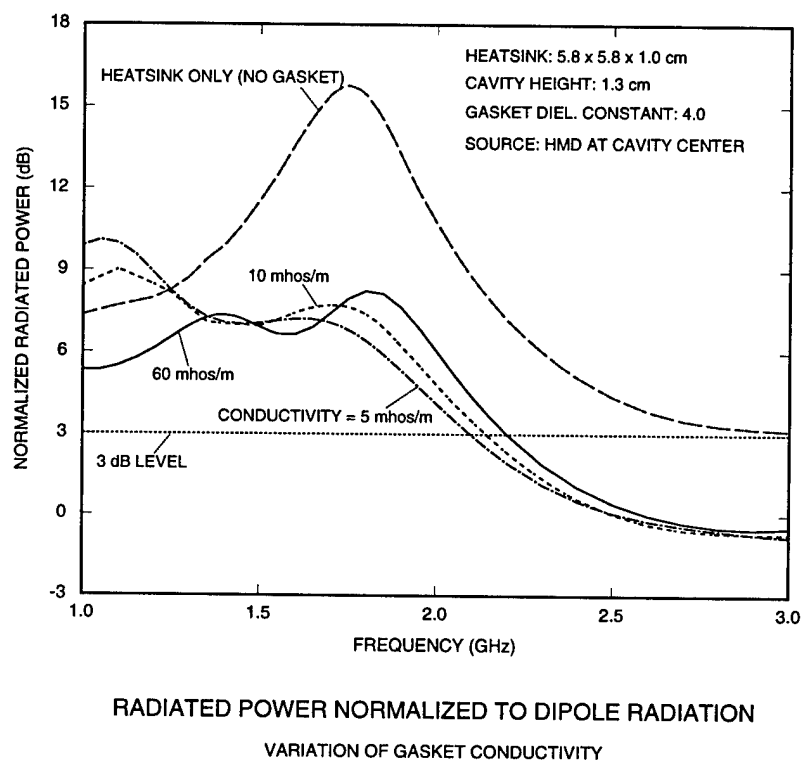
Figure 3.17: Comparison of normalized total radiated power with HMD source for heatsink *B* with gasketing of varying conductivity.

effective cavity dimensions and hence the position of the resonant frequencies.

In practice, compliant gasket materials suitable for such applications have bulk conductivities of the order of 10^3–10^4 mhos/m. For such conductivities, the skin depth would be of the order of 0.1 mm at 5 GHz. To resolve the field variations across the gasket material (1–2 grid cells per skin depth) would require such a fine discretization that the computation requirements for the 3-D problem would be impractical even with the non-uniform discretization scheme used. This is therefore a limitation of the solution method.

Since the posting option pushes the resonances upward in frequency where gasketing functions best, it is logical to expect radiation reduction over a broad frequency band when both posts and gasket are implemented. Figure 3.18 illustrates the normalized total radiated power for the corresponding model. Although the level of reduction in radiation at a given frequency is not the lowest when compared to the two implementation options considered separately, it is observed that peak radiation has been reduced to below the peaks obtained using either of the other two implementation options. Total radiation is also always lower when compared to the case of an isolated or floating heatsink over a reference plane. The observed results are desirable since any suppression scheme to satisfy regulatory emissions limits should be effective over a broad range of frequencies as excessive radiation at a single frequency is sufficient to result in test failure.

Even though the analyzed configurations exhibit resonances, they are of sufficiently low Q's that fewer than 8000 time steps are necessary for the analysis of any of the configurations discussed. For configurations having higher Q's, the required

NORMALIZED TOTAL RADIATED POWER

GASKET-AND-POSTS OPTION
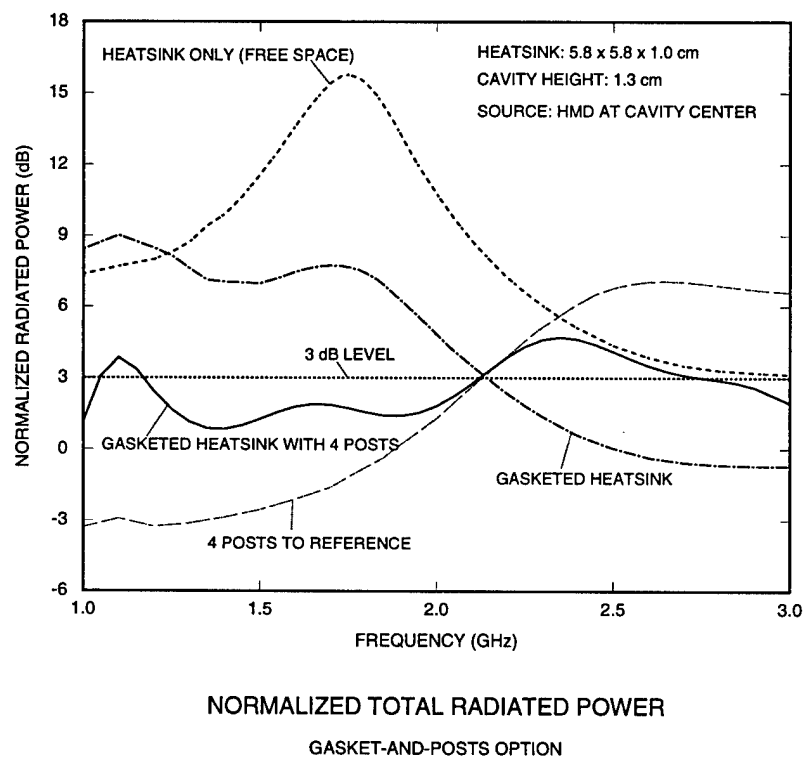
Figure 3.18: Comparison of normalized total radiated power with HMD source for heatsink *B*, with gasketing, with 4 ground posts, and with combined gasketing and 4 ground posts.

time response can be obtained by using an extrapolation scheme based on Prony's method [114]. A typical computational domain may contain up to $50 \times 50 \times 40$ grid cells, depending on the frequency range of interest and the expansion factors selected for the non-uniform gridding implementation.

The numerical simulations performed for the presented data on radiated powers take on the order of 5 to 30 CPU hours on mini-computer and RISC-based workstation systems, including pre- and post-processing. A significant fraction of the computation time is attributed to processing the complex fields at multiple frequencies — necessary for frequency domain analyses. The actual computation times also depend on the available memory and other system parameters.

3.5 Summary

The FD-TD technique has been applied to analyze radiation from a VLSI heatsink and package configuration. The technique was chosen for its flexibility in treating this class of problems which include potentially complex configurations for which neither approximate nor analytical methods are practical. The multi-zone gridding scheme implemented allowed a high grid resolution in the vicinity of the heatsink without sacrificing overall cell number thereby allowing increased numerical efficiency for low frequencies. Additional advantages of this discretization scheme include improved geometrical and material modeling.

The analysis of the heatsink, a critical component within the computer packaging environment, illustrated the significance of resonance due to appreciable electrical dimensions on the spurious electromagnetic radiation from the VLSI packaging environment. Simulations with typical heatsinks dimensions showed the occurrence of resonance in the low gigahertz range. The effects of the presence of a heatsink on the radiation properties of dipole models have been explained and the features of resonant behavior presented. The effectiveness and consequences of exploiting practical heatsink implementation options such as grounding and shielding to reduce electromagnetic emissions have been discussed and quantified using the FD-TD numerical technique.

Chapter 4

EM Radiation from Modules-on-Backplane Configurations

4.1 Introduction

In this chapter, the electromagnetic emissions characteristics of a modules-on-back-plane configuration found in computers are examined [34]. Primary motivation for studying the effect of various structures present within a computer on electromagnetic interference (EMI) is that computers are now operating at faster speeds and consuming more power which results in significantly increased levels of power at higher frequencies. The modules-on-backplane is of interest because it is a common packaging hierarchy. The modules are the popular plug-in printed circuit boards which are mounted on the backplane (motherboard). Also a typical modules-on-backplane configuration has reference plane dimensions which are appreciable electrically at frequencies in the hundreds of megahertz, and the structure, as a whole, may function as an antenna. The objective is to identify and quantify the radiation mechanisms

in a modules-on-backplane configuration and to validate the numerical model with measurements.

Section 4.2 presents the model used to analyze the modules-on-backplane configuration. The method of solution is the finite-difference time-domain (FD-TD) technique, which is discussed in Section 4.3. In addition, Prony's method is outlined in Section 4.3. Section 4.4 describes the measurement procedure and provides some validation of the model and measurement procedure. Measurements and numerical predictions are presented and discussed for various configurations in Section 4.5. Overall observations are drawn in Section 4.6 regarding the effectiveness of the method, and the electromagnetic emission characteristics of the modules-on-backplane configuration.

4.2   Problem Configuration and Model

A typical configuration for the modules-on-backplane is shown in Figure 4.1. The elements of the packaging hierarchy of interest in this study are the backplane, the connector and the module. The modules and backplane are printed wiring boards with at least one reference layer. The connector contains numerous wires for carrying signals, for providing power to the various power planes, and for grounding the reference planes. Due to the complexity of the modules-on-backplane configuration, it is necessary to simplify the problem to some reasonable level of detail. The modules and backplanes are populated with numerous chips and contain many signal paths. However, the single largest conductor or signal path in them is typically one of the ground or power planes. These planes, because of their larger dimensions, tend to

enhance radiation at lower frequencies more than the other elements associated with the modules/backplane. For this reason, the modules and backplane will be modeled as perfectly conducting plates. The source considered is the transient, inductive voltage developed across the connector between the module and the backplane. The implementation of this source was done by connecting the outer conductor of a coaxial line to the backplane and the center conductor to the module. The choice of a coaxial probe to excite the module was made primarily because of its simplicity. In addition, the treatment of multi-pin connectors that may provide simultaneous non-uniform excitation should in principle be analyzable through the use of superposition. The resulting simplified model of the modules-on-backplane configuration is shown in Figure 4.2. The use of a model with reduced complexity for both source and modules-on-backplane configuration is to facilitate the interpretation of results based on underlying physics. The extension to other modules-on-backplane configurations (e.g., multiple modules, enclosed) may be accomplished with the numerical method employed. In addition, as other significant excitation sources are identified and better understood, they can be incorporated into the simulation model.
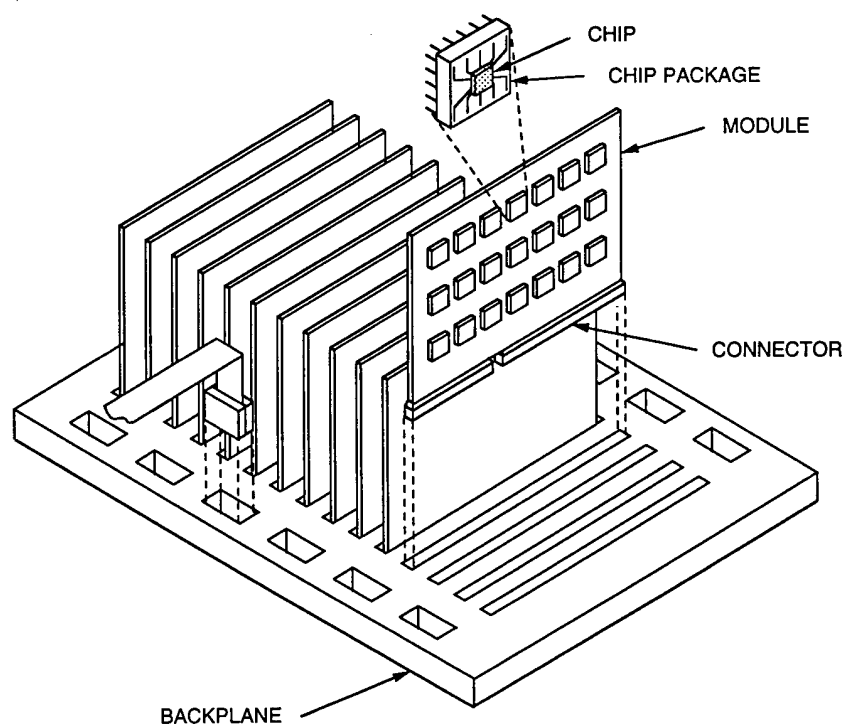
Figure 4.1: A typical modules-on-backplane configuration.
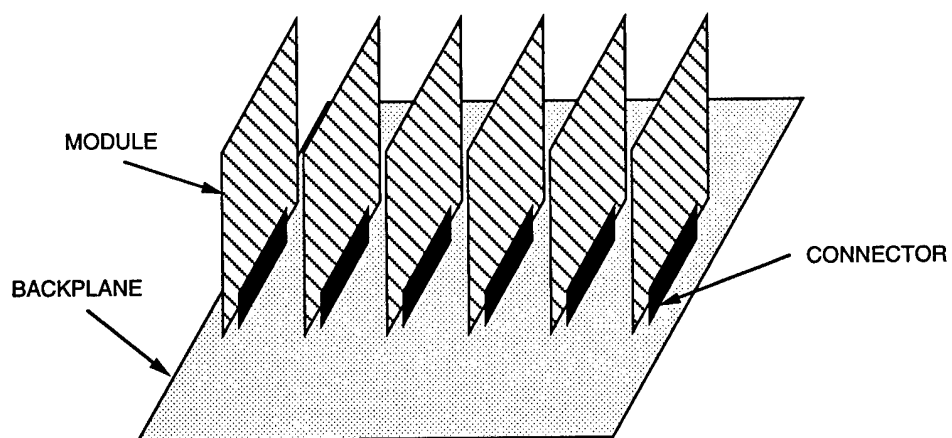
Figure 4.2: Simplified model of the modules-on-backplane configuration.

4.3 Method of Solution

4.3.1 FD-TD Technique

The finite difference-time domain (FD-TD) technique is used to analyze this problem [1]-[12]. This method was chosen because it has the capability of analyzing multiple frequencies with a single simulation, is well suited for low loss models and rectilinear geometries, and is a proven method, as it has been previously used to successfully analyze radiation from a VLSI chip package and heatsink structure [31]-[33].

A rectangular three-dimensional grid is used as the computational domain. Spatially, the computational domain is discretized such that the largest grid dimension is less than about a twentieth of the shortest wavelength of interest. A higher resolution was chosen over the typical tenth of a wavelength criteria in order to more accurately model the resonance phenomena associated with this configuration. The time step approximately must be less than the smallest grid dimension divided by the speed of light in order to guarantee the stability of the algorithm [6]. Some cell dimensions which were typical of the simulations performed for this paper are $\Delta x = 5.00$ mm, $\Delta y = 3.65$ mm, and $\Delta z = 4.98$ mm. The time step associated with these grid dimensions is 8.06 picoseconds. The difference equations which are utilized to update the electric and magnetic fields in a leap frog manner are obtained from Maxwell's equations in differential form by approximating spatial and temporal derivatives with center differences. Electric and magnetic fields are discretized on Yee's lattice, which places them such that they are interlaced in time and space [1]. Initial conditions, which are imposed at the beginning of the simulation, are that all

electric and magnetic fields start at zero. At each subsequent time step, fields are imposed at appropriate locations in order to simulate the excitation source. In this problem, the source is implemented at the wire (connector) connecting the bottom of the module to the backplane by adjusting the electric field value which is parallel with and coincides with the wire location [25]. Assuming that the wire is oriented in the z direction, then the difference equation utilized to update the electric field at the source location is

$$E_z^{n+1}(i,j,k+1/2) = E_s^{n+1} + \left(\frac{1 - \sigma c_0 \Delta t \eta_0/2}{1 + \sigma c_0 \Delta t \eta_0/2}\right) (E_z^n(i,j,k+1/2) - E_s^n)$$

$$+\frac{c_0 \Delta t \eta_0}{1 + \sigma c_0 \Delta t \eta_0/2} \left[\frac{1}{\Delta x}\left(H_y^{n+1/2}(i+1/2,j,k+1/2) - H_y^{n+1/2}(i-1/2,j,k+1/2)\right)\right.$$

$$\left.-\frac{1}{\Delta y}\left(H_x^{n+1/2}(i,j+1/2,k+1/2) - H_x^{n+1/2}(i,j-1/2,k+1/2)\right)\right] \qquad (4.1)$$

where n is the temporal index, i, j, and k are the spatial indices in the x, y, and z directions. E_z, H_x, and H_y simply represent the electric and magnetic fields in the directions corresponding to their subscripts. E_s represents the excitation source and is chosen to be a Gaussian pulse modulated by a sine wave in time and hence contains energy in a band of frequencies allowing multiple frequencies to be analyzed simultaneously. A time profile for E_s would have the form

$$E_s = e^{-(t-4\alpha)^2/2\alpha^2} \sin(2\pi f_0 t) \qquad (4.2)$$

with typical values of $\alpha = 0.6$ ns and $f_0 = 800$ MHz. ϵ_0 is the free space permittivity

and σ is the conductivity which is chosen as

$$\sigma = \frac{\Delta z}{Z_0 \Delta x \Delta y} \qquad (4.3)$$

where Z_0 is the characteristic impedance of the line, and was chosen to be 50Ω in order to match the coaxial line used in the measurements. This equation models a matched source coaxial cable transmission line excitation. Alternatively, setting the electric field to have a predetermined time profile is equivalent to a zero source impedance coaxial transmission line. So the source used to drive this configuration is a 50Ω coaxial cable transmission line with its center conductor connected to the module and the outer conductor connected to the backplane. Boundary conditions are imposed at perfectly conducting surfaces and at the outer boundary. At the perfectly conducting surfaces, the tangential electric field is set to zero. Absorbing boundary conditions must be applied at the outer boundary of the computational domain in order to simulate unbounded space [67]-[75]. Second-order Mur [67] absorbing boundary conditions (ABC) are used at the outer boundary, except at the corners and edges where first-order ABCs are used. Finally, by applying the difference equations obtained from Maxwell's equations in addition to the appropriate initial and boundary conditions, the electric and magnetic fields can be calculated everywhere within the computational domain for each time step. The FD-TD simulation is executed until steady state is reached, which for excitations with pulse time profiles occurs when the fields in the computational domain have become negligibly small. The simulations executed for this paper required from 2000 to 6000 time steps to achieve steady state.

The calculation of total radiated power and radiation impedance is done using

time domain results from the FD-TD simulation. First, the electric and magnetic fields are calculated everywhere in the computational domain. Both the voltage and current on the connector are recorded, and then their frequency domain amplitudes are calculated, whose ratio determines the radiation impedance [25]. The current on the connector I_{con} is calculated using Ampere's Law.

$$I_{\mathrm{con}}(t) = \int_{\substack{\text{around} \\ \text{connector}}} \overline{H}(t) \cdot d\bar{l} \tag{4.4}$$

The voltage V_{con} is defined as

$$V_{\mathrm{con}}(t) = \int_{\mathrm{module}}^{\mathrm{backplane}} \overline{E}(t) \cdot d\bar{l} \tag{4.5}$$

In the FD-TD scheme with the excitation being applied to the electric field $E_z(i,j,k)$, the time domain current and voltage are calculated using

$$
\begin{aligned}
I^{n+1/2} = \; & \Delta y \left[H_y^{n+1/2}(i+1/2, j, k+1/2) - H_y^{n+1/2}(i-1/2, j, k+1/2) \right] \\
& -\Delta x \left[H_x^{n+1/2}(i, j+1/2, k+1/2) - H_x^{n+1/2}(i, j-1/2, k+1/2) \right] \tag{4.6}
\end{aligned}
$$

$$V^n = -\Delta z E_z^n(i, j, k+1/2) \tag{4.7}$$

Finally, Fourier transforming the voltage and current and taking their ratio, the radiation impedance Z_{rad} is obtained.

$$Z_{\mathrm{rad}}(f) = R_{\mathrm{rad}}(f) + jX_{\mathrm{rad}}(f) = \frac{V_{\mathrm{con}}(f)}{I_{\mathrm{con}}(f)} \tag{4.8}$$

This radiation impedance is at the connector between the module and the backplane.

The total radiated power can also be obtained from the complex amplitudes of the current and voltage.

$$P_{\text{rad}}(f) = \frac{1}{2} \operatorname{Re}\left(I_{\text{con}}(f)V_{\text{con}}(f)\right) \tag{4.9}$$

4.3.2 Prony's Method

In applying the FD-TD technique to certain of the more resonant modules-on-backplane configurations, a large number of time steps (on the order of thousands) are required in order to achieve steady state. An extrapolation scheme based on Prony's method is used in conjunction with a relatively short FD-TD time response to efficiently obtain the late time response [114]. This extrapolation method was applied to the time response of the current and voltage on the connector. The FD-TD simulation is executed long enough such that the remaining time response approximately contains only a few decaying complex exponentials. Prony's method approximately determines the complex amplitudes and complex frequencies of these exponentials. Once the complex amplitudes and frequencies are determined then the time response is extrapolated to the desired extent. In analyzing the more resonant modules-on-backplane configurations, the FD-TD simulation would typically be executed for 3000 time steps and then Prony's method would be applied to extrapolate the next 3000 time steps.

The time response is assumed to have the following form:

$$f[n] = f(n\Delta t) = \sum_{m=1}^{M} A_m e^{s_m n \Delta t} = \sum_{m=1}^{M} A_m z_m^n \tag{4.10}$$

where n is the number of the time step, Δt is the size of a single time step, M is the number of complex exponentials being used to estimate the spectral content of the time response, and A_m and s_m are the complex amplitudes and complex frequencies of the exponentials. The time response $f[n]$ can be written as a polynomial where

$$f[n] = \sum_{m=1}^{M} A_m z_m^n \tag{4.11}$$

and

$$z_m = e^{s_m \Delta t} \tag{4.12}$$

A characteristic polynomial is used, which is defined as

$$P(z) = \Pi_{m=1}^{M}(z - z_m) = -\sum_{l=0}^{M} p_l z^{M-l} \tag{4.13}$$

where $p_0 = -1$.

By rearranging the two previous equations, the following expressions can be obtained.

$$\sum_{m=1}^{M} A_m z_m^{n-M} \{P(z_m)\} = \sum_{m=1}^{M} A_m z_m^{n-M} \left\{ -\sum_{l=0}^{M} p_l z_m^{M-l} \right\} \tag{4.14}$$

$$0 = -\sum_{l=0}^{M}\sum_{m=1}^{M} A_m z_m^{n-l} p_l = \sum_{l-0}^{M} f[n-l]p_l \tag{4.15}$$

$$f[n] = \sum_{l=1}^{M} f[n-l]p_l \tag{4.16}$$

The coefficients p_l to the characteristic equation, can be found using a least squares fit to the time response $f[n]$. The time step used in conjunction with Prony's method is typically an integer multiple of the time step used in the FD-TD simulation. The time step only has to be small enough to capture the variation of the time response, or more exactly,

$$-\pi < \mathrm{Im}(s_m)\Delta t < \pi \tag{4.17}$$

Once the coefficients are determined, the roots z_m of the characteristic equation can be calculated. Another constraint on the time step is that $s_m\Delta t$ should not be too small, since that will result in all the roots z_m being very close to 1. When a number of the roots are too close to 1 then the solution for the roots becomes numerically unreliable. Hence trying to use too many complex exponentials or too small a time step will cause numerical problems.

Finally, the complex amplitudes A_m can be found using the following linear system of equations.

$$f[n] = \sum_{m=1}^{M} A_m z_m^n \tag{4.18}$$

where n is chosen to be the last M evenly spaced samples of the time response.

4.4 Measurement Procedure

Measurements were performed using an HP 8510 Network Analyzer. The network analyzer was connected to the modules-on-backplane configuration to be tested by a test port cable and semi-rigid coaxial cable [see Figure 4.3]. While the measurements were not conducted within an anechoic chamber, absorbers were utilized to reduce the effects of the surrounding environment. In addition to the room effects, the presence of the test port cable and semi-rigid coaxial cable on the backside of the backplane could have caused differences with the FD-TD predictions, since all the cables were absent in the FD-TD simulations. However, since the backside of the backplane is shielded by the backplane, presumably the presence of the cable would not significantly affect the measurements. In each of the measurements, the center conductor of the coaxial cable was soldered to the module under test such that the coaxial cable was in contact with at least one of the reference planes in the module. S-parameter data (S_{11}) was recorded using this set-up.

The radiation impedance is deduced from these measurements by performing the following steps. The reflection coefficient, Γ, at the connector between the module and backplane is related to the S_{11} data which is obtained at the end of the test port cable by the following phase term.

$$\Gamma = S_{11}e^{j2kl} \qquad (4.19)$$

**MODULE-ON-BACKPLANE
MODEL**

**HP 8510
NETWORK ANALYZER**

PORT 1

**SEMI-RIGID
COAXIAL CABLE**

TEST PORT CABLE
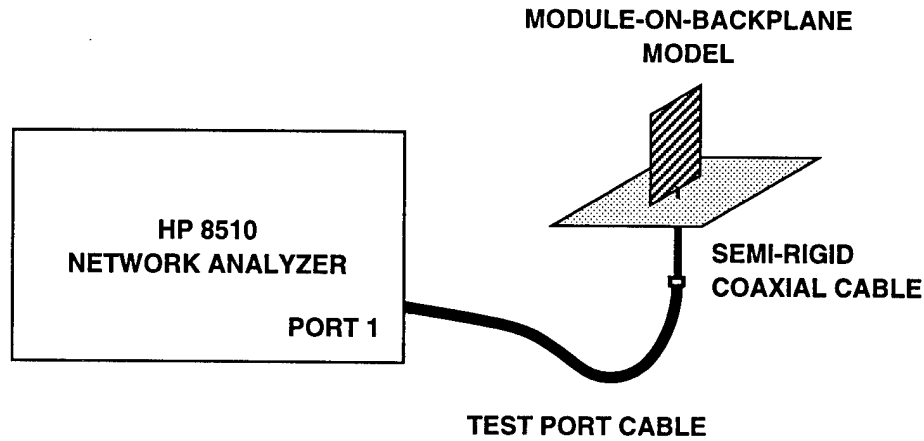
Figure 4.3: Measurement setup.

where $k = 2\pi f / c_1$, f is the frequency, and c_1 is the speed of light within the semi-rigid coaxial cable of length l. Then the load (radiation) impedance can be found using this relation.

$$Z_L = Z_0 \frac{1 + \Gamma}{1 - \Gamma} \qquad (4.20)$$

where Z_0 is the characteristic impedance of the coaxial line. The characteristic impedance of the line used in our study was 50Ω.

The following two configurations were examined: monopoles of lengths 7.5 cm and 5 cm, both over a ground plane of dimensions 30.48 cm by 31.75 cm. The real and imaginary portions of the radiation impedance of the 7.5 cm and 5 cm monopoles over a finite ground plane are plotted in Figures 4.4 and 4.5, respectively. The lowest resonances of these structures, which correspond to purely real radiation impedances, occur at 0.913 GHz and 1.393 GHz for the 7.5 cm and 5 cm monopoles, respectively.
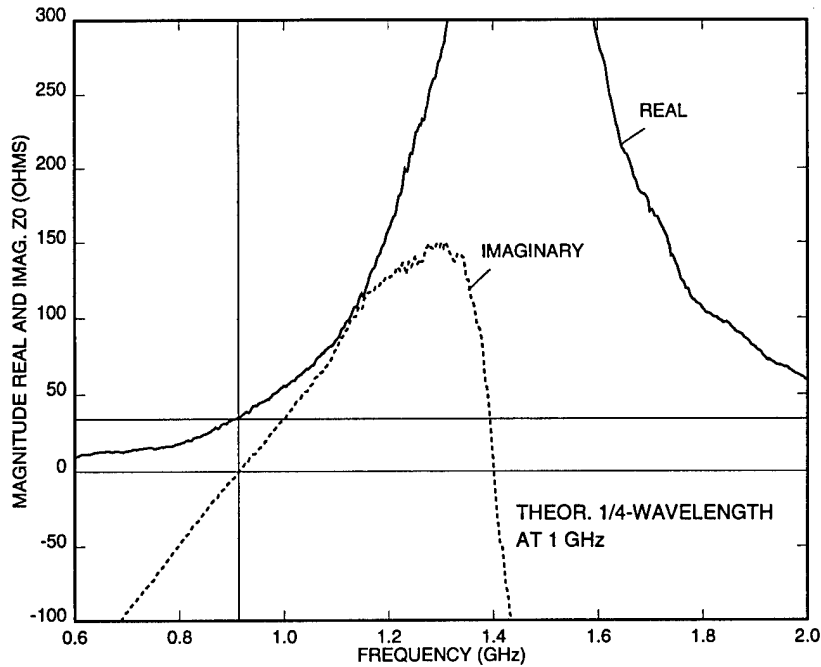
Figure 4.4: Radiation impedance of a 7.5 cm monopole over a ground plane of dimensions 30.48 cm by 31.75 cm as a function of frequency.

The radiation impedances at resonance are 34.2Ω and 36.3Ω for the 7.5 cm and 5 cm monopoles, respectively. Theoretically, the resonant frequencies of 7.5 cm and 5 cm monopoles over an infinite ground plane should occur at 1 GHz and 1.5 GHz, respectively. However, due to finite size of the ground planes, the resonant frequencies are slightly shifted. The radiation impedance at resonance of the monopoles over infinite ground planes should theoretically be about 36.5Ω, which corresponds well with the measured data.
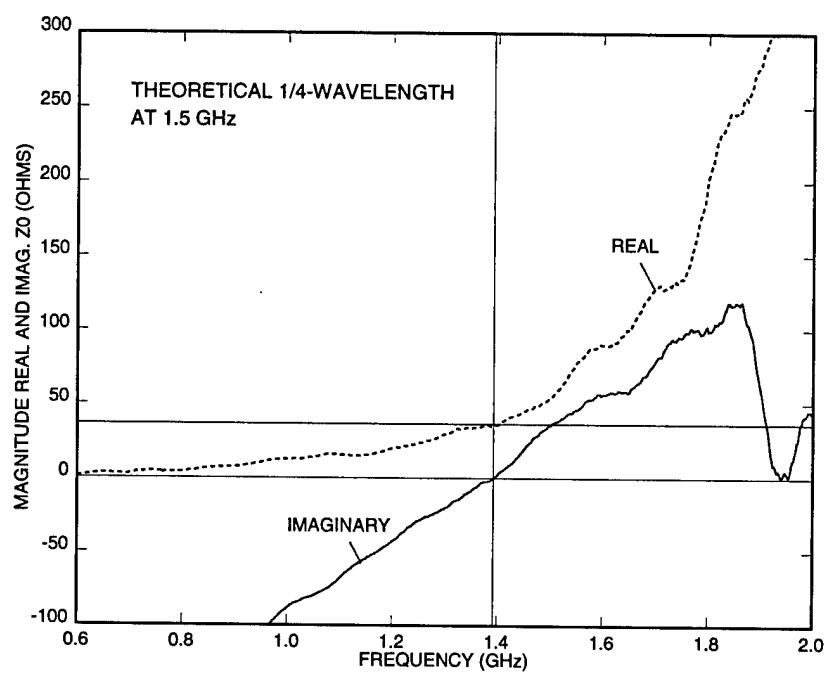
Figure 4.5: Radiation impedance of a 5 cm monopole over a ground plane of dimensions 30.48 cm by 31.75 cm as a function of frequency.

4.5   Results and Discussion

Measurements are obtained for single module configurations, multiple module configurations and for partially enclosed configurations. FD-TD numerical results have been obtained for each of the measured configurations and fairly good agreement has been achieved.

In order to justify the simplified model, measurements of the radiation impedance of modules-on-backplane configurations with plain copper modules and populated modules are compared. The populated modules were standard plug-in printed circuit boards with all the chips and devices intact. The populated module was excited, in each case, by the center conductor of a coaxial probe which was connected to a reference plane in the printed wire board. The connection was accomplished by soldering the center conductor to a pin on the printed wire board which leads to the ground plane of the board. The outer conductor of the coaxial line was soldered to the backplane and the length of the coaxial probe connector extending above the backplane in this case and in all subsequent cases is 1 cm. Figures 4.6 and 4.7 show the radiation impedance of the populated and plain copper modules for two different feed (source) points. The feed points are located 2.5 cm away from the center of the bottom edge of the module. The modules have dimensions of 13.02 cm in width and 21.43 cm in height. The backplane is 29.21 cm by 30.48 cm. The module is centered on the backplane and the width of the module is parallel to the 29.21 cm side of the backplane. The real and imaginary portions of the radiation impedances for the populated and plain copper modules show good correlation. The good correlation between the radiation impedances for the populated and plain copper modules at
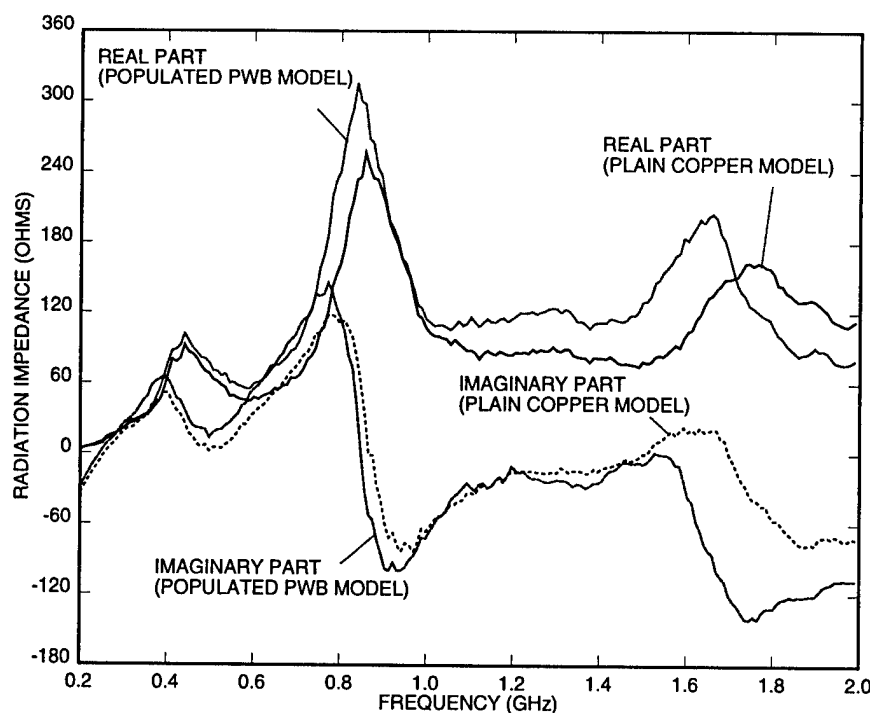
Figure 4.6: Radiation impedance of a populated and a plain copper module of dimension 13.01 cm by 21.43 cm over a finite ground plane as a function of frequency with the source connected to the bottom edge of the left side of the module.

both feed points justifies the study of the simplified model.

Figure 4.8 compares the radiation impedance as a function of frequency obtained from measurements and FD-TD simulations for a 2.54 cm wide and 16.51 cm high module with a backplane of size 29.21 cm by 30.48 cm. In this case, and in all subsequent single module cases, the module is centered on the backplane with the bottom edge of the module parallel to the 29.21 cm side of the backplane. The connector, in this and all subsequent cases, is attached to the middle of the bottom edge of the module. This first case has dimensions atypical of a standard plug-in printed circuit board module. However, this case was chosen, because the module is thin and tall, to determine if the measurements and FD-TD predictions would
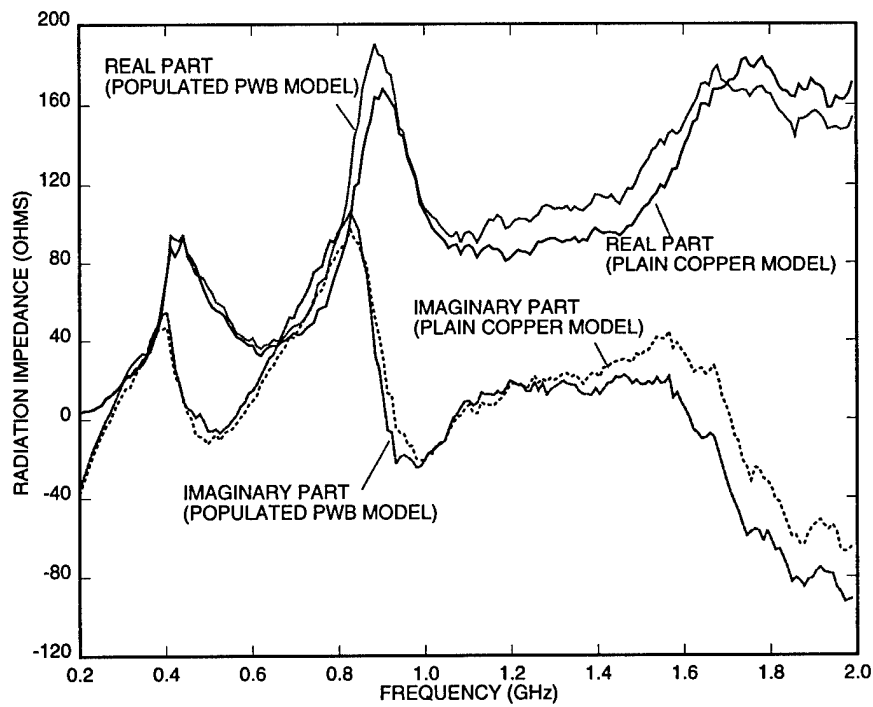
Figure 4.7: Radiation impedance of a populated and a plain copper module of dimension 13.01 cm by 21.43 cm over a finite ground plane as a function of frequency with the source connected to the bottom edge of the right side of the module.
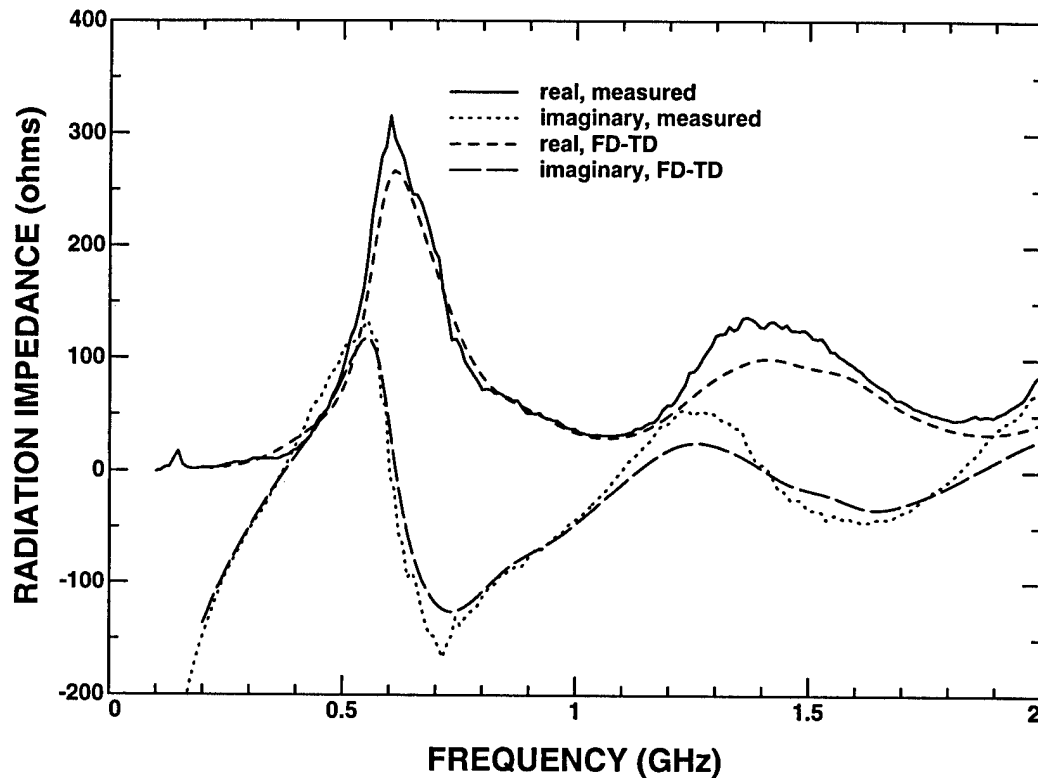
Figure 4.8: Radiation impedance of a 2.54 cm by 16.51 cm module over a finite ground plane as a function of frequency.

correspond well with an analytical solution of a monopole over an infinite ground plane. The first resonance occurs at 375 MHz (the first zero crossing in the reactance) which is somewhat below the expected quarter-wavelength resonance associated with a monopole over an infinite ground plane of 438 MHz. This discrepancy is primarily due to finite nature of the the ground plane. The next resonance, which corresponds to a three quarter-wavelength resonance, occurs at the expected frequency of 1.125 GHz, which is three times higher than the first resonance. Fairly good agreement was achieved for the radiation impedance between the FD-TD prediction and the measurements.

In Figure 4.9, Prony's method is demonstrated for the previous case [Section

4.3.2]. The time response of the current on the connector to a 2.54 cm by 16.51 cm module over a 29.21 cm by 30.48 cm ground plane is used as a sample time response. The FD-TD simulation was executed for 3000 time steps and Prony's method was applied using only the first 1000 time steps. The excitation used had the form of Equation 4.2, with $\alpha = 2$ ns, and $f_0 = 1$ GHz with a peak voltage of 1 volt. In applying Prony's method, nine complex exponentials were used to fit the data, every tenth time step was utilized, and only 40 data points were used. From Figure 4.9, it is apparent that the Prony's method extrapolation fits the actual FD-TD simulation results reasonably well but shows a slight phase difference as time progresses. Note that Figure 4.9 only plots the time response after the point at which Prony's method is applied. Prony's method was also applied to the voltage on the connector in order to obtain the radiation impedance using the Prony's method extrapolated time sequences. Figure 4.10 plots the radiation impedance of the module, and illustrates: (1) the good agreement in the frequency domain between the long FD-TD simulation and the short FD-TD simulation with Prony's method extrapolations, and (2) the improvement of the short FD-TD simulation with the Prony's method extrapolations.

The significance of searching for the radiation impedance is that the radiative properties of the module can then be easily incorporated in a circuit model as a lumped element with a complex impedance as shown in Figure 4.11. The power radiated for the configuration can be expressed in terms of the voltage across or the current through the radiator model.

$$P_{\text{rad}} = \frac{1}{2} \frac{R_{\text{rad}}}{R_{\text{rad}}^2 + X^2} \left| V^2 \right| \qquad (4.21)$$
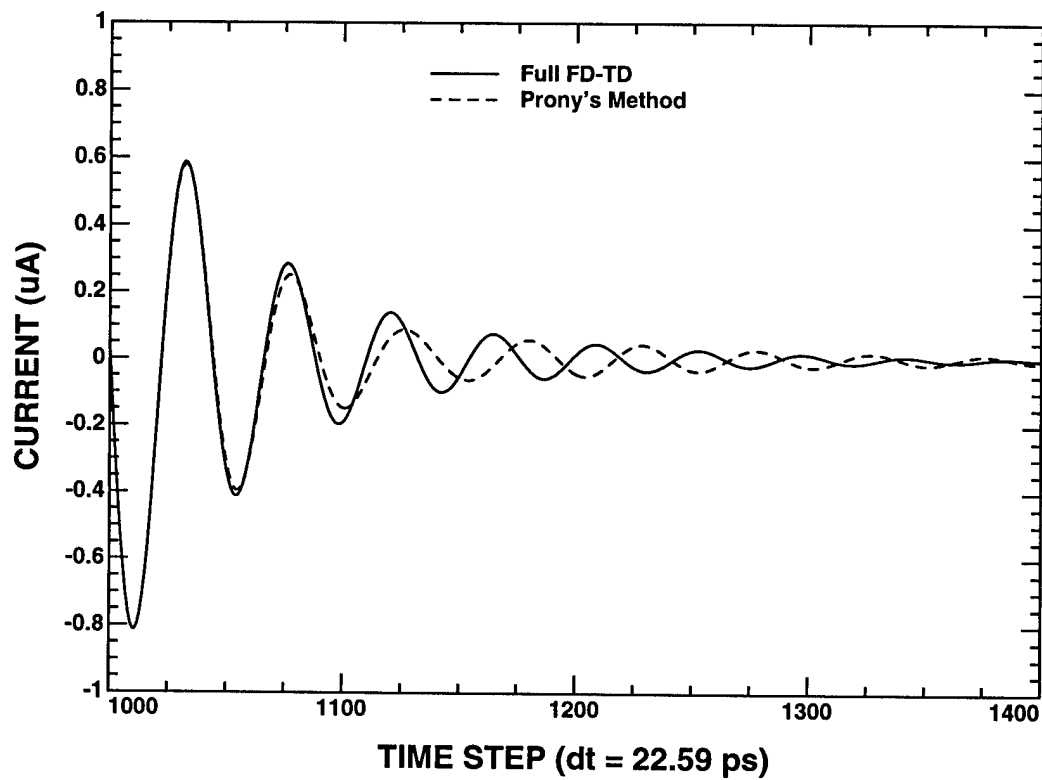
Figure 4.9: Time response of the current on the connector to a 2.54 cm by 16.51 cm module over a 29.21 cm by 30.49 cm ground plane as calculated using direct FD-TD calculations and Prony's method extrapolations.
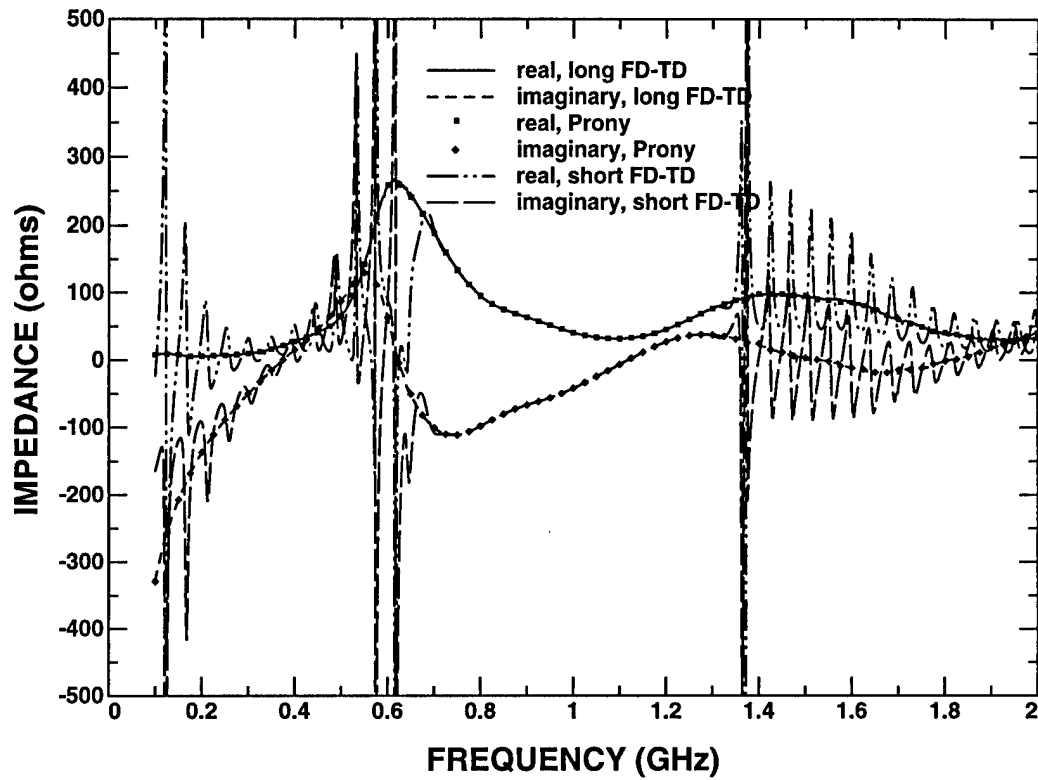
Figure 4.10: Comparison of radiation impedance for a 2.54 cm by 16.51 cm module over a 29.21 cm by 30.49 cm ground plane calculated using a short FD-TD simulation, a FD-TD simulation with Prony's method extrapolations, and a long FD-TD simulation.
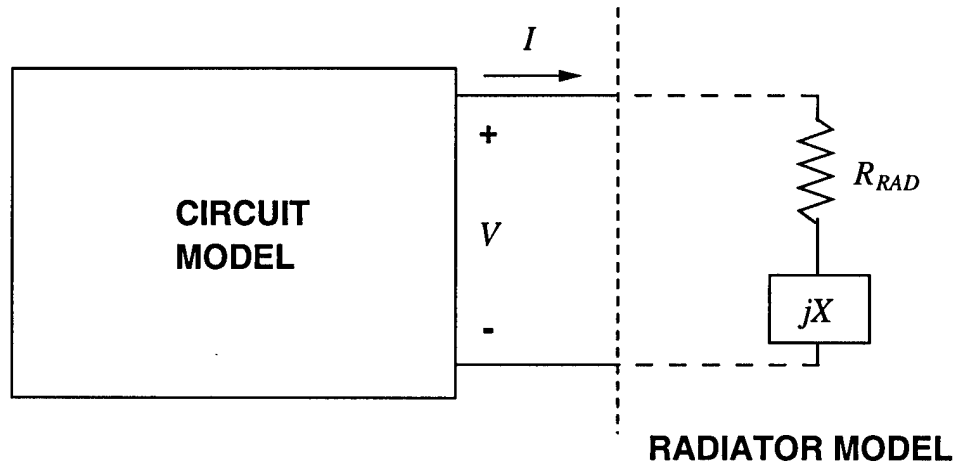
Figure 4.11: Characterization of radiative properties of modules-on-backplane as circuit parameters.

$$P_{\text{rad}} = \frac{1}{2} R_{\text{rad}} \left| I^2 \right| \tag{4.22}$$

So when a voltage source is used, the reactance of the radiator becomes an important factor in determining the amount of radiation emitted.

In practice the radiated power is of greater interest than the radiation impedance. In determining the radiated power, a 1 mV voltage source is utilized (i.e. the complex amplitude at all frequencies was 1 mV), with zero source impedance. Since the power distribution to the reference planes is designed to have low impedance, a zero source impedance voltage source is a reasonable model [113]. Figure 4.12 shows the radiated power in dBnW. The peak radiation occurs at the first resonance around 375 MHz and the resulting radiation is about 37 nW for a 1 mV source.

The radiated power for a 2.54 cm wide and 29.21 cm high module with a backplane of size 29.21 cm by 30.48 cm is examined in Figure 4.13. This case, which also has atypical dimensions, was examined to determine if the measurements and FD-
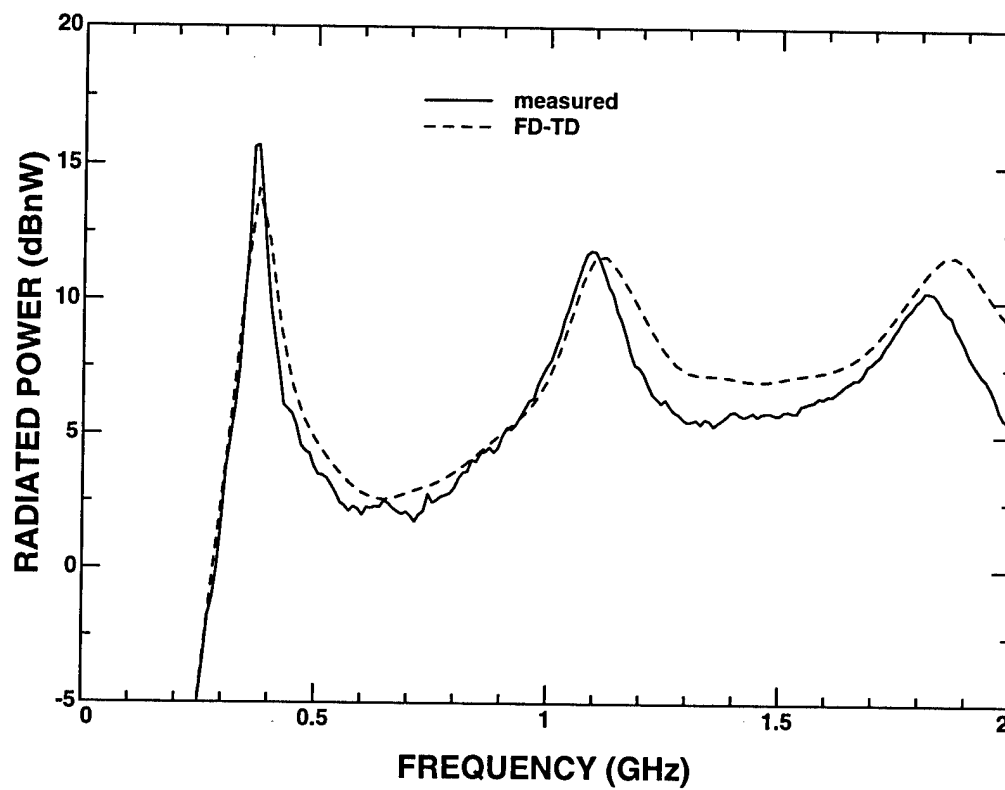
Figure 4.12: Radiated power from a 2.54 cm by 16.51 cm module over a finite ground plane excited by a 1 mV voltage source with zero impedance as a function of frequency.
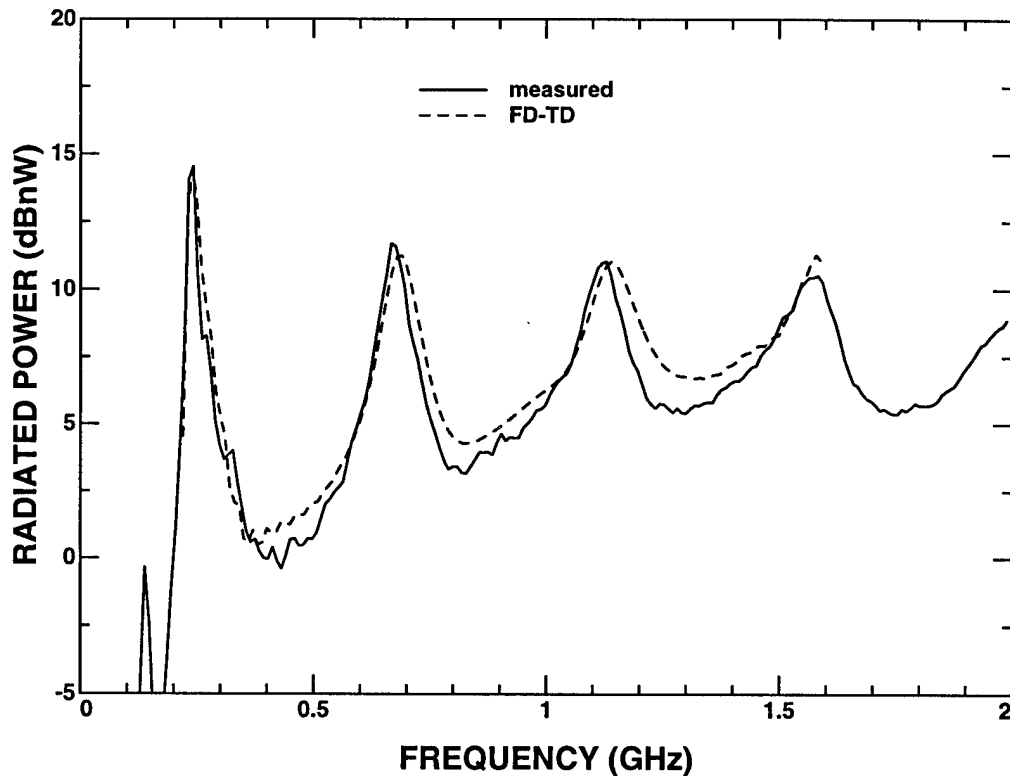
Figure 4.13: Radiated power from a 2.54 cm by 29.21 cm module over a finite ground plane excited by a 1 mV voltage source with zero impedance as a function of frequency.

TD predictions displayed the expected trends predicted by an analytical solution of a monopole over an infinite ground plane. Results obtained from FD-TD simulations and from measurements are plotted. The measured data agrees fairly well with the FD-TD simulation calculations. The first resonance occurs at 240 MHz which again is slightly below the expected quarter-wavelength of a monopole over an infinite ground plane of 248 MHz. Again resonances are observed at approximately odd multiples of the first resonance, which is consistent with a monopole over an infinite ground plane model. As expected, more peaks in the radiation resistance and zero crossings in the radiation reactance are apparent compared to the smaller module.

Figure 4.14 compares the radiated power obtained from measurements and from
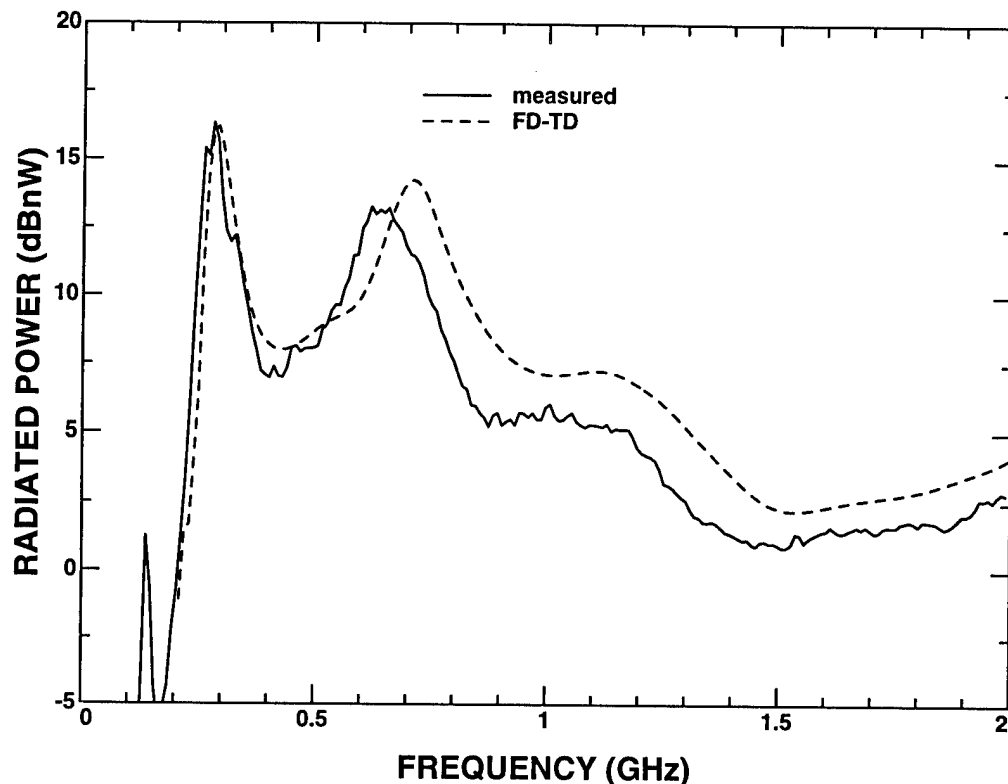
Figure 4.14: Radiated power from a 13.01 cm by 21.43 cm module over a finite ground plane by a 1 mV voltage source with zero impedance as a function of frequency.

FD-TD simulations for a 13.01 cm by 21.43 cm module with a backplane of size 29.21 cm by 30.48 cm. This module represents a standard plug-in printed wire board module. Due to the more squarish dimensions, the module will no longer appear to be a simple monopole. The first resonance of 280 MHz still roughly corresponds to the quarter-wavelength monopole over a ground plane resonance of 334 MHz. However, the higher resonances are more difficult to explain, as resonances across the module become important at the higher frequencies. The measured data agree fairly well with the FD-TD simulation calculations. Although for frequencies above 0.7 GHz, there is a 3 to 5 dB discrepancy in power between the measurements and the FD-TD predictions.

In the previous cases, single modules were examined, so that the physics of the simpler cases could be understood. In examining multiple modules, only two and three module configurations were considered. The modules are aligned to be parallel to each other, as shown in Figure 4.2. In the multiple module cases, the collection of modules are centered on the backplane, with the bottom edges of the modules parallel to the shorter side of the backplane. The modules are 13.01 cm by 21.43 cm in size. The separation between the modules is 2.54 cm. Only one of the multiple modules is excited and in the three module case the center module is excited. The unexcited modules are grounded at the center of their bottom edges to the backplane by a 1 cm wire. Figures 4.15 and 4.16 compare the radiated powers obtained from measurements and from FD-TD simulations for two and three 13.01 cm by 21.43 cm modules with a backplane of size 29.21 cm by 30.48 cm. The addition of a second and a third module each significantly enhance the radiated power at the resonant frequencies of the individual configuration. In particular, with two modules there is 7 dB enhancement, and with three modules there is about 18 dB enhancement of radiation. The radiated power has sharper peaks with the addition of the second and third modules. These trends are consistent with the fact that the structure resembles a resonator and has a higher Q as modules are added. The agreement in these cases is not as good as in previous cases, although the general shape and location of the resonances of the measurements and FD-TD predictions are the same. The FD-TD predictions tend to overestimate the radiation. Possible explanations for the difference are: First, in the FD-TD model there are no resistive losses. Second, the modules in the measurement cases may not have been precisely aligned in that the modules may not have been perfectly parallel with each other, which would tend to lower the Q
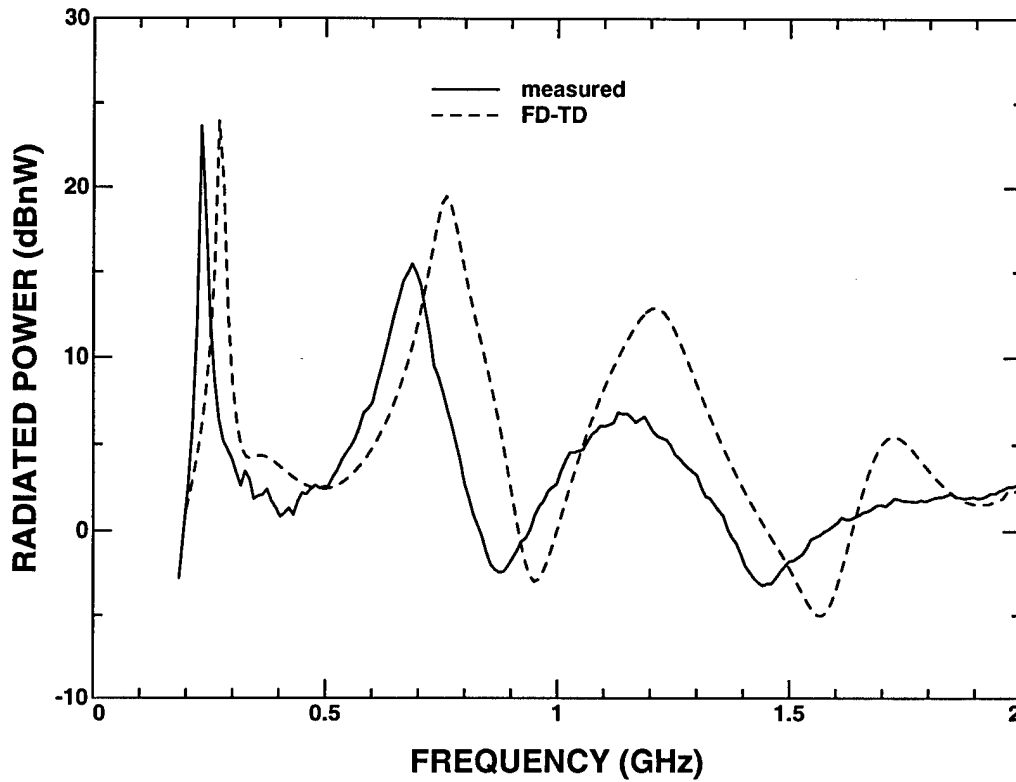
Figure 4.15: Radiated power from two 13.01 cm by 21.43 cm modules over a finite ground plane excited by a single 1 mV voltage source with zero impedance as a function of frequency.

factor.

In Figure 4.17, the effect of partially enclosing a single 13.01 cm by 21.43 cm module is examined. The structure is closed on the bottom and four sides and is open on top, and the specific dimensions are shown in Figure 4.18. The module is again excited by a coaxial probe connected to the center of the bottom edge of the module. With the addition of the enclosure, the radiated power of this configuration has sharp peaks as a function of frequency, with a peak value of about 32 dBnW. The radiated power predicted by the FD-TD simulation shows the same general characteristics as the measured radiated power. Similar arguments explaining the discrepancies in the
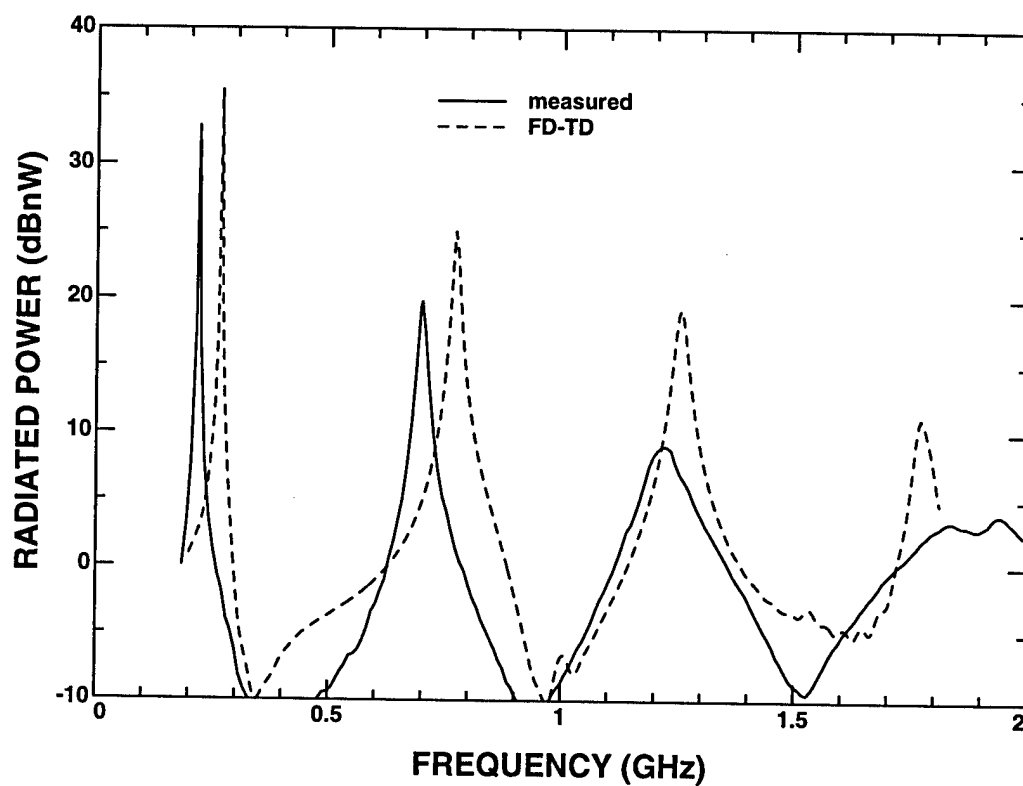
Figure 4.16: Radiated power from three 13.01 cm by 21.43 cm modules over a finite ground plane excited by a single 1 mV voltage source with zero impedance as a function of frequency.
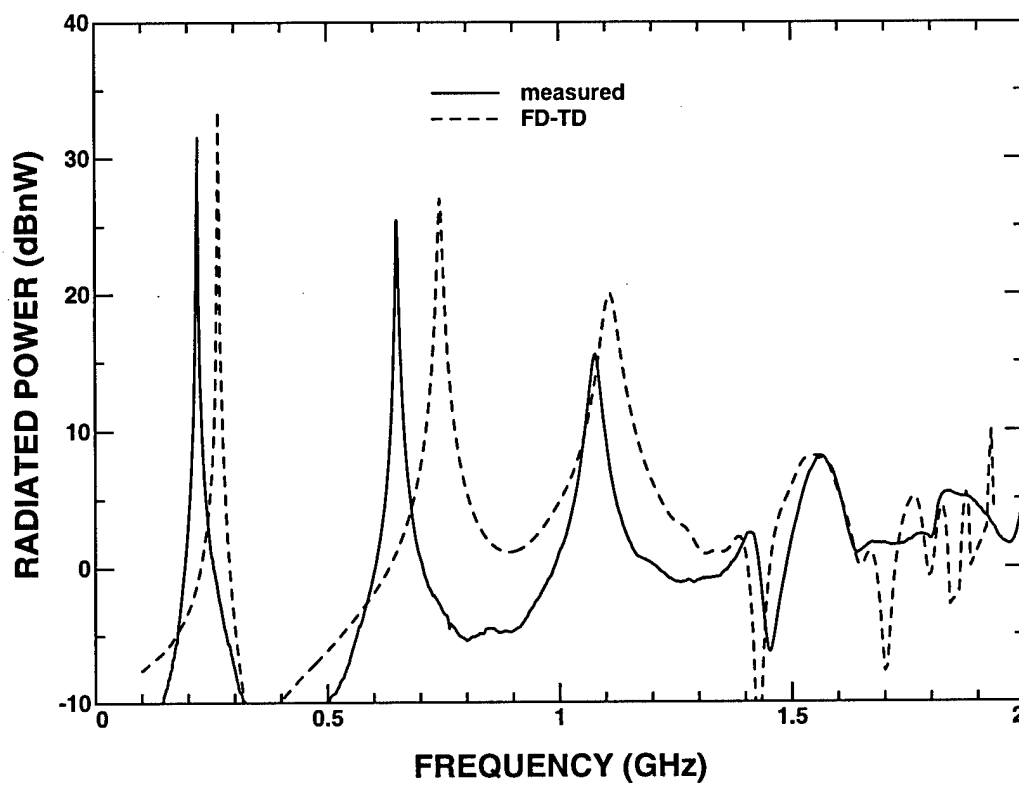
Figure 4.17: Radiated power from a partially enclosed 13.01 cm by 21.43 cm module over a finite ground plane excited by a 1 mV voltage source with zero impedance as a function of frequency.

multiple module cases can be applied to the enclosed configuration.
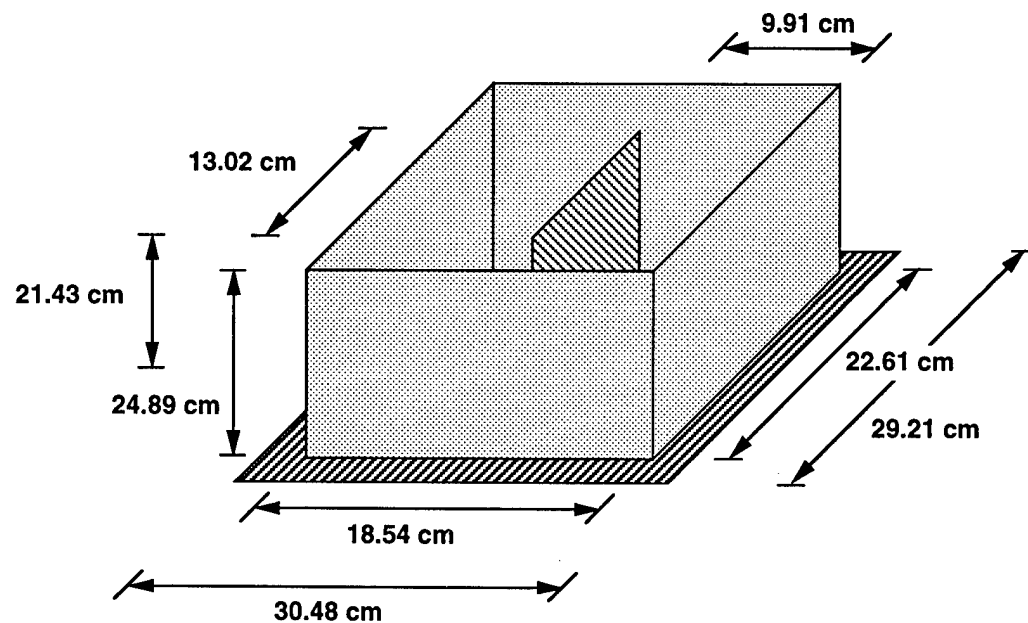
Figure 4.18: Partially enclosed module-on-backplane configuration.

4.6   Conclusions

The radiation properties of modules-on-backplane configurations have been analyzed by using the FD-TD technique and by taking measurements. The FD-TD technique was chosen for its flexibility in analyzing this class of potentially complex problems, for which neither approximate nor analytical solutions are applicable. Fairly good agreement was obtained between the measurements and the FD-TD analysis. The FD-TD analysis provides radiation impedances, which when used as circuit model parameters can be utilized to estimate overall radiated power. The FD-TD analysis also provides the capability of determining near-fields and far-field radiation patterns.

The analysis of the modules-on-backplane configuration, a common structure in the computer environment, has shown that radiation enhancement occurs in the hundreds of megahertz. The addition of modules or an enclosure have been shown to enhance the radiation from the structure. The potential for increased radiation due to the modules-on-backplane configuration has been demonstrated with measurements and numerical simulations.

Chapter 5

Coupling of EM Energy by a Wire Penetrating a Metallic Screen

5.1 Introduction

The primary motivation for studying various structures which compose a computer is that computers are now operating at faster speeds and consuming more power resulting in significantly increased levels of power at higher frequencies. Metallic enclosures are commonly used to house computer systems and always have cables and wires exiting from them. A simplified configuration of the problem of interest is shown in Figure 5.1. Since the metallic enclosure functions both as a electromagnetic shield and as a resonator structure, the most important sources of radiation come from any holes in the box which are required for ventilation and from any cables exiting from the box which are required for power and communications. In particular for cables, the radiation sources inside the enclosure can couple to a wire exiting the enclosure, and the wire can function as an antenna in the hundreds of MHz frequency range. For these reasons, the coupling of electromagnetic energy out of the metallic

MODULES-ON-BACKPLANE AS SOURCE

METAL ENCLOSURE

**SMALL
APERTURE**
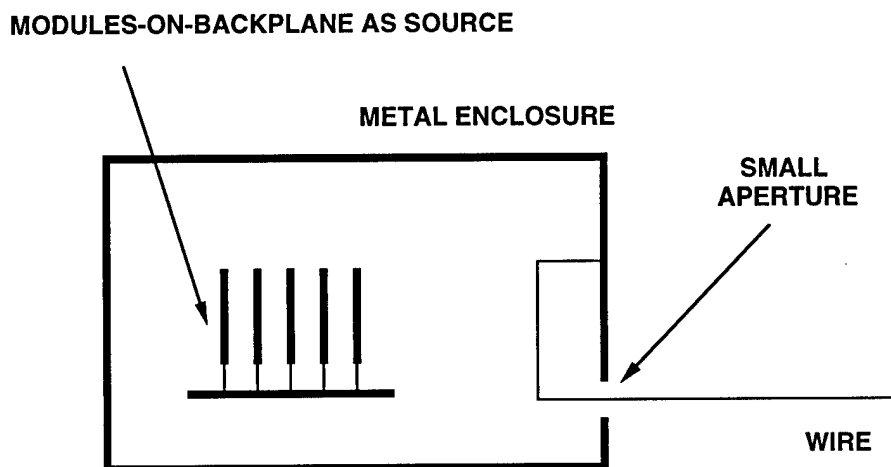
WIRE

Figure 5.1: A simple wire exiting a metal enclosure configuration.

enclosure by cables is of great interest. The objective of this research is to be able to quantify the amount of radiation emitted by these cables as a function of frequency.

In analyzing the problem, the following assumptions and simplifications were used. The radiation admittance of the external portion of the wire is assumed to be simple enough such that it can be adequately modeled by a set of of series RLC circuits which are in parallel (lumped element model). Essentially, one RLC circuit is used to match each resonance present in the wire's radiation admittance. An additional assumption is that the radiation mechanism is primarily due to the current on the wire and not the fields traveling through the aperture, since the aperture size is only being modeled in a simple manner and will depend on the FD-TD cell size. Since the aperture has dimensions much smaller than those of the external wire, then the radiation through the aperture at frequencies where the external wire resonates

will be in the Rayleigh region. Hence, the radiation through the aperture should be very small. The ground planes and wires are all assumed to be perfectly conducting.

The motivation for using the lumped element model within the FD-TD technique instead of a full FD-TD simulation is to obtain significant computational savings. In particular, the lumped element model replaces the model of the region outside the enclosure, thus eliminating the need to include the outer region in the FD-TD simulation. If the external wire is significantly large or larger than the enclosure, then the reduction in the computational domain size can be significant. In analyzing a completely enclosed metal box, the FD-TD technique does not need to impose any absorbing boundary conditions since the metal enclosure naturally imposes conditions at the outer boundary. As a consequence of this, the FD-TD technique also does not need the typical free space buffer between the object and the absorbing boundary. However, in performing a simulation of an enclosure with a wire exiting it, a large free space region surrounding the enclosure and the wire must be included in order to facilitate the implementation of the absorbing boundary condition. For example, the computational domain required to model a one meter length external wire attached to a 0.75m by 0.75m by 0.15m metal enclosure would be, on the order of, 10 times larger than the one required for just the metal enclosure. The computational requirements of the lumped element model are a mere fraction of the FD-TD requirements, on the order of tens of storage variables compared to tens of thousands of storage variables, and similar ratios for arithmetic operations.

In applying the lumped element model, the original wire exiting an enclosure configuration has been split, requiring both the internal and external regions to be

solved. The external region can be solved using any method which is most efficient or convenient. In addition, if the external region is simple enough, the radiation admittance of the wire can be approximated using analytical solutions for wires over infinite ground planes. Hence, the external problem can be solved first, and then the internal region can be analyzed using the FD-TD technique with the appropriate lumped element model. Also by splitting the problem into two regions, the probable problem of a significant difference in scale between features in the two regions is naturally solved, as each region can be solved separately using whatever scale is most appropriate for each region. This natural solution obviates the need for using variable size grid cells within one computational domain in order to accommodate the scale difference in the external and internal regions.

In Section 5.2, the models used to examine the wire penetrating a metal enclosure are outlined. Section 5.3 discusses the finite difference-time domain technique briefly, analytical solutions for wires over a ground plane, and the lumped element model used in conjunction with the FD-TD technique. The results include the radiation admittance and total radiated power as functions of frequency, and the lumped element FD-TD simulation results are compared with the full FD-TD simulation results in Section 5.4. Section 5.5 draws overall observations regarding the accuracy and usefulness of the lumped element model and the coupling of electromagnetic energy by wires penetrating a metal enclosure.

5.2 Problem Configuration and Model

Two simplified configurations were considered in analyzing the real configuration. The simplest model involves a wire over an infinite ground plane being excited by a coaxial line. The full FD-TD model and the FD-TD lumped element model are shown in Figure 5.2. This first model is used to validate the lumped element model, since analytical solutions exist for a complex load terminating a coaxial transmission line. This model will also provide a measure for how well the lumped element can model the true radiation admittance. The next model involves a wire connected to an infinite metal screen exiting through a small aperture, with a dipole source on the "inner" side of the metal screen. Both full and lumped element FD-TD models are shown in Figure 5.3 for this configuration.

LUMPED ELEMENT

Z_0

COAXIAL LINE

(a)

INFINITE GROUND
PLANE

Z_0

WIRE ANTENNA

COAXIAL LINE

(b)
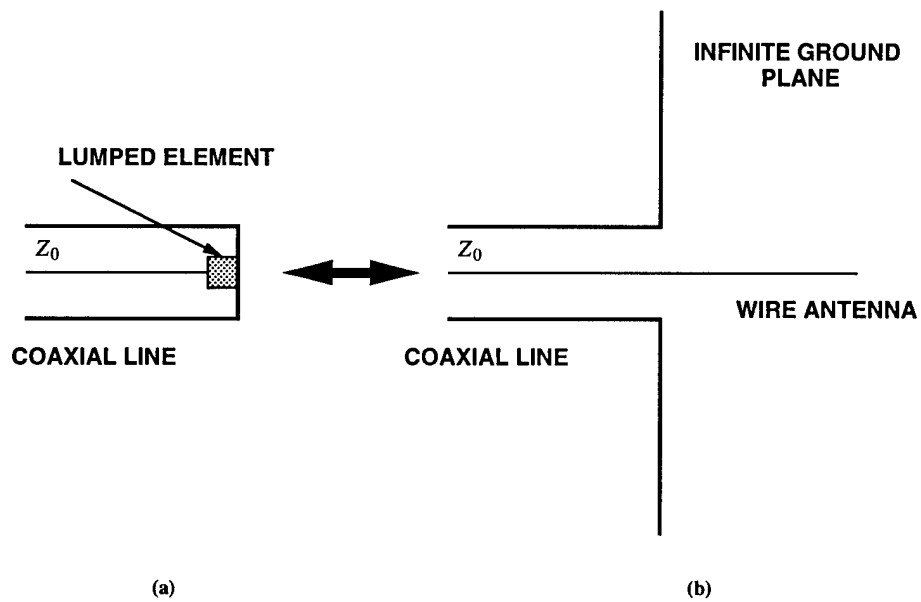
Figure 5.2: Full FD-TD model and lumped element FD-TD model for a wire over a ground plane fed by a coaxial line.
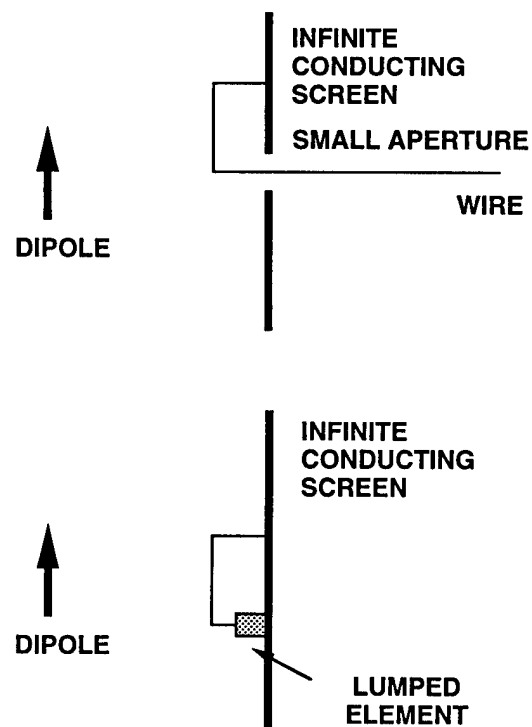
Figure 5.3: Full FD-TD model and lumped element FD-TD model for a wire exiting a small aperture in a metal screen excited by a dipole.

5.3   Method of Solution

5.3.1   Finite Difference – Time Domain Technique

The finite difference-time domain (FD-TD) technique was used to analyze this problem [1]-[12]. This method was chosen because it has the capability of analyzing multiple frequencies with a single simulation, it is well suited for low loss models and rectilinear geometries, and it is a proven method, as it has been previously used to successfully analyze radiation from a heatsink configuration [31]-[33] and radiation from modules-on-backplane configurations [34],[35].

A rectangular three-dimensional grid was used as the computational domain. Spatially, the computational domain is discretized such that the largest grid dimension is less than about a twentieth of the shortest wavelength of interest. The time step must be approximately less than the smallest grid dimension divided by the speed of light in order to guarantee the stability of the algorithm. The difference equations which are utilized to update the electric and magnetic fields are obtained from Maxwell's equations in differential form by approximating spatial and temporal derivatives with center differences. Electric and magnetic fields are discretized on Yee's lattice [1]. Initial conditions, which are imposed at the beginning of the simulation, are that all electric and magnetic fields start at zero. At each subsequent time step, fields are imposed at appropriate locations in order to simulate the excitation source. The imposed electric field has a time dependence of a Gaussian pulse modulated by a sine wave, which contains energy in a band of frequencies allowing multiple frequencies to be analyzed simultaneously. Boundary conditions are imposed at per-

fectly conducting surfaces and at the outer boundary. At the perfectly conducting surfaces, the tangential electric field is set to zero. Absorbing boundary conditions must be applied at the outer boundary of the computational domain in order to simulate unbounded space. Second-order absorbing boundary conditions (ABC) are used at the outer boundary, except at the corners and edges where first-order ABCs are used [67]-[75]. Finally, by applying the difference equations obtained from Maxwell's equations in addition to the appropriate initial and boundary conditions, the electric and magnetic fields can be calculated everywhere within the computational domain for each time step.

The calculation of total power radiated is done using time domain results from the FD-TD simulation. First, the electric and magnetic fields are calculated everywhere in the computational domain and then the current and voltage on the wire are recorded at the aperture of the screen. The current on the probe, which models the connector, is calculated using Ampere's Law.

$$I_{\text{aperture}}(t) = \int_{\substack{\text{around} \\ \text{probe}}} \overline{H}(t) \cdot d\bar{l} \tag{5.1}$$

and the voltage on the probe is

$$V_{\text{aperture}}(t) = \int_{\text{center conductor}}^{\text{outer conductor}} \overline{E}(t) \cdot d\bar{l} \tag{5.2}$$

Fourier transforming the voltage and current to obtain their complex amplitudes,

their product give the power radiated.

$$P_{\text{rad}}(f) = \frac{1}{2} \, \text{Re} \left(I^*_{\text{aperture}}(f) V_{\text{aperture}}(f) \right) \tag{5.3}$$

The radiation admittance can also be calculated from the frequency domain voltage and current using [25]

$$Y_{\text{rad}}(f) = \frac{I_{\text{aperture}}(f)}{V_{\text{aperture}}(f)} \tag{5.4}$$

5.3.2   Analytical Solution for Wire over a Ground Plane

In applying the lumped element model discussed in the next section, it was necessary to obtain the radiation admittance for the wire exiting from the enclosure. The simplest wire model involves a wire which is normal to an infinite ground plane. This configuration has analytic solutions for the radiation admittance.

The analytical expression for the radiation impedance of wire over an infinite ground plane is as follows [116]-[118]:

$$Y_{\text{wire}} = \frac{1}{Z_{\text{wire}}} = \frac{1}{R_{\text{wire}} + iX_{\text{wire}}} \tag{5.5}$$

$$R_{\text{wire}} = \frac{\eta_0}{4\pi \sin^2(k\ell/2)} (\gamma + \ln(k\ell) - \text{Ci}(k\ell) + 0.5 \sin(k\ell)[\text{Si}(2k\ell) - 2\text{Si}(k\ell)]$$

$$+ 0.5 \cos(k\ell)[\gamma + \ln(k\ell/2) + \text{Ci}(2k\ell) - 2\text{Ci}(k\ell)]) \tag{5.6}$$

$$X_{\text{wire}} = \frac{\eta_0}{8\pi \sin^2(k\ell/2)} (2\text{Si}(k\ell) + \cos(k\ell)[2\text{Si}(k\ell) - \text{Si}(2k\ell)]$$

$$- \sin(k\ell)[2\text{Ci}(k\ell) - \text{Ci}(2k\ell) - \text{Ci}(2ka^2/\ell)]) \tag{5.7}$$

where k is the wavenumber, ℓ is the imaged length (or twice the true length l) of the wire, a is the radius of the wire, $\eta_0 = 377\Omega$ is the free space impedance, $\gamma = 0.5772$ and Si and Ci are sine and cosine integrals.

Figure 5.4 compares the theoretical radiation admittance of a wire with a length of $l = 0.5$ m and a radius of $a = 2$ mm with the radiation admittance obtained from a full FD-TD simulation. The figure shows good agreement, and demonstrates the usefulness of the theoretical solution for the radiation admittance of a wire.

5.3.3 Lumped Element Model

The implementation of single Rs, Ls and Cs has been done previously [22],[23], however the modeling of a collection of these elements at a single node is new. The lumped element model used is shown in Figure 5.5 and consists of a set of N series RLC circuits in parallel. The total admittance has the form

$$Y = \frac{I}{V} = \sum_{m=1}^{N} Y_m = G + iS \tag{5.8}$$

where G and S are the conductance and susceptance respectively, and the admittance of each individual RLC circuit is

$$Y_m(s) = \frac{s/L_m}{s^2 + sR_m/L_m + 1/(L_mC_m)} \tag{5.9}$$
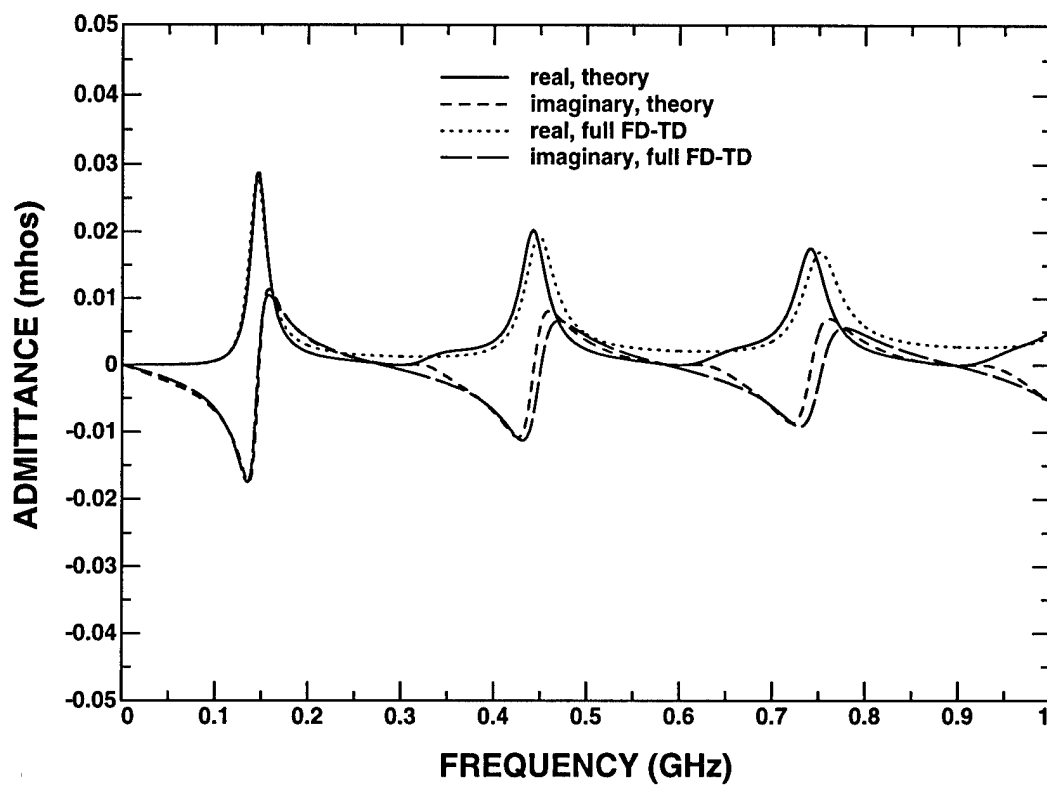
Figure 5.4: Comparison of theoretical vs. full FD-TD simulation of radiation admittance of a wire over an infinite ground plane with a length of 0.5 m and a radius 2 mm.
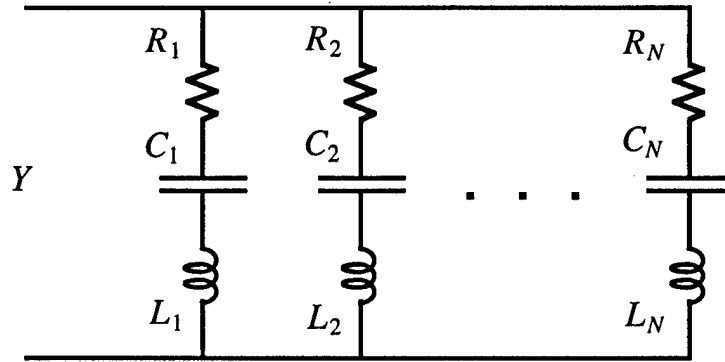
Figure 5.5: Lumped element model.

where $s = -i2\pi f$.

The circuit elements for a single RLC circuit are chosen to match one resonance in the wire's radiation admittance.

$$R_m = \frac{1}{G_m^{max}} \qquad (5.10)$$

$$L_m = \frac{R_m}{2\pi \Delta f_m} \qquad (5.11)$$

$$C_m = \frac{1}{(2\pi f_m)^2 L_m} \qquad (5.12)$$

where G_m^{max} is the peak of the conductance at resonance, Δf_m is the half-power bandwidth of the resonance in Hz, and f_m is the resonant frequency in Hz.

The transfer function relating the voltage to the current in the s domain is

$$V(s) = \left(L_m s + R_m + \frac{1}{C_m s} \right) I_m(s) \tag{5.13}$$

where

$$I = \sum_{m=1}^{N} I_m \tag{5.14}$$

The equivalent equation in the time domain is

$$V(t) = \left(L_m \frac{\partial}{\partial t} + R_m \frac{1}{C_m} \int_0^t dt \right) I_m(t) \tag{5.15}$$

This equation needs to be discretized, and backwards differences are applied to insure stability. The resulting equation is

$$V^{n+1/2} = L_m \left(\frac{I_m^{n+1/2} - I_m^{n-1/2}}{\Delta t} \right) + R_m I_m^{n+1/2} + \frac{\Delta t}{C_m} \sum_{l=0}^{n} I_m^{l-1/2} \tag{5.16}$$

The update equation for the current is

$$I_m^{n+1/2} = \frac{1}{L_m/\Delta t + R_m} V + \frac{L_m/\Delta t}{L_m/\Delta t + R_m} I^{n-1/2} - \frac{\Delta t/C_m}{L_m/\Delta t + R_m} \sum_{l=0}^{n} I_m^{l-1/2} \tag{5.17}$$

In order to incorporate the above difference equation which is in terms of voltages and currents into the FD-TD scheme, the voltages and currents need to be converted to electric field and current densities.

$$I^{n+1/2} = \Delta x \Delta y J_z^{n+1/2} \tag{5.18}$$

$$V^{n+1/2} = \frac{V^{n+1} - V^n}{2} = \frac{E_z^{n+1} + E_z^n}{2} \Delta z \qquad (5.19)$$

The standard difference equation for updating E_z is

$$\epsilon_r \epsilon_0 \frac{E_z^{n+1}(i,j,k+1/2) - E_z^n(i,j,k+1/2)}{\Delta t} =$$

$$\frac{H_y^{n+1/2}(i+1/2,j,k+1/2) - H_y^{n+1/2}(i-1/2,j,k+1/2)}{\Delta x}$$

$$-\frac{H_x^{n+1/2}(i,j+1/2,k+1/2) - H_x^{n+1/2}(i,j-1/2,k+1/2)}{\Delta y}$$

$$-J_z^{n+1/2}(i,j,k+1/2) \qquad (5.20)$$

Combining the expressions for the voltage in terms of the electric field, and the current in terms of the current density, the following equation for updating E_z is obtained.

$$E_z^{n+1}(i,j,k+1/2) \left[\frac{\epsilon_r \epsilon_0}{\Delta t} + \sum_{m=1}^{N} \frac{\Delta z}{2\Delta x \Delta y (L_m/\Delta t + R_m)} \right] =$$

$$E_z^n(i,j,k+1/2) \left[\frac{\epsilon_r \epsilon_0}{\Delta t} - \sum_{m=1}^{N} \frac{\Delta z}{2\Delta x \Delta y (L_m/\Delta t + R_m)} \right]$$

$$+\frac{H_y^{n+1/2}(i+1/2,j,k+1/2) - H_y^{n+1/2}(i-1/2,j,k+1/2)}{\Delta x}$$

$$-\frac{H_x^{n+1/2}(i,j+1/2,k+1/2) - H_x^{n+1/2}(i,j-1/2,k+1/2)}{\Delta y}$$

$$-\frac{1}{\Delta x \Delta y} \sum_{m=1}^{N} \left[\frac{L_m/\Delta t}{L_m/\Delta t + R_m} I_m^{n-1/2} - \frac{\Delta t/C_m}{L_m/\Delta t + R_m} \sum_{l=0}^{n} I_m^{l-1/2} \right] \qquad (5.21)$$

Resonance	f_0 (GHz)	G^{max} (mhos)	Δf (GHz)
1	0.1465	2.9096×10^{-2}	0.0210
2	0.4420	2.0300×10^{-2}	0.0355
3	0.7410	1.7582×10^{-2}	0.0438
4	1.0405	1.6129×10^{-2}	0.0497
5	1.3400	1.5184×10^{-2}	0.0543
6	1.6395	1.4500×10^{-2}	0.0580
7	1.9395	1.3976×10^{-2}	0.0609

Table 5.1: Theoretical resonances for a wire of length 0.5 m and radius of 2 mm over an infinite ground plane.

5.4   Results and Discussion

The two configurations examined include a wire over an infinite ground plane fed by a coaxial line [Figure 5.2] and a grounded wire exiting an infinite metal screen through a small aperture [Figure 5.3]. For both cases, an identical wire configuration is used on the external (right-hand) side of each model. The external wire extends in a direction normal to the infinite ground plane and has a length of $l = 0.5$ m and a radius of $a = 2$ mm.

In order to obtain a lumped element approximation to the radiation admittance of this wire, it is necessary to characterize its radiation admittance. Table 5.1 describes the peaks in the radiation admittance of the wire antenna. From the theoretical radiation admittance, the following RLC lumped element model was constructed. Table 5.2 contains the values of the circuit elements used to approximate the wire antenna's admittance.

Figure 5.6 shows the analytical solution for the radiation admittance of the wire

Resonance	R (Ω)	L (H)	C (F)
1	34.36	2.6047×10^{-7}	4.5310×10^{-12}
2	49.26	2.2084×10^{-7}	5.8708×10^{-13}
3	56.87	2.0667×10^{-7}	2.2321×10^{-13}
4	62.00	1.9854×10^{-7}	1.1784×10^{-13}
5	65.85	1.9303×10^{-7}	7.3079×10^{-14}
6	68.96	1.8924×10^{-7}	4.9795×10^{-14}
7	71.55	1.8699×10^{-7}	3.6011×10^{-14}

Table 5.2: *RLC* circuit parameters used to model the admittance of a wire of length 0.5 m and radius 2 mm over an infinite ground plane.

and the admittance of the single *RLC* circuit. The match appears to be reasonably good up to about 240 MHz. By using 2 *RLC* circuits, a reasonable match is obtained between the radiation admittance of the wire and the *RLC* circuit, up to 570 MHz as shown in Figure 5.7. Figure 5.8 shows a reasonable match up to 860 MHz between the analytical solution for the radiation admittance of the wire and the admittance of the three parallel *RLC* circuits. Finally, Figure 5.9 shows a reasonable match up to 2000 MHz between the analytical solution for the radiation admittance of the wire and the admittance of the seven parallel *RLC* circuits. Figures 5.6 to 5.9 illustrate that the radiation admittance of an antenna can be approximated over any frequency range with the use of additional *RLC* circuit elements.

The simplest configuration which is shown in Figure 5.2 is considered first. In this case, the coaxial line is excited some distance below the ground plane. The coaxial line cross section is shown in Figure 5.10. A cut away view of the coaxial line is shown in Figure 5.11. The excitation source is a voltage source, $V_0(t)$, backed by a perfect conductor for the early time steps. Once the wave has been launched, the conductor is replaced by a first-order absorbing boundary condition. This implementation of
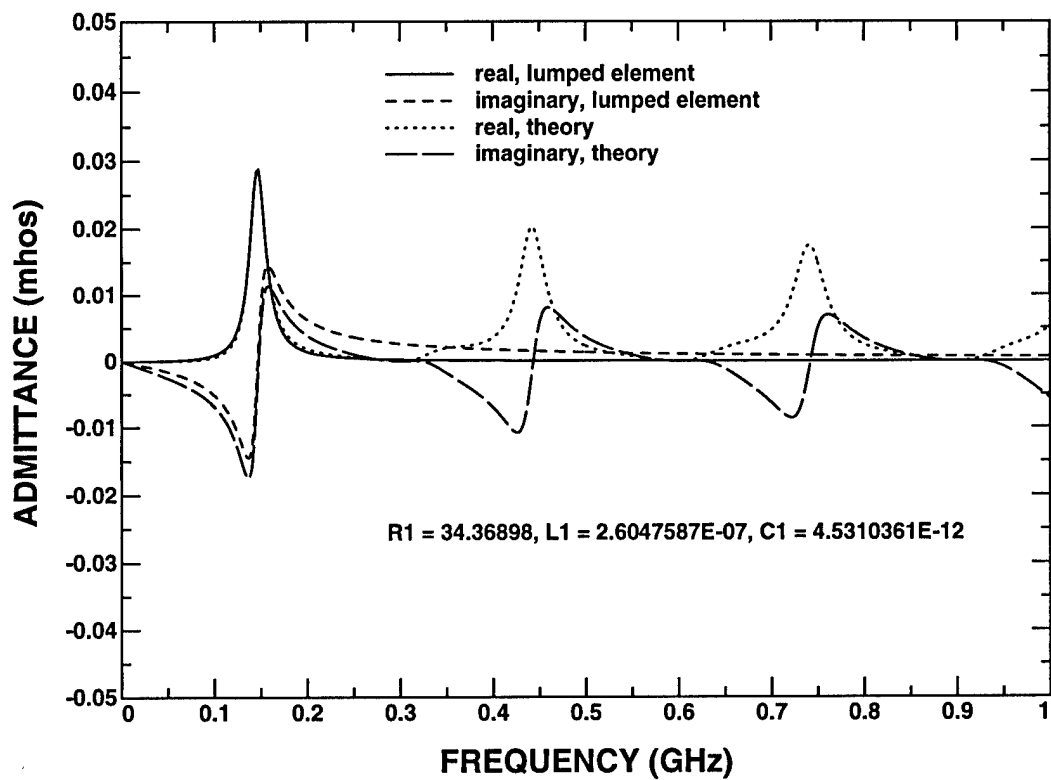
Figure 5.6: Radiation admittance of a wire of length 0.5 m and radius 2 mm over a ground plane vs. the admittance of a lumped element consisting of a single *RLC* circuit.
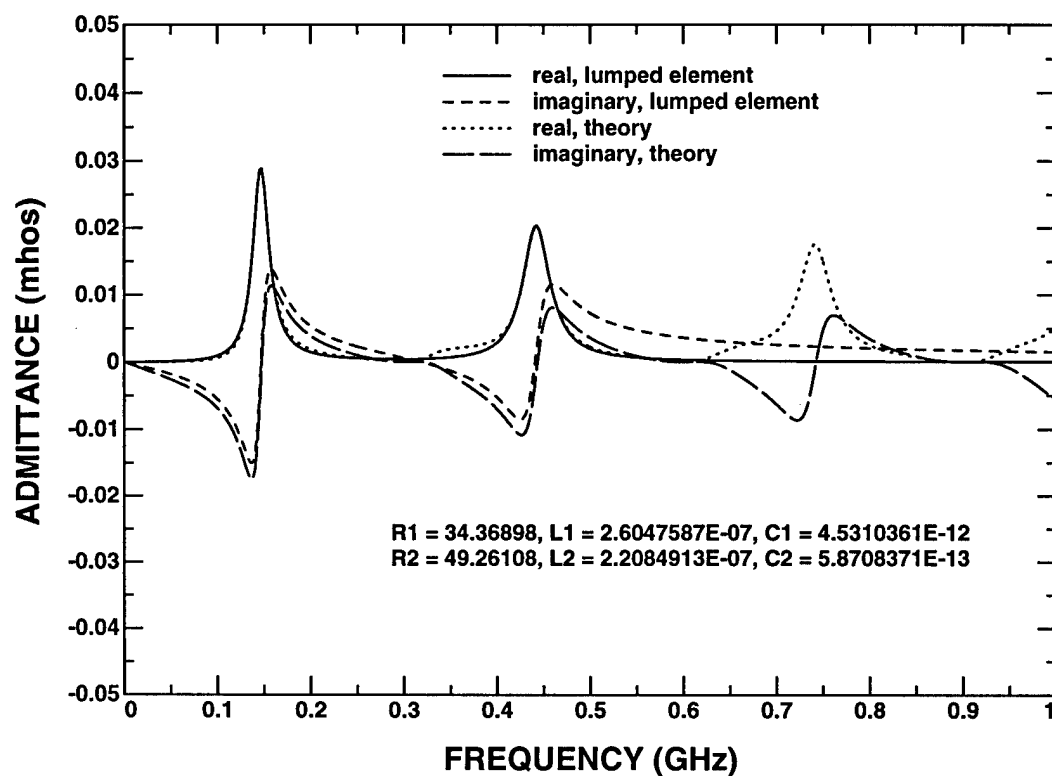
Figure 5.7: Radiation admittance of a wire of length 0.5 m and radius 2 mm over a ground plane vs. the admittance of a lumped element consisting of two *RLC* circuits.
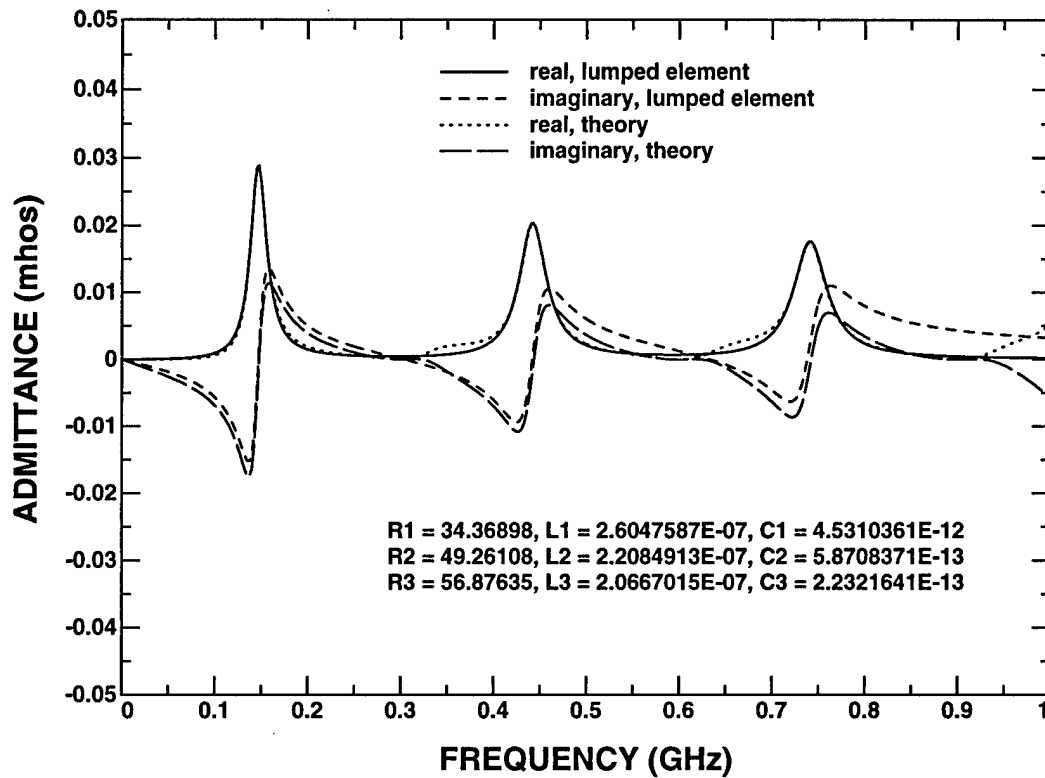
Figure 5.8: Radiation admittance of a wire of length 0.5 m and radius 2 mm over a ground plane vs. the admittance of a lumped element consisting of three *RLC* circuits.
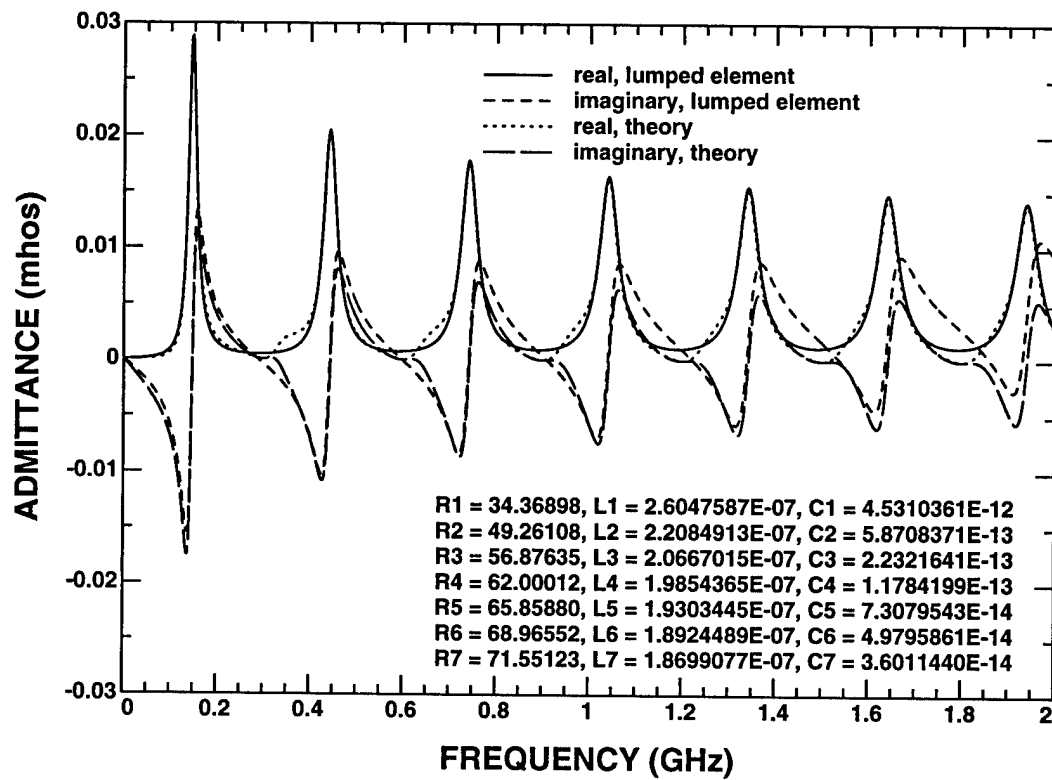
Figure 5.9: Radiation admittance of a wire of length 0.5 m and radius 2 mm over a ground plane vs. the admittance of a lumped element consisting of seven *RLC* circuits.
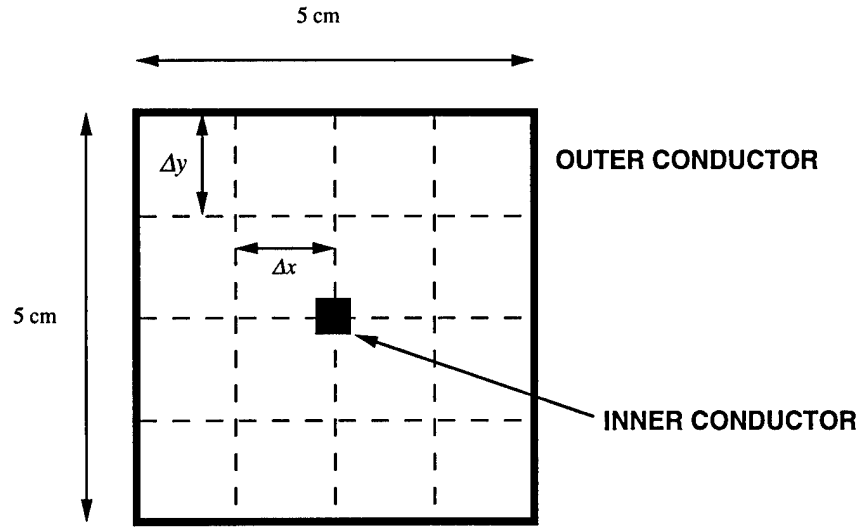
Figure 5.10: Cross section of the coaxial line.

the excitation source is the equivalent of launching a forward traveling wave with $V_+(t) = V_0(t)$ on an infinite transmission line, or a matched source with $V_s(t) = 2V_0(t)$.

Figure 5.12 compares the lumped element FD-TD results and the circuit solutions for the input admittance at the termination of the coaxial line for seven RLC lumped elements. The figure shows near perfect agreement between the FD-TD lumped element solution and the circuit solution for the input admittance at the termination of the coaxial line. For Figure 5.12, the cell dimensions used in the FD-TD simulation were $\Delta x = \Delta y = \Delta z = 0.0125$m. The characteristic impedance of the coaxial line was $Z_0 = 141.5\ \Omega$. An additional test of the lumped element model was performed by comparing the power dissipated in the lumped element calculated by two different methods. The first method involved simply using Equation 5.3, which uses the current and voltage at the lumped element to determined the dissipated
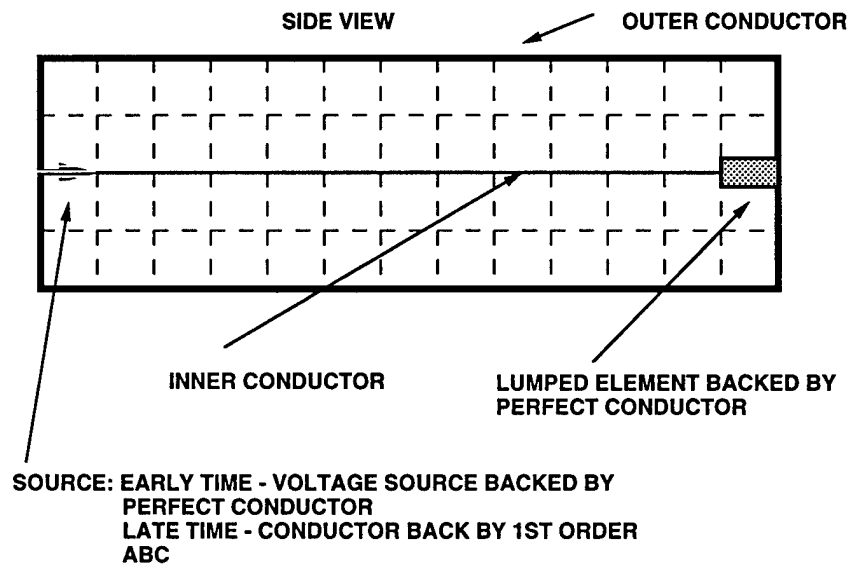
Figure 5.11: Cut away view of coaxial line.

power. The second method used the lumped element FD-TD calculated admittance, the known excitation profile on the transmission line, $V_+(t)$, and the characteristic impedance of the transmission line Z_0, in conjunction with transmission line theory to determined the dissipated power. Figure 5.13 shows the comparison between the two methods for calculating the dissipated power. The source is normalized such that the complex amplitude of the exciting matched voltage source, V_s, is 2 volts at all frequencies. The excellent agreement illustrates that the lumped element model exhibits the correct behavior with respect to the fields and power.

For the given grid cell size, the coaxial line was atypically large. This large coaxial line was examined so that a comparison with the full FD-TD simulation, which requires the larger cell size in order to have a tractable size computational domain, would be feasible. Figure 5.14 compares the radiation admittance obtained using a
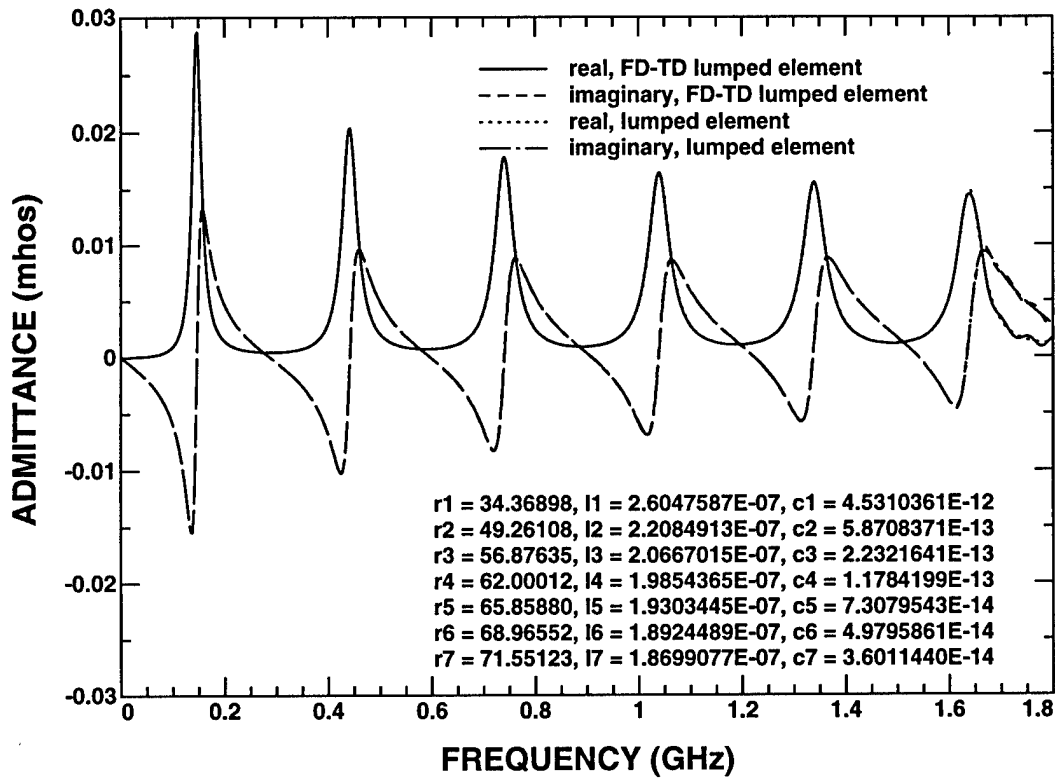
Figure 5.12: Input admittance at the termination of the coaxial line. Lumped element FD-TD with seven RLC vs. circuit solution.
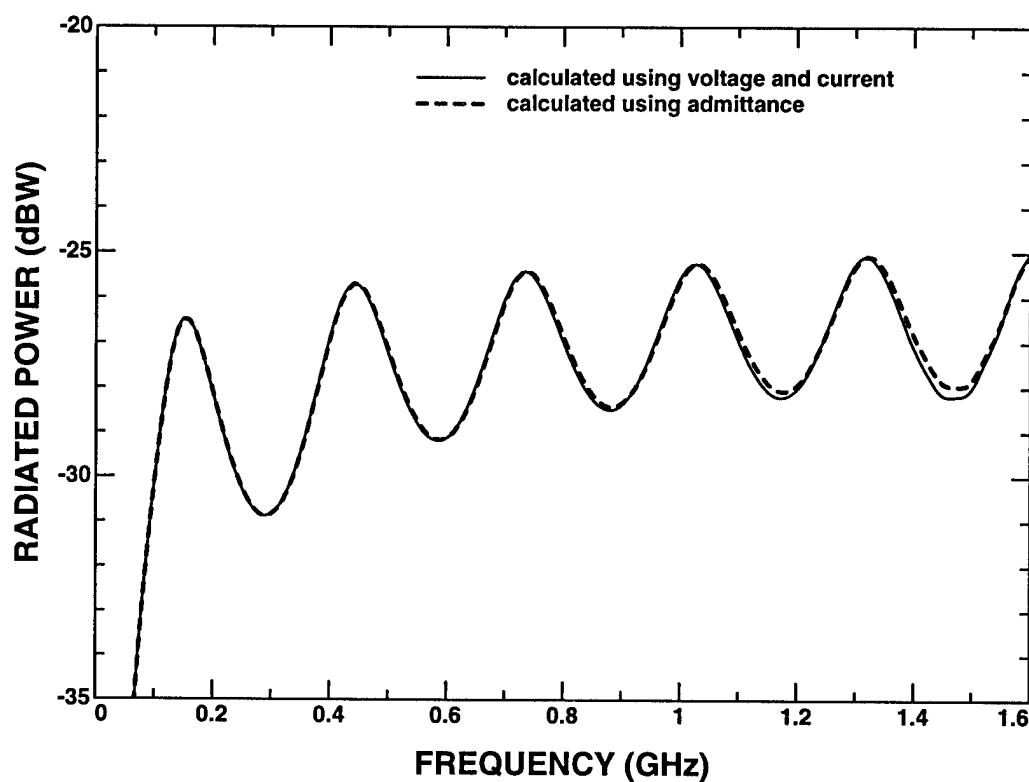
Figure 5.13: Radiated power of a coaxial line fed wire of length 0.5 m and radius 2 mm for the lumped element FD-TD with seven RLC circuits calculated using the admittance vs. calculated using the current and voltage.
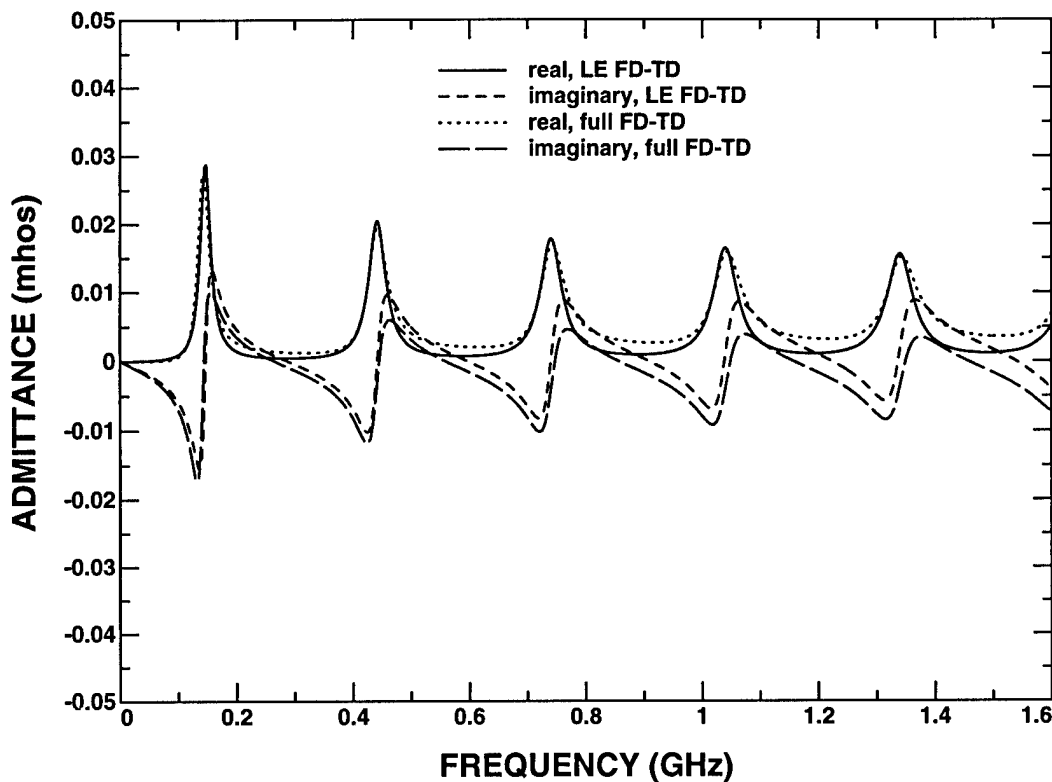
Figure 5.14: Radiation admittance of coaxial line fed wire of length 0.5 m and radius 2 mm obtained using lumped element FD-TD with seven RLC circuits vs. full FD-TD.

lumped element FD-TD simulation and a full FD-TD simulation. The agreement here appears to be relatively good, as all the peaks in the radiation conductance are matched in magnitude and in frequency.

In Figure 5.15, the radiated power is compared between the full FD-TD simulation and lumped element FD-TD simulation. In both cases, the source is normalized such that the complex amplitude of the exciting matched voltage source, V_s, is 2 volts at all frequencies. For reference, the power dissipated in a matched load would be -24.5 dBW for this transmission line and source. Figure 5.15 shows that a significant portion of the power delivered to the lumped element is radiated (only 1 to 2 dB less then the maximum possible) at frequencies at which the radiation admittance peaks

and is purely real. The overall levels and shape correspond fairly well, however, the locations of the peaks show a slight difference. The radiated power is determined by the mismatch between the coaxial line admittance of $Y_0 = 7.07$ mΩ^{-1}, and the input admittance at the termination of the coaxial line. In the lumped element FD-TD simulation, the terminating admittance is the lumped element. In the full FD-TD simulation, the terminating admittance is the radiation admittance of the wire over the infinite ground plane. The mismatch for these cases is minimized when the terminating admittance is closest to being the complex conjugate of Y_0. So for these two cases, the radiation is maximized when the terminating admittance is real and at a maximum. The maxima in radiated power for the full FD-TD simulation occur at higher frequencies than the the maxima for the lumped element FD-TD because the zero crossings in reactance associated with the peaks in the conductance for the full FD-TD simulation also occur at slightly higher frequencies than those associated with the lumped element FD-TD simulation. The maxima in radiated power calculated by the two methods are very similar in magnitude because the peaks in the radiation admittance are also very similar in magnitude. The minima in the radiated power occur at the zero crossings in the reactance associated with the minima in the conductance. Since at these frequencies, the lumped element FD-TD calculated conductance is much lower than the full FD-TD calculated conductance, the mismatch with the transmission line admittance is greater, which results in lower radiated power for the lumped element FD-TD simulation. Better correlation can be obtained by improving the lumped element model to better match the radiation admittance of the wire.

The next configurations involve an infinite metal screen, and their geometry
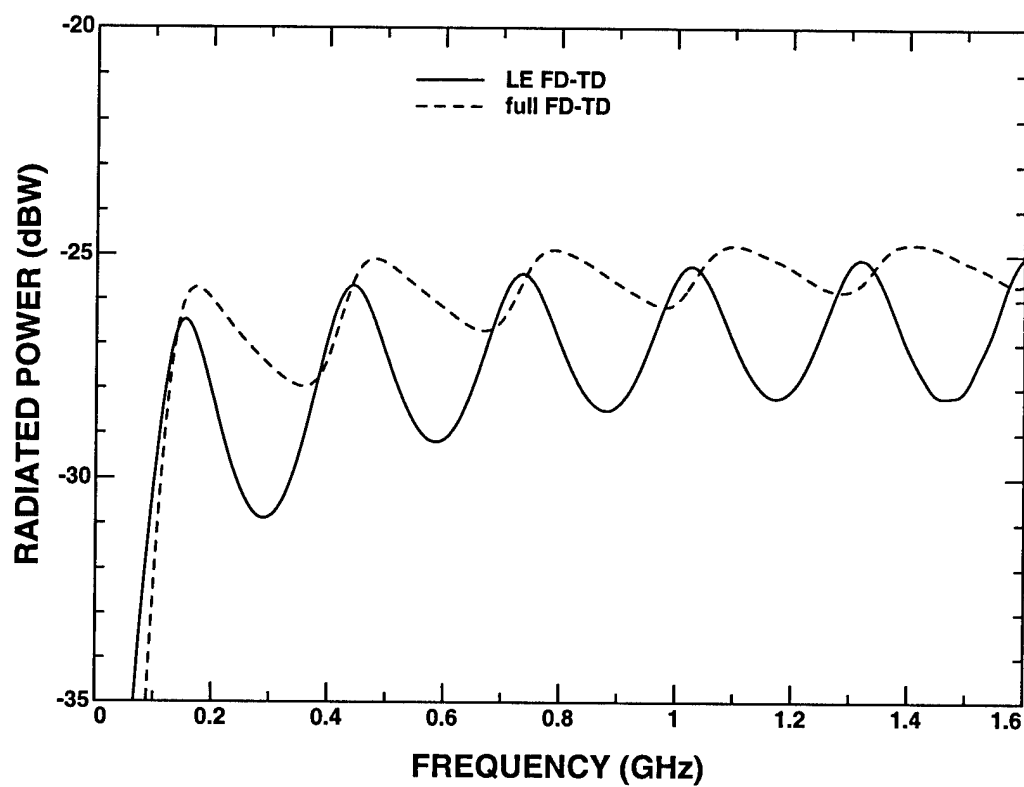
Figure 5.15: Radiated power of a coaxial line fed wire obtained using lumped element FD-TD with seven *RLC* circuits vs. full FD-TD.
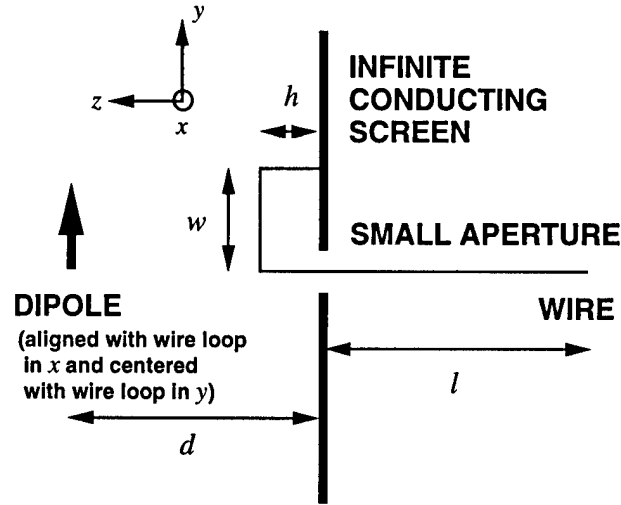
Figure 5.16: Dimensions of wire penetrating a metal screen configuration.

is shown in Figure 5.16. For configuration A, the length of the external wire is $l = 50$ cm. The internal wire loop has height, $h = 12.5$ cm, and width $w = 12.5$ cm. The exciting dipole is $d = 25$ cm displaced from the metal screen. The cell dimensions for FD-TD simulations for this configuration were $\Delta x = \Delta y = 0.0125$m and $\Delta z = 0.025$m. Figure 5.17 compares the radiation admittance obtained using the lumped element FD-TD model and using a full FD-TD model. The agreement is fairly good and comparable to the agreement seen earlier between the theoretical radiation admittance of the wire and its lumped element approximation.

In Figure 5.18, the radiated power is compared between the full FD-TD simulation and lumped element FD-TD simulation for configuration A. The source is normalized such that the power radiated from the exciting dipole in free space is constant for all frequencies. Again the overall levels and shape correspond fairly well.
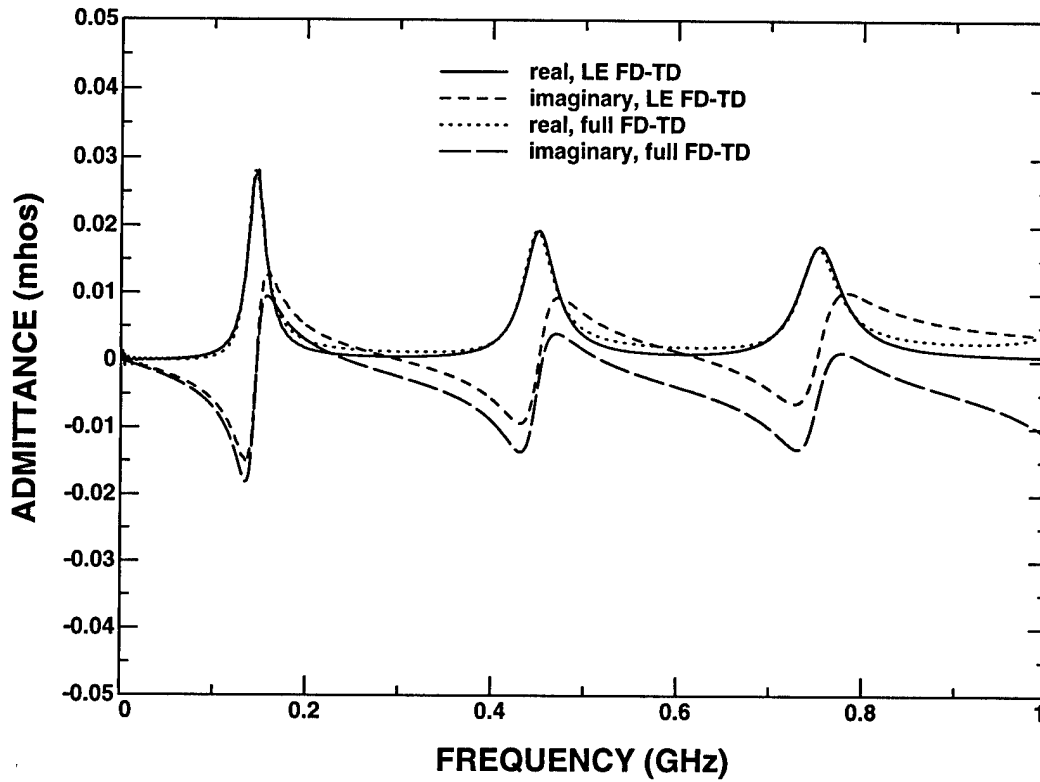
Figure 5.17: Radiation admittance using a lumped element FD-TD simulation with three *RLC* circuits and using a full FD-TD simulation of the infinite metal screen configuration *A*.

However, the locations of the peaks show a difference. The maximum coupling occurs near 100 MHz and the amount of power coupled is only 2 to 3 dB less than the total power radiated by the dipole in free space. Note that the presence of the metal screen and wires will alter the total power radiated by the dipole. The radiated power from the external wire will be determined by two factors. The first factor is the coupling between the exciting dipole and the internal wire loop. The second factor is the mismatch between the radiation impedance of the internal wire loop, and the radiation (lumped element) impedance of the external wire. Figure 5.19 shows the radiation admittance of the internal wire loop for configuration A. Figures 5.19 and 5.17 show that the frequencies at which the two admittances are closest to being conjugates of each other, approximately coincide with the frequences at which the radiated power peaks.

For configuration B (Figure 5.16), the length of the external wire is again $l = 50$ cm. However, the internal wire loop has height, $h = 10$ cm, and width $w = 7.5$ cm. The exciting dipole is $d = 25$ cm displaced from the metal screen. The same cell dimensions were used for configuration B as in configuration A. The radiation admittance obtained using the lumped element FD-TD model and using a full FD-TD model are nearly identical to those shown in Figure 5.17, which is expected as the external wire configuration was unchanged. In Figure 5.20, the radiated power is compared between the full FD-TD simulation and lumped element FD-TD simulation for configuration B. Again the source is normalized such that the power radiated from the exciting dipole in free space is constant for all frequencies. The maximum coupling occurs again near 100 MHz and the amount of power coupled is 5 to 6 dB less than
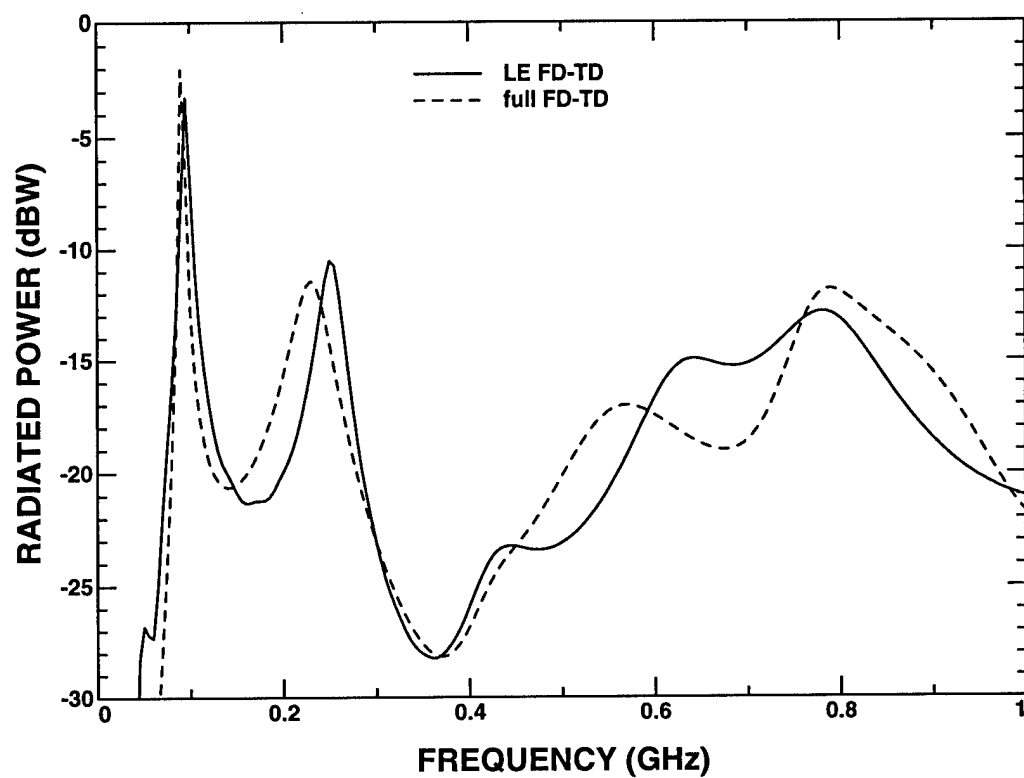
Figure 5.18: Radiated power using a lumped element FD-TD simulation with three *RLC* circuits and using a full FD-TD simulation of the infinite metal screen configuration *A*.
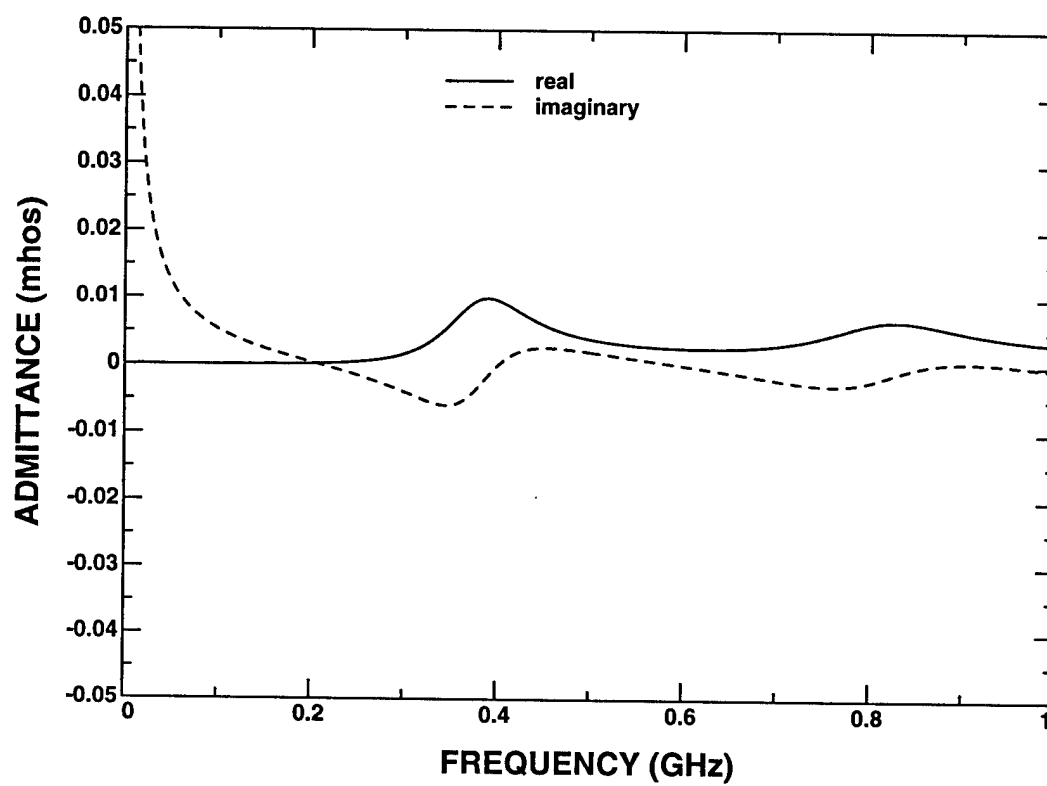
Figure 5.19: Radiation admittance of internal wire loop of dimensions $h = 12.5$ cm and $w = 12.5$ cm.
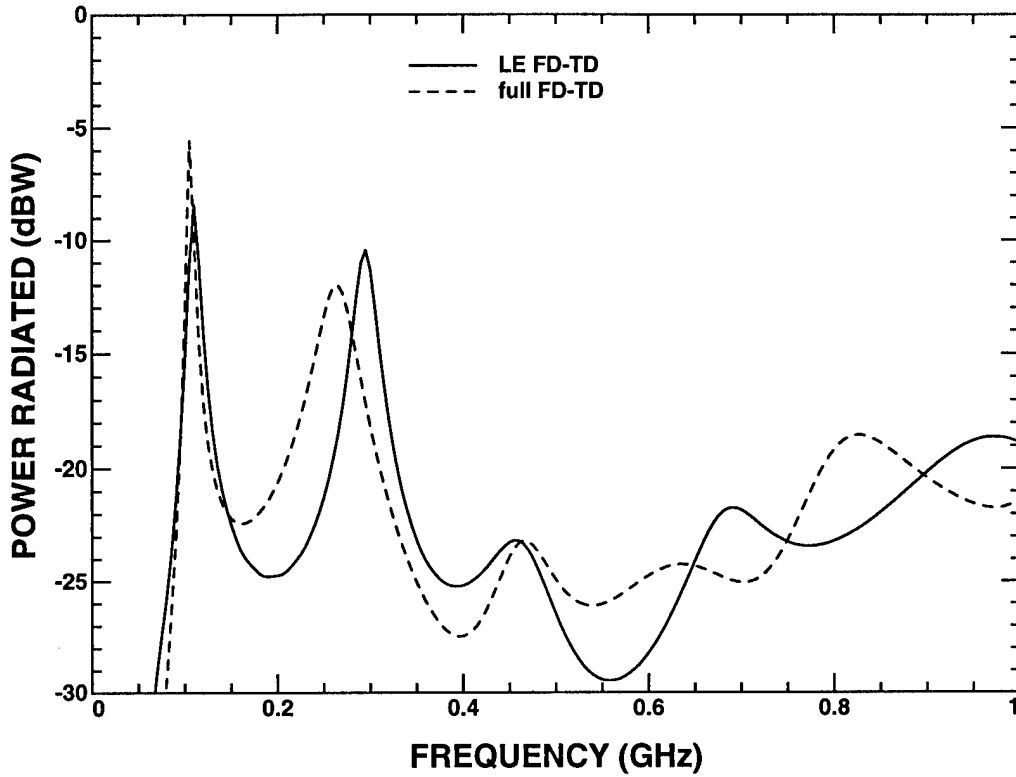
Figure 5.20: Radiated power using a lumped element FD-TD simulation with three *RLC* circuits and using a full FD-TD simulation of the infinite metal screen configuration *B*.

the total power radiated by the dipole in free space. The reason for the lower coupling in configuration *B* compared to configuration *A* is simply that a better admittance match occurs for configuration *A*. The overall levels and shape correspond fairly well. Figure 5.21 shows the radiation admittance of the internal wire loop. Figures 5.21 and 5.17 show that the frequencies at which the two admittances are closest to being conjugates of each other, approximately coincide with the frequencies at which the radiated power peaks.

The differences between the lumped element FD-TD simulation and the full FD-TD simulation can be attributed to the inaccuracies of the lumped element model.
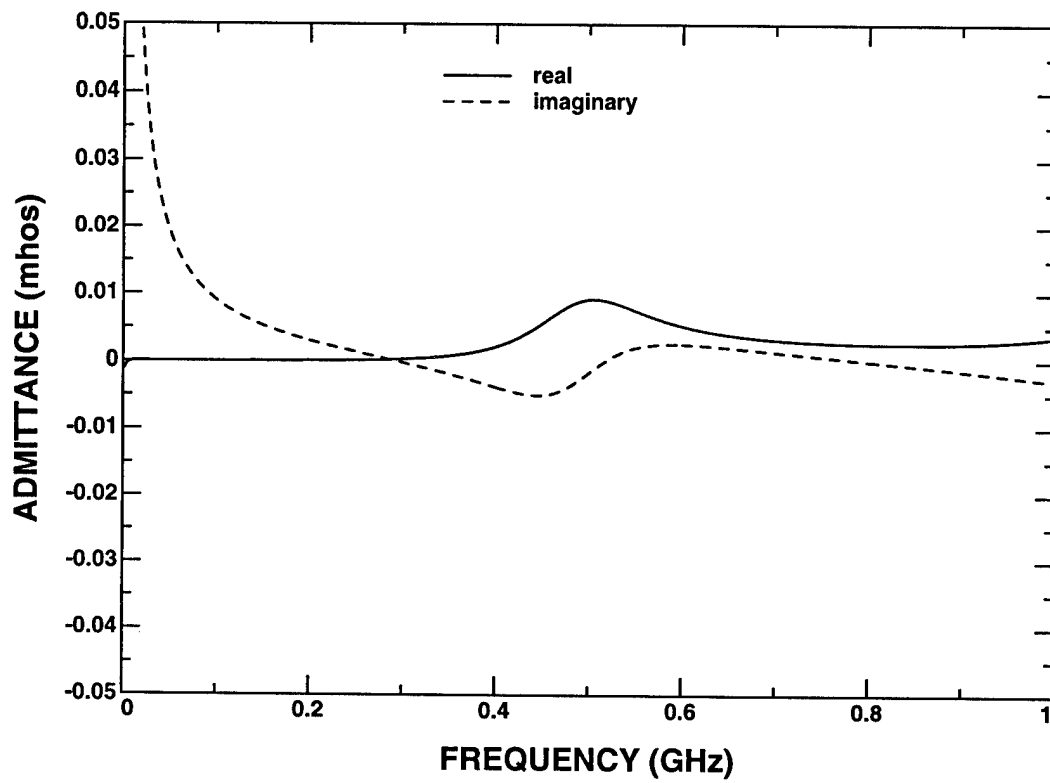
Figure 5.21: Radiation admittance of internal wire loop of dimensions $h = 10$ cm and $w = 7.5$ cm.

In particular, since the radiation susceptance has greater variation with increasing frequency, the error in the radiated power, as seen in Figures 5.18 and 5.20, is expected to increase with frequency as well.

5.5   Conclusions

Radiation levels associated with the two configurations were quantified. Significant coupling of electromagnetic energy occurs when the admittance of the external wire is matched by the admittance associated with internal side. In the coaxial line configuration, the characteristic admittance of the coaxial line matches the peaks in the external wire's radiation admittance well, and results in radiated power only 1 to 2 dB less than the maximum possible. For the infinite metal screen configurations, fairly significant levels of radiation occur at frequencies where the radiation admittance of the inner wire loop match the radiation admittance of the external wire antenna. For configuration A, the maximum coupling is only 3dB less than the power radiated by the dipole in free space, and for configuration B, the maximum coupling is only 6 dB less.

A "smart" cell in the FD-TD scheme, which can model the radiation admittance of a wire antenna, has been developed and tested. Analytical solutions for the radiation admittance of a straight wire over a ground plane have been recited and approximated using the lumped element model, which consists of a set of series RLC circuits in parallel. The admittance of the lumped element implemented in the FD-TD simulations match the circuit solution admittance extremely well. Both a wire over a ground plane excited by a coaxial line, and a wire penetrating a metal screen excited by a dipole, were examined. Fairly good correlation between lumped element FD-TD simulations and full FD-TD simulations have been obtained for each of the configurations for both radiation admittances and radiated powers.

One clear limitation of the use of lumped elements in modeling radiation admittances is that the results will only be as accurate as the lumped element model of the radiation admittance. The lumped element model considered here, most accurately modeled the peaks in the radiation conductance, and hence produced the most accurate results at those frequencies. Correspondingly, the lumped element FD-TD model had increasing errors as the lumped element admittance varied from the theoretical radiation admittance. In the future, if methods for designing passive RLC circuits to more accurately approximate arbitrary admittances as a function of frequency are developed, then the lumped element model could be correspondingly more accurate.

Chapter 6

EM Radiation from a Microstrip Patch Antenna on a Non-Uniform Substrate

6.1 Introduction

This chapter investigates microstrip patch antennas on non-uniform substrates with special emphasis on the reduction of surface wave losses using the finite difference-time domain technique. A microstrip patch antenna is chosen as the radiating element since it is a popular choice for a low profile antenna which is used with a substrate [147]-[152],[111],[139]-[144]. In designing microstrip antennas, a few of the key features, which are commonly optimized, are: minimizing the overall antenna size, maximizing the antenna's bandwidth in frequency, and minimizing the losses due to surface waves. The overall antenna size for operation at a specified frequency range can typically be reduced by using a higher dielectric constant substrate. The bandwidth can be increased by increasing the height of the microstrip patch. However, these two changes tend to increase the loss due to surface waves, which is undesirable.

191

The presence of guided waves in the substrate is undesirable for the following reasons. First of all, power coupled into guided waves is power which is not radiated which results in a lower radiation efficiency for the antenna [140]. Also with a finite size substrate, the interaction of the guided waves with termination of the substrate could cause unwanted high side lobes or back lobes. When phased arrays are mounted on a common substrate, significant coupling between elements can occur which can cause limitations in the scanning range of the array [147],[148].

The uniform substrate is altered by removing a rectangular ring of the dielectric substrate which surrounds the radiating element, and is shown in Figure 6.1. By removing rings of dielectric from the substrate which surround the microstrip patch, the surface or guided waves are reflected at the interfaces and can couple more efficiently into radiated modes.

In Section 6.2 a brief discussion of the finite difference-time domain technique is given. A perfectly matched layer absorbing boundary condition is used because of its superior performance over other absorbing boundary conditions and is described in detail in Section 6.2. The results are shown and discussed in Section 6.3. In Section 6.4 the usefulness and effectiveness of the non-uniform substrate in terms of reducing the surface wave generation is discussed and additional configurations and uses of non-uniform substrates are commented on.

TOP VIEW

SIDE VIEW
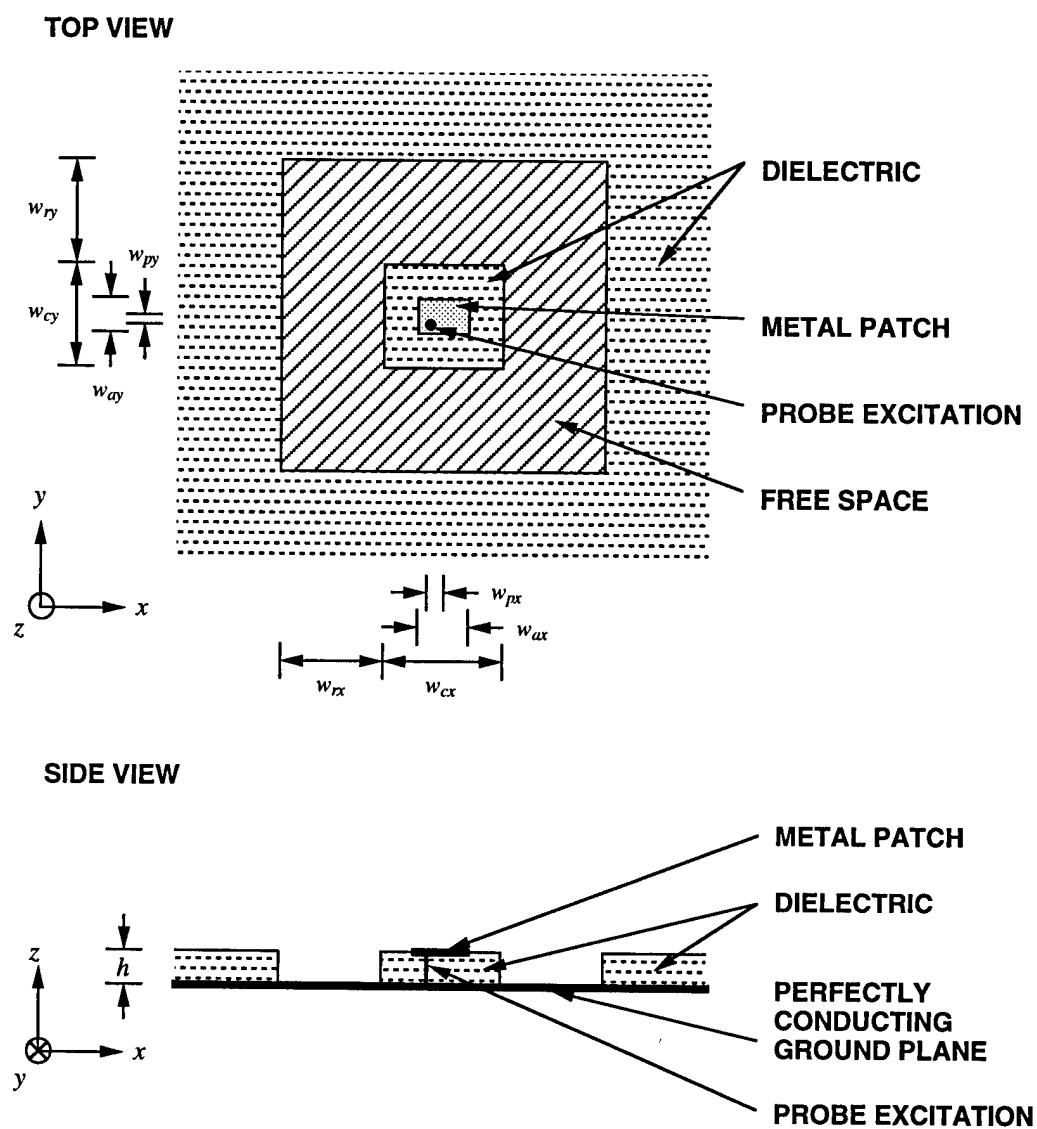
Figure 6.1: Microstrip patch antenna on a non-uniform dielectric substrate.

6.2 Method of Solution

6.2.1 Finite Difference – Time Domain Technique

The finite difference-time domain (FD-TD) technique is used to analyze this problem [1]-[12]. This method was chosen because it can be used to analyze multiple frequencies with a single simulation, and it is a good choice for low loss models and rectilinear geometries.

A rectangular three-dimensional grid was used as the computational domain. Spatially, the computational domain is discretized such that the largest grid dimension is less than about a twentieth of the shortest wavelength of interest. The time step approximately must be less than the smallest grid dimension divided by the speed of light in order to guarantee the stability of the algorithm. The difference equations which are utilized to update the electric and magnetic fields are obtained from Maxwell's equations in differential form by approximating spatial and temporal derivatives with center differences. Electric and magnetic fields are discretized on Yee's lattice [1]. Initial conditions, which are imposed at the beginning of the simulation, are that all electric and magnetic fields start at zero. At each subsequent time step, fields are imposed at appropriate locations in order to simulate the excitation source. The imposed electric field has a time dependence of a Gaussian pulse modulated by a sine wave, which contains energy in a band of frequencies allowing multiple frequencies to be analyzed simultaneously. Boundary conditions are imposed at perfectly conducting surfaces and at the outer boundary. At the perfectly conducting surfaces, the tangential electric field is set to zero. Absorbing boundary conditions

must be applied at the outer boundary of the computational domain in order to simulate unbounded space. Perfectly matched layer absorbing boundary conditions are used at the outer boundary [78]-[83]. Finally, by applying the difference equations obtained from Maxwell's equations in addition to the appropriate initial and boundary conditions, the electric and magnetic fields can be calculated everywhere within the computational domain for each time step.

The source used with this problem was a coaxial line probe exciting the microstrip patch. The treatment of the source condition is discussed in Subsection 4.3.1. The equation governing the update of the electric field at the source is given in Equation 4.1. The calculation for the radiation impedance of the antenna and the current and voltage on the coaxial probe are also discussed in Subsection 4.3.1.

The calculations for total radiated and guided power are done using time domain results from the FD-TD simulation. First, the electric and magnetic fields are calculated everywhere in the computational domain and then the tangential electric and magnetic fields on a surface enclosing the antenna are recorded. The fields are then Fourier transformed to obtain frequency domain data and the time average Poynting power, $\langle \overline{S}(f) \rangle$, is calculated.

$$\langle \overline{S}(f) \rangle = \frac{1}{2}\text{Re}[\overline{E}(f) \times \overline{H}^*(f)] \qquad (6.1)$$

The total guided power is then approximated by integrating the Poynting power passing through the integration surface which lies within the substrate. The integration surface is placed far enough from the source such that most of the power

in the substrate is presumably guided. The total radiated power is then calculated by integrating the Poynting power passing through the integration surface above the substrate.

6.2.2 Perfectly Matched Layer Absorbing Boundary Condition

The perfectly matched layer (PML) absorbing boundary condition (ABC) [78]-[83] was recently introduced in 1994 by Berenger, and was chosen to be used over the standard one-way equation absorbing boundary conditions (Section 2.11) [67]-[77] because of its superior performance in general and especially with dielectric substrates.

The basic premise of the PML ABC is to implement a media which is reflectionless for waves incident from a free space or dielectric region, and which is highly lossy. By providing sufficient loss in the PML layer the truncation of the computational domain can then be performed by using perfect electric conductor and still not introduce significant reflections.

In order to facilitate the analysis of the perfectly matched layer absorbing boundary condition, a two dimensional case will be considered first. Then the two dimensional treatment will be extrapolated to three dimensions.

The electromagnetic fields, in a PML for a two dimensional case where there is no variation in the z direction, are governed by the following equations for the TM polarization.

$$\epsilon_r \epsilon_0 \frac{\partial E_x}{\partial t} + \sigma_y E_x = \frac{\partial (H_{zx} + H_{zy})}{\partial y} \qquad (6.2)$$

$$\epsilon_r \epsilon_0 \frac{\partial E_y}{\partial t} + \sigma_x E_y = -\frac{\partial (H_{zx} + H_{zy})}{\partial x} \tag{6.3}$$

$$\mu_r \mu_0 \frac{\partial H_{zx}}{\partial t} + \sigma_{mx} H_{zx} = -\frac{\partial E_y}{\partial x} \tag{6.4}$$

$$\mu_r \mu_0 \frac{\partial H_{zy}}{\partial t} + \sigma_{my} H_{zy} = \frac{\partial E_x}{\partial y} \tag{6.5}$$

Note that there are four field components (E_x, E_y, H_{zx} and H_{zy}) instead of the standard three. The sum of H_{zx} and H_{zy} can be interpreted as the normal H_z. σ_x and σ_y can be interpreted as anisotropic electric conductivities. σ_{mx} and σ_{my} have a similar interpretation as magnetic conductivities with respect to H_{zx} and H_{zy}; however they have a less clear relationship with H_z. Note that when $\sigma_{mx} = \sigma_{my}$, the PML equations reduce to Maxwell's equations and the PML medium becomes a normal dielectric or magnetic material.

The following conditions are imposed on the properties of the PML layer in order to make it reflectionless:

$$\frac{\sigma_x}{\epsilon_r \epsilon_0} = \frac{\sigma_{mx}}{\mu_r \mu_0} \tag{6.6}$$

$$\frac{\sigma_y}{\epsilon_r \epsilon_0} = \frac{\sigma_{my}}{\mu_r \mu_0} \tag{6.7}$$

These conditions are essentially identical to those imposed for the impedance matching problem for a wave at normal incidence. It will be shown that with the alterations to Maxwell's equations outlined above that reflectionless transmission can be achieved for all angles of incidence once additional constraints on the PML parameters are im-

posed.

The continuity of tangential electric and magnetic fields at a dielectric/PML layer interface can be established by integrating the sum of Equations 6.4 and 6.5 on the surface S_1 shown in Figure 6.2. Applying Gauss' theorem, the following equation is obtained:

$$\int_{S_1} \nabla \times \overline{E} \cdot d\overline{S} = \int_{C_1} \overline{E} \cdot d\overline{l} = \int_{S_2} \mu_{r2} \mu_0 \frac{\partial H_{zy} + H_{zx}}{\partial t} + \sigma_{mx} H_{zx} + \sigma_{my} H_{zy}$$

$$+ \int_{S_3} \mu_{r1} \mu_0 \frac{\partial H_{zy} + H_{zx}}{\partial t} \tag{6.8}$$

Making Δy of S_1 vanishingly thin, the surface integral of H_{zy} and H_{zx} vanishes, and it is apparent that

$$E_x^{\text{dielectric}} \Delta x - E_x^{\text{pml}} \Delta x = 0 \tag{6.9}$$

$$E_x^{\text{dielectric}} = E_x^{\text{pml}} \tag{6.10}$$

Similar arguments apply to show that other components of the electric and magnetic fields which are tangential to the interface are continuous.

Since the tangential fields are continuous, phase matching must apply, and thus the tangential wavenumber, k_x, must be continuous

$$k'_{xi} = k'_{xr} = k'_{xt} \tag{6.11}$$
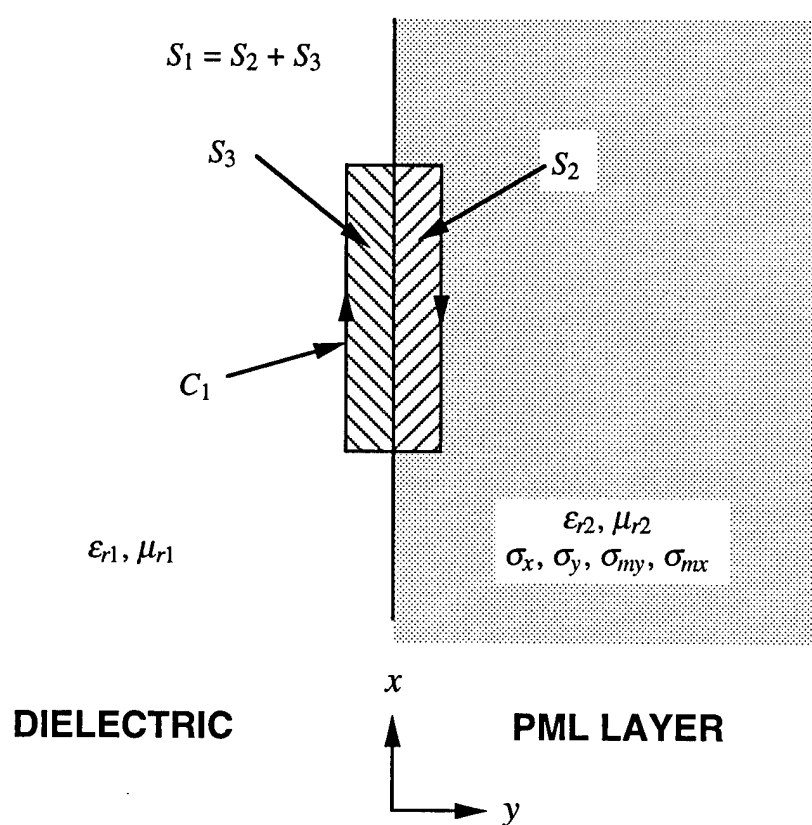
Figure 6.2: Integration surface for interface between a dielectric medium and a PML medium.

$$k''_{xi} = k''_{xr} = k''_{xt} = 0 \tag{6.12}$$

for propagating plane wave incidence. k'_x and k''_x are the real and imaginary portions of the tangential wave number and the subscripts i, r and t denote incident, reflected and transmitted wavenumbers respectively.

In deriving a wave equation for a PML medium, the time-harmonic equations in a PML layer will be used and a $e^{-i\omega t}$ time dependence is assumed.

$$E_x(-i\omega\epsilon_r\epsilon_0 + \sigma_y) = ik_y(H_{zx} + H_{zy}) \tag{6.13}$$

$$E_y(-i\omega\epsilon_r\epsilon_0 + \sigma_x) = -ik_x(H_{zx} + H_{zy}) \tag{6.14}$$

$$H_{zx}(-i\omega\mu_r\mu_0 + \sigma_{mx}) = -ik_x(E_{yx} + E_{yz}) \tag{6.15}$$

$$H_{zy}(-i\omega\mu_r\mu_0 + \sigma_{my}) = ik_y(E_{xy} + E_{xz}) \tag{6.16}$$

By simple manipulation of the above equations a wave equation in a PML medium with ϵ_r, μ_r, σ_x, σ_y, σ_{mx}, and σ_{my} can be derived.

$$k_x^2 \left(\frac{-i\omega\epsilon_r\epsilon_0 + \sigma_y}{-i\omega\mu_r\mu_0 + \sigma_{mx}} \right) + k_y^2 \left(\frac{-i\omega\epsilon_r\epsilon_0 + \sigma_x}{-i\omega\mu_r\mu_0 + \sigma_{my}} \right)$$

$$+(-i\omega\epsilon_r\epsilon_0 + \sigma_y)(-i\omega\epsilon_r\epsilon_0 + \sigma_x) = 0 \tag{6.17}$$

$$k_x^2 \left[\frac{1 - \sigma_y/(i\omega\epsilon_r\epsilon_0)}{1 - \sigma_{mx}/(i\omega\mu_r\mu_0)} \right] + k_y^2 \left[\frac{1 - \sigma_x/(i\omega\epsilon_r\epsilon_0)}{1 - \sigma_{my}/(i\omega\mu_r\mu_0)} \right] \tag{6.18}$$

$$-k_0^2[1 - \sigma_y/(i\omega\epsilon_r\epsilon_0)][1 - \sigma_x/(i\omega\epsilon_r\epsilon_0)] = 0$$

$$k_y = \left\{ k_r^2[1 - \sigma_y/(i\omega\epsilon_r\epsilon_0)][1 - \sigma_{my}/(i\omega\mu_r\mu_0)] \right.$$

$$\left. -k_x^2 \left[\frac{1 - \sigma_y/(i\omega\epsilon_r\epsilon_0)}{1 - \sigma_x/(i\omega\epsilon_r\epsilon_0)}\right] \left[\frac{1 - \sigma_{my}/(i\omega\mu_r\mu_0)}{1 - \sigma_{mx}/(i\omega\mu_r\mu_0)}\right] \right\}^{1/2} \tag{6.19}$$

where $k_r = \omega\sqrt{\epsilon_r\epsilon_0\mu_r\mu_0}$.

In calculating the reflection coefficient for a plane wave incident from a dielectric region on a PML layer, a plane wave with $\overline{H}_{\text{inc}} = \hat{z}H_0 e^{ik_x x + ik_y y}$ is used. Using Equations 6.11-6.14, the equations in the dielectric region characterized by ϵ_{r1} and μ_{r1} are

$$(H_{zx} + H_{zy}) = H_0(e^{ik_{iy}y} + Re^{-ik_{iy}y})e^{ik_{ix}x} \tag{6.20}$$

$$E_x = \frac{ik_{iy}}{-i\omega\epsilon_0\epsilon_{r1}}H_0(e^{ik_{iy}y} - Re^{-ik_{iy}y})e^{ik_{ix}x} \tag{6.21}$$

$$E_y = \frac{-ik_{ix}}{-i\omega\epsilon_0\epsilon_{r1}}H_0(e^{ik_{iy}y} + Re^{-ik_{iy}y})e^{ik_{ix}x} \tag{6.22}$$

where R is reflection coefficient between the dielectric and PML regions. The equations in the PML region characterized by ϵ_{r2}, μ_{r2}, σ_x, σ_y, σ_{mx} and σ_{my} are

$$(H_{zx} + H_{zy}) = TH_0 e^{ik_{ix}x}e^{ik_{ty}y} \tag{6.23}$$

$$E_x = \frac{ik_{ty}}{-i\omega\epsilon_0\epsilon_{r2} + \sigma_y}TH_0 e^{ik_{ix}x}e^{ik_{ty}y} \tag{6.24}$$

$$E_y = \frac{-ik_{ix}}{-i\omega\epsilon_0\epsilon_{r2} + \sigma_x} T H_0 e^{ik_{ix}x} e^{ik_{ty}y} \tag{6.25}$$

where T is the transmission coefficient between the dielectric and PML regions.

Setting the tangential electric and magnetic fields continuous at the boundary results in

$$1 + R = T \tag{6.26}$$

$$\frac{ik_{iy}}{-i\omega\epsilon_0\epsilon_{r1}}(1 - R) = \frac{ik_{ty}}{-i\omega\epsilon_0\epsilon_{r2} + \sigma_y}T \tag{6.27}$$

Combining Equations 6.26 and 6.27, the reflection coefficient is found to be

$$R = \frac{1 - p}{1 + p} \tag{6.28}$$

where

$$p = \frac{k_{ty}}{k_{iy}}\frac{1}{\epsilon_{r2}/\epsilon_{r1} - \sigma_y/(i\omega\epsilon_0\epsilon_{r1})} \tag{6.29}$$

It is apparent that the interface will be reflectionless when $p = 1$.

Applying the conditions for a matched medium, Equations 6.6 and 6.7, the normal transmitted wave number is

$$k_{ty} = \sqrt{k_{r2}^2[1 - \sigma_y/(i\omega\epsilon_0\epsilon_{r2})]^2 - k_{ix}^2\left[\frac{1 - \sigma_y/(i\omega\epsilon_0\epsilon_{r2})}{1 - \sigma_x/(i\omega\epsilon_0\epsilon_{r2})}\right]^2} \tag{6.30}$$

where $k_{r2} = \omega\sqrt{\epsilon_{r2}\epsilon_0\mu_{r2}\mu_0}$. After some consideration, it can be observed that reflectionless transmission for all angles will occur only under the following conditions:

$$\epsilon_{r1} = \epsilon_{r2} \tag{6.31}$$

$$\mu_{r1} = \mu_{r2} \tag{6.32}$$

$$\sigma_x = \sigma_{mx} = 0 \tag{6.33}$$

Under these conditions,

$$k_{ty} = [1 - \sigma_y/(i\omega\epsilon_0\epsilon_{r2})]\sqrt{k_{r1}^2 - k_{ix}^2} \tag{6.34}$$

and it is observed that $p = 1$ in this case. To summarize the conditions for reflectionless transmission, all the parameters in the PML layer must be identical to those in the dielectric layer except the loss factors, σ and σ_m in the direction normal to the interface. The same conditions hold for interfaces between two PML layers.

As mentioned earlier, the operating principle of the PML ABC is that the PML layer is reflectionless and provides significant loss as the wave propagates through it. Since the PML layer is typically backed by a perfect conductor, the total loss as a wave propagates through the PML layer will be determined by its thickness and its conductivities. In order to achieve low reflections from the conductor backed PML layer, large values of conductivity are used. Applying center differences to the

PML equations, Equations 6.2-6.5, is impractical since the grid cell would need to be greatly reduced in order to accommodate the desired high conductivities. Instead, explicit exponentially differenced equations are used in order to maintain accuracy and stability.

The explicit exponentially differenced equations are obtained from solving the quasi-static charge relaxation problem. The following equation for E_y is solved using quasi-static approximations.

$$\epsilon_r \epsilon_0 \frac{\partial E_y}{\partial t} + \sigma_x E_y = -\frac{\partial (H_{zx} + H_{zy})}{\partial x} \tag{6.35}$$

Assuming that the time constant associated with the conductivity is small compared to the period of the frequency of interest, the magnetic field terms can be considered slowly varying in time and is approximated as constant. The homogeneous solution to Equation 6.35 is

$$E_{yh}(t) = E_y(t = 0)e^{-t\sigma_x/\epsilon_r \epsilon_0} \tag{6.36}$$

The particular solution, approximating the magnetic field as constant in time, is

$$E_{yp}(t) = -\frac{1}{\sigma_x}\frac{\partial (H_{zx} + H_{zy})}{\partial x} \tag{6.37}$$

Combining the homogeneous and particular solutions results in

$$E_y(t) = E_y(t = 0)e^{-t\sigma_x/\epsilon_r \epsilon_0} - \frac{1}{\sigma_x}\frac{\partial (H_{zx} + H_{zy})}{\partial x} \tag{6.38}$$

By taking the solution at time step $n+1$ and subtracting the solution at time step n times $e^{-\Delta t \sigma_x / \epsilon_r \epsilon_0}$, the following difference equation is obtained.

$$E_y^{n+1}(i, j+1/2) = e^{-\sigma \Delta t / \epsilon_r \epsilon_0} E_y^n(i, j+1/2) + \frac{1}{\sigma \Delta x}(e^{-\sigma \Delta t / \epsilon_r \epsilon_0} - 1) \qquad (6.39)$$

$$\times \left(H_z^{n+1/2}(i+1/2, j+1/2) - H_z^{n+1/2}(i-1/2, j+1/2) \right)$$

In theory the loss factor can be chosen to be arbitrarily large and an arbitrarily thin PML layer could be used. However, in implementing the equations in the FD-TD method, the discretized nature of space must be considered since the electric and magnetic fields are separated by half grid cells. Hence, it is desirable to chose PML layers which are 4 to 16 cells thick, and to grade the conductivity smoothly from zero to some maximum such that discretization errors will be minimized. One manner of grading the conductivity is by using a polynomial curve.

$$\sigma(\rho) = \sigma_{\max}[\rho/(\Delta \rho)]^n \qquad (6.40)$$

where $\Delta \rho$ is the PML thickness, ρ is the position in the PML layer, and n is a smoothness factor. Quadratic grading of the conductivity has shown itself to work well. Note that since the electric and magnetic fields are separated by a half cell, this half cell should be accounted for in computing the desired conductivities for the affected electric and magnetic fields.

The effective reflection coefficient for a PML layer backed by a perfect conductor
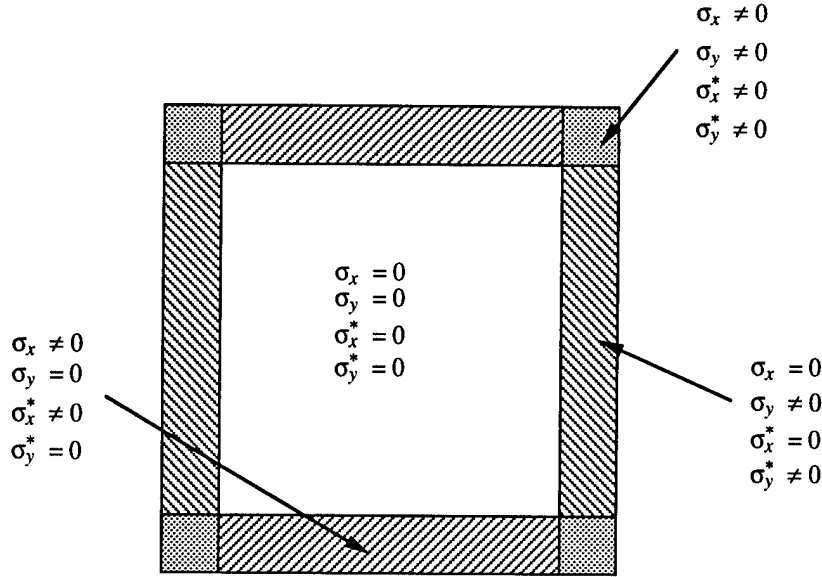
Figure 6.3: Selection of conductivities for a PML ABC in two-dimensions.

will be

$$R(\theta) = e^{-2\sigma_{max}\Delta\rho\cos\theta/[(n+1)\epsilon_r\epsilon_0 c_r]} \qquad (6.41)$$

where θ is the angle of incidence, $\theta = 0$ degrees for normal incidence, and $c_r = 1/\sqrt{\epsilon_r\epsilon_0\mu_r\mu_0}$. The reflection coefficient is typically chosen to be around $R(0) = 10^{-5}$ as a compromise between minimizing reflections and avoiding numerical noise. Once the cell size, PML layer thickness, permittivity, permeability and desired reflection coefficient are determined, then the conductivities in the PML layer can be determined using Equations 6.6-6.7, and 6.40-6.41. Figure 6.3 shows the selection of the various conductivities needed to implement a PML ABC.

In extending the use of the PML ABC to three-dimensions, only a few modifications are needed. All six field components in rectangular coordinates are split in

two, and a separate PML conductivity is used in each direction. The resulting set of twelve equations are

$$\epsilon_r \epsilon_0 \frac{\partial E_{xy}}{\partial t} + \sigma_y E_{xy} = \frac{\partial (H_{zx} + H_{zy})}{\partial y} \tag{6.42}$$

$$\epsilon_r \epsilon_0 \frac{\partial E_{xz}}{\partial t} + \sigma_z E_{xz} = -\frac{\partial (H_{yx} + H_{yz})}{\partial z} \tag{6.43}$$

$$\epsilon_r \epsilon_0 \frac{\partial E_{yx}}{\partial t} + \sigma_x E_{yx} = -\frac{\partial (H_{zx} + H_{zy})}{\partial x} \tag{6.44}$$

$$\epsilon_r \epsilon_0 \frac{\partial E_{yz}}{\partial t} + \sigma_z E_{yz} = \frac{\partial (H_{xy} + H_{xz})}{\partial z} \tag{6.45}$$

$$\epsilon_r \epsilon_0 \frac{\partial E_{zx}}{\partial t} + \sigma_x E_{zx} = \frac{\partial (H_{yx} + H_{yz})}{\partial x} \tag{6.46}$$

$$\epsilon_r \epsilon_0 \frac{\partial E_{zy}}{\partial t} + \sigma_y E_{zy} = -\frac{\partial (H_{xy} + H_{xz})}{\partial y} \tag{6.47}$$

$$\mu_r \mu_0 \frac{\partial H_{xy}}{\partial t} + \sigma_{my} H_{xy} = -\frac{\partial (E_{zx} + E_{zy})}{\partial y} \tag{6.48}$$

$$\mu_r \mu_0 \frac{\partial H_{xz}}{\partial t} + \sigma_{mz} H_{xz} = \frac{\partial (E_{yx} + E_{yz})}{\partial z} \tag{6.49}$$

$$\mu_r \mu_0 \frac{\partial H_{yx}}{\partial t} + \sigma_{mx} H_{yx} = \frac{\partial (E_{zx} + E_{zy})}{\partial x} \tag{6.50}$$

$$\mu_r \mu_0 \frac{\partial H_{yz}}{\partial t} + \sigma_{mz} H_{yz} = -\frac{\partial (E_{xy} + E_{xz})}{\partial z} \tag{6.51}$$

$$\mu_r \mu_0 \frac{\partial H_{zx}}{\partial t} + \sigma_{mx} H_{zx} = -\frac{\partial (E_{yx} + E_{yz})}{\partial x} \tag{6.52}$$

$$\mu_r \mu_0 \frac{\partial H_{zy}}{\partial t} + \sigma_{my} H_{zy} = \frac{\partial (E_{xy} + E_{xz})}{\partial y} \tag{6.53}$$

These twelve equations for a PML medium reduce to Maxwell's equations when $\sigma_x = \sigma_y = \sigma_z$ and $\sigma_{mx} = \sigma_{my} = \sigma_{mz}$.

In selecting the PML layer parameters the same rules are used for three-dimensions as for two-dimensions. The summary of the rule is that: all parameters in the PML layer must be identical to the dielectric layer except for the conductivities in the direction normal to the interface. This same rule still applies to interfaces between two PML layers.

In setting up the PML ABC surrounding a free space region in three-dimensions, the selection of conductivities will be as follows: (1) the faces of the computational domain will have loss only in the direction normal to them, (2) the edges will have loss in the two directions normal to them, and (3) the corners will have loss in all three directions.

The parameters for a PML layer which is adjacent at a constant x plane to a dielectric medium with parameters ϵ_r, μ_r, $\sigma = 0$, and $\sigma_m = 0$, are ϵ_r, μ_r, $\sigma_y = \sigma_z = \sigma_{my} = \sigma_{mz} = 0$, and $\sigma_x/(\epsilon_r \epsilon_0) = \sigma_{mx}/(\mu_r \mu_0) = \sigma_0/(\epsilon_r \epsilon_0) \neq 0$. The difference equations in the PML layer at the $+x$ face of the computational domain are

$$E_{xy}^{n+1}(i + \tfrac{1}{2}, j, k) = E_{xy}^n(i + \tfrac{1}{2}, j, k) + \eta_0 \left[\frac{\Delta\tau}{\epsilon_r \Delta y} \right] \left[H_{zx}^{n+\frac{1}{2}}(i + \tfrac{1}{2}, j + \tfrac{1}{2}, k) \right. \tag{6.54}$$

$$\left. + H_{zy}^{n+\frac{1}{2}}(i + \tfrac{1}{2}, j + \tfrac{1}{2}, k) - H_{zx}^{n+\frac{1}{2}}(i + \tfrac{1}{2}, j - \tfrac{1}{2}, k) - H_{zy}^{n+\frac{1}{2}}(i + \tfrac{1}{2}, j - \tfrac{1}{2}, k) \right]$$

$$E_{xz}^{n+1}(i + \tfrac{1}{2}, j, k) = E_{xz}^n(i + \tfrac{1}{2}, j, k) - \eta_0 \left[\frac{\Delta\tau}{\epsilon_r \Delta z} \right] \left[H_{yx}^{n+\frac{1}{2}}(i + \tfrac{1}{2}, j, k + \tfrac{1}{2}) \right. \tag{6.55}$$

$$\left. + H_{yz}^{n+\frac{1}{2}}(i + \tfrac{1}{2}, j, k + \tfrac{1}{2}) - H_{yx}^{n+\frac{1}{2}}(i + \tfrac{1}{2}, j, k - \tfrac{1}{2}) - H_{yz}^{n+\frac{1}{2}}(i + \tfrac{1}{2}, j, k - \tfrac{1}{2}) \right]$$

$$E_{yx}^{n+1}(i, j + \tfrac{1}{2}, k) = E_{yx}^n(i, j + \tfrac{1}{2}, k) e^{-\sigma_0 \Delta t/\epsilon_r \epsilon_0} + \left(\frac{e^{-\sigma_0 \Delta t/\epsilon_r \epsilon_0} - 1}{\sigma_0 \Delta x} \right) \tag{6.56}$$

$$\times \left[H_{zx}^{n+\frac{1}{2}}(i+\tfrac{1}{2},j+\tfrac{1}{2},k) + H_{zy}^{n+\frac{1}{2}}(i+\tfrac{1}{2},j+\tfrac{1}{2},k) \right.$$

$$\left. -H_{zx}^{n+\frac{1}{2}}(i-\tfrac{1}{2},j+\tfrac{1}{2},k) - H_{zy}^{n+\frac{1}{2}}(i-\tfrac{1}{2},j+\tfrac{1}{2},k) \right]$$

$$E_{yz}^{n+1}(i,j+\tfrac{1}{2},k) = E_{yz}^{n}(i,j+\tfrac{1}{2},k) + \eta_0 \left[\frac{\Delta\tau}{\epsilon_r \Delta z} \right] \left[H_{xy}^{n+\frac{1}{2}}(i,j+\tfrac{1}{2},k+\tfrac{1}{2}) \right. \tag{6.57}$$

$$\left. +H_{xz}^{n+\frac{1}{2}}(i,j+\tfrac{1}{2},k+\tfrac{1}{2}) - H_{xy}^{n+\frac{1}{2}}(i,j+\tfrac{1}{2},k-\tfrac{1}{2}) - H_{xz}^{n+\frac{1}{2}}(i,j+\tfrac{1}{2},k-\tfrac{1}{2}) \right]$$

$$E_{zx}^{n+1}(i,j,k+\tfrac{1}{2}) = E_{zx}^{n}(i,j,k+\tfrac{1}{2})e^{-\sigma_0\Delta t/\epsilon_r\epsilon_0} - \left(\frac{e^{-\sigma_0\Delta t/\epsilon_r\epsilon_0}-1}{\sigma_0\Delta x} \right) \tag{6.58}$$

$$\times \left[H_{yx}^{n+\frac{1}{2}}(i+\tfrac{1}{2},j,k+\tfrac{1}{2}) + H_{yz}^{n+\frac{1}{2}}(i+\tfrac{1}{2},j,k+\tfrac{1}{2}) \right.$$

$$\left. -H_{yx}^{n+\frac{1}{2}}(i-\tfrac{1}{2},j,k+\tfrac{1}{2}) - H_{yz}^{n+\frac{1}{2}}(i-\tfrac{1}{2},j,k+\tfrac{1}{2}) \right]$$

$$E_{zy}^{n+1}(i,j,k+\tfrac{1}{2}) = E_{zy}^{n}(i,j,k+\tfrac{1}{2}) - \eta_0 \left[\frac{\Delta\tau}{\epsilon_r \Delta y} \right] \left[H_{xy}^{n+\frac{1}{2}}(i,j+\tfrac{1}{2},k+\tfrac{1}{2}) \right. \tag{6.59}$$

$$\left. +H_{xz}^{n+\frac{1}{2}}(i,j+\tfrac{1}{2},k+\tfrac{1}{2}) - H_{xy}^{n+\frac{1}{2}}(i,j-\tfrac{1}{2},k+\tfrac{1}{2}) - H_{xz}^{n+\frac{1}{2}}(i,j-\tfrac{1}{2},k+\tfrac{1}{2}) \right]$$

$$H_{xy}^{n+\frac{1}{2}}(i,j+\tfrac{1}{2},k+\tfrac{1}{2}) = H_{xy}^{n-\frac{1}{2}}(i,j+\tfrac{1}{2},k+\tfrac{1}{2}) - \frac{1}{\eta_0} \left[\frac{\Delta\tau}{\mu_r \Delta y} \right] \tag{6.60}$$

$$\times \left[E_{zx}^{n}(i,j+1,k+\tfrac{1}{2}) + E_{zy}^{n}(i,j+1,k+\tfrac{1}{2}) - E_{zx}^{n}(i,j,k+\tfrac{1}{2}) - E_{zy}^{n}(i,j,k+\tfrac{1}{2}) \right]$$

$$H_{xz}^{n+\frac{1}{2}}(i,j+\tfrac{1}{2},k+\tfrac{1}{2}) = H_{xz}^{n-\frac{1}{2}}(i,j+\tfrac{1}{2},k+\tfrac{1}{2}) + \frac{1}{\eta_0} \left[\frac{\Delta\tau}{\mu_r \Delta z} \right] \tag{6.61}$$

$$\times \left[E_{yx}^{n}(i,j+\tfrac{1}{2},k+1) + E_{yz}^{n}(i,j+\tfrac{1}{2},k+1) - E_{yx}^{n}(i,j+\tfrac{1}{2},k) - E_{yz}^{n}(i,j+\tfrac{1}{2},k) \right]$$

$$H_{yx}^{n+\frac{1}{2}}(i+\tfrac{1}{2},j,k+\tfrac{1}{2}) = H_{yx}^{n-\frac{1}{2}}(i+\tfrac{1}{2},j,k+\tfrac{1}{2})e^{-\sigma_0\Delta t/\epsilon_r\epsilon_0} - \left[\frac{\epsilon_0\epsilon_r(e^{-\sigma_0\Delta t/\epsilon_r\epsilon_0}-1)}{\sigma_0\mu_r\mu_0\Delta x} \right]$$

$$\times \left[E_{zx}^{n}(i+1,j,k+\tfrac{1}{2}) + E_{zy}^{n}(i+1,j,k+\tfrac{1}{2}) \right. \tag{6.62}$$

$$\left. -E_{zx}^{n}(i,j,k+\tfrac{1}{2}) - E_{zy}^{n}(i,j,k+\tfrac{1}{2}) \right]$$

$$H_{yz}^{n+\frac{1}{2}}(i+\tfrac{1}{2},j,k+\tfrac{1}{2}) = H_{yz}^{n-\frac{1}{2}}(i+\tfrac{1}{2},j,k+\tfrac{1}{2}) - \frac{1}{\eta_0}\left[\frac{\Delta\tau}{\mu_r\Delta z}\right] \quad (6.63)$$

$$\times \left[E_{xy}^n(i+\tfrac{1}{2},j,k+1) + E_{xz}^n(i+\tfrac{1}{2},j,k+1) - E_{xy}^n(i+\tfrac{1}{2},j,k) - E_{xz}^n(i+\tfrac{1}{2},j,k)\right]$$

$$H_{zx}^{n+\frac{1}{2}}(i+\tfrac{1}{2},j+\tfrac{1}{2},k) = H_{zx}^{n-\frac{1}{2}}(i+\tfrac{1}{2},j+\tfrac{1}{2},k)e^{-\sigma_0\Delta t/\epsilon_r\epsilon_0} + \left[\frac{\epsilon_0\epsilon_r\left(e^{-\sigma_0\Delta t/\epsilon_r\epsilon_0}-1\right)}{\sigma_0\mu_r\mu_0\Delta x}\right]$$

$$\times \left[E_{yx}^n(i+1,j+\tfrac{1}{2},k) + E_{yz}^n(i+1,j+\tfrac{1}{2},k)\right. \quad (6.64)$$

$$\left. - E_{yx}^n(i,j+\tfrac{1}{2},k) - E_{yz}^n(i,j+\tfrac{1}{2},k)\right]$$

$$H_{zy}^{n+\frac{1}{2}}(i+\tfrac{1}{2},j+\tfrac{1}{2},k) = H_{zy}^{n-\frac{1}{2}}(i+\tfrac{1}{2},j+\tfrac{1}{2},k) + \frac{1}{\eta_0}\left[\frac{\Delta\tau}{2\mu_r\Delta y}\right] \quad (6.65)$$

$$\times \left[E_{xy}^n(i+\tfrac{1}{2},j+1,k) + E_{xz}^n(i+\tfrac{1}{2},j+1,k) - E_{xy}^n(i+\tfrac{1}{2},j,k) - E_{xz}^n(i+\tfrac{1}{2},j,k)\right]$$

Note that these equations for the split field quantities can be used for non-PML media, and the standard field quantities can be obtained simply by adding the split quantities.

6.2.3 Radiation Pattern over a Multi-Layer Media

In order to calculate the far-field radiation pattern, it is necessary to use a multi-layer Green's function [106],[153]. For this configuration, there are three layers with the top layer being free space, the middle layer being a dielectric with ϵ_r, and the lower layer being a perfect conductor as shown in Figure 6.4. The source is located in the upper two layers and the far-field electric fields are only calculated in the free space region. The mathematical formulation of Huygens' principle for this configuration,
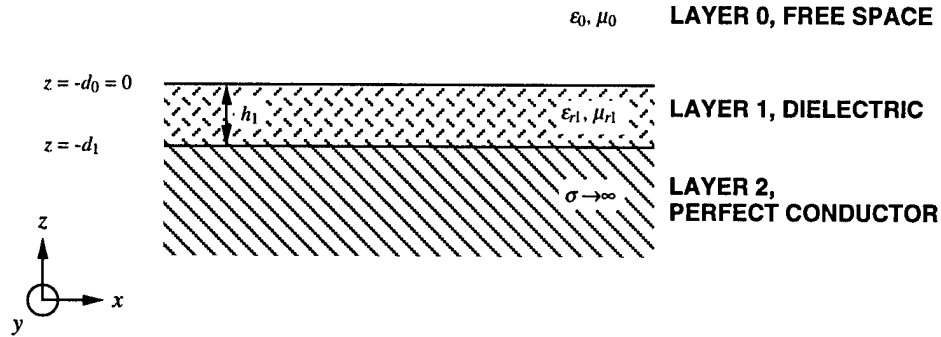
Figure 6.4: Three layer configuration. A dielectric substrate on a perfect conductor.

assuming a $e^{-i\omega t}$ time dependence, for the electric field, is

$$\overline{E}^{ff}(\overline{r}) = \int\int_{S_1'} \left\{ i\omega\mu_0 \overline{\overline{G}}_{00}^{hff}(\overline{r},\overline{r}') \cdot \hat{n} \times \overline{H}(\overline{r}') + \nabla \times \overline{\overline{G}}_{00}^{eff}(\overline{r},\overline{r}') \cdot \hat{n} \times \overline{E}(\overline{r}') \right\}$$

$$+ \int\int_{S_2'} \left\{ i\omega\mu_0 \overline{\overline{G}}_{01}^{hff}(\overline{r},\overline{r}') \cdot \hat{n} \times \overline{H}(\overline{r}') + \nabla \times \overline{\overline{G}}_{01}^{eff}(\overline{r},\overline{r}') \cdot \hat{n} \times \overline{E}(\overline{r}') \right\}$$

$$(6.66)$$

where $S_1' + S_2'$ form a closed surface with the ground plane, S_1' is the portion in the free space region, and S_2' is the portion in the dielectric layer. The subscripts to the Green's function, G_{ab}, are a for the observation layer, and b for the source layer. The superscripts, eff and mff, to the Green's function indicate that the Green's function is only valid in the far-field and that it is applied to the electric field and the magnetic field respectively. $\overline{r}$ is the far-field observation location and $\overline{r}'$ is the source location. Note that the observation location is always higher in z than the source location.

The Green's function, $\overline{\overline{G}}_{00}^{mff}$, in the spectral domain, is

$$
\begin{aligned}
\overline{\overline{G}}_{00}^{mff}(\overline{r}_>, \overline{r}'_<) &= \frac{i}{8\pi^2} \int_{-\infty}^{\infty} dk_x \int_{-\infty}^{\infty} dk_y e^{ik_x(x-x')} e^{ik_y(y-y')} \frac{1}{k_{0z}} \\
&\quad \left\{ \left[\hat{h}(k_{0z})\hat{h}(k_{0z}) e^{ik_{0z}(z-z')} + R_{\cap 0}^{\mathrm{TE}} \hat{h}(k_{0z})\hat{h}(-k_{0z}) e^{ik_{0z}(z+z')} \right] \right. \quad (6.67) \\
&\quad \left. + \left[\hat{v}(k_{0z})\hat{v}(k_{0z}) e^{ik_{0z}(z-z')} + R_{\cap 0}^{\mathrm{TM}} \hat{v}(k_{0z})\hat{v}(-k_{0z}) e^{ik_{0z}(z+z')} \right] \right\}
\end{aligned}
$$

where the wavenumbers are defined as

$$
k_j = \omega\sqrt{\epsilon_j \mu_j} \tag{6.68}
$$

and j is the number of the layer, where 0 is the free space region, 1 is the dielectric region, and 2 is the perfect conductor.

$$
\overline{k}_j = \hat{x}k_x + \hat{y}k_y + \hat{z}k_{jz} \tag{6.69}
$$

$$
k_{jz} = \sqrt{k_j^2 - k_x^2 - k_y^2} \tag{6.70}
$$

$$
\overline{\rho} = \hat{x}x + \hat{y}y \tag{6.71}
$$

$$
\overline{k}_\rho = \hat{x}k_x + \hat{y}k_y \tag{6.72}
$$

The horizontal and vertical unit vectors are defined as

$$\hat{h}(k_{jz}) = \frac{\overline{k}_j \times \hat{z}}{\left|\overline{k}_j \times \hat{z}\right|} = \frac{1}{k_\rho}(\hat{x}k_y - \hat{y}k_x) \tag{6.73}$$

$$\hat{v}(k_{jz}) = \hat{h}(k_{jz}) \times \hat{k}_j = \frac{-k_{jz}(\hat{x}k_x + \hat{y}k_y)}{k_j k_\rho} + \hat{z}\frac{k_\rho}{k_j} \tag{6.74}$$

$$\hat{h}(-k_{jz}) = \hat{h}(k_{jz}) \tag{6.75}$$

$$\hat{v}(-k_{jz}) = \frac{k_{jz}(\hat{x}k_x + \hat{y}k_y)}{k_j k_\rho} + \hat{z}\frac{k_\rho}{k_j} \tag{6.76}$$

The reflection coefficient looking down from layer ℓ is

$$R^s_{\cap\ell} = \frac{R^s_{\ell(\ell+1)} + R^s_{\cap(\ell+1)}e^{2ik_{(\ell+1)z}h_{(\ell+1)}}}{1 + R^s_{\cap(\ell+1)}R^2_{\ell(\ell+1)}e^{2ik_{(\ell+1)z}h_{(\ell+1)}}} \tag{6.77}$$

The reflection coefficient looking up from layer ℓ is

$$R^s_{\cup\ell} = \frac{R^s_{\ell(\ell-1)} + R^s_{\cup(\ell-1)}e^{2ik_{(\ell-1)z}h_{(\ell-1)}}}{1 + R^s_{\cup(\ell-1)}R^2_{\ell(\ell-1)}e^{2ik_{(\ell-1)z}h_{(\ell-1)}}} \tag{6.78}$$

where s represents either the TE or TM polarization. The reflection coefficients looking from layer i to layer j are

$$R^{\text{TE}}_{ij} = \frac{\mu_j k_{iz} - \mu_i k_{jz}}{\mu_j k_{iz} + \mu_i k_{jz}} \tag{6.79}$$

$$R_{ij}^{\mathrm{TM}} = \frac{\epsilon_j k_{iz} - \epsilon_i k_{jz}}{\epsilon_j k_{iz} + \epsilon_i k_{jz}} \tag{6.80}$$

$$z = r \cos \theta \tag{6.81}$$

$$\rho = r \sin \theta \tag{6.82}$$

$$x = \rho \cos \phi \tag{6.83}$$

$$y = \rho \sin \phi \tag{6.84}$$

$$k_{0z} = \sqrt{k_0^2 - k_x^2 - k_y^2} = k_0 \cos \gamma \tag{6.85}$$

$$k_\rho = \sqrt{k_0^2 - k_{0z}^2} = k_0 \sin \gamma \tag{6.86}$$

$$k_x = k_\rho \cos \delta \tag{6.87}$$

$$k_y = k_\rho \sin \delta \tag{6.88}$$

Changing the integrals of Equation 6.67 into cylindrical coordinates gives

$$
\overline{\overline{G}}_{00}^{mff}(\overline{r}_>, \overline{r}'_<) = \frac{i}{8\pi^2} \int_0^\infty dk_\rho k_\rho \int_0^{2\pi} d\delta e^{ik_\rho\rho[\cos\delta\cos\phi+\sin\delta\sin\phi]} e^{i\sqrt{k_0^2-k_\rho^2}z} e^{-i\overline{k}_\rho\cdot\overline{\rho}'} \frac{1}{k_{0z}}
$$

$$
\left\{ \left[\hat{h}(k_{0z})\hat{h}(k_{0z})e^{-ik_{0z}z'} + R_{\cap 0}^{\mathrm{TE}}\hat{h}(k_{0z})\hat{h}(-k_{0z})e^{ik_{0z}z'} \right] \right. \qquad (6.89)
$$

$$
\left. + \left[\hat{v}(k_{0z})\hat{v}(k_{0z})e^{-ik_{0z}z'} + R_{\cap 0}^{\mathrm{TM}}\hat{v}(k_{0z})\hat{v}(-k_{0z})e^{ik_{0z}z'} \right] \right\}
$$

Approximating the above $d\delta$ integral using the stationary phase approximation at $\delta = \phi$ results in

$$
\overline{\overline{G}}_{00}^{mff}(\overline{r}_>, \overline{r}'_<) = \frac{i}{8\pi^2} \int_0^\infty dk_\rho e^{ik_\rho\rho} e^{-i\pi/4} \sqrt{\frac{2\pi}{k_\rho\rho}} e^{i\sqrt{k_0^2-k_\rho^2}z} e^{-i\overline{k}_\rho\cdot\overline{\rho}'} \frac{k_\rho}{k_{0z}} \qquad (6.90)
$$

$$
\left\{ \left[\hat{h}(k_{0z})\hat{h}(k_{0z})e^{-ik_{0z}z'} + R_{\cap 0}^{\mathrm{TE}}\hat{h}(k_{0z})\hat{h}(-k_{0z})e^{ik_{0z}z'} \right] \right.
$$

$$
\left. + \left[\hat{v}(k_{0z})\hat{v}(k_{0z})e^{-ik_{0z}z'} + R_{\cap 0}^{\mathrm{TM}}\hat{v}(k_{0z})\hat{v}(-k_{0z})e^{ik_{0z}z'} \right] \right\}_{\delta=\phi}
$$

Approximating the above dk_ρ integral using the stationary phase approximation at $k\rho = k_0 \sin\theta$ results in

$$
\overline{\overline{G}}_{00}^{mff}(\overline{r}_>, \overline{r}'_<) = \frac{i}{8\pi^2} e^{ik_\rho\rho} e^{-i\pi/2} \sqrt{\frac{2\pi}{k_\rho\rho}} \sqrt{\frac{2\pi \sin\theta \cos^2\theta}{\rho}} e^{-i\overline{k}_\rho\cdot\overline{\rho}'} \frac{k_\rho}{k_{0z}} \qquad (6.91)
$$

$$
\left\{ \left[\hat{h}(k_{0z})\hat{h}(k_{0z})e^{-ik_{0z}z'} + R_{\cap 0}^{\mathrm{TE}}\hat{h}(k_{0z})\hat{h}(-k_{0z})e^{ik_{0z}z'} \right] \right.
$$

$$
\left. + \left[\hat{v}(k_{0z})\hat{v}(k_{0z})e^{-ik_{0z}z'} + R_{\cap 0}^{\mathrm{TM}}\hat{v}(k_{0z})\hat{v}(-k_{0z})e^{ik_{0z}z'} \right] \right\}_{\delta=\phi,k_\rho=k_0\sin\theta}
$$

And simplifying, results in

$$\overline{\overline{G}}_{00}^{mff}(\vec{r}_>, \vec{r}'_<) = \frac{e^{ik_0 r}}{4\pi r} e^{-i\vec{k}_\rho \cdot \vec{\rho}'} \tag{6.92}$$

$$\left\{ \left[\hat{h}(k_{0z})\hat{h}(k_{0z})e^{-ik_{0z}z'} + R_{\cap 0}^{\text{TE}}\hat{h}(k_{0z})\hat{h}(-k_{0z})e^{ik_{0z}z'} \right] \right.$$

$$\left. + \left[\hat{v}(k_{0z})\hat{v}(k_{0z})e^{-ik_{0z}z'} + R_{\cap 0}^{\text{TM}}\hat{v}(k_{0z})\hat{v}(-k_{0z})e^{ik_{0z}z'} \right] \right\}_{\delta=\phi, k_\rho=k_0 \sin\theta}$$

With the far-field approximations, the solution is only valid for observations points in the far-field in layer 0 and not in the near-field of layer 1. The associated Green's function for a source in layer 1 and a far-field observation point in layer 0 is

$$\overline{\overline{G}}_{01}^{mff}(\vec{r}_>, \vec{r}'_<) = \frac{e^{ik_0 r}}{4\pi r} e^{-i\vec{k}_\rho \cdot \vec{\rho}'} \frac{k_{0z}}{k_{mz}} \tag{6.93}$$

$$\left\{ \frac{X_{\text{U}1\to0}^{\text{TE}}}{1 - R_{\text{U}1}^{\text{TE}} R_{\cap 1}^{\text{TE}} e^{2ik_{1z}h_1}} \left[\hat{h}(k_{0z})\hat{h}(k_{0z})e^{-ik_{0z}z'} + R_{\cap 1}^{\text{TE}} e^{2ik_{1z}h_1}\hat{h}(k_{0z})\hat{h}(-k_{0z})e^{ik_{0z}z'} \right] \right.$$

$$\left. + \frac{X_{\text{U}1\to0}^{\text{TM}}}{1 - R_{\text{U}1}^{\text{TM}} R_{\cap 1}^{\text{TM}} e^{2ik_{1z}h_1}} \left[\hat{v}(k_{0z})\hat{v}(k_{0z})e^{-ik_{0z}z'} + R_{\cap 1}^{\text{TM}} e^{2ik_{1z}h_1}\hat{v}(k_{0z})\hat{v}(-k_{0z})e^{ik_{0z}z'} \right] \right\}$$

where the upward transmission coefficients from layer m to layer ℓ with $m > \ell$ are defined as

$$X_{\text{U}m\to\ell}^{\text{TE}} = X_{\text{U}m\to\ell+1}^{\text{TE}} e^{ik_{(\ell+1)z}h_{(\ell+1)}} \frac{\left(1 + R_{\text{U}(\ell+1)}^{\text{TE}}\right)}{\left(1 + R_{\text{U}\ell}^{\text{TE}} e^{2ik_{\ell z}h_\ell}\right)} \tag{6.94}$$

$$X_{\text{U}m\to\ell}^{\text{TM}} = \frac{k_\ell}{k_{\ell z}} \frac{k_{(\ell+1)z}}{k_{(\ell+1)}} X_{\text{U}m\to\ell+1}^{\text{TM}} e^{ik_{(\ell+1)z}h_{(\ell+1)}} \frac{\left(1 - R_{\text{U}(\ell+1)}^{\text{TM}}\right)}{\left(1 - R_{\text{U}\ell}^{\text{TM}} e^{2ik_{\ell z}h_\ell}\right)} \tag{6.95}$$

The upward transmission coefficients for adjacent layers are defined as

$$X^{\text{TE}}_{\cup m \to m-1} = \frac{\left(1 + R^{\text{TE}}_{\cup m}\right)}{\left(1 + R^{\text{TE}}_{\cup(m-1)} e^{2ik_{(m-1)z}h_{(m-1)}}\right)} \tag{6.96}$$

$$X^{\text{TM}}_{\cup m \to m-1} = \frac{k_{m-1}}{k_{(m-1)z}} \frac{k_{mz}}{k_m} \frac{\left(1 - R^{\text{TM}}_{\cup m}\right)}{\left(1 - R^{\text{TM}}_{\cup(m-1)} e^{2ik_{(m-1)z}h_{(m-1)}}\right)} \tag{6.97}$$

The Green's function applied to the electric field is identical to the one for the magnetic field, except that the horizontal direction is now associated with the TM polarization and the vertical direction with the TE polarization.

$$\overline{\overline{G}}^{eff}_{00}\left(\vec{r}_>, \vec{r}'_<\right) = \frac{e^{ik_0 r}}{4\pi r} e^{-i\bar{k}_\rho \cdot \vec{\rho}'} \tag{6.98}$$

$$\left\{ \left[\hat{h}(k_{0z})\hat{h}(k_{0z})e^{-ik_{0z}z'} + R^{\text{TE}}_{\cap 0}\hat{h}(k_{0z})\hat{h}(-k_{0z})e^{ik_{0z}z'} \right] \right.$$

$$\left. + \left[\hat{v}(k_{0z})\hat{v}(k_{0z})e^{-ik_{0z}z'} + R^{\text{TM}}_{\cap 0}\hat{v}(k_{0z})\hat{v}(-k_{0z})e^{ik_{0z}z'} \right] \right\}$$

The associated Green's function for a source in layer 1 and a far-field observation point in layer 0 is

$$\overline{\overline{G}}^{eff}_{01}\left(\vec{r}_>, \vec{r}'_<\right) = \frac{e^{ik_0 r}}{4\pi r} e^{-i\bar{k}_\rho \cdot \vec{\rho}'} \frac{k_{0z}}{k_{mz}} \tag{6.99}$$

$$\left\{ \frac{X^{\text{TM}}_{\cup 1 \to 0}}{1 - R^{\text{TM}}_{\cup 1} R^{\text{TM}}_{\cap 1} e^{2ik_{1z}h_1}} \left[\hat{h}(k_{0z})\hat{h}(k_{0z})e^{-ik_{0z}z'} + R^{\text{TM}}_{\cap 1} e^{2ik_{1z}h_1}\hat{h}(k_{0z})\hat{h}(-k_{0z})e^{ik_{0z}z'} \right] \right.$$

$$\left. + \frac{X^{\text{TE}}_{\cup 1 \to 0}}{1 - R^{\text{TE}}_{\cup 1} R^{\text{TE}}_{\cap 1} e^{2ik_{1z}h_1}} \left[\hat{v}(k_{0z})\hat{v}(k_{0z})e^{-ik_{0z}z'} + R^{\text{TE}}_{\cap 1} e^{2ik_{1z}h_1}\hat{v}(k_{0z})\hat{v}(-k_{0z})e^{ik_{0z}z'} \right] \right\}$$

6.3 Results and Discussion

In performing the FD-TD simulations on the microstrip antenna and the vertical and horizontal dipole configurations, the grid cell which was used had dimensions of $\Delta x = \Delta y = 1.25$ cm, and $\Delta z = 1.2$ cm. The PML ABC boundary condition was chosen to be 6 cells thick in all directions, a quadratic grading of the conductivity was used, and a reflection coefficient of 10^{-5} was chosen for the PML ABC at normal incidence.

Before examining a microstrip patch antenna configuration, two simple dipole cases are examined. The first is a vertical dipole configuration in a non-uniform substrate as shown in Figure 6.5 which is compared with an identical vertical dipole in a uniform substrate.

Three vertical dipole configurations are examined, and all three have the same dipole height and substrate characteristics. One configuration is for a uniform substrate and the other two are for non-uniform substrates. h is the thickness of the substrate and the height of the vertical dipole.

$$h = 4.8 \text{ cm} \qquad (6.100)$$

The dielectric constant of the substrate is

$$\epsilon_r = 12.8 \qquad (6.101)$$

Both non-uniform substrate configurations have the vertical dipole located at

TOP VIEW

SIDE VIEW
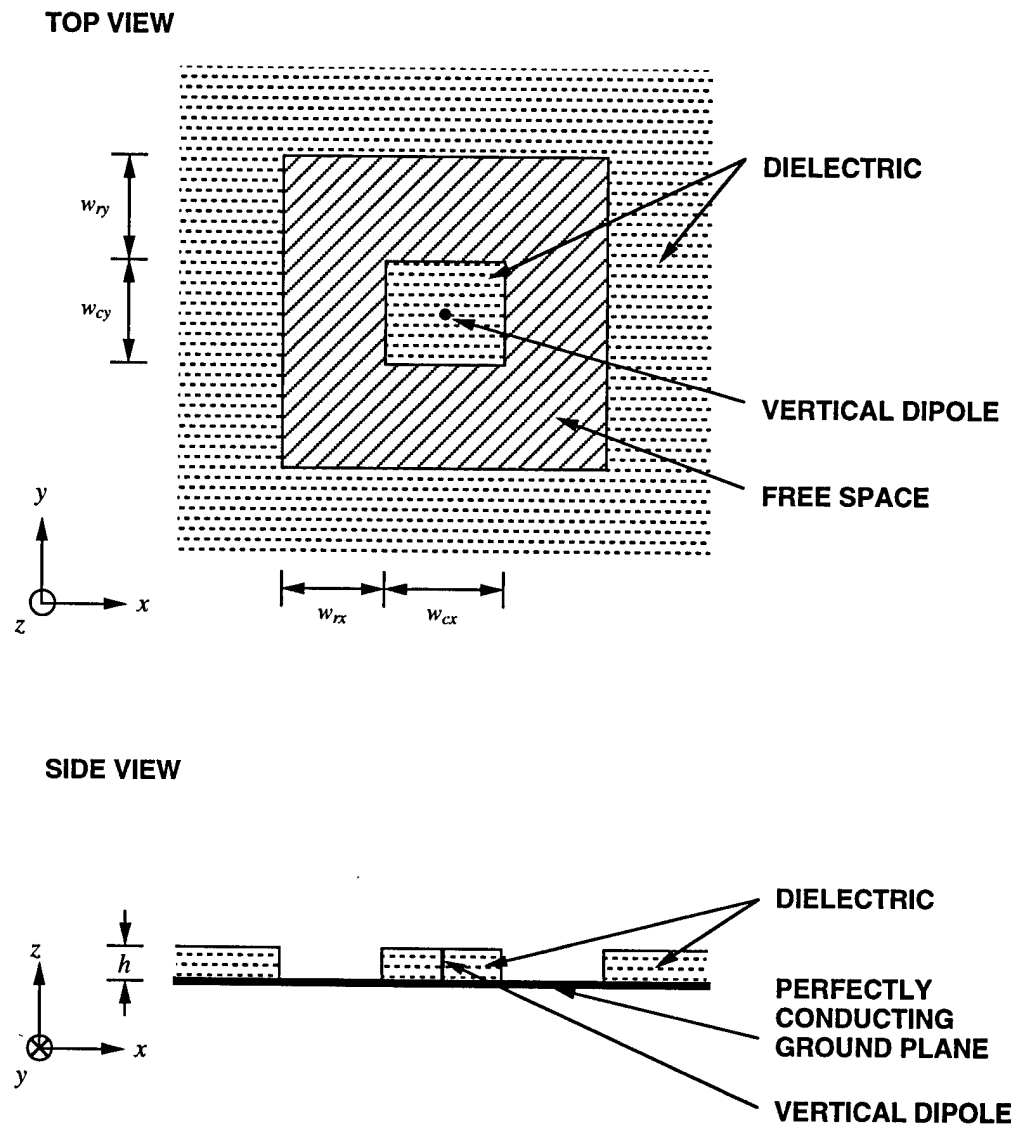
Figure 6.5: Vertical dipole in a non-uniform dielectric substrate.

the center of the center block of dielectric substrate. w_{cx1}, w_{cy1}, w_{cx2} and w_{cy2} are the dimensions of the center block of dielectric substrate for the first and second non-uniform substrate configurations.

$$w_{cx1} = w_{cy1} = 10 \text{ cm} \tag{6.102}$$

$$w_{cx2} = w_{cy2} = 7.5 \text{ cm} \tag{6.103}$$

w_{rx1}, w_{ry1}, w_{rx2} and w_{ry2} are the widths of the free space ring surrounding the center block of dielectric for both configurations.

$$w_{rx1} = w_{ry1} = 17.5 \text{ cm} \tag{6.104}$$

$$w_{rx2} = w_{ry2} = 11.25 \text{ cm} \tag{6.105}$$

These widths were chosen to be between a quarter and half a wavelength in size in order to allow the power to radiate into the free space region.

The surfaces waves are guided modes and have cut-off frequencies of

$$f_{cn} = \frac{nc_0}{4h\sqrt{\epsilon_r\mu_r - 1}} \tag{6.106}$$

where $n = 0, 1, 2, 3, ...$, with n even for TM modes and n odd for TE modes [106],[140]. c_0 is the speed of light, h is the substrate height, ϵ_r the relative permittivity and μ_r the relative permeability of the substrate. So the TM$_0$ mode will always be present

since it is never cut-off, and for this case, the cut-off frequency for the TE_1 mode is 455 MHz, and for the TM_2 mode is 910 MHz.

Figure 6.6 shows the radiation impedance of all three of the vertical dipole configurations. The peaks in the radiation impedance occur at 940 MHz for the uniform substrate case, at 835 MHz for the first non-uniform substrate case, and at 935 MHz for the second non-uniform substrate case. It is noted that 2 guided wave modes can propagate in the first non-uniform substrate case and 3 guided modes can propagate in the other two cases. It is observed from this that the resonant frequency can be shifted by using different size free space rings surrounding the antenna. These resonances correspond to the full wavelength resonance of a dipole, or a half-wavelength resonance of a monopole over a ground plane. The corresponding bandwidths are 260 MHz, 90 MHz, and 95 MHz for the uniform, first and second non-uniform substrate cases. The addition of the non-uniformity has significantly increased the configuration's Q which results in much lower bandwidths.

The approximate percentage of power guided by these configurations are shown in Figure 6.7. The surface on which the Poynting power is integrated, is always chosen to enclose the antenna and the free space ring. The surface is approximately 2-4 cells larger in the x and y directions than the free space ring for all the cases considered. The approximate percentages of power guided by these three configurations over the frequency range surrounding their resonant frequencies are 98% for the uniform substrate case, 22% for the first non-uniform substrate case, and 30% for the second non-uniform substrate case. The reduction with both non-uniform cases is significant compared to the uniform case over the frequency range around the resonant frequency.

Figure 6.6: Radiation impedance of a vertical dipole in a uniform and two non-uniform substrate configurations.
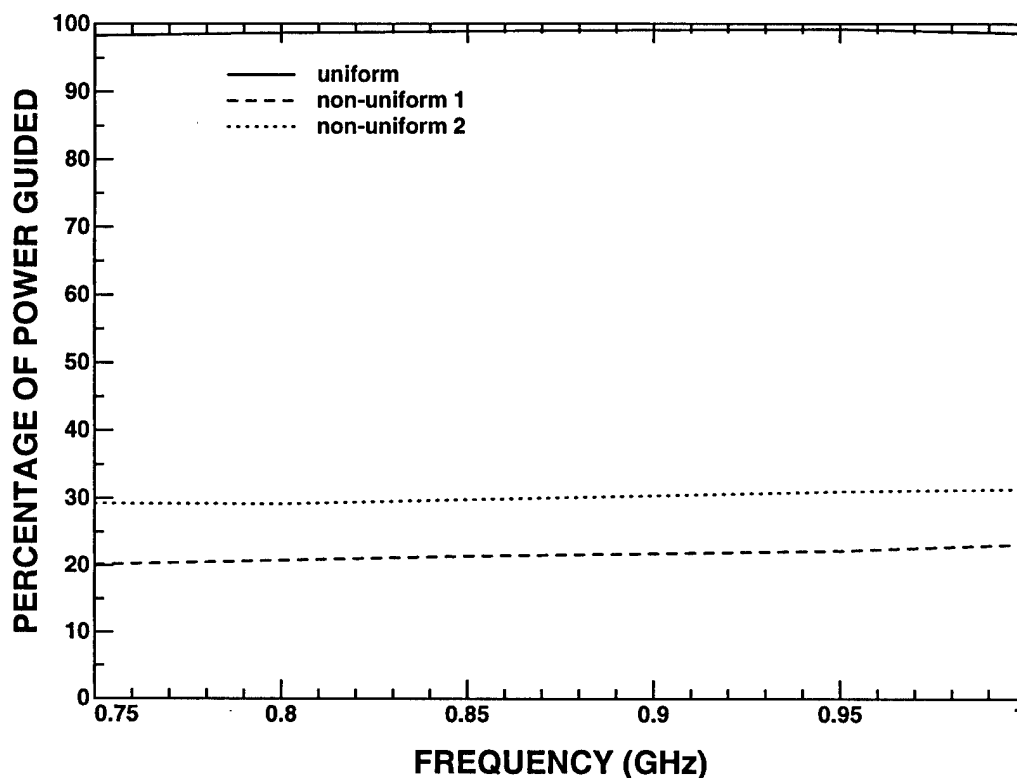
Figure 6.7: Guided power of a vertical dipole in a uniform and two non-uniform substrate configurations.

The gain patterns for the three configurations at their respective resonant frequencies in the x-z plane are shown in Figure 6.8. Only the vertical polarization is plotted since the gain for the horizontal polarization is negligible. There is a difference in the overall levels of the three gain patterns since significantly different amounts of power are trapped in the guided wave modes for each case. The highest gain pattern is for the first non-uniform case which has the lowest amount of guided waves and the lowest gain pattern is for the uniform case which has almost all of its power trapped in the substrate.
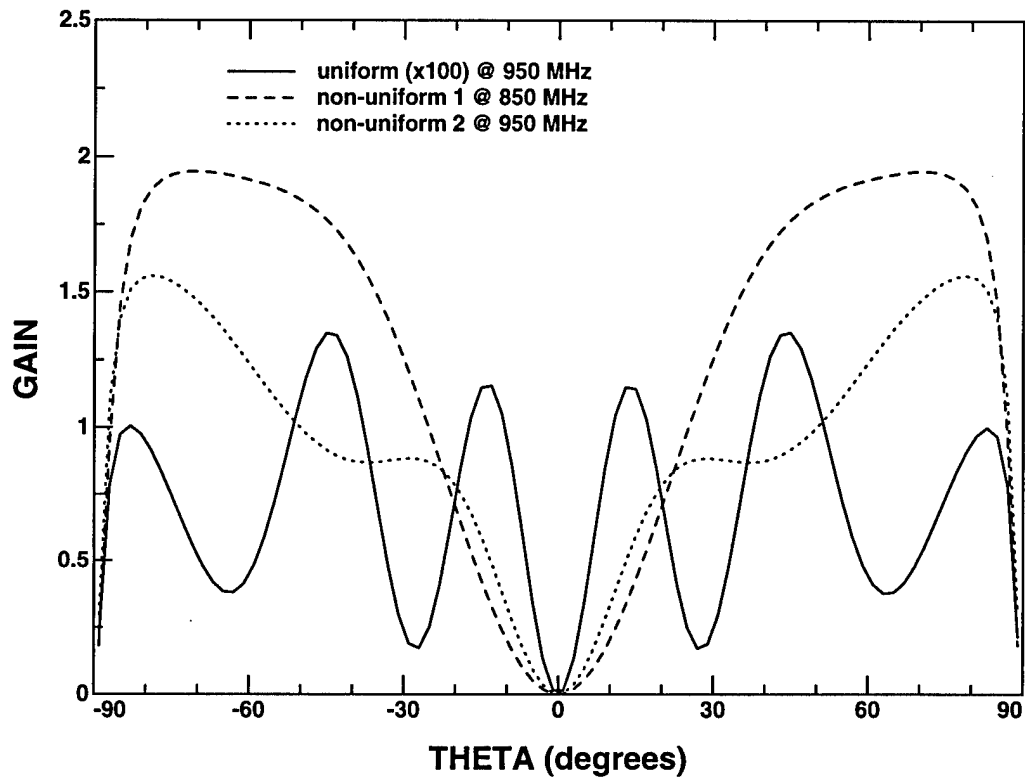
Figure 6.8: Gain pattern for a vertical dipole in a uniform and two non-uniform substrate configurations in the x-z plane for the vertical polarization.

The second dipole case examined is a horizontal dipole on a non-uniform substrate and is shown in Figure 6.9. The dimensions of this configuration are as follows: h is the thickness of the substrate.

$$h = 4.8 \text{ cm} \tag{6.107}$$

The dielectric constant of the substrate is

$$\epsilon_r = 12.8 \tag{6.108}$$

The horizontal dipole lies on top of the substrate and is centered in the dielectric box. w_{hd} is the width of the dipole.

$$w_{hd} = 15 \text{ cm} \tag{6.109}$$

w_{cx} and w_{cy} are the dimensions of the center block of dielectric substrate.

$$w_{cx} = 25 \text{ cm} \tag{6.110}$$

$$w_{cy} = 10 \text{ cm} \tag{6.111}$$

w_{rx} and w_{ry} are the widths of the free space ring surrounding the center block of

TOP VIEW

SIDE VIEW
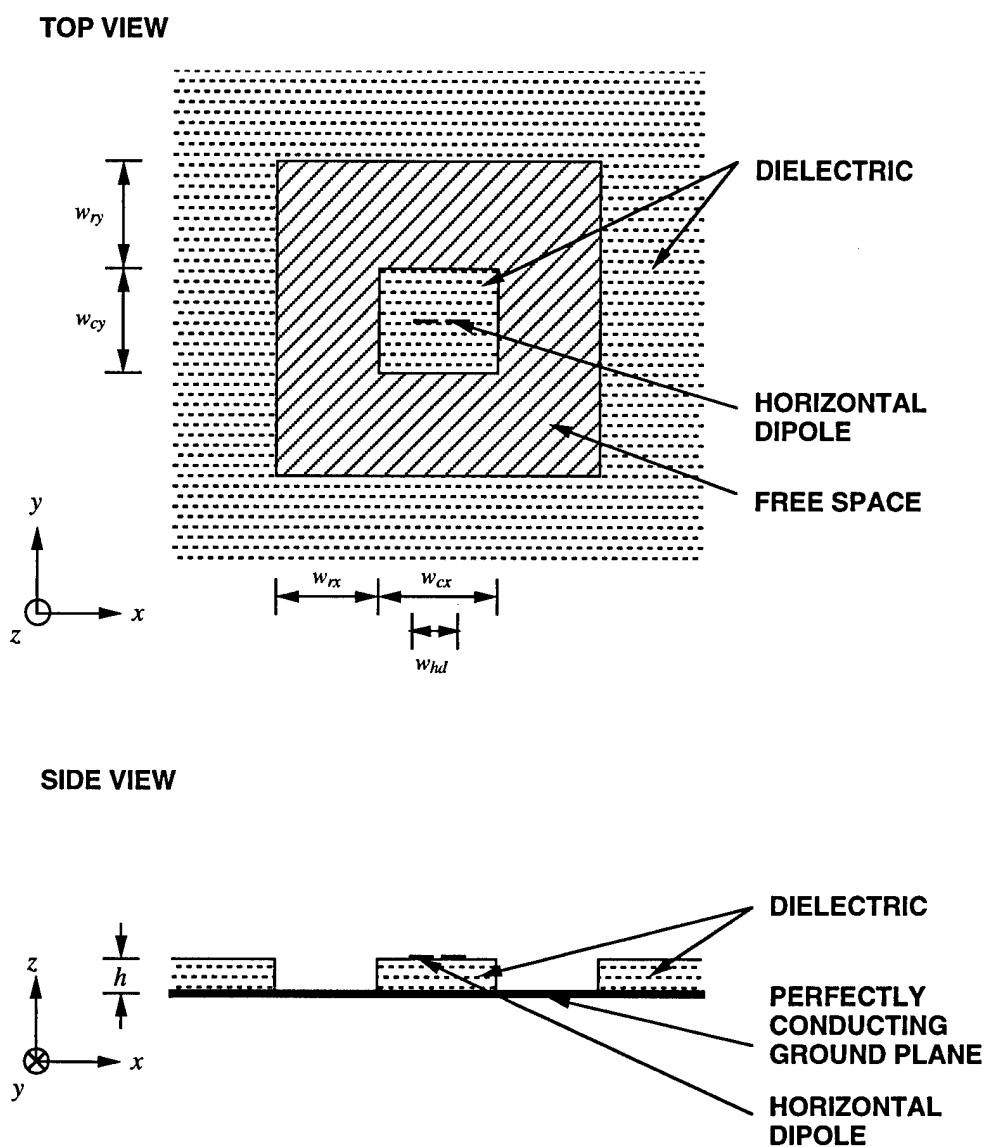
Figure 6.9: Horizontal dipole on a non-uniform dielectric substrate.

dielectric.

$$w_{rx} = w_{ry} = 15 \text{ cm} \tag{6.112}$$

Figure 6.10 shows the radiation impedance of the horizontal dipole over uniform and non-uniform substrates. For the uniform substrate case, the first peak in radiation impedance occurs at 437 MHz, while for the non-uniform substrate the first peak is at 447 MHz. These resonances correspond to a full wavelength resonance. The bandwidth of the uniform case is 198 MHz and the bandwidth for the non-uniform case is 25 MHz. Again the addition of the non-uniformity is observed to significantly reduce the antenna's bandwidth.

The approximate percentages of power guided by these configurations are shown in Figure 6.11. The approximate percentages of power guided by these configurations at their resonant frequencies are 41% for the uniform substrate case, and 15% for the non-uniform substrate case. The reduction with the non-uniform case is significant compared to the uniform case over the frequency range around their resonant frequencies.
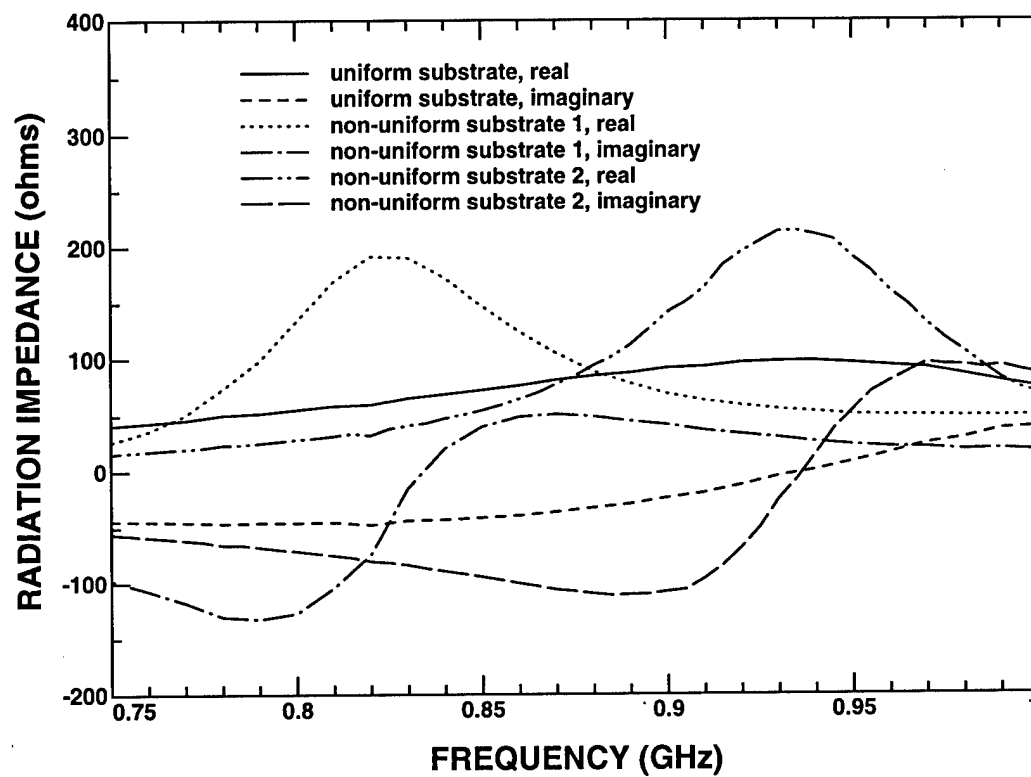
The gain patterns for the horizontal dipole configurations at their respective resonant frequencies in the x-z plane are shown in Figure 6.12 and the gain patterns in the y-z plane are shown in Figure 6.13. Only the vertical polarization is plotted in the x-z plane since the horizontal polarization is negligible, and only the horizontal polarization is plotted in the y-z plane since the vertical polarization is negligible. The gain for the non-uniform substrate case is about twice the uniform substrate case
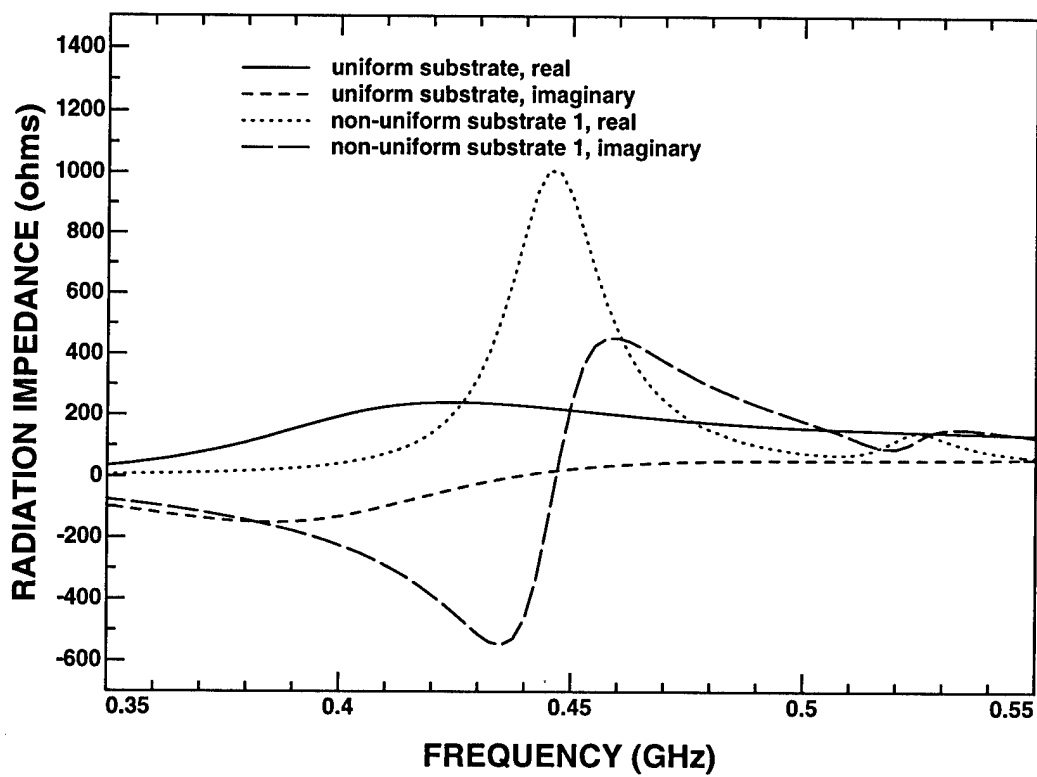
Figure 6.10: Radiation impedance of a horizontal dipole on a uniform and on a non-uniform substrate.
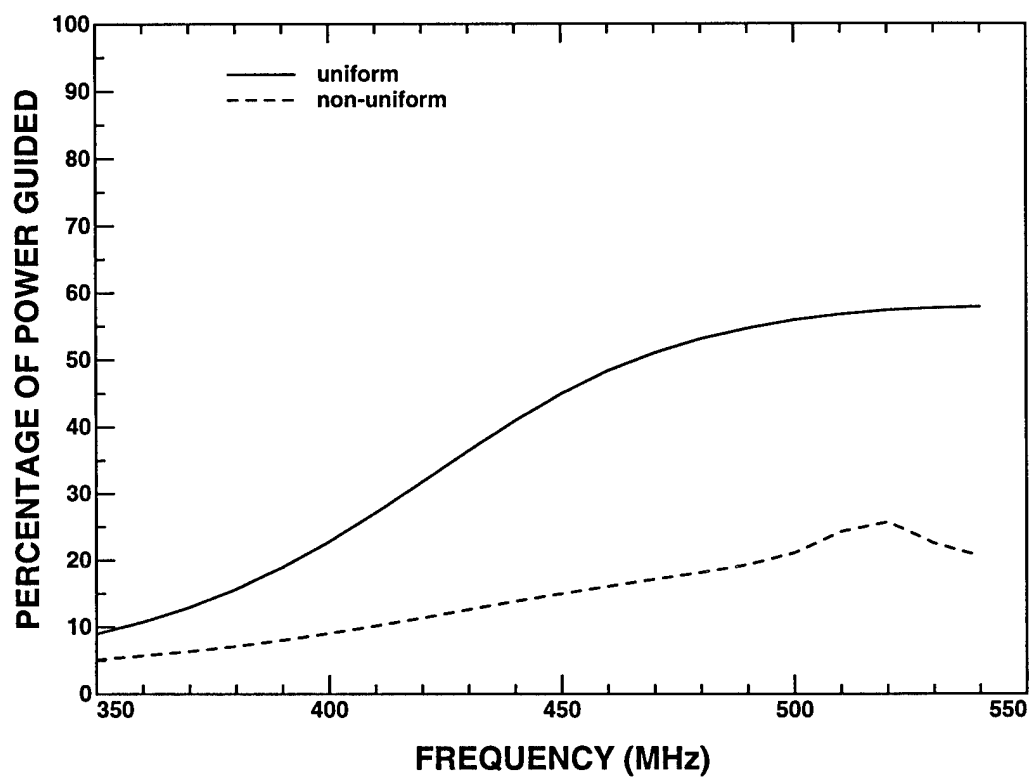
Figure 6.11: Guided power of a horizontal dipole on a uniform and on a non-uniform substrate.
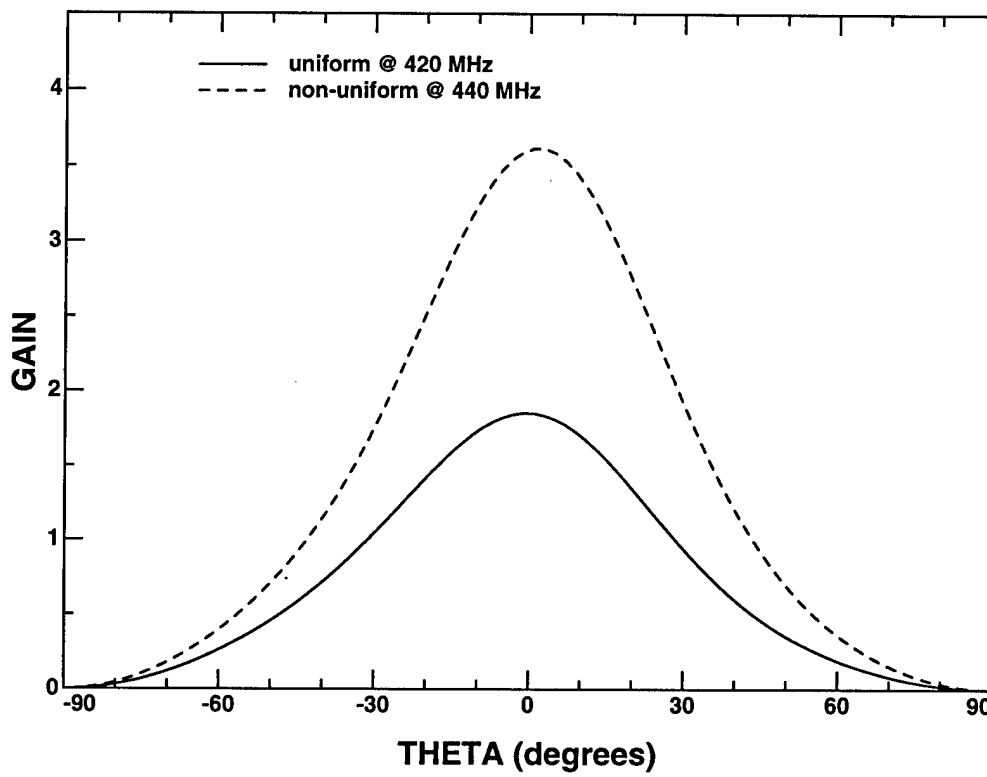
Figure 6.12: Gain pattern for a horizontal dipole on a uniform and on a non-uniform substrate in the x-z plane for the vertical polarization.
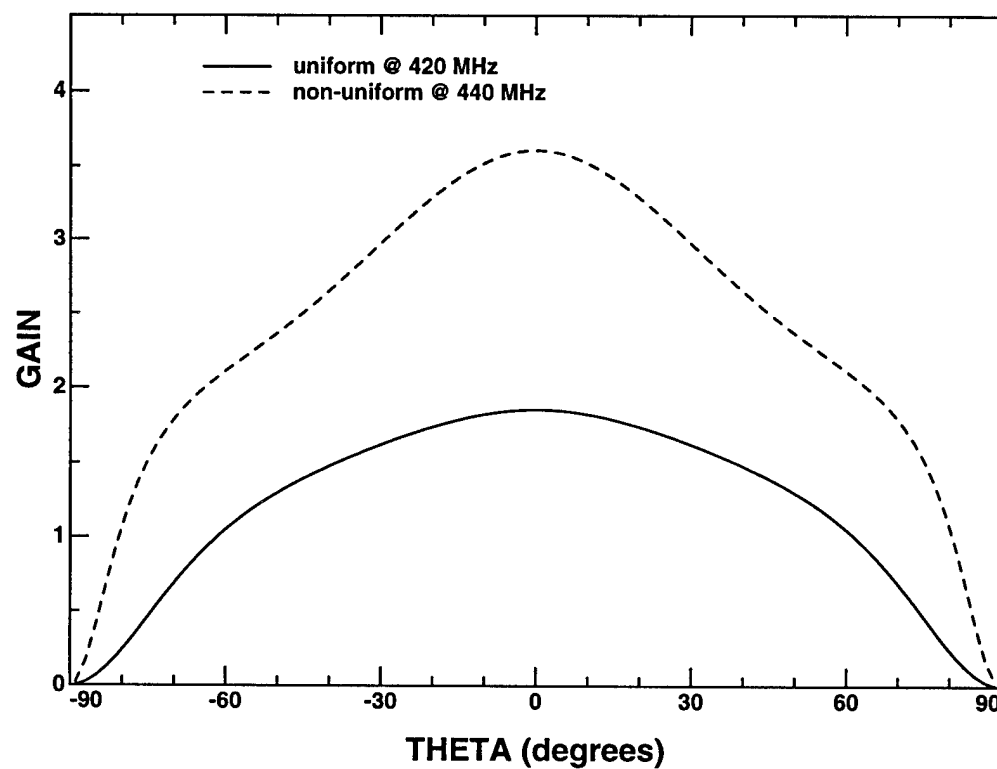
Figure 6.13: Gain pattern for a horizontal dipole on a uniform and on a non-uniform substrate in the y-z plane for the horizontal polarization.

which is consistent with the guided power associated with each case.

Having shown that the non-uniform substrate can reduce losses due to surface waves with simple dipoles, a microstrip patch antenna with an identical substrate is analyzed. The investigated microstrip patch antenna over a non-uniform substrate is shown in Figure 6.1 and has the following dimensions. h is the thickness of the substrate and the height of the microstrip patch.

$$h = 4.8 \text{ cm} \tag{6.113}$$

The dielectric constant of the substrate is

$$\epsilon_r = 12.8 \tag{6.114}$$

w_{ax} and w_{ay} are the dimensions of the microstrip patch.

$$w_{ax} = 10.0 \text{ cm} \tag{6.115}$$

$$w_{ay} = 12.5 \text{ cm} \tag{6.116}$$

w_{px} and w_{py} give the location of the probe excitation from the center of the microstrip patch.

$$w_{px} = 2.5 \text{ cm} \tag{6.117}$$

$$w_{py} = 0 \text{ cm} \tag{6.118}$$

w_{cx} and w_{cy} are the dimensions of the center block of dielectric substrate.

$$w_{cx} = 20 \text{ cm} \tag{6.119}$$

$$w_{cy} = 22.5 \text{ cm} \tag{6.120}$$

w_{rx} and w_{ry} are the widths of the free space ring surrounding the microstrip patch antenna.

$$w_{rx} = 20 \text{ cm} \tag{6.121}$$

$$w_{ry} = 20 \text{ cm} \tag{6.122}$$

The radiation characteristics of this microstrip antenna on a non-uniform substrate are compared with an identical microstrip antenna on a uniform substrate. Figure 6.14 shows the radiation impedance of the two configurations. The resonances for the antenna on the non-uniform substrate are slightly higher since there is more free space in close proximity to the antenna. The resonant frequencies are determined by the dimensions of the antenna and the effective permittivity surrounding it, which in turn, is some average of the dielectrics surrounding the antenna. The higher the permittivity, the denser the medium is electrically, which results in a lower resonant

frequency for this antenna configuration. Since the antenna over the uniform substrate will have a higher effective permittivity than the antenna over the non-uniform substrate, it has slightly lower resonant frequencies.

From Figure 6.14, it is observed that the first two resonances of the antenna over the uniform substrate occur at 295 MHz and at 409 MHz, and that the corresponding resonances for the antenna over the non-uniform substrate occur at 300 MHz and 421 MHz. At these frequencies only the lowest order surface mode, the TM_0 mode, will propagate. While the resonant frequencies were only slightly altered, the bandwidth was significantly changed. The bandwidth for the first resonance changed from 15 MHz to 9 MHz with the addition of the free space ring, and the second resonance changed from 35 MHz to 11 MHz. This reduction in bandwidth is consistent with the fact that the free space ring forms an additional dielectric box resonator which tends to increase the structure's Q which is inversely proportional to an antenna's bandwidth.

The first resonance corresponds to the microstrip patch resonating in the x direction. The first patch resonance occurs when the patch is approximately half a wavelength long in the substrate in the x direction. This resonance in the x direction occurs at a lower frequency than the first one in the y direction because the patch is excited by a probe which is only off-center in the x direction. Hence, the lowest resonance in the x direction occurs at half a wavelength (anti-symmetric mode), while the lowest resonance in the y direction occurs at a full wavelength (symmetric mode). The magnetic-wall approximation without considering fringing fields (see Section 3.4, Equation 3.3 [116],[111]) places the first resonance at 419 MHz. However, the effect
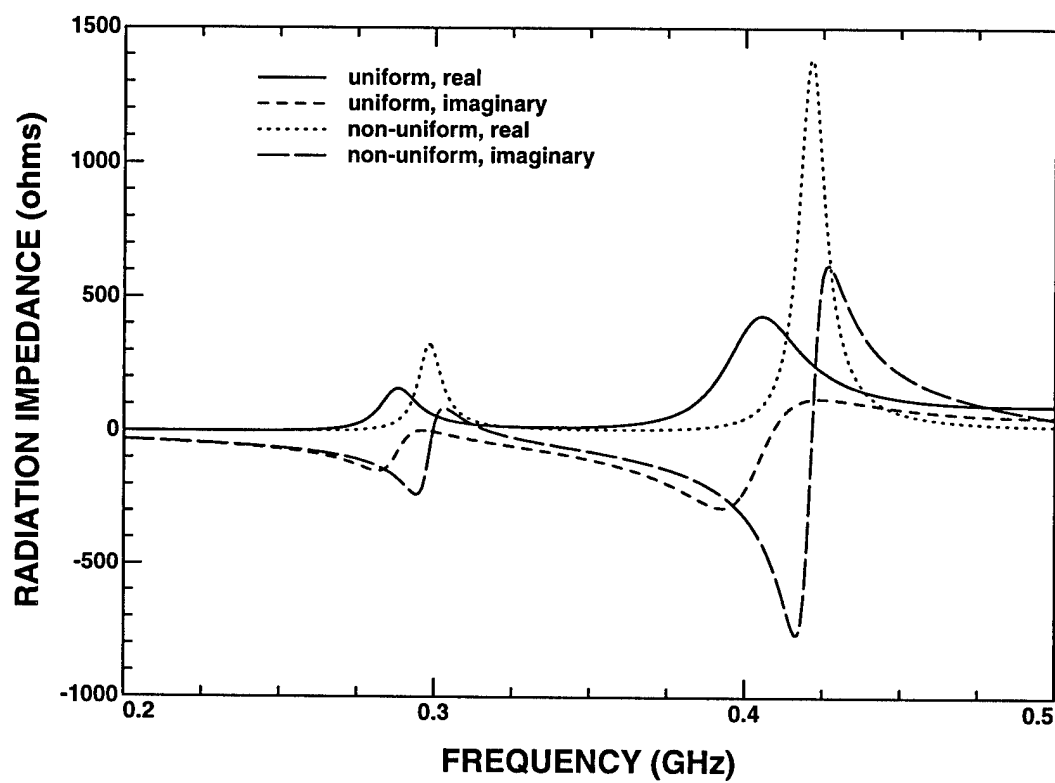
Figure 6.14: Radiation impedance of a microstrip patch antenna over a uniform and over a non-uniform substrate.

of the fringing fields, which in this case is quite significant due to the large height of the patch, will reduce the first resonance to the observed 295 MHz for the uniform substrate case and 300 MHz for the non-uniform substrate case.

The second resonance corresponds to a vertical resonance, where the patch is approximately a half-wavelength in height. The resonance is lower than the resonance associated with a wire without a patch since the capacitive loading of the patch reduces the resonant frequency in this case.

The amounts of power coupled into the substrate or surface waves for the uniform and non-uniform substrate cases are shown in Figure 6.15. The percentage of guided power for the uniform substrate case at its resonant frequency of 295 MHz is 3.9% and for the non-uniform substrate at its resonant frequency of 300 MHz is 2.7%, which is approximately a 30% reduction in the amount of power coupled into guided modes. At slightly higher frequencies, the percentage of guided power greatly increases for both configurations, however the non-uniform substrate case has markedly less guided power than the uniform substrate case. For example, the second resonance of the uniform substrate case of 409 MHZ has 39% of the power guided while the second resonance of the non-uniform substrate case at 421 MHZ has only 14% of the power guided. Upon examining Figure 6.15, it is observed that inserting the discontinuity into the substrate can lower the loss due to surface waves over a wide range of frequencies, at least from 275 MHz to 500 MHz for this case.

The gain for the vertical polarization in the x-z plane is plotted in Figure 6.16 for both configurations for the lower resonance near 300 MHz. The gain for the horizontal polarization is negligible and is not plotted. The gain for the horizontal
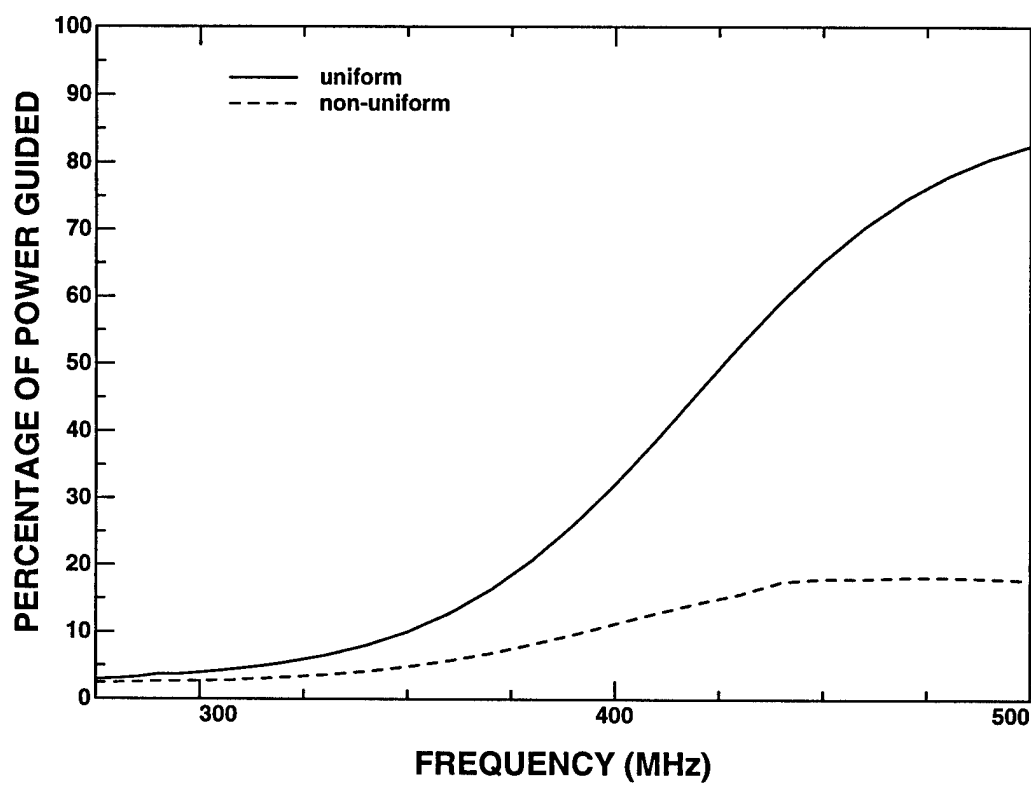
Figure 6.15: Guided power of a microstrip patch antenna over a uniform and over a non-uniform substrate.
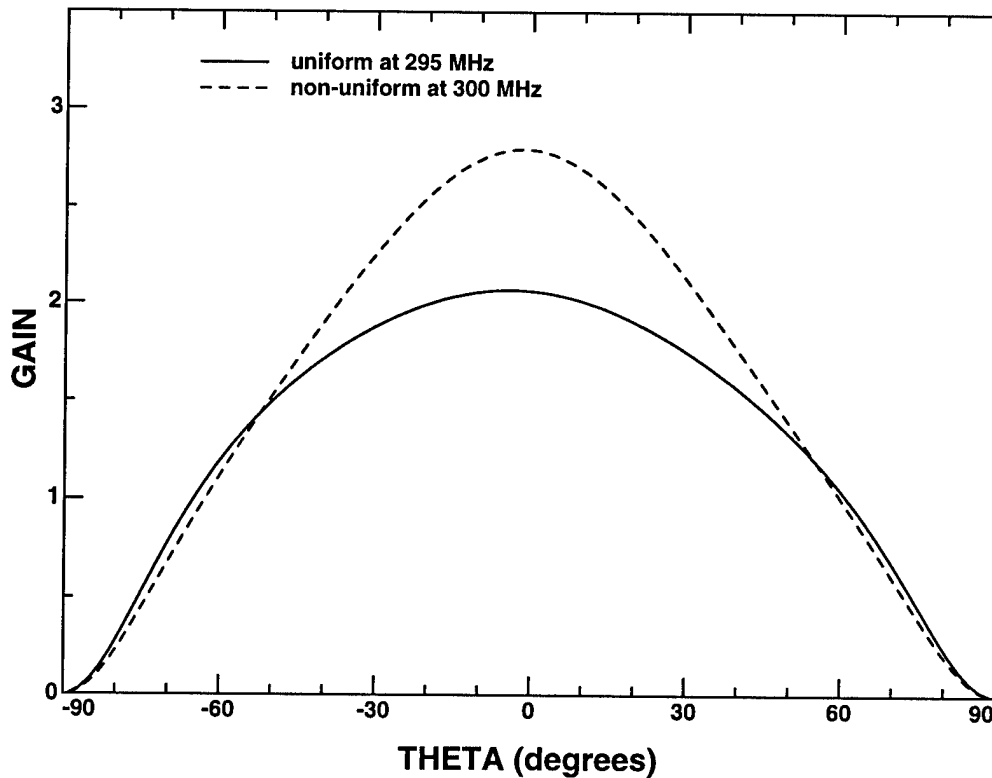
Figure 6.16: Radiation pattern of a microstrip patch antenna over a uniform and over a non-uniform substrate in the x-z plane for the vertical polarization at the first resonance.

polarization in the y-z plane is plotted in Figure 6.17, and for this plane the vertical polarization gain is negligible and not plotted. For the uniform case, the gain is shown at its resonant frequency of 295 MHz, and for the non-uniform case, the gain is shown at its resonant frequency of 300 MHz. In both gain plots, the non-uniform case has a higher gain in the z direction, primarily due to the lower loss to surface waves.

The gain for the vertical polarization in the x-z plane is plotted in Figure 6.18 for both configurations at the second resonance which is near 410 MHz. The gain for the horizontal polarization is negligible and is not plotted. The gain in the y-z plane is plotted in Figure 6.19. For the uniform case, the gain is shown at its resonant
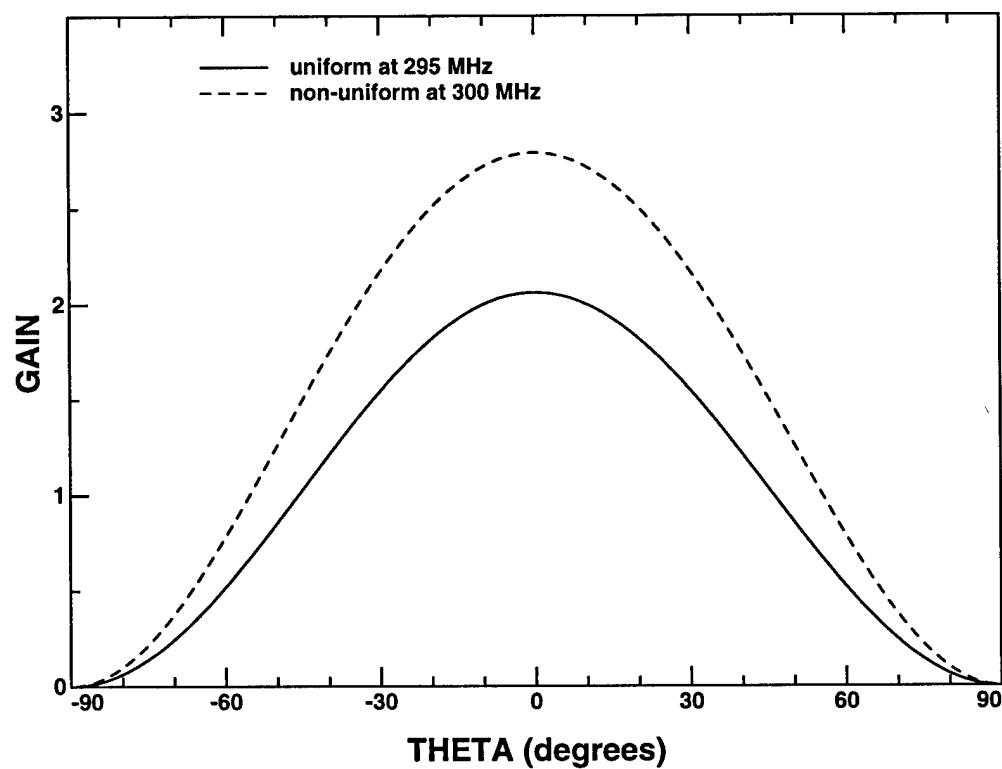
Figure 6.17: Radiation pattern of a microstrip patch antenna over a uniform and over a non-uniform substrate in the y-z plane for the horizontal polarization at the first resonance.
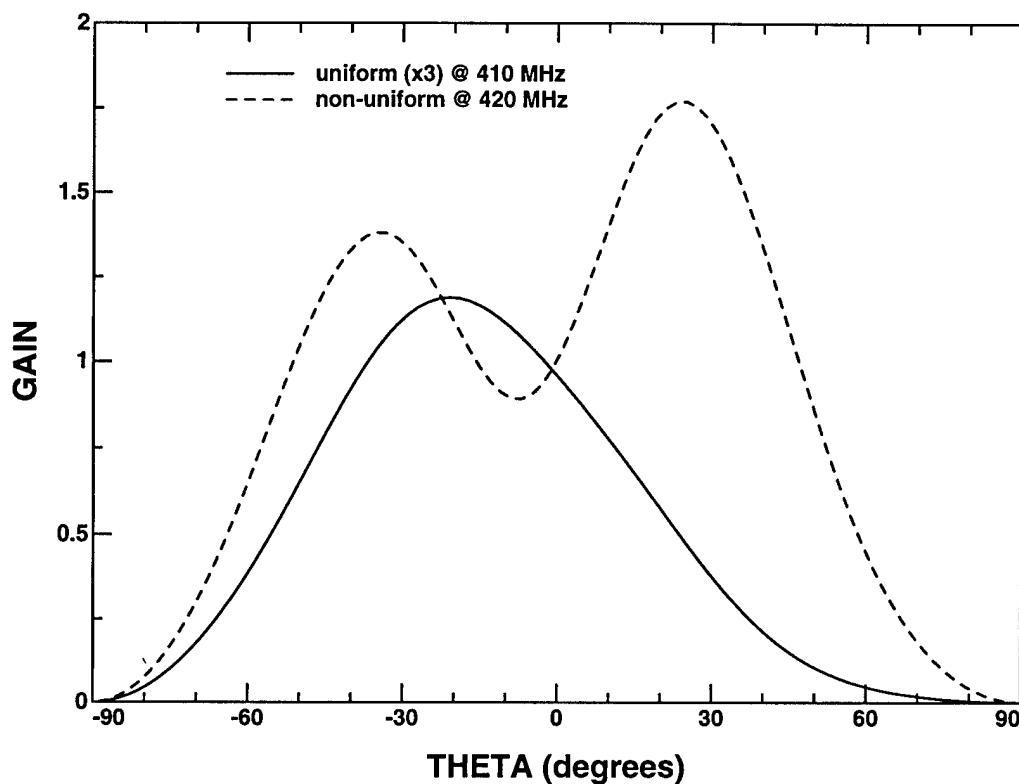
Figure 6.18: Radiation pattern of a microstrip patch antenna over a uniform and over a non-uniform substrate in the x-z plane for the vertical polarization at the second resonance.

frequency of 409 MHz, and for the non-uniform case, the gain is shown at its resonant frequency of 421 MHz. In both gain plots, the non-uniform case has a higher gain by about a factor of 3, due to the significantly lower loss to surface waves.
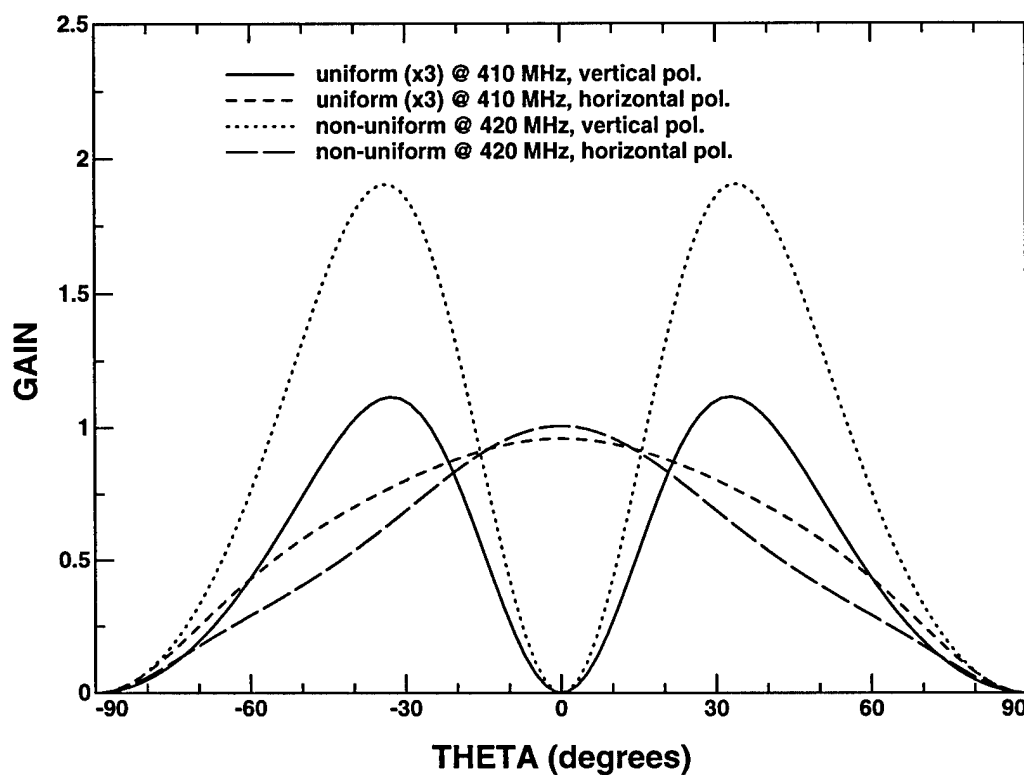
Figure 6.19: Radiation pattern of a microstrip patch antenna over a uniform and over a non-uniform substrate in the y-z plane at the second resonance.

6.4 Conclusions

The finite difference-time domain technique with the perfectly matched layer absorbing boundary conditions successfully analyzed the microstrip patch antenna on a non-uniform substrate. The method proved to be flexible and accurate in handling complex dielectric environments. The use of a non-uniform substrate with a microstrip patch antenna has been shown to significantly reduce the losses due to surface wave generation. However, the addition of the non-uniformity can change the resonant frequency and tends to reduce the bandwidth of the antenna. This research only begins the investigation of possible uses for non-uniform substrates with radiating elements. Other antennas and other substrate configurations can be investigated with only minor modifications to this method.

Chapter 7

Conclusions

The finite difference-time domain technique has been used to successfully analyze a variety of electromagnetic interference and radiation problems. Enhancements to the method are developed and implemented which increase its accuracy and/or efficiency. The basic FD-TD algorithm and the enhancements which were developed and used are described in detail. The technique is demonstrated to be flexible in treating this class of problems which include potentially complex configurations for which neither approximate nor analytical methods are practical.

All the electromagnetic interference problems examined concerned potential radiation sources within a computer system. The design and implementation of components within computers must be conducted with additional consideration for electromagnetic emissions because regulatory electromagnetic emissions limits have been extended to the gigahertz range of frequencies. The avoidance of potentially efficient radiators at the design and development phases is of interest because cost-prohibitive corrective measures ,which are used when assembled systems encounter problems, can be reduced.

Radiation from a VLSI heatsink and package configuration is analyzed using the FD-TD technique. This configuration is of interest for the following reasons. Heatsinks are usually metallic and in close proximity to a chip which uses large amounts of power. The heatsink in conjunction with the ground plane will have radiation characteristics similar to a microstrip patch antenna. The electrical dimensions of the heatsink are comparable to the wavelengths of concern. In light of the ever-increasing power levels used in high-performance integrated circuits, the heatsink is and will continue to be an indispensable component of the VLSI chip packaging configuration.

The heatsink is modeled as a perfectly conducting rectangular slab positioned over a finite-size dielectric medium representing the chip package. The package in turn lies on a dielectric layer on a ground plane of infinite extent, which models the substrate or printed wiring board with at least one reference layer. Simplified excitation sources are used which include electric and magnetic dipoles oriented vertically and horizontally.

In applying the FD-TD technique, a multi-zone gridding scheme was developed and implemented. The multi-zone gridding scheme implemented allowed a high grid resolution in the vicinity of the heatsink without sacrificing overall cell number, thereby allowing increased numerical efficiency for low frequencies. This discretization scheme has the additional advantages of improved geometrical and material modeling.

The analysis of the heatsink, a critical component within the computer packaging environment, illustrated the significance of resonance due to appreciable electrical dimensions on the spurious electromagnetic radiation from the VLSI packaging en-

vironment. Simulations with typical heatsinks dimensions showed the occurrence of resonance in the low gigahertz range. The effects of the presence of a heatsink on the radiation properties of dipole models have been explained and the features of resonant behavior have been presented. The effects of dielectric loading to the cavity and the addition of fins to the heatsink have been examined and quantified. The effectiveness and consequences of exploiting practical heatsink implementation options such as grounding and shielding to reduce electromagnetic emissions have been discussed and quantified using the FD-TD numerical technique.

The radiation properties of modules-on-backplane configurations have been analyzed by using the FD-TD technique and by taking measurements. The modules-on-backplane configuration is of interest because it is commonly used in computers. Also the reference plane dimensions have electrical dimensions which are appreciable at frequencies in the hundreds of megahertz and can function as antennas.

The modules and backplanes, which are printed circuit boards, were modeled as perfectly conducting plates. In implementing the excitation source, a voltage source is applied between the module and the backplane at the location of the connector. The substrate and chips populating the modules were not considered since their effect on the lowest resonances is secondary to the effect on the resonances from the ground planes in the modules.

An extrapolation scheme based on Prony's method was used in conjunction with a relatively short FD-TD time response to efficiently obtain the late time response. This extrapolation method was applied to the time response of the current and voltage on the connector. Prony's method is shown to be useful and to produce accurate

results.

Measurements were performed using an HP 8510 Network Analyzer. The network analyzer was connected to the modules-on-backplane configuration to be tested by a test port cable and semi-rigid coaxial cable. In each of the measurements, the center conductor of the coaxial cable was soldered to the module under test such that the coaxial cable was in contact with at least one of the reference planes in the module. Fairly good agreement was obtained between the measurements and the FD-TD simulations.

The FD-TD analysis provided radiation impedances, which were used as circuit model parameters to estimate overall radiated power. The analysis of the modules-on-backplane configuration has shown that radiation enhancement occurs in the hundreds of megahertz. The addition of modules or an enclosure have been shown to enhance the radiation from the structure. The potential for increased radiation due to the modules-on-backplane configuration has been demonstrated with measurements and numerical simulations.

The finite difference-time domain technique was used to examine the coupling of electromagnetic energy by a wire penetrating a metallic enclosure. Metallic enclosures are commonly used to house computer systems and usually have cables and wires, which transmit data or power, connected to them. Since the metallic enclosure functions both as a electromagnetic shield and as a resonator structure, the coupling of energy from any cables exiting from the box is especially important. The currents on the interior surface of the enclosure can couple to wires exiting the enclosure, and the wire can function as an antenna in the hundreds of MHz frequency range.

Two configurations were examined: a wire extending from and normal to a ground plane which is excited by a coaxial line, and a grounded wire looping up from a metal screen and then penetrating the metal screen and extending out from the screen in a normal direction which is excited by a dipole on the side of the screen on which the wire is grounded. Radiation levels associated with the two configurations were quantified. Significant coupling of electromagnetic energy occured when the admittance of the external wire was matched by the admittance associated with internal side. In the coaxial line configuration, the characteristic admittance of the coaxial line matched the peaks in the external wire's radiation admittance well, and resulted in radiated power only 1 to 2 dB less than the maximum possible. For the infinite metallic screen configurations, fairly significant levels of radiation occured at frequencies where the radiation admittance of the inner wire loop matched the radiation admittance of the external wire antenna. For the two cases examined, the maximum coupling was only 3dB and 6dB less than the power radiated by the dipole in free space.

A "smart" cell in the FD-TD scheme, which can model the radiation admittance of a wire antenna, has been developed and tested. Analytical solutions for the radiation admittance of a straight wire over a ground plane have been recited and approximated using the lumped element model, which consists of a set of series RLC circuits in parallel. The admittance of the lumped element implemented in the FD-TD simulations matched the circuit solution admittance extremely well. Fairly good correlation between lumped element FD-TD simulations and full FD-TD simulations have been obtained for each of the configurations for both radiation admittances and

radiated powers.

One clear limitation of the use of lumped elements in modeling radiation admittances is that the results were only as accurate as the lumped element model of the radiation admittance. The lumped element model considered here most accurately modeled the peaks in the radiation conductance, and hence produced the most accurate results at those frequencies. Correspondingly, the lumped element FD-TD model had increasing errors as the lumped element admittance varied from the theoretical radiation admittance. In the future, if methods for designing passive RLC circuits to more accurately approximate arbitrary admittances as a function of frequency are developed, then the lumped element model could be correspondingly more accurate.

The finite difference-time domain technique with the perfectly matched layer absorbing boundary conditions successfully analyzed the microstrip patch antenna on a non-uniform substrate. The non-uniformity considered was the removal of a rectangular ring of dielectric from the substrate which surrounded the microstrip patch antenna. The method proved to be very flexible in handling the complicated geometries considered here. The perfectly matched layer absorbing boundary condition displayed excellent absorbing behavior at the free space and dielectric interfaces.

Radiation impedance, percentages of guided power, and far-field gain patterns were calculated, presented and discussed. The use of a non-uniform substrate with a microstrip patch antenna has been shown to significantly reduce the losses due to surface wave generation. However, the addition of the non-uniformity was observed to change the resonant frequency and to reduce the bandwidth of the antenna.

This research only begins the investigation of possible uses for non-uniform substrates with radiating elements. Other antennas and other substrate configurations can be investigated with only minor modifications to this method. In particular, the use of multiple rings instead of a single ring of free space could provide additional suppression of surface waves. An alternative to non-uniform substrates would be periodic substrates. In addition, examining arrays of antennas and their mutual coupling would be of interest. The application of the FD-TD method to all of these areas is worthy of consideration.

In summary, this thesis utilized the finite difference-time domain technique in analyzing various problems and discussed enhancements which extended the method's range of usefulness by increasing its accuracy and/or efficiency. Important issues in electromagnetic interference in computer systems were examined and discussed. The use of non-uniform substrates which radiating elements was examined and explored. Finally, some future directions for research in these areas are outlined.

References

[1] Yee, K. S., "Numerical Solution of Initial Boundary Value Problems Involving Maxwell's Equations in Isotropic Media," *IEEE Trans. Antennas Propagat.*, Vol. AP-14, No. 8, pp. 302–307, 1966.

[2] Li, K., M. A. Tassoudji, R. T. Shin, and J. A. Kong, "Simulation of Electromagnetic Radiation and Scattering Using a Finite Difference - Time Domain Technique," *Computer Applications in Engineering Education,* Vol. 1, No. 1, pp. 45-63, 1992/1993.

[3] Li, K., M. A. Tassoudji, R. T. Shin, and J. A. Kong, "Simulation of Electromagnetic Phenomena Using a Finite Difference - Time Domain Technique," *NSF/IEEE Center for Computer Applications in Electromagnetics Education (CAEME): Software Book Volume I,* edited by Dr. Magdy F. Iskander, University of Utah, Salt Lake City, UT, 1991.

[4] Li, K., M. A. Tassoudji, R. T. Shin, and J. A. Kong, "FD-TD Simulation of Electromagnetic Phenomena," *Progress in Electromagnetics Research Symposium,* Cambridge, Massachusetts, July 1-5, 1991.

[5] Li, K., M. A. Tassoudji, R. T. Shin, and J. A. Kong, "Simulation of Electromagnetic Phenomena Using a Finite Difference - Time Domain Technique," *7th Annual Review of Progress in Applied Computational Electromagnetics,* Monterey, California, March 19-21, 1991.

[6] Taflove, A. and M. E. Brodwin, "Numerical Solution of Steady-State Electromagnetic Scattering Problems Using the Time-Dependent Maxwell's Equations," *IEEE Trans. Microwave Theory Tech.,* Vol. MTT-23, No. 8, pp. 623–630, 1975.

[7] Taflove, A., "Review of the Formulation and Application of the Finite-Difference Time-Domain Method for Numerical Modeling of Electromagnetic Wave Interactions with Arbitrary Structures," *Wave Motion,* Vol. 10, No. 12, pp. 547-582, 1988.

[8] Taflove, A., and K. R. Umashankar, "The Finite-Difference Time-Domain Method for Numerical Modeling of Electromagnetic Wave Interactions," *Electromagnetics,* Vol. 10, No. 1-2, pp. 105-126, 1990.

[9] Lee, C. F., R. T. Shin, and J. A. Kong, "Finite Difference Method for Electromagnetic Scattering Problems," *PIER 4: Progress in Electromagnetics Research,* J. A. Kong ed., Elsevier Science Publishing Co., Inc., New York, pp. 373-437, 1991.

[10] Lee, C. F., "Finite Difference Method for Electromagnetic Scattering Problems," Ph.D. Thesis, Department of Electrical Engineering and Computer Science, M. I. T., Cambridge, Massachusetts, 1990.

[11] Morgan, M. A. ed., *PIER 2: Finite Element and Finite Difference Methods in Electromagnetic Scattering,* Elsevier Science Publishing Co., Inc., New York, 1990.

[12] Umashankar K. R. and A. Taflove, "A Novel Method to Analyze Electromagnetic Scattering of Complex Objects," *IEEE Trans. Electromagn. Compat.,* Vol. EMC-24, No. 4, pp. 397-405, 1982.

[13] Li, K., "Electromagnetic Wave Scattering by Surface Discontinuities in a Perfectly Conducting Ground Plane," Master's Thesis, Department of Electrical Engineering and Computer Science, M. I. T., Cambridge, Massachusetts, 1990.

[14] Li, K., R. T. Shin and J. A. Kong, "Radar Cross Section Prediction of Slots in Ground Planes," *Progress in Electromagnetics Research Symposium,* Boston, Massachusetts, July 25-26, 1989.

[15] Oates, J. H., "Propagation and Scattering of Electromagnetic Waves in Complex Environments," Ph.D. Thesis, Department of Electrical Engineering and Computer Science, M. I. T., Cambridge, Massachusetts, 1994.

[16] Schattenburg, M. L., K. Li, R. T. Shin, J. A. Kong, D. B. Olster, and H. I. Smith, "Electromagnetic Calculation of Soft X-ray Diffraction from 0.1-μm Gold Structures," *J. Vac. Sci. Technol. B,* Vol. 9, No. 6, pp. 3232-3236, 1991.

[17] Schattenburg, M. L., K. Li, R. T. Shin, J. A. Kong, and H. I. Smith, "Calculation of Soft X-ray Diffraction from Nanometer-Scale Gold Structures Using a Finite-Difference Time-Domain Method," *Progress in Electromagnetics Research Symposium,* Cambridge, Massachusetts, July 1-5, 1991.

[18] Taflove, A., K. R. Umashankar, and T. G. Jurgens, "Validation of FD-TD Modeling of the Radar Cross Section of Three-Dimensional Structures Spanning up

to Nine Wavelengths," *IEEE Trans. Antennas Propagat.*, Vol. AP-33, No. 6, pp. 662-666, 1985.

[19] Tirkas, P. A., and C. A. Balanis, "Finite-Difference Time-Domain Method for Antenna Radiation," *IEEE Trans. Antennas Propagat.*, Vol. AP-40, No. 3, pp. 334-340, 1992.

[20] Luebbers, R., L. Chen, T. Uno, and S. Adachi, "FDTD Calculation of Radiation Patterns, Impedance, and Gain for a Monopole Antenna on a Conducting Box," *IEEE Trans. Antennas Propagat.*, Vol. AP-40, No. 12, pp. 1577-1583, 1992.

[21] Lam, C. W., "Frequency-Domain and Time-Domain Methods for Analysis of Microstrip Structures in Anisotropic Media," Master's Thesis, Department of Electrical Engineering and Computer Science, M. I. T., Cambridge, Massachusetts, 1989.

[22] Piket-May, M., J. Baron and A. Taflove, "FD-TD Modeling of Digital Signal Propagation in 3-D Microstrip Circuits with Passive and Active Loads," *Progress In Electromagnetics Research Symposium, 1993,* Pasadena, California, July 12-16, 1993.

[23] Piket-May, M., A. Taflove and J. Baron, "FD-TD Modeling of Digital Signal Propagation in 3-D Circuits With Passive and Active Loads," *IEEE Trans. Microwave Theory Tech.*, Vol. MTT-42, No. 8, pp. 1514-1523, 1994.

[24] Sheen, D. M., *Numerical Modeling of Microstrip Circuits and Antennas,* Ph.D. Thesis, Research Laboratory of Electronics, Massachusetts Institute of Technology, Cambridge, Massachusetts, 1991.

[25] Sheen, D. M., S. M. Ali, M. D. Abouzahra, and J. A. Kong, "Application of the Three-Dimensional Finite-Difference Time-Domain Method to the Analysis of Planar Microstrip Circuits," *IEEE Trans. Microwave Theory Tech.*, Vol. MTT-38, No. 7, pp. 849-857, 1990.

[26] Okoniewski, M., "Vector Wave Equation 2-D-FDTD Method for Guided Wave Problems," *IEEE Microwave Guided Wave Letters,* Vol. MGWL-3, No. 9, pp. 307-309, 1993.

[27] Lee, J.-F., R. Panlandech, and R. Mittra, "Modeling Three-Dimensional Discontinuities in Waveguides Using Nonorthogonal FDTD Algorithm," *IEEE Trans. Microwave Theory Tech.*, Vol. MTT-40, No. 2, pp. 346-352, 1992.

[28] Brankovic, V. J., D. V. Krupezevic, and F. Ardnt, "An Efficient Two-Dimensional Graded Mesh Finite-Difference Time-Domain Algorithm for

Shielded or Open Waveguide Structures," *IEEE Trans. Microwave Theory Tech.*, Vol. MTT-40, No. 12, pp. 2272-2277, 1992.

[29] Cangellaris, A. C., M. Gribbons, and G. Sohos, "A Hybrid Spectral/FDTD Method for the Electromagnetic Analysis of Guided Waves in Periodic Structures," *IEEE Microwave Guided Wave Letters,* Vol. MGWL-3, No. 10, pp. 375-377, 1993.

[30] Lam, C. W., S. M. Ali, R. T. Shin, J. A. Kong, and S. Y. Poh, "Radiation from Discontinuities in VLSI Packaging Structures," Progress in Electromagnetics Research Symposium (PIERS), Cambridge, Massachusetts, July 1–5, 1991.

[31] Li, K., C. F. Lee, S. Y. Poh, R. T. Shin, and J. A. Kong, "Application of FD-TD Method to Analysis of Electromagnetic Radiation from VLSI Heatsink Configurations," *IEEE Trans. Electromagn. Compat.,* Vol. MTT-35, No. 2, pp. 204-214, 1993.

[32] Lee, C. F., K. Li, S. Y. Poh, R. T. Shin, and J. A. Kong, "Electromagnetic Radiation from a VLSI Package and Heatsink Configuration," *IEEE International Symposium on Electromagnetic Compatibility Symposium Record,* Cherry Hill, NJ, August 12–16, 1991.

[33] Poh, S. Y., C. F. Lee, K. Li, R. T. Shin, and J. A. Kong, "Electromagnetic Radiation from a VLSI Chip Package Environment," *Progress in Electromagnetics Research Symposium,* Cambridge, Massachusetts, July 1-5, 1991.

[34] Li, K., M. A. Tassoudji, S. Y. Poh, R. T. Shin, and J. A. Kong, "Electromagnetic Radiation from Modules-on-Backplane Configurations in Computer Systems," *Progress in Electromagnetics Research Symposium,* Pasadena, California, July 12–16, 1993.

[35] Li, K., M. A. Tassoudji, S. Y. Poh, M. Tsuk, R. T. Shin, and J. A. Kong, "FD-TD Analysis of Electromagnetic Radiation from Modules-on-Backplane Configurations," submitted to *IEEE Trans. Electromagn. Compat.,* in August, 1994.

[36] Tassoudji, M. A., "Electromagnetic Interference in Electronic Circuits and Systems," Ph.D. Thesis, Department of Electrical Engineering and Computer Science, M. I. T., Cambridge, Massachusetts, 1994.

[37] Tassoudji, M. A., K. Li, R. T. Shin, and J. A. Kong, "Electromagnetic Fields in Metallic Enclosures Lined with Resistive Material," *Progress in Electromagnetics Research Symposium,* Pasadena, California, July 12-16, 1993.

[38] Tirkas, P. A., C. A. Balanis, M. P. Purchine, and G. C. Barber, "Finite-Difference Time-Domain Method for Electromagnetic Radiation, Interference, and Interac-

tion with Complex Structures," *IEEE Electromagn. Compat.,* Vol. EMC-35, No. 2, pp. 192-203, 1993.

[39] Archambeault, B., "EMI Modeling of Air Vents and Slots in Shielded Cabinets," *IEEE International EMC Symposium,* Anaheim, California, Aug. 17–21, 1992.

[40] Moaveni, M. K., "Plane Wave Diffraction by Dielectric Gratings, Finite-Difference Formulation," *IEEE Trans. Antennas Propagat.,* Vol. AP-37, No. 8, pp. 1026-1031, 1989.

[41] Ren, J., O. P. Gandhi, L. R. Walker, J. Faschilla, and C. R. Boerman, "Floquet-Based FDTD Analysis of Two-dimensional Phased Array Antennas," *IEEE Microwave Guided Wave Letters,* Vol. MGWL-4, No. 4, pp. 109-111, 1994.

[42] Veysolgu, M. E., "Direct and Inverse Scattering Models for Random Media and Rough Surfaces," Ph.D. Thesis, Department of Electrical Engineering and Computer Science, M. I. T., Cambridge, Massachusetts, 1994.

[43] Veysolgu, M. E., R. T. Shin, and J. A. Kong, "A Finite-Difference Time-Domain Analysis of Wave Scattering from Periodic Surfaces: Oblique Incidence Case," *J. Electromagn. Waves and Appl.,* Vol. 7, No. 12, pp. 1595-1608, 1993.

[44] Prescott, D. T., and N. V. Shuley, "Extensions to the FDTD Method for the Analysis of Infinitely Periodic Arrays," *IEEE Microwave Guided Wave Letters* Vol. MGWL-4, No. 10, pp. 352-354, 1994.

[45] Harms, P., and R. Mittra, "Implementation of the Periodic Boundary Condition in the Finite-Difference Time-Domain Algorithm for FSS Structures," *IEEE Trans. Antennas Propagat.,* Vol. AP-42, No. 9, pp. 1317-1324, 1994.

[46] Lee, C. F., R. T. Shin, J. A. Kong and B. J. McCartin, "A triangular-grid finite-difference time-domain method for electromagnetic scattering problems," *J. Electromagn. Waves and Appl.,* Vol. JEWA-8, No. 4, pp. 449-470, 1994.

[47] McCartin, B., G. Meltz, R. Mittra, and L. Bahrmasel, "Application of the Control Region Approximation in Conjunction with Absorbing Boundary Conditions to the Direct Solution of Electromagnetic Scattering Problems," *URSI Radio Science Meeting,* Syracuse, New York, pp. 14, 1988.

[48] Holland, R., "A Finite-Difference Time-Domain EMP Code in 3D Spherical Coordinates," *IEEE Trans. Nuclear Science,* Vol. NS-30, No. 6, pp. 4592-4595, 1983.

[49] Holland, R., "Finite-Difference Solution of Maxwell's Equations in Generalized Nonorthogonal Coordinates," *IEEE Trans. Nuclear Science,* Vol. NS-30, No. 6, pp. 4589-4591, 1983.

[50] Yee, K. S., and J. S. Chen, "Conformal Hybrid Finite Difference Time Domain and Finite Volume Time Domain," *IEEE Trans. Antennas Propagat.,* Vol. AP-42, No. 10, pp. 1450-1455, 1994.

[51] Fusco, M., "FDTD algorithm in curvilinear coordinates," *IEEE Trans. Antennas Propagat.,* Vol. AP-38, No. 1, pp. 76-89, 1990.

[52] Kim, I. S., and W. J. R. Hoefer, "A local mesh refinement algorithm for the time-domain finite-difference method using Maxwell's curl equations," *IEEE Trans. Microwave Theory Tech.,* Vol. MTT-38, No. 6, pp. 812–815, 1990.

[53] Prescott, D. T., N. V. Shuley, "A Method for Incorporating Different Sized Cells into the Finite-Difference Time-Domain Analysis Technique," *IEEE Microwave Guided Wave Letters,* Vol. MGWL-2, No. 11, pp. 434-436, 1992.

[54] Zivanovic, S. S., K. S. Yee, and K. K. Mei, "A subgridding method for the time-domain finite-difference method to solve Maxwell's equations," *IEEE Trans. Microwave Theory Tech.,* Vol. MTT-39, No. 3, pp. 471-479, 1991.

[55] Kunz, K. S., and L. Simpson, "A technique for increasing the resolution of finite-difference solutions to the Maxwell equation," *IEEE Trans. Electromagn. Compat.,* Vol. EMC-23, No. 11, pp. 419-422, 1981.

[56] Luebbers, R. J., "Lossy Dielectrics in FDTD," *IEEE Trans. Antennas Propagat.,* Vol. AP-41, No. 11, pp. 1586-1588, 1993.

[57] Gandhi, O. P., B.-Q. Gao, and J.-Y. Chen, "A Frequency-Dependent Finite-Difference Time-Domain Formulation for General Dispersive Media," *IEEE Trans. Microwave Theory Tech.,* Vol. MTT-41, No. 4, pp. 658-665, 1993.

[58] Hunsberger, F., R. Luebbers, and K. Kunz, "Finite-Difference Time-Domain Analysis of Gyrotropic Media – I: Magnetized Plasma," *IEEE Trans. Antennas Propagat.,* Vol. AP-40, No. 12, pp. 1489-1495, 1992.

[59] Beggs, J. H., R. J. Luebbers, K. S. Yee, and K. S. Kunz, "Finite-Difference Time-Domain Implementation of Surface Impedance Boundary Conditions," *IEEE Trans. Antennas Propagat.,* Vol. AP-40, No. 1, pp. 49-56, 1992.

[60] Luebbers, R. J., K. Kunz, "FDTD modeling of Thin Impedance Sheets," *IEEE Trans. Antennas Propagat.,* Vol. AP-40, No. 3, pp. 349-351, 1992.

[61] Maloney, J. G., G. S. Smith, "The Use of Surface Impedance Concepts in the Finite Difference Time Domain Method," *IEEE Trans. Antennas Propagat.,* Vol. AP-40, No. 1, pp. 38-48, 1992.

[62] Maloney, J. G., G. S. Smith, "The Efficient Modeling of Thin Material Sheets in the Finite-Difference Time-Domain (FDTD) Method," *IEEE Trans. Antennas Propagat.,* Vol. AP-40, No. 3, pp. 323-330, 1992.

[63] Maloney, J. G., G. S. Smith, "A Comparison of Methods for Modeling Electrically Thin Dielectric and Conducting Sheets in the Finite-Difference Time-Domain Method," *IEEE Trans. Antennas Propagat.,* Vol. AP-41, No. 5, pp. 690-694, 1993.

[64] Lee, C. F., R. T. Shin, and J. A. Kong, "Time Domain Modeling of Impedance Boundary Condition," *IEEE Trans. Microwave Theory Tech.,* Vol. MTT-40, No. 9, pp. 1847-1850, 1992.

[65] Wu, L. K., L. T. Han, "Implementation and Application of Resistive Sheet Boundary Condition in the Finite-Difference Time-Domain Method," *IEEE Trans. Antennas Propagat.,* Vol. AP-40, No. 6, pp. 628-633, 1992.

[66] Zheng, E., R. F. Harrington, and J. R. Mautz, "Electromagnetic Coupling Through a Wire-Penetrated Small Aperture in an Infinite Conducting Plane," *IEEE Trans. Electromagn. Compat.,* Vol. EMC-35, No. 2, pp. 295-300, 1993.

[67] Mur, G., "Absorbing Boundary Conditions for the Finite-Difference Approximation of the Time-Domain Electromagnetic-Field Equations," *IEEE Trans. Electromagn. Compat.,* Vol. EMC-23, No. 4, pp. 377–382, 1981.

[68] Engquist, B. and A. Majda, "Absorbing Boundary Conditions for the Numerical Simulation of Waves," *Math. Comp.,* Vol. 31, No. 139, pp. 629–651, 1977.

[69] Bayliss, A., C. I. Goldstein, and E. Turkel, "On Accuracy Conditions for the Numerical Computation of Waves," *J. of Comp. Physics,* Vol. 59, pp. 396-404, 1985.

[70] Bayliss, A. and E. Turkel, "Radiation Boundary Conditions for Wave-Like Equations," *Comm. on Pure and App. Math.,* Vol. 33, pp. 707-725, 1980.

[71] Higdon, R. L., "Absorbing Boundary Conditions for Difference Approximations to the Multi-Dimensional Wave Equation," *American Math. Soc.,* Vol. 47, No. 176, pp. 437-459, 1986.

[72] Higdon, R. L., "Numerical Absorbing Boundary Conditions for the Wave Equation," *Math. Comp.,* Vol. 49, No. 179, pp. 65-90, 1987.

[73] Trefethen, L. N., and L. Halpern, "Well-Posedness of One-Way Wave Equations and Absorbing Boundary Conditions," *Math. Comp.*, Vol. 47, No. 176, pp. 421-435, 1986.

[74] Moore, T. G., J. G. Blaschak, A. Taflove, and G. A. Kriegsmann, "Theory and Application of Radiation Boundary Operators," *IEEE Trans. Antennas Propagat.*, Vol. AP-36, No. 12, pp. 1797-1812, 1988.

[75] Liao, Z. P., H. L. Wong, B. P. Yang, and Y. F. Yuan, "A transmitting boundary for transient wave analysis," *Scintia Sinica A*, pp. 1063-1076, October, 1984.

[76] Fang, J., "Absorbing Boundary Conditions Applied to Model Wave Propagation in Microwave Integrated Circuits," *IEEE Trans. Microwave Theory Tech.*, Vol. MTT-42, No. 8, pp. 1506-1513, 1994.

[77] Lee, C. F., R. T. Shin, J. A. Kong and B. J. McCartin, "Absorbing Boundary Conditions on Circular and Elliptic Boundaries," *J. Electromagn. Waves and Appl.*, Vol. JEWA-4, No. 10, pp. 945-962, 1990.

[78] Berenger, J.-P., "A perfectly matched layer for absorption of electromagnetic waves," *J. Computational Physics*, Vol. 114, pp. 185-200, 1994.

[79] Reuter, C. E., R. M. Joseph, E. T. Thiele, D. S. Katz, and A. Taflove, "Ultrawideband Absorbing Boundary Condition for Termination of Waveguiding Structures in FD-TD Simulations," *IEEE Microwave Guided Wave Letters*, Vol. MGWL-4, No. 10, pp. 344-346, 1994.

[80] Mittra, R., and Ü. Pekel, "A New Look at the Perfectly Matched Layer (PML) Concept from the Reflectionless Absorption of Electromagnetic Waves," *IEEE Microwave Guided Wave Letters*, Vol. MGWL-5, No. 3, pp. 84-86, 1995.

[81] Rappaport, C. M., "Perfectly Matched Absorbing Boundary Conditions Based on Anisotropic Lossy Mapping of Space," *IEEE Microwave Guided Wave Letters*, Vol. MGWL-5, No. 3, pp. 90-92, 1995.

[82] Chew, W. C., and W. H. Weedon, "A 3D Perfectly Matched Medium from Modified Maxwell's Equations with Stretched Coordinates," *Microwave Optical Tech. Letters*, Vol. 7, No. 13, pp. 599-604, 1994.

[83] Katz, D. S., E. T. Thiele, and A. Taflove, "Validation and Extension to Three Dimensions of the Berenger PML Absorbing Boundary Condition for FD-TD Meshes," *IEEE Microwave Guided Wave Letters*, Vol. MGWL-4, No. 8, pp. 268-270, 1994.

[84] Harrington, R. F., *Field Computation by Moment Methods,* Robert E. Krieger Publishing Co., Inc., Florida, 1968.

[85] Harrington, R. F., "Matrix Methods for Fields," *Proc. IEEE,* Vol. 55, No. 2, pp. 136-149, 1967.

[86] Arvas, E., R. F. Harrington and J. R. Mautz, "Radiation and Scattering from Electrically Small Conducting Bodies of Arbitrary Shape," *IEEE Trans. Antennas Propagat.,* Vol. AP-34, No. 1, pp. 66-77, 1986.

[87] Mittra, R. ed., *Computer Techniques for Electromagnetics,* Pergamon Press, New York, 1973.

[88] Mittra, R. ed., *Numerical and Asymptotic Techniques for Electromagnetics,* Springer-Verlag, New York, 1975.

[89] Moore, J. and R. Pizer, *Moment Methods in Electromagnetics,* John Wiley & Sons, Inc., New York, 1984.

[90] Newman, E. H. (1988),"Simple Examples of the Method of Moments in Electromagnetics," *IEEE Trans. Educ.,* Vol. E-31, No. 3, pp. 193-200, 1988.

[91] Tsai, L. L. and C. E. Smith, "Moment Methods in Electromagnetics for Undergraduates," *IEEE Trans. Educ.,* Vol. E-21, pp. 14-22, 1978.

[92] Asvestas, J. S., "Line Integrals and Physical Optics. Part I. The Transformation of the Solid-Angle Surface Integral to a Line Integral," *J. Opt. Soc. Am. A,* Vol. 2, pp. 891-895, 1985.

[93] Asvestas, J. S., "Line Integrals and Physical Optics. Part II. The Conversion of the Kirchoff Surface Integral to a Line Integral," *J. Opt. Soc. Am. A,* Vol. 2, pp. 896-902, 1985.

[94] Atkins, R. G., "Effect of Multiple Scattering on the Radar Cross Section of Polygonal Plate Structures," Master's Thesis, Research Laboratory of Electronics, M. I. T., Cambridge, Massachusetts, 1987.

[95] James, G., *Geometrical Theory of Diffraction for Electromagnetic Waves,* Peter Peregrinus Ltd., London, England, 1976.

[96] Kouyoumjian, R. G., P. H. Pathak, "A Uniform Geometrical Theory of Diffraction for an Edge in a Perfectly Conducting Surface," *IEEE Proc.,* Vol. 62, pp. 1448-1461, 1974.

[97] Plonus, M. A., R. Williams, and S. C. Wang, "Radar Cross Section of Curved Plates using Geometrical and Physical Diffraction Techniques," *IEEE Trans. Antennas Propagat.,* Vol. AP-26, No. 3, pp. 488-493, 1978.

[98] Bowman, J. J., T. B. A. Senior, and P. L. E. Uslenghi, *Electromagnetic and Acoustic Scattering by Simple Shapes,* John Wiley & Sons, Inc., New York, 1969.

[99] Knott, E. F., J. F. Shaeffer and M. T. Tuley, *Radar Cross Section: Its Prediction, Measurement, and Reduction,* Artech House, Inc., Dedham, Massachusetts, 1986.

[100] Ruck, G. T., D. E. Barrick, W. D. Stuart, and C. K. Krichbaum, *Radar Cross Section Handbook,* Vol. 1 and 2, Plenum Press, New York, 1970.

[101] Skolnik, M. I. *Introduction to Radar Systems,* McGraw-Hill, New York, 1962.

[102] Weston, D. A., *Electromagnetic Compatibility: Principles and Applications,* Marcel Dekker, Inc., New York, 1991.

[103] Duff, W. G., *Fundamentals of Electromagnetic Compatibility,* Interference Control Technologies, Inc., Gainesville, Virginia, 1988.

[104] Eckert, J. K., *Commercial EMC Standards of the United States,* Interference Control Technologies, Inc., Gainesville, Virginia, 1988.

[105] National Telecommunications and Information Administration, U.S. Department of Commerce, *Manual of Regulations and Procedures for Federal Radio Frequency Management,* May 1992 edition, revised January and May 1993.

[106] Kong, J. A., *Electromagnetic Wave Theory,* Wiley-Interscience, New York, 1986.

[107] Kong, J. A. and L. C. Shen, *Applied Electromagnetism,* Brooks/Cole Engineering Division, Monterey, California, 1983.

[108] Harrington, R. F., *Time-Harmonic Electromagnetic Fields,* McGraw-Hill, New York, 1961.

[109] Van Bladel, J., *Electromagnetic Fields,* McGraw-Hill, Inc., New York, 1964.

[110] Haus, H. A., *Waves and Fields in Optoelectronics,* Prentice-Hall, Inc., New Jersey, 1984.

[111] Bahl, I. J., and P. Bhartia, *Microstrip Antennas,* Artech House, New York, 1986.

[112] Gupta, K. C., and M. D. Abouzahra, ed., *Analysis and Design of Planar Microwave Components,* IEEE Press, New Jersey, 1994.

[113] Evans, R., and M. Tsuk, "Modeling and measurement of a high performance computer power distribution system," *IEEE Trans. on Components, Packaging, and Manufacturing Technology,* Part B, Vol. 17, No. 4, pp. 467–471, 1994.

[114] Ko, W. L., and R. Mittra, "A Combination of FD-TD and Prony's Methods for Analyzing Microwave Integrated Circuits," *IEEE Trans. Microwave Theory Tech.,* Vol. MTT-39, No. 12, pp. 2176–2180, 1991.

[115] Chen, J., C. Wu, T. K. Y. Lo, K.-L. Wu, and J. Litva, "Using Linear and Nonlinear Predictors to Improve the Computational Efficiency of the FD-TD Algorithm," *IEEE Trans. Microwave Theory Tech.,* Vol. MTT-42, No. 10, pp. 1992-1997, 1994.

[116] Balanis, C. A., *Antenna Theory: Analysis and Design,* Harper & Row, Publishers, New York, 1982.

[117] Kraus, J. D., *Antennas,* 2nd ed., McGraw-Hill Book Company, New York, 1988.

[118] Lo, Y. T., and S. W. Lee, *Antenna Handbook,* Van Nostrand Reinhold Company Inc., New York, 1988.

[119] Grounds, P. W., and K. J. Webb, "Numerical Analysis of Finite Frequency Selective Surfaces with Rectangular Patches of Various Aspect Ratios," *IEEE Trans. Antennas Propagat.,* Vol. AP-39, No. 5, pp. 569-574, 1991.

[120] Janhsen, A., and V. Hansen, "Arrays of finite or infinite extent in multilayered media for use as passive frequency-selective surfaces," *IEE Proc.-H,* Vol. 138, No. 1, pp. 1-8, 1991.

[121] Mittra, R., C. H. Chan, and T. Cwik, "Techniques for Analyzing Frequency Selective Surfaces – A Review," *Proc. IEEE,* Vol. 76, No. 12, pp. 1593-1615, 1988.

[122] Magnusson, R., S. S. Wang, T. D. Black, and A. Sohn, "Resonance Properties of Dielectric Waveguide Gratings: Theory and Experiments at 4-18 GHz," *IEEE Trans. Antennas Propagat.,* Vol. AP-42, No. 4, pp. 567-569, 1994.

[123] Pous, R., and D. M. Pozar, "A Frequency-Selective Surface Using Aperture-Coupled Microstrip Patches," *IEEE Trans. Antennas Propagat.,* Vol. AP-39, No. 12, pp. 1763-1768, 1991.

[124] Kipp, R. A., and C. H. Chan, "A Numerically Efficient Technique for the Method of Moments Solution for Planar Periodic Structures in Layered Media," *IEEE Trans. Microwave Theory Tech.*, Vol. MTT-42, No. 4, pp. 635-643, 1994.

[125] Schimert, T. R., A. J. Brouns, C. H. Chan, and R. Mittra, "Investigation of Millimeter-Wave Scattering from Frequency Selective Surfaces," *IEEE Trans. Microwave Theory Tech.*, Vol. MTT-39, No. 2, pp. 315-322, 1991.

[126] Chung, S.-J., and J.-L. Chen, "A Modified Finite Element Method for Analysis of Finite Periodic Structures," *IEEE Trans. Microwave Theory Tech.*, Vol. MTT-42, No. 7, pp. 1561-1566, 1994.

[127] Chan, C. H., and R. Mittra, "The Propagation Characteristics of Signal Lines Embedded in a Multilayered Structure in the Presence of a Periodically Perforated Ground Plane," *IEEE Trans. Microwave Theory and Tech.*, Vol. MTT-36, No. 6, pp. 968-975, 1988.

[128] Glandorf, F. J., and I. Wolff, "A Spectral-Domain Analysis of Periodically Nonuniform Microstrip Lines," *IEEE Trans. Microwave Theory and Tech.*, Vol. MTT-35, No. 3, pp. 336-343, 1987.

[129] Nair, N. V., and A. K. Mallick, "An Analysis of a Width-Modulated Microstrip Periodic Structure," *IEEE Trans. Microwave Theory Tech.*, Vol. MTT-32, No. 2, pp. 200-204, 1984.

[130] Ghaderi, M., and A. Bhattacharyya, "Investigations on Planar Periodic Structures with Uniform Microstrip Lines," *Microwave Optical Tech. Letters,* Vol. 3, No. 10, pp. 370-372, 1990.

[131] Elachi, C., "Waves in Active and Passive Periodic Structures: A Review," *Proc. IEEE,* Vol. 64, No. 12, pp. 1666-1698, 1976.

[132] Peng, S. T., T. Tamir, and H. L. Bertoni, "Theory of Periodic Dielectric Waveguides," *IEEE Trans. Microwave Theory Tech.*, Vol. MTT-23, No. 1, pp. 123-133, 1975.

[133] Wu, K., V. Dzougaiev, and P. Saguet, "Complete theoretical and experimental analysis on properties of planar periodic waveguides," *IEE Proc., Pt. H,* Vol. 135, No. 1, pp. 27-33, 1988.

[134] Wu, K., P. Saguet, and A. Coumes, "Toward a Unified Efficient Algorithm for Characterizing Planar Periodic Waveguides and Their Applications to MIC and MMIC Circuits," *IEEE Trans. Microwave Theory Tech.*, Vol. MTT-39, No. 3, pp. 583-586, 1991.

[135] Tsuji, M., S. Matsumoto, H. Shigeasawa, and K. Takiyama, "Guided-Wave Experiments with Dielectric Waveguides Having Finite Periodic Corrugation," *IEEE Trans. Microwave Theory Tech.,* Vol. MTT-31, No. 4, pp. 337-344, 1983.

[136] Araki, K., and T. Itoh, "Analysis of Periodic Ferrite Slab Waveguides by Means of Improved Perturbation Method," *IEEE Trans. Microwave Theory Tech.,* Vol. MTT-29, No. 9, pp. 911-916, 1981.

[137] Ogusu, K. "Propagation Properties of a Planar Dielectric Waveguide with Periodic Metallic Strips," *IEEE Trans. Microwave Theory Tech.,* Vol. MTT-29, No. 1, pp. 16-21, 1981.

[138] Rubin, B. J., and H. L. Bertoni, "Waves Guided by Conductive Strips Above a Periodically Perforated Ground Plane," *IEEE Trans. Microwave Theory Tech.,* Vol. MTT-31, No. 7, pp. 541-549, 1983.

[139] Liao, S. Y., *Microwave Devices and Circuits,* 2nd ed., Prentice-Hall, Inc., New Jersey, 1985.

[140] Pozar, D. M., "Considerations for Millimeter Wave Printed Antennas," *IEEE Trans. Antennas and Propagat.,* Vol. AP-31, No. 5, pp. 740-747, 1983.

[141] Bahl, I. J., and P. Bhartia, "Design considerations in microstrip antenna fabrication," *Conference Proceedings of the 10th European Microwave Conference,* Warsaw, Poland, pp. 122-126, Sept. 8-12, 1980.

[142] Helszajn, J., *Microwave Planar Passive Circuits and Filters,* John Wiley & Sons, Inc., New York, 1994.

[143] Wadell, B. C., *Transmission Line Design Handbook,* Artech House, Boston, Massachusetts, 1991.

[144] Konishi, Y., ed., *Microwave Integrated Circuits,* Marcel Dekker, Inc., New York, 1991.

[145] Abramowitz, M. and I. A. Stegun, *Handbook of Mathematical Functions with Formulas, Graphs, and Mathematical Tables,* National Bureau of Standards, Department of Commerce, Washington D. C., 1964.

[146] Gradshteyn, I. S. and I. M. Ryzhik, *Table of Integrals, Series, and Products,* Academic Press, New York, 1965.

[147] Davidovitz, M., "Extension of the E-Plane Scanning Range in Large Microstrip Arrays by Substrate Modification," *IEEE Microwave Guided Wave Letters,* Vol. MGWL-2, No. 12, pp. 492-494, 1992.

[148] Haddad, P. R., and D. M. Pozar, "Anomalous Mutual Coupling Between Microstrip Antennas," *IEEE Trans. Antennas Propagat.*, Vol. AP-42, No. 11, pp. 1545-1549, 1994.

[149] Liu, C.-C., J. Shmoys, and A. Hessel, "E-Plane Performance Trade-Offs in Two-Dimensional Microstrip-Patch Element Phased Arrays," *IEEE Trans. Antennas Propagat.*, Vol. AP-30, No. 6, pp. 1201-1206, 1982.

[150] Pozar, D. M., and D. M. Schaubert, "Analysis of Infinite Array of Rectangular Microstrip Patches with Idealized Probe Feeds," *IEEE Trans. Antennas Propagat.*, Vol. AP-32, No. 10, pp. 1101-1107, 1984.

[151] Agi, K., E. R. Brown, O. B. McMahon, C. Dill III, and K. J. Malloy, "Design of ultrawideband photonic crystals for broadband antenna applications," *Electronics Letters*, Vol. 30, No. 25, pp. 2166-2167, 1994.

[152] Brown, E. R., C. D. Parker, and E. Yablonovitch, "Radiation properties of a planar antenna on a photonic-crystal substrate," *J. Opt. Soc. Am. B.*, Vol. 10, No. 2, pp. 404-407, 1993.

[153] Atkins, R. G., "Microwave Scattering and Synthetic Aperture Radar Imaging of Targets Buried in Random Media," Ph.D. Thesis, Research Laboratory of Electronics, M. I. T., Cambridge, Massachusetts, 1993.